

Optimization of Resin Infusion Processing for Composite Materials:  
Simulation and Characterization Strategies

A thesis accepted by the Faculty of Aerospace Engineering and Geodesy of the  
University of Stuttgart in partial fulfillment of the requirements for the degree of  
Doctor of Engineering Sciences (Dr.-Ing.)

by

Andrew George

born in California, USA

Committee chair: Prof. Dr.-Ing. Klaus Drechsler

Committee member: Prof. Staffan Lundström Ph.D.

Committee member: Prof. Dipl.-Ing. Rudolf Voit-Nitschmann

Date of Defense: 15 March 2011

Institute of Aircraft Design

University of Stuttgart

2011



## TABLE OF CONTENTS

English Abstract.....	v
Deutscher Abstract .....	vii
Nomenclature .....	ix
1 Introduction .....	1
2 Literature review.....	5
2.1 Composite materials .....	5
2.1.1 Fibers.....	6
2.1.2 Resins .....	8
2.2 Processes.....	9
2.2.1 Hand lay-up .....	9
2.2.2 Prepreg.....	9
2.2.3 Resin infusion .....	10
2.3 Flow modeling.....	18
2.3.1 Darcy’s law .....	19
2.3.2 Numerical simulation .....	21
2.3.3 Permeability .....	23
2.3.4 Compressibility.....	37
2.3.5 Viscosity .....	46
2.3.6 Dual-scale flow effects .....	53
2.3.7 Vacuum bag sealing of fabric surface .....	57
2.3.8 Void prediction.....	57
2.4 Final part characterization .....	61
2.4.1 Fiber volume content measurement .....	61
2.4.2 Void content measurement .....	63
3 Materials .....	66
3.1 NCF.....	66
3.2 TFP.....	68
3.3 Binders .....	69
3.4 Braids.....	69
3.5 Fiber volume content calculation .....	70
4 Modeling experimentation .....	73
4.1 VARI benchmark infusions .....	73
4.1.1 Results .....	76
4.2 In-plane permeability characterization.....	79
4.2.1 Test fluid.....	79
4.2.2 Equipment.....	80
4.2.3 Results .....	82
4.2.4 Validation of results .....	90
4.2.5 Saturated vs. unsaturated comparison.....	91
4.2.6 Summary of in-plane permeability characterization .....	92
4.3 Through-thickness permeability .....	93
4.3.1 Materials and experimental procedure .....	93
4.3.2 Data analysis .....	97

4.3.3	Results .....	106
4.3.4	Validation by variable variation .....	109
4.3.5	Validation by numerical simulation .....	112
4.4	Compressibility characterization .....	114
4.4.1	Experimental procedure .....	115
4.4.2	Results .....	118
4.4.3	Fluid differences.....	120
4.4.4	Comparison of materials.....	124
4.4.5	Viscoelasticity.....	128
4.4.6	Maximum fiber content .....	130
4.4.7	Model validation .....	131
4.5	Viscosity characterization .....	132
4.5.1	Non-isothermal curing model.....	132
4.5.2	Model validation .....	136
4.5.3	Temperature distribution modeling .....	139
4.5.4	Theoretical temperature distribution .....	144
4.5.5	Summary: sensitivity to exotherm.....	146
4.6	Pressure gradient characterization.....	150
4.6.1	Inlet pipe pressure loss .....	151
4.6.2	Pressure differences for dimensionality .....	152
4.6.3	Capillary pressure.....	153
4.7	Vacuum bag sealing of tows .....	156
5	Coupled model solution results .....	158
5.1	Sensitivity of results to each model .....	166
5.2	Comparison with VARI experiments .....	170
5.3	Complex flow dimensionality.....	171
5.4	Other possible sources of flowrate reduction .....	175
5.5	Relative comparison of materials by fill time .....	177
5.6	Updating $K_{zz}$ test results for capillary pressure.....	178
5.7	Bindered samples permeability determination.....	182
6	Final part quality characterization .....	185
6.1	Fiber content measurement methods.....	185
6.1.1	Density .....	185
6.1.2	Acid digestion.....	186
6.1.3	Optical microscopy.....	187
6.2	Void content measurement methods.....	198
6.3	VAP membrane qualification .....	201
6.3.1	Materials .....	201
6.3.2	Infusion processing and membrane wetting .....	202
6.3.3	Resin flow velocity comparison .....	204
6.3.4	Fiber volume content and thickness gradient measurement.....	204
6.3.5	Void content measurement .....	206
6.3.6	Shear property determination and correlation .....	209
6.3.7	VAP membrane qualification summary .....	210
7	Final Conclusions.....	211
Appendices.....		229
7.1	Appendix 1 - In-plane permeability model constants.....	229
7.2	Appendix 2 - Viscosity modeling for 235H system in $K_{zz}$ measurements. ....	230
7.3	Appendix 3 - PAM-OPT code for solving all three permeabilities. ....	232

7.4	Appendix 4 - Compressibility model constants. ....	234
7.5	Appendix 5 – MATLAB code for 1D flow simulation. ....	235
7.6	Appendix 6 – Image-J macro scripts for automation of image analysis. ....	237
	Curriculum Vitae (CV).....	243



## English Abstract

Composite materials, especially those made with carbon fiber, have better specific properties than many traditional materials. But despite their promised advantages, industry has been slow to apply composites as they wait to see if an automatable composites manufacturing solution with high properties will become available. Resin infusion processing is being developed in many laboratories in an attempt to find this suitable process. Qualification of an optimized resin infusion process will require significant performance data and accurate manufacturing simulation tools. This is currently hindered by a lack of standardized methods for part characterization, and a lack of understanding of the different flow phenomena that are involved in the simulation of flow processing.

This work aims to help meet these needs, so as to allow further implementation of fiber-reinforced composite materials in industry. To improve simulation capabilities, individual modeling systems for each of the following flow phenomena are developed: permeability, compressibility, dynamic viscosity, and dual-scale flow. These models were developed based on relationships previously proposed in the literature, as well as characterization experiments with modern carbon fabrics in this study.

A new numerical model is presented in which all the above-mentioned individual models are coupled. This new coupled model is limited to predicting 1-dimensional flow. But it is the first model known to couple all of these phenomena into one solution. The coupled model works well at describing the independent effects and interactions of each of the separate flow phenomenon models. The effects of dual scale flow, as modeled by incorporation of a modeled capillary pressure, proved to be more significant to flow velocity than the viscosity or compressibility for the infusion conditions studied here.

The coupled model was compared to benchmark experimental VARI infusions of a variety of modern carbon preforming materials. The change in flow velocity due to fabric selection, relative to a baseline material, exhibited fairly good consistency between experiment and prediction. Further applicability of the coupled model was demonstrated with 3-dimensional point infusion experiments. The permeability in each of the three component directions for 3D flow can be

determined from a single point-infusion experiment, independent of any dual scale flow or viscosity effects as they are modeled in the coupled solution.

Nevertheless, both in-plane flow and 3-dimensional flow exhibit slower flow velocity than predicted by the model when compared on an absolute basis. It is suspected that this is due to some unknown shear effect. The accurate simulation of resin infusion will require characterization of the permeability for each liquid-fiber combination until these differences, whether from shear or something else, can be explained and modeled.

This study also contributes towards the needs of industry by reviewing and optimizing the available measurement methods for fiber content and void content. A demonstration of using the optimized tools for these measurements is made by qualifying different membranes for VAP manufacturing – a promising variant of resin infusion. A demonstration is also made of the correlation between these measurements and resultant shear properties.



## Deutscher Abstract

Verbundwerkstoffe, vor allem diejenigen die mit Carbonfasern gefertigt sind, haben bessere Eigenschaften als viele herkömmliche Materialien. Trotz ihrer viel versprechenden Vorteile hat die Industrie nur langsam die Verwendung von Verbundwerkstoffen angenommen, um auf eine automatisierbare Herstellungslösung von Verbundwerkstoffen mit hohen Eigenschaften zu warten. In vielen Laboren wird versucht ein geeignetes Verfahren mittels "Resin Infusion" (Harzinfusion) zu entwickeln. Die Qualifizierung eines optimierten Harzinfusionsprozesses erfordert hohe Verfahrensgüte und präzise Fertigungssimulationswerkzeuge. Dies gestaltet sich, derzeit durch den Mangel an standardisierten Methoden zur Teilcharakterisierung und dem Mangel an Verständnis für die unterschiedlichen Flussphänomene, die in der Simulation von Flussverarbeitung beteiligt sind, schwierig.

Diese Arbeit soll dazu beitragen, die weitere Umsetzung der faserverstärkten Werkstoffe in der Industrie zu ermöglichen. Um die Simulationsfähigkeit zu verbessern, werden individuelle Systeme für die Modellierung der folgenden Flussphänomene entwickelt: Permeabilität, Kompressibilität, dynamische Viskosität und "dual-scale flow". Diese Systeme wurden aus Modellen von Literatur adoptiert, und in dieser Studie bei Charakterisierungsversuche mit modernem Kohlenstoff-Gewebe entwickelt.

Ein neues numerisches Modell, bei dem alle oben genannten einzelnen Modelle gekoppelt sind wurde dargestellt. Dieses neue Modell ist voraussichtlich auf den eindimensionalen Fluss begrenzt, aber es ist das erste Modell, welches all diese Phänomene in einer Lösung beinhaltet. Das gekoppelte Modell funktioniert gut beim Beschreiben unabhängiger Effekte und Wechselwirkungen der einzelnen Flussphänomene. Die Auswirkungen des "dual-scale flow", basierend auf dem Modell des Kapillardrucks, erweisen sich bei den hier untersuchten Infusionsbedingungen als bedeutenderer Faktor auf die Fließgeschwindigkeit, als die Viskosität oder die Kompressibilität.

Die Resultate von VARI(vacuum assisted resin infusion)-Experimenten und einer Vielzahl von modernen Kohlenstoffmaterialien wurden mit dem neuen Modell verglichen. Die Veränderung der Fließgeschwindigkeit durch die Gewebeauswahl, bezogen auf ein Basismaterial, zeigten recht gute Übereinstimmung zwischen Experiment und Vorhersage. Weitere Anwendungsmöglichkeiten der

gekoppelten Modelle wurden experimentell mit der dreidimensionalen Punkt-Infusionen bewiesen. Die Permeabilität lässt sich von einem einzigen Punkt-Infusionsexperiment in alle drei Komponentenrichtungen (für 3D) bestimmen, unabhängig von "dual-scale flow effects" oder Viskositätseffekten, da sie in der Lösung beinhaltet sind.

Dennoch wurden, wenn auf absoluter Basis verglichen, sowohl im ebenen Fluss sowie im dreidimensionalen Fluss langsamere Fließgeschwindigkeiten gemessen als im Modell vorausgesagt. Es wird vermutet, dass dies auf einen unbekanntem Schereffekt zurückzuführen ist. Die genaue Simulation der Harz-Infusion benötigt eine Charakterisierung der Permeabilität für jede liquide-Faser-Kombination, bis die Unterschiede zwischen den Messungen und dem Modell, sei es durch Scherung oder anderes, erklärt und modelliert werden können.

Diese Studie hat durch die Überprüfung und Optimierung, der verfügbaren Messmethoden von Fasergehalt und Porenanteil, auch Antworten auf die Bedürfnisse der Industrie. Mit der Verwendung der optimierten Werkzeuge, konnten zum Beispiel die unterschiedlichen Qualitäten verschiedener Membranen für die VAP (Vacuum Assisted Process)-Fertigung gemessen werden. Dies ist eine viel versprechende Variante der Harzinfusion. Ein anderes Beispiel zeigt die Korrelation zwischen diesen Messungen und den daraus resultierenden Scher-Eigenschaften.

## Nomenclature

(acronyms)

RI: Resin Infusion

VARI: Vacuum Assisted Resin Infusion

VAP: Vacuum Assisted Process

DM: Distribution Media

(variables)

$A$ : Cross-sectional area of flow ( $m^2$ ) / In-plane surface area of preform stack ( $m^2$ )

$A_F$ : Areal weight of only carbon fiber ( $kg/m^2$ )

$A_D$ : Areal weight of all solids ( $kg/m^2$ )

$A_0, E_0$ : Constants for Arrhenius model of initial viscosity (Pa·s, J/mol)

$A_C, E_C$ : Constants for the critical exponent in the Pichaud model for viscosity (dimensionless)

$A_k, B_k$ : Power law constants for  $K(v_F)$  model ( $m^2$ , unitless)

$A_V, B_V, a_A, b_A, a_B, a_B$ : Constants for isothermal viscosity model,  $\mu_0(t, T)$

$a_w, b_w, c_w$ : Grimsley model constants for wet expansion of fabric (% , % , Pa)

$b_t$ : Inner radius of injection inlet tube (m)

$Ca$ : Capillary number (dimensionless)

$c_p$ : specific heat at constant pressure (J/kg·K)

$D_f$ : Diameter of single carbon fiber (m)

$F_C$ : Form factor for fiber alignment in  $P_{cap}$  calculation (m)

$F_z$ : Error function of Ratio Simplification of Isotropic Transformation Model

$g$ : Gravitational acceleration ( $m/s^2$ )

$h$ : Thickness of the preform stack

$h_C$ : Rate of convective heat transfer ( $W/m^2 \cdot K$ )

$k$ : Thermal conductivity ( $W/m \cdot K$ )

$k_1, k_0$ : Effective reaction rates for epoxy 2<sup>nd</sup> order autocatalytic model

$k_R(t, T)$ : reaction rate at any time during cure (% / s)

$K$ : Permeability ( $m^2$ )

$K_{xy}$ : In-plane permeability ( $m^2$ )

$K_{xx}$ : Major in-plane component of the permeability tensor ( $m^2$ )

$K_{yy}$ : Minor in-plane component of the permeability tensor ( $m^2$ )

$K_{zz}$ : Through-thickness component of the permeability tensor ( $m^2$ )

$K_0$ : Effective permeability for flow forced along 0° general coordinate axis ( $m^2$ )

$K_{90}$ : Effective permeability for flow forced along 90° general coordinate axis ( $m^2$ )

$K_{45}$ : Effective permeability for flow forced along 45° general coordinate axis ( $m^2$ )

$L$ : Length (m)

$L_t$ : Length of injection inlet tube (m)

$n$ : Number of fabric layers in the preform stack

$M_F$ : Mass of only carbon fibers (kg)

$M_D$ : Mass of all solids (dry mass) (kg)

$M_R$ : Mass of resin (kg)

$M_W$ : Mass solid when immersed in liquid during density testing (kg)

$M_S$ : Mass of stitching (kg)

$M_{residue}$ : Mass of remaining solids after solvent digestion in  $v_F$  determination (kg)

$P$ : Pressure (Pa)  
 $\Delta P$ : Differential pressure gradient (Pa)  
 $P_A$ : Ambient pressure (Pa)  
 $P_I$ : Pressure at infusion inlet (Pa)  
 $P_R$ : Resin pressure (Pa)  
 $P_C$ : Compaction pressure on the fibers (Pa)  
 $P_V$ : Vacuum pressure (Pa)  
 $P_{cap}$ : Capillary pressure (Pa)  
 $P_{CO}$ : Initial pressure at onset of holding thickness in Robitaille pressure decay model (Pa)  
 $q$ : Heat transfer (W)  
 $q_V$ : Volumetric heat generation (W/m<sup>3</sup>)  
 $Q$ : Flowrate (m<sup>3</sup>/s)  
 $r$ : Position in spherical flow along radius in isotropic medium (m)  
 $R$ : Inverse of the permeability (m<sup>2</sup>) or total radius of sphere (m), or ideal gas constant = 8.314 (J/k·mol)  
 $Re$ : Reynolds number for fluid flow  
 $t$ : Time (s)  
 $t_{10}$ : Time for flow to reach milestone length of 100 mm (s)  
 $t_{16}$ : Time for flow to reach milestone length of 160 mm (s)  
 $t_C$ : Constant for non-dimensionalization of time in Isotropic Transformation Solution (s)  
 $t_G$ : Target time (goal) in optimization scripts (s)  
 $t_x$ : Time for flow to reach a particular point in direction  $x$  (s)  
 $t_y$ : Time for flow to reach a particular point in direction  $y$  (s)  
 $t_z$ : Time for flow to reach a particular point in direction  $z$  (s)  
 $T$ : Temperature (°C)  
 $T_A$ : Temperature at ambient (°C)  
 $T_L$ : Temperature of liquid (K)  
 $T_\infty$ : Temperature of infinite surroundings (K)  
 $u$ : Flux (m/s)  
 $v$ : Fluid velocity (m/s) / Kinematic viscosity (m<sup>2</sup>/s)  
 $v_F$ : Fiber volume content (%)  
 $v_O$ : Void volume content (%)  
 $v_{FO}$ : Minimum initial fiber volume content of dry fabric in Grimsley model (%)  
 $x$ : Position in flow along axis coinciding with  $K_{xx}$  (m)  
 $x_f$ : Flow front position along axis coinciding with  $K_{xx}$  (m)  
 $y_f$ : Flow front position along axis coinciding with  $K_{yy}$  (m)  
 $y$ : Position in flow along axis coinciding with  $K_{yy}$  (m)  
 $z$ : Position in flow along axis coinciding with  $K_{zz}$  (m)  
 $z_f$ : Flow front position along axis coinciding with  $K_{zz}$  (m)  
 $\alpha(t)$ : reaction conversion at any time during cure (%)  
 $\alpha_{gel}$ : critical reaction conversion at gelation (%)  
 $\alpha_T$ : Thermal diffusivity (m<sup>2</sup>/s)  
 $\alpha_X$ : Location along filled region normalized by total length of filled region =  $x / x_F$   
 $\beta$ : Ratio of molar concentrations of unreacted amine and cured epoxy  
 $\beta_C$ : Percent change in resin thickness during curing (%)  
 $\beta_S$ : Ratio of stitching mass to fiber mass ( $M_S / M_F$ )  
 $\gamma$ : Surface tension (N/m)  
 $\gamma_K$ : Ratio of the secondary to primary amino hydrogens' rate constants in epoxy curing  
 $\epsilon_w$ : Wet strain in compression/expansion (%)

$\phi$ : Porosity (%)  
 $\lambda$ : Aspect ratio for size of simulation elements  
 $\mu$ : Dynamic viscosity (Pa·s)  
 $\mu_0(T)$ : initial viscosity of uncured resin at point of mixing at temperature  $T$  (Pa·s)  
 $\theta$ : Orientation angle between principle axis and general axis (°)  
 $\theta_C$ : Contact angle between fluid and fiber (°)  
 $\theta_{CS}$ : Static contact angle between fluid and fiber (°)  
 $\theta_{CD}$ : Dynamic advancing contact angle between fluid and fiber (°)  
 $\rho_F$ : Density of fibers (kg/m<sup>3</sup>)  
 $\rho_R$ : Density of resin (kg/m<sup>3</sup>)  
 $\rho_T$ : Total density of composite material (kg/m<sup>3</sup>)  
 $\rho_W$ : Density of water (kg/m<sup>3</sup>)  
 $\rho_A$ : Density of air (kg/m<sup>3</sup>)  
 $\rho_S$ : Density of PES stitching (kg/m<sup>3</sup>)



# 1 Introduction

Composite materials, especially those made with carbon fiber, have better specific properties than many traditional materials. In many manufacturing applications the maximization of the strength/weight ratio is critical to part design. This is especially true for the high volume industries of transport and wind-energy; both are strongly driven by weight reduction. The replacement of aluminum/steel with composite materials promises lighter transportation vehicles, meaning less fuel consumption. The same replacement in the wind-energy industry means easier assembly of extremely large parts and greater energy efficiency.

There has historically been a continual increase in transportation demand for centuries. This is especially true in the modern day for civil air traffic. But the current world is also rapidly being drained of its natural petroleum reserves. Thus the need for increased fuel economy has never been greater. The aerospace industry has already begun to address this problem by replacement of heavier traditional materials with composites. The Airbus A340 contained 17% of fiber composite materials, which was considered a significant engineering feat [1]. Currently, both Airbus (A350) and Boeing (787) are developing next-generation aircraft with over 50% composites.

Justification of this application of composite materials has not yet been fully realized, however. The common method of autoclave manufacturing is a slow batch process. Yet the production demand for aircraft such as the Airbus A320x will increase to 40 aircraft / day in the near future. For 50% composites aircraft to be built at that rate will require extensive innovation in 1) efficient use of fibers, 2) rapid fiber placement, and 3) net-shape preforming [1].

Autoclave manufacturing is severely restricted in its potential for automation. And the typical prepreg materials used in this type of process are too stiff to shape into complex (but necessary) geometries. If suitable alternative processing methods are not developed within the next 2-3 years, then aircraft manufacture will go back to aluminum, as the cost of composites outweighs the benefits [1].

The automotive industry usually follows the trends in aerospace; processing innovations applied to aerospace are adopted by auto manufacturers a few years later. The higher volume in the automotive industry makes it harder and slower to try out new technologies. Small production cars already require rates of 100 cars / day. With cycle times of seconds there is not much room

for error. Some of the materials in modern cars have already been replaced with composite materials. The autoclave processing typical to aerospace has hardly ever been applied to automobiles due to the long cycle times involved. Instead, current composite automobile manufacturing focuses on resin transfer molding (RTM) [2]. This involves a sacrifice in specific properties and repeatability.

Therefore, despite their promised advantages, industry has been slow to apply composites as they wait to see if a better composites manufacturing solution will become available. Autoclave manufacturing is too expensive, slow, hard to automate, and geometry-limited. But other less expensive and more flexible manufacturing processes have lower properties and repeatability. Recent advances in resin infusion (RI) processes have produced properties and repeatability close to autoclave processing. Concurrent research in textile preforming has allowed many complex net-shapes to be made with RI. Thus, the aim of much research is to optimize RI processing to provide a solution for the majority of industrial composite manufacturing.

For an optimized RI process to gain trust in the industry, two things will be required:

1. More performance data
2. Accurate manufacturing simulation tools

Traditional materials such as metals have been characterized for over 50 years. Extensive data on the relationship between manufacturing parameters and final part qualities are available. The qualities include (and are not limited to) strength, stiffness, fatigue resistance, damage characteristics, and service life. Composites are relatively new materials, and more of an engineered material than metals, especially with modern anisotropic preform materials. The properties are directionally specific and can be tailored to meet design needs. There are more design choices regarding orientation, architecture, and composition than with isotropic materials. The many choices in materials and manufacturing design parameters have only begun to be characterized for composite materials.

Characterization is greatly accelerated with accurate simulation tools. No one wants to design/prototype by hand anymore as it's too slow, costly, and difficult. But there's a lack of accuracy in current manufacturing simulation tools due to the complicated phenomena involved in RI's resin flow through a textile.



Software products are available to model the Darcian flow in 1D, 2D, and even 3D based on Finite Element Modeling (FEM). But these tools are difficult to implement by the average manufacturing engineer. In most cases, the manufacturers resort to out-sourcing simulation-based design to flow simulation experts. Even with flow simulation experience, it is difficult to achieve simulation accuracy for an industrial infusion experiment. Many laboratories are working on improving simulation capabilities to respond to this need. But in the current state, flow simulation is not being attempted by many companies doing resin infusion. This is especially true in the marine industry where smaller companies with less capital for simulation attempts also have more years of experience as boat building has commonly involved composites for many years.

The lack of agreement between simulation and actual industrial infusion is due to a degree to the simulation code's approach to FEM analysis. These codes have been adapted from many successful applications to other FEM modeling, such as modeling the mechanical properties of a laminate. With previous successes, it is assumed that all software codes have a few respective disadvantages, but that it will be difficult to improve upon the existent codes.

Beyond the FEM approach, the accuracy of simulation is limited by the industry's lack of understanding of various flow phenomena. The most discussed of these flow phenomena are:

- Permeability variation
- Fabric compressibility
- Dynamic viscosity
- Dual-scale flow
- Pressure reduction in 2D/3D Flow
- Vacuum bag sealing of fabric surface

Many deviations from classic Darcian flow in resin infusion experimentation have been discussed in the literature and attributed to these phenomena. Many approximate solutions have been proposed to address them on an individual basis. But few have been implemented in industrial simulation practice, due to:

- Too much characterization work entailed
- Difficulty of implementation
- Lack of efforts to couple the individual models into one flow simulation

The approach of this work is to address these simulation problems to provide a better solution to industry. All the individual phenomena are modeled in this work with the intention of incorporating them into one solution. Each model is developed to require a minimum of empirical (fitted) data. Experiments are done to get the empirical data for a variety of modern carbon textiles and manufacturing options. The sensitivity of the empirical data to fabric design parameters is shown, so that similar fabrics can be modeled without additional experiments. This approach of database interpolation is being adapted more widely than theoretical data generation or individual experimentation for reasons of simplicity. Finally, a fully-coupled solution is developed that is fairly easy to evaluate with a typical PC, and that uses this database of parameters for any fabric or manufacturing setup.

But this work also has the larger aim of aiding in the implementation of composite materials in industry. The goal of improving simulation is only part of the problem. The total three-fold approach of this study addresses the global challenges to industrial application of composites:

1. To model the most significant phenomena in flow processing to improve simulation capabilities.
2. To develop tools to characterize composite parts and predict their final properties in service.
3. To use those characterization tools to optimize resin infusion processing.

## 2 Literature review

### 2.1 Composite materials

A composite material consists of two or more different materials that are combined in a way to achieve better properties than the two single components by themselves. In manufacturing, “composite” material typically refers to a 2-part substance with high-tensile fibers and a resin matrix. The fibers have much higher mechanical properties than the resin, and thus carry the applied loads. The matrix surrounds the fibers, holds them in place, transfers the load to the fibers, and protects the fibers [3].

With fiber reinforced composites, meso- and micro-scale variations are possible that are not possible with isotropic materials like steel. Possible variations include:

- Alignment of fibers (random, parallel, or any other orientation)
- Fiber length (short, long, or continuous)
- Fiber material (glass, carbon, etc.)
- Matrix system (polyester, epoxy, or thermoplastic)

All of these parameters determine the final properties of the composite part. Due to the large length to diameter ratio of the fiber, their orientation aligns the highest properties in a particular direction. A design engineer can take advantage of this anisotropy by aligning the fibers to best resist the typical modes of failure for a part. This makes the material more efficient than isotropic materials from a weight perspective, as high strength is not needed in every direction.

Another part of maximizing the strength to weight ratio is the amount of fiber in the composite part. As the resin matrix has insignificant mechanical properties compared to the fibers, the composite properties are determined by the fibers alone. Adding matrix to the composite only adds weight and not any more properties. But the matrix is vital to the performance of a composite part for the previously mentioned reasons. For the maximum load to be sustained by the fibers, each must be completely wetted by the resin matrix. Complete wetting becomes more and more difficult as less resin is applied. Thus, maximum properties are achieved when the resin amount is at the minimum amount necessary to wet all the fibers.

The term used to describe the amount of fiber in a material is  $v_F$ , the fiber volume content. This is the fraction by volume of the composite material consisting of fiber reinforcement. Research has shown that the mechanical properties dominated by the fibers, such as tensile load and modulus, are directly proportional to the fiber content [4,5]. Thus, fiber-dominated mechanical properties should always be normalized by  $v_F$  when comparing data. The inverse of the fiber volume content is the porosity,  $\phi$  which represents the volume ratio of the empty space in the composite material;  $1 = \phi + v_F$ .

One of the key challenges associated with fiber wet-out is the minimization of voids. Carbon fibers are not as easily wetted by resins as they are by oils with more similar chemical structures. To fill all the micro air pockets between all the microscopic fibers in an entire fabric is a challenging task. High pressure gradients make this easier, as does lower resin viscosity. But no textile is ever completely filled; there always is some % volume amount of air. This is termed the void content,  $v_0$ . In contrast to fiber-dominated properties, resin-dominated properties like shear, compression, and transverse tension are inversely related to  $v_0$  as well as  $v_F$ . For every 1% increase in the void content, resin-dominated properties generally decrease in the range of 2 to 10% for all typical composite materials [4]. Resin-dominated properties cannot be compared across experiments therefore, without knowledge of both  $v_0$  and  $v_F$ .

### 2.1.1 Fibers

The most commonly used fibers in the composites industry are carbon, glass, and aramid. The typical range of tensile strength and E-modulus for various types of these fiber materials are shown in Figure 2.1 compared to the typical isotropic materials aluminum, titanium, and steel.

Glass fibers offer the best cost/performance ratio. They exhibit a high tensile strength but low modulus. Glass fibers are not usually used in primary structures because of this low stiffness. Both the production of and demand for carbon fiber have exponentially increased in the last 20 years. As seen in Figure 2.1, carbon fibers exhibit a high range of properties from very stiff to high tensile strength, and all values are higher than typical isotropic materials. As it is the most commonly used fiber in modern design projects, this paper focuses exclusively on materials based on carbon fibers.

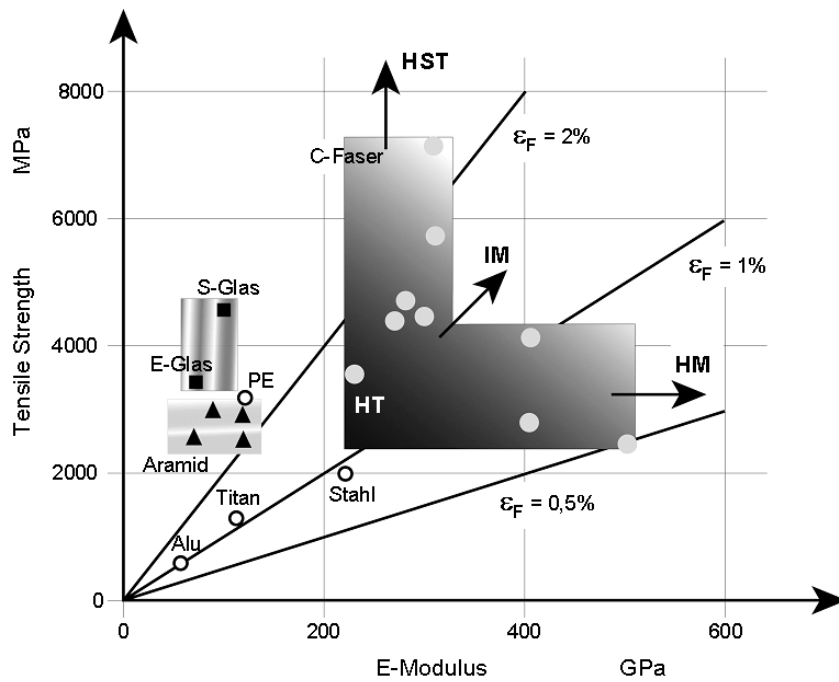


Figure 2.1 - Mechanical performance of typical reinforcement fibers [6].

For pre-infusion (dry) handling, microscopic carbon fibers must be held together somehow. The textile industry's practice of combining other synthetic fibers into yarns was adopted with carbon fibers. The term "tow" is usually used to differentiate a carbon fiber yarn from one made from synthetic fibers, and is used in this paper. A tow usually consists of a few thousand untwisted fibers. A fiber's weight is described by the term "tex" which is the mass in grams of 1km of the tow.

These tows are arranged to make a fabric of regular thickness that can be laid in a mold in preparation for resin infusion. Controlling the thickness of the part is done by increasing or decreasing the number of layers ("plies") in the stack.

The first fabrics for composites were mats with random orientation of the tows. This results in low  $v_F$ , however, and takes no advantage of anisotropic design capabilities. Uni-directional (UD) tows laid in parallel together held in place by partially cured resin (pre-impregnated) became known as prepreg. But this material is expensive and stiff and limited in geometry. Fabric weaves of tows allowed for resin infusion processing to achieve materials with higher  $v_F$  than random mats, and still allowed draping and incorporation of the textile industry's geometrical flexibility. But the cross-over points of every tow become local high-stress points in loading, resulting in lower mechanical properties compared to any UD fabric. Innovative carbon fabrics have recently become available to optimize resin infusion. They will be discussed in the Section 3.

### 2.1.2 Resins

In addition to the functions mentioned above, the matrix determines other properties of the composite material associated with the outer surface such as temperature resistance, fire resistance, surface compatibility, and photooxidation resistance. The damage tolerance of the composite material is also largely determined by the matrix. This is due both to its role of protecting the fibers, and because voids are always located in the matrix. Voids act as stress concentrations and crack-initiation sites, thus reducing the energy required to failure [7].

Resin matrices in composite materials can be either thermosets or thermoplastics. Thermosets are the more commonly used resin choice as their viscosity is inherently low in the uncured state, thus facilitating infusion. Some type of bisphenol-A based epoxide is mixed with any of a variety of amines resulting in condensation reaction of the two. As three or more epoxide groups are available on each macromolecule, the cross-linking density is high and the resulting epoxy is very stiff. The reaction speed can be controlled by constituent choice and temperature, so that infusion can finish before the viscosity becomes high with curing. In industry, the infused part is usually heated to accelerate the cure and reduce cycle times. The minimization of injection time doesn't help as much as cure time minimization, as cure usually takes longer [8].

Thermoplastics are currently being investigated academically as matrix resins for composites. Thermoplastics offer the advantages of less toxicity and greater recyclability over thermoset matrices due to lower glass transition temperature than decomposition temperature. Their viscosity is much higher than thermosets however, and the energy required to melt the resin before infusion is much higher than typical curing energy loads for thermosets. Other forms of composite processing different from resin infusion are being investigated to thoroughly wet the fibers with high viscosity resins. As thermoset resins are much farther along the development road for industry than thermoplastics, only thermosets will be used in this study.

The two most common thermoset resins are polyester and epoxy. Polyester resins are the most used resin systems. Their low price and low water absorption have made them a mainstay of the marine industry for many years. But due to lower thermal properties and higher shrinkage of polyester, the aerospace industry has traditionally favored epoxies over polyester for higher performance applications.

Epoxy formulations can be made to cure either at room temperature or at elevated temperature. High temperature curing epoxies naturally offer greater thermal properties over room-temperature curing systems. Hexcel's RTM6, a high-temperature curing epoxy is thus the only qualified resin by Airbus for resin infusion processing. For the sake of experimental simplicity, however, a room-temperature curing epoxy, Hexion's Epikure RIM235, was used throughout this study. It is assumed that although final mechanical properties using RIM235 will be slightly lower than with RTM6, the trends when changing other variables should be approximately the same.

## 2.2 Processes

Since the advent of fiber-reinforced composite materials, many creative ways have been suggested to wet fibers with viscous resins. The most intuitive way is to directly pour the resin onto the fabric. Better wetting and higher  $v_F$  is understandably achieved when some form of pressure is applied to the resin-fiber mix. Controlling the amount of resin applied to the fiber results in better repeatability. Of the processing methods used today, hand lay-up represents the minimum in pressure and resin control, whereas autoclaving of prepreg represents the maximum. Many variations between these two extremes have been developed for specific processing demands.

### 2.2.1 Hand lay-up

Hand (wet) lay-up consists of placement of fabric in a 1-sided mold, and then applying resin by brush, roller, or spray. This is by far the cheapest of any composite processing method. Only one smooth surface is achieved, and control over  $v_F$ ,  $v_D$ , and the thickness of the part is severely limited. Typical resins contain volatile organic compounds (VOC's) such as styrene that are released to the atmosphere in an open environment like hand lay-up. These hazardous gases are being controlled by increasing environmental legislation, thus decreasing the application of hand lay-up processing.

### 2.2.2 Prepreg

No other composites processing method has yielded the properties and repeatability as high as autoclaving of prepreg materials. Thus they have been the most common choice for aerospace applications.

The philosophy behind prepreg materials was to provide a composite material that already has the correct amount of resin infused into the fabric (pre-impregnated = “prepreg”). The resin is applied with high pressure to thoroughly wet the fabric, and partially cured to remain in place. A manufacturer then has only to place it in/on a mold (Figure 2.2) and complete the curing. To ensure the highest possible  $v_F$  and lowest  $v_0$ , the curing cycle takes place in a vacuum bag assembly in an autoclave oven with high pressure and heat. This also prevents any of the VOC emissions typical to hand lay-up.

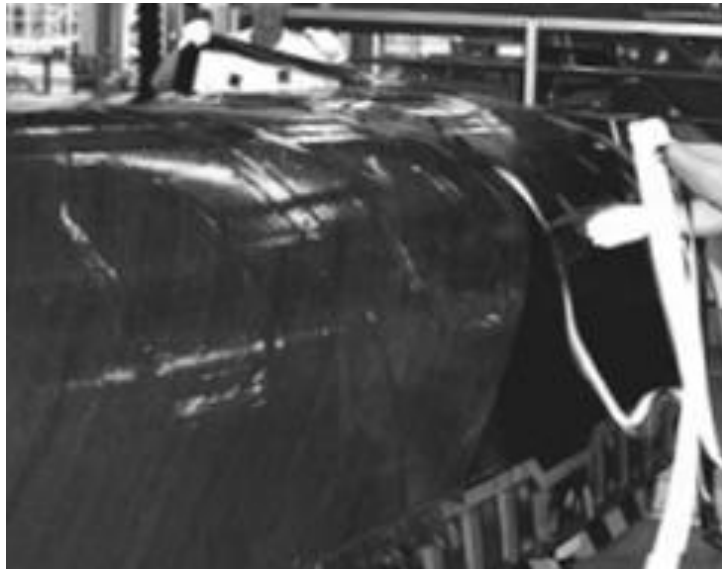


Figure 2.2 - Prepreg tape laying of a Euro-fighter skin section preform [9].

Because it contains partially cured resin, prepreg fabric is relatively stiff and difficult to shape. Placement of the stiff material in complex shape easily results in trapped air pockets. A heated vacuum chamber is often used to consolidate the lay-up after each layer is applied in the mold. The always-curing resin in prepreg material gives it a short shelf life at room temperature and therefore uncured prepreg has to be stored at temperatures below zero.

### 2.2.3 Resin infusion

These two processes are the two extremes on either side of the processing cost spectrum. Industry needed an alternative somewhere in the middle. Resin infusion (RI) processing has become that successful middle ground. RI consists of the resin infiltration of a textile perform by either positive or negative pressure, followed by curing of the matrix. Various types of RI processing have emerged as popular manufacturing options due to their relatively low cost-per-properties ratio.



Compared to hand lay-up, RI has significantly better potential for  $v_F$ ,  $v_O$ , dimensional, and properties control. It also has no VOC emissions; the resin is closed within the mold or a vacuum bag. The cost of implementing RI can range from just above hand lay-up to just under prepreg given the many variants.

Compared to prepreg, RI materials generally have a longer shelf life, and the large autoclave ovens and associated energy and pressure are no longer needed. The largest advantage over prepreg however is the geometrical flexibility obtained by incorporation of techniques borrowed from the textile industry. The textile industry has been around for thousands of years. Highly complex 3D shapes can be made with textile preforming techniques. RI processing can take any complex dry fiber shape and force resin into it (Figure 2.3). Within any processing choice, there is always a tradeoff between processing costs and geometric complexity. But RI can achieve much higher complexity than autoclaving, and is substantially cheaper [10].



Figure 2.3 - Example of complex part shape capable in RI.

This brings up the greatest challenge however to RI: that of completely wetting all of the fibers as mentioned in Section 2.1.1. Optimization of infusion to maximize wetting with a minimal amount of resin is the main goal of any flow simulation tools. This challenge is what has kept RI-produced materials from meeting the same properties standards established in autoclaving. Nevertheless, the economic advantages of RI over prepreg manufacturing, and the quality advantages of RI over hand lay-up have kept the industry's interest [8,11].

A general comparison between the three main process types is shown in Figure 2.4. Of the three, autoclave processing may still deliver the highest properties and repeatability. But optimization of RI processing has substantially decreased the gap between the two. And it is hoped that future optimization will allow RI to surpass autoclaving while still maintaining the lower costs (Figure 2.5).

	Cost	Repeatability	Specific Properties	Flexibility	Safety
Hand lay-up	↓	↓	↓	+	-
Resin Infusion	↓	↓	↓	+	+
Prepreg	↓	↓	↓	-	+

Figure 2.4 - Basic comparison of major composites manufacturing methods.

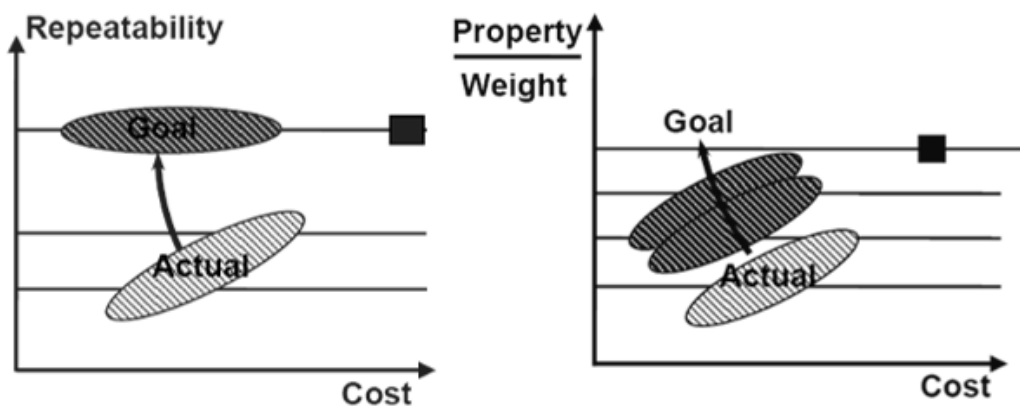


Figure 2.5 - Autoclave vs. RI processing: optimization goals for RI processing (■: Autoclave, slashes: RI) [12].

The major variants of RI are resin transfer molding (RTM), vacuum assisted resin transfer molding (VARTM), vacuum assisted resin infusion (VARI), and vacuum assisted processing (VAP).

### 2.2.3.1 RTM

In the case of resin transfer molding (RTM), high positive pressure forces the resin to fill all voids of a preform-containing cavity between two rigid mold sides (Figure 2.6). This process is rapid due to the high pressures that can be applied. The limit on pressure is determined by the tooling setup as well as the fabric's resistance to deformation (wash-out). High pressures also allow the usage of relatively high viscosity resins.

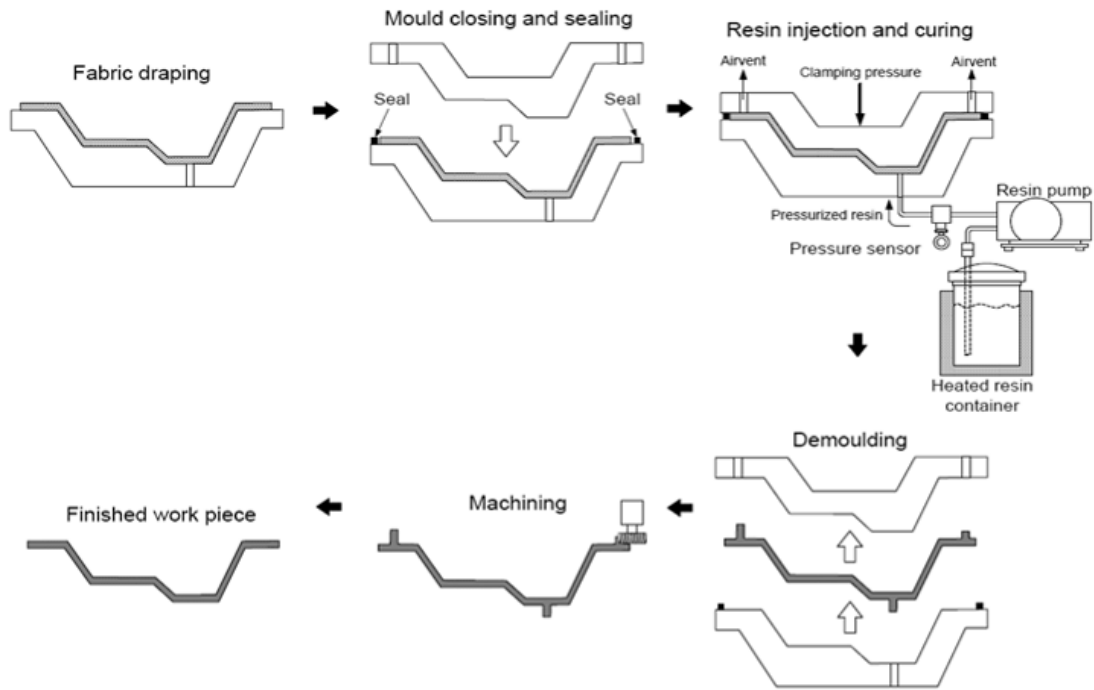


Figure 2.6 - Traditional RTM (closed mold) [9].

### 2.2.3.2 VARTM

To aid in fiber wet-out, vacuum can be applied at the vent to a typical RTM setup with double-walled tooling. This is the closed mold version of vacuum assisted RTM, or VARTM. To reduce the cost of molding, one-sided molds are commonly used with a vacuum bag on top, and the resin flow is driven exclusively by vacuum (Figure 2.7).

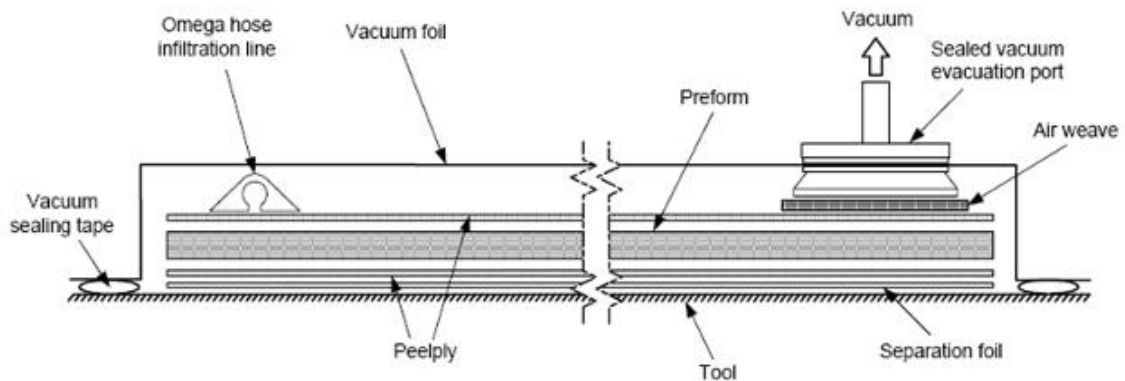


Figure 2.7 - Typical VARTM (open mold) setup [9].

The main weakness of VARTM has to do with the reliance on vacuum pressure. As the air is drawn by vacuum through the preform (instead of being pushed), complex geometries can result in dry spots if the vents are not placed properly (Figure 2.8). To avoid this, additional vacuum vents must

be placed around the preform to ensure that the pressure gradient forces flow through every section. The design of inlet and vent placement is not always intuitive, prompting trial and error optimization with either experimentation (costly) or flow simulation.

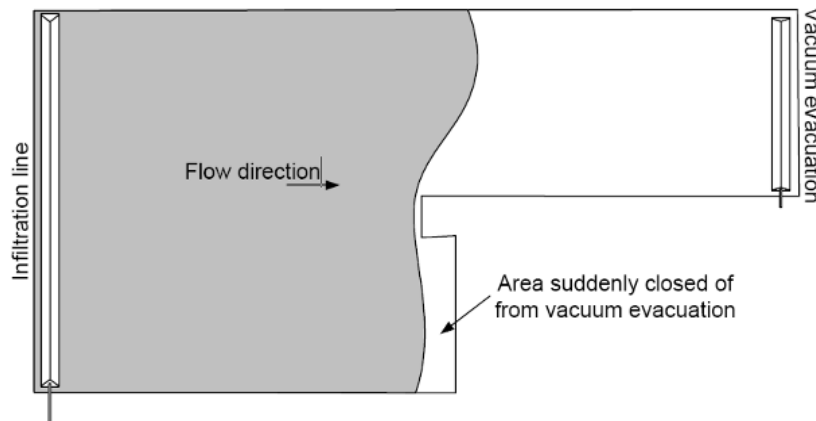


Figure 2.8 - Demonstration of need for vent location optimization in VARTM [9].

### 2.2.3.3 VARI/SCRIMP

The VARTM process was better suited for large parts to reduce the cost of building 2 sides of a large mold, and the equipment to open and close the large mold. But vacuum pressure by itself cannot move resin through a large part quickly enough. This is due to the quadratic relationship between length and time in Darcy's law:  $t \propto L^2$ . As the length of the flow front increases, the velocity will quickly slow down. Cycle time and viscosity curing time limits how long the infusion can go on.

This led to a significant innovation in RI processing: the use of high permeability distribution media (DM) laid on the top of the fabric to speed the resin along the in-plane dimensions (Figure 2.9). This leaves only the short length through thickness saturation to be achieved through the preform. Thus, the z component of permeability becomes the dominant variable in saturating the preform and the most time-consuming step of the infiltration [13]. This process is known as vacuum assisted resin infusion (VARI) in Europe, and patented in the US as "Seeman Composites Resin Infusion Process" (SCRIMP) [14].

In VARI, the resin pot is usually left at atmospheric pressure (approximately 1 atm). Once the inlet is opened and infusion starts, the resin separates the pot from the vacuum vent and a pressure gradient (again, approximately 1 atm) is created that draws the resin through the preform. The

maximum achievable  $v_F$  is limited due to relying on pressure gradients less than 1atm (ambient). As in VARTM, the challenge of flow modeling is high, but aids in optimization.

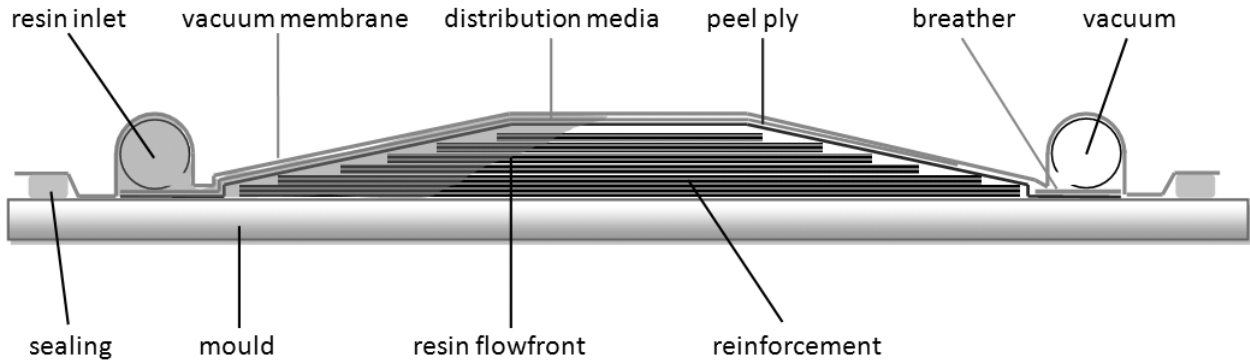


Figure 2.9 - Typical VARI setup [15].

#### 2.2.3.4 VAP

VAP is a patented [13] variation of resin infusion, where a semi-permeable membrane separates the vacuum outlet from the surface of the part (Figure 2.10). This creates a full vacuum gradient and continued degassing across the part surface, as opposed to only at the end-edge of the part in traditional resin infusion. The full vacuum gradient theoretically results in fewer voids and reduced thickness gradients compared to traditional resin infusion, thus higher mechanical properties and repeatability.

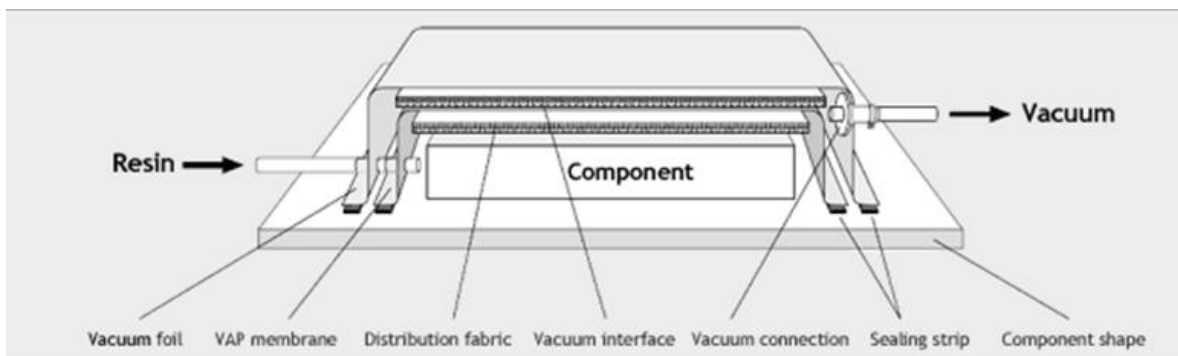


Figure 2.10 - Typical VAP Setup [17].

VAP was developed by the EADS composite research lab in Augsburg, Germany. The innovation began from the idea of using polytetrafluoroethylene (PTFE) to protect only the vacuum port from getting resin in it, much like the PTFE in a waterproof but breathable jacket functions [18]. But this was expanded to the entire part as its benefits to part quality were discerned. It is now marketed as an RI process with higher part quality than with VARI, while still only having to cure in an oven

instead of an autoclave [19]. Large aerospace parts have already been successfully manufactured with VAP, such as the EADS A400M cargo door [20].

A major benefit of VAP is that degassing of the resin can occur at every point in the mold through the thickness to the membrane. Air no longer has to pass through the entire preform before being evacuated as it does in VARI. This diminishes both macro and micro voids. Hence this technique diminishes dry spots without any vent placement optimization. But more importantly, mechanical properties are enhanced due to the natural degassing of micro voids. This was illustrated in a study comparing  $v_0$  for a glass fabric in both VARI and VAP [21]. Without any pre-infusion degassing, switching from VARI to VAP resulted in a decrease of  $v_0$  from 1.64 to 0.37%. With degassing for both, the decrease in  $v_0$  was 1.07 to 0.23%.

The other major advantage of VAP is its contribution to reduction of the thickness gradient in RI under flexible tooling (discussed later in Section 2.3.4). A 77% reduction in the gradient was reported by switching from VARI to VAP [21].

The disadvantages of VAP are the extra cost and manufacturing steps associated with adding the semi-permeable membrane to the lay-up. The membrane is considered less durable than the other disposables in a lay-up. Care must be taken to not stretch (increasing pore size) or otherwise compromise the membrane [21]. VAP membranes cost  $\sim 15 \text{ €/m}^2$  for PTFE and  $\sim 5 \text{ €/m}^2$  for polyurethane (PUR). But handling requirements and even the PTFE membrane cost are insignificant when compared to costs for all the carbon and resin for a thick part, and the resultant return on quality [22].

Another VAP disadvantage is that flow on the tool side is slower than in VARI. This was attributed to higher compaction by the vent during infusion from the uniform vacuum on the entire panel [21]. Higher compaction reduces fabric permeability. But this may not be too detrimental to fill times when DM is used, as resin flow in DM was no different in VARI or VAP.

A unique challenge to process design with VAP is the wettability of the membrane. For a membrane to function correctly, it must not be saturated by the resin for the duration of infusion to full cure. Certain membranes work with a particular set of process parameters, and do not work with others (membrane saturation) [12,23]. These process parameters include temperature, pressure, viscosity, and surface chemistry between the membrane and resin.

The applicability of a membrane to a set of process parameters depends on its pore size and distribution [24,25]. Membranes are usually either PUR or PTFE. The morphology of a PUR membrane is foam-like. The size and concentration of holes can be easily varied during the manufacturing steps. The PTFE morphology is mesh-like and not as easy to vary.

#### 2.2.3.4.1 Fiber volume fraction control in VAP

As the resin has no way to escape to the vent in VAP, it is up to the process designer to control how much resin ends up in the fabric, and hence the  $v_f$ . This can be done in one of three ways:

- Infiltration with the exactly needed resin amount. By using a mass scale, one can stop the infusion at the moment a particular amount of resin has entered the preform. The resin then slowly distributes itself throughout the preform by vacuum pressure and capillary forces.
- Infiltration of an excess of resin and then removing the excess by applying vacuum to the pot. This again entails watching the resin mass in the cavity; one removes resin until the correct mass is achieved. This can achieve an equilibrium pressure gradient throughout the mold faster than the previous method. It can also help ensure that all preform areas are infused with the excess of resin before extraction of the excess.
- Either of the above methods, but by watching mass flow rates instead of total mass in the cavity. As more resin builds up in the cavity, the compaction pressure relaxes and the flowrate across the pressure gradient slows down. Through experimentation, the correct flowrate threshold to either stop the infusion or stop the extraction of excess can be determined.

Each of these methods was compared by Jensen [9]. In this study, removing excess resin showed a limited ability to control the  $v_f$ . This is probably due to the capillary forces holding the resin in after tow saturation.

VAP infusion entails various parts that will take up resin. To ensure that the right amount of resin is in the fibers, one must know the total mass of resin that has left the pot, as well as how much resin is in other places besides the pot and the preform. Resin take-up rates must be calculated for the inlet tube length, the area of distribution media used, as well as the peel-ply and any other disposables. The inlet tube resin take-up is simply the volume calculation for a tube of length  $L_t$  and radius  $b_t$ .

The resin take-up rates of the other disposables require simple infusion experimentation. Measured surfaces of each of the disposables are weighed, then infused with resin at the same pressure gradients used in VAP, and then weighed again after infusion. The difference in weight from dry to wet is the resin take-up for that surface area of disposable material. The average take-up rate for a number of repeats was calculated. The peel-ply used in this study was measured to take up an average of 87.3g of resin per square meter. The distribution media used in this study took up on average 416.3 g/m<sup>2</sup>. A perforated foil used to prevent resin build-up between the peel-ply and DM took up hardly any resin and is considered insignificant.

The resin mass in a composite part can be solved for from a target  $v_F$  by:

$$v_F = \frac{1}{1 + \frac{\rho_F}{\rho_M} \left( \frac{M_F + M_R}{M_F} - 1 \right)} \quad (2.1)$$

Thus, a target value of  $v_F$  is chosen for a preform of mass  $M_F$ , and the total resin amount  $M_R$  is calculated. The resin mass for the take-up of each disposable is added to  $M_R$ , which results in the total amount of resin for the pot.

These are only approximate figures; the actual resin take-up rates vary from independent infusion tests due to nesting in each other and the fabric [26]. So *in-situ* take-up rates will be lower as their porosity is lower. Thus,  $v_F$  will be slightly lower in experiments than predicted with calculations using these take-up rates.

## 2.3 Flow modeling

A significant amount of work has been done in modeling RI mold-filling for process optimization [27]. As mentioned in Section 2.2.3.2, numerical simulations allow, for example, the prediction of the optimum location of resin-inlets and vents, while the trial-and-error approach to mold design is usually prohibited by cost and time. Optimization of flow and tooling can be used to minimize dry spots, voids, resin rich areas, fiber washing, high porosity zones and cracks following cure shrinkage.



### 2.3.1 Darcy's law

The flow in RI is modeled in usual practice by Darcy's Law. This law was stated by the French physicist Darcy in the middle of the 19th century while studying the flow of water through already saturated porous sand beds [28]. The law states that the total discharge flowrate ( $Q$ ) divided by the cross sectional area of flow ( $A$ ) through a porous medium is proportional to the pressure gradient ( $\Delta P$ ) applied across the length of the medium ( $\Delta L$ , m) and the constant of proportionality is given by the permeability ( $K$ ,  $m^2$ ) of the media divided by the viscosity of the fluid ( $\mu$ ):

$$\frac{Q}{A} = -\frac{K}{\mu} \frac{\Delta P}{\Delta L} \quad (2.2)$$

The term permeability was first defined by Darcy as the critical term to his new model. The equation of Darcy's Law implies a uniform (linear) pressure drop along the distance of the medium. When this pressure drop is graphed against the position  $x$  along  $L$ , the permeability is the slope [29]. More general notation is the starting point for most 2D or 3D flow models. Neglecting the effects of gravity (common in RI due to the magnitude of the pressure gradient) this is:

$$u = -\frac{K}{\mu} \nabla P \quad (2.3)$$

where  $u$  is the "Darcy flux" (now a vector) or the volume averaged velocity. The density of the fluid is  $\rho$ ,  $\nabla P$  is the pressure gradient in 3D, and  $K$  is now a 3D tensor. The flux  $u$ , is not the same as the velocity of the fluid through the pores [30]. The fluid velocity ( $v$ ) can be related to the flux by the porosity ( $\phi$ ):

$$v = \frac{u}{\phi} \quad (2.4)$$

$\phi$  reflects the fraction of the total media volume through which the flow can pass, and is the inverse of the fiber volume content;  $1 = v_F + \phi$ .

Within the last 35 years Darcy's law has been extended to describe the flow of polymer resin through a fibrous preform [31]. This time frame coincides with the large-scale development of resin infiltration practices. As the model of Darcy's Law has been the standard for more than a century in the field of porous media theory, it was used as the starting point for RI flow modeling. The assumptions of Darcy's Law of low Reynold's number, and a Newtonian and incompressible

fluid all apply to RI flow [32]. This extension of Darcy's Law has been validated to an extent by various authors through comparisons of numerical modeling and experimental data [33,34,35,36,37,38,39,40,41,42].

Nevertheless, challenges have been made to the validity of applying Darcy's Law to RI, especially regarding compressible media, non-rectilinear flow, pressure-flowrate nonlinearity, fluid-permeability dependence, and flow front phenomena. The issue of compressible media is addressed by characterization of the local porosity response to the compaction pressure. Thus, in a finite element analysis environment, each element's porosity can be evaluated at a given location and time and treated as an incompressible element at that instant [43,44,45]. This is demonstrated later in this work.

Non-rectilinear flow errors are minimized by maintaining a larger length to width ratio than the anisotropy of the reinforcement in 1D testing [46] or by employing a radial-flow test. The pressure-flowrate non-linearity was explained early on by deformation of the fiber mat at higher pressures [47]. It was later also attributed by Kim and Daniel [49] to the rate-dependent slip of flow in micro-channels (shear effects), and accordingly modeled.

The permeability dependence on fluid choice [49,50,51,52] has been challenged and attributed to experimental error [42,53,54]. There must be a relationship between the surface chemistry of differing fluids and the wetting flow effects. But these effects should be included in the calculation of the pressure gradient in flow modeling, and not the permeability. Thus, each challenge has been addressed to a certain extent, and Darcy's Law is still widely accepted for modeling RI flow.

An often-discussed deviation of RI from Darcian assumptions is that of the unsaturated wetting flow in resin infiltration. Darcy's Law was intended for time-independent, steady-state flow through an already-saturated medium. Although the moving boundary of the flow front complicates modeling, a quasi-steady-state assumption (succession of permanent flows) is invoked in the saturated region (behind the flow front), where the liquid follows the following form of the equation of continuity for incompressible fluids [55,56,57]:

$$\nabla \cdot u = 0 \tag{2.5}$$

Coupling this with Equation 2.3 gives the Laplace equation for the fluid pressure field inside a region permeated by the fluid [58]:

$$\nabla \cdot \left( \frac{K}{\mu} \nabla P \right) = 0 \quad (2.6)$$

Application of appropriate boundary conditions to this gives a modeling solution for various flow scenarios [36]. Further complications arise from wetting phenomena; this will be discussed later in this work.

### 2.3.2 Numerical simulation

The application of the computer processing to flow simulation was begun with [59]. Various applications of the finite element method have been applied since [60]. The VARI environment, with DM flow followed by through-thickness flow has been successfully simulated with a 2D perspective [61], 2.5D with a layer of shells on top of 3D elements [62], or a full 3D flow simulation [63]. Closed form solutions have been presented as well [62,64].

The unique pressure gradients in VAP may require adaptations to VARI flow modeling [65]. The resulting pressure gradients in VAP for various manufacturing setups have been characterized [9,66]. A model to predict the wettability of the VAP membranes has been developed [12,23,25]. But implementation of the unique pressure field in flow simulation programs is still a challenge. A possible solution suggested here is to add very low permeability elements along the top of the mesh. This has been done at the vent in VARI for simulation of flow resistance at the vent to decrease resin bleeding [67].

Some efforts have been made to couple multiple dynamic models into one solution or simulation approach [68,69,70,71,72]. A computational fluid dynamics approach with coupled compressibility and permeability has been presented [73].

The three most common software packages used in flow simulation are:

- RTM-worx: especially used in the marine industry for optimization of large 1-time infusions [61,74]
- LIMS: Academic-oriented software sponsored by the University of Delaware's Center for Composite Materials [75]
- PAM-RTM: Industrial-oriented software by ESI based on non-conforming elements [34,63]

As stated in the Introduction, it is not within the scope of this work to compare these codes or produce a new one. With previous successes in the literature for each of them, it is assumed that

all software codes have a few respective disadvantages, but that it will be difficult to improve upon the existent codes. As ESI is an industrial partner for the fellowship sponsoring this work, PAM-RTM will be the focus of simulation efforts. But all three of the above programs have been used over the course of this work.

PAM-RTM is a commercial 1D/2D/3D resin infusion simulation tool continuously developed and distributed by ESI Group. The 2008 version is used in this work. PAM-RTM supports three different types of meshes: 2D plane mesh of triangles,

2.5D surface mesh (thin shell) with triangular shell elements and 3D solid mesh of tetrahedrons (Figure 2.11). The 2008 version added support of 6 node prismatic elements, the natural result of extrusion of a triangular 2D mesh into 3D. Prisms were shown to be more efficient in 3D simulation than tetrahedra [76]. Choosing between 2D, 2.5D, and 3D is decided by the constraints on the flow that is to be simulated. When through-thickness flow is significant, 3D modeling is the only suitable option, even if it takes up much more computer resources.

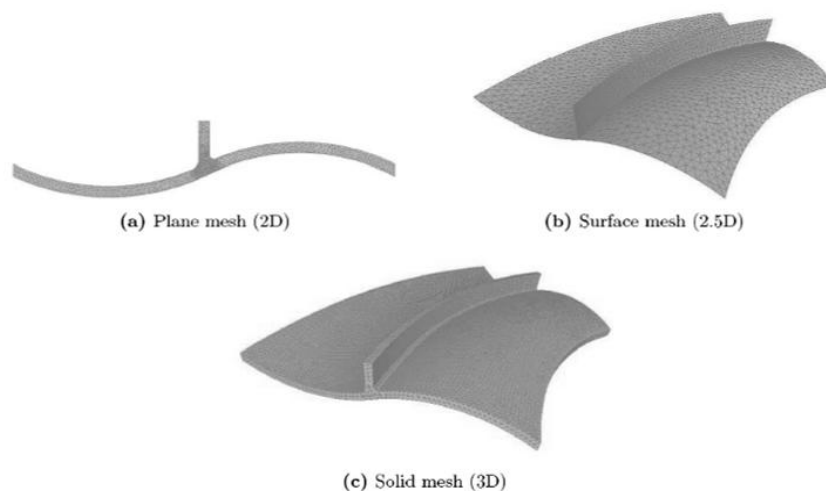


Figure 2.11 - Different mesh types (based on triangles in PAM-RTM) [63].

The required inputs for any simulation program are:

- Resin – density:  $(\rho_R)$ , and viscosity at time and location:  $\mu(t,x)$
- Textile - thickness, porosity, and permeability at time and location:  $h(t,x)$ ,  $\phi(t,x)$ ,  $K(t,x)$

And the outputs are:

- Location of flow front at time:  $x_f(t)$
- Resin pressure at time and location:  $P_R(t,x)$
- Time to fill the part

For both RTM and VARI, the critical processing dynamic is the flow of the resin. The fabric reinforcement is initially dry and must be completely impregnated by the resin. For high performance materials, the porosity of the textiles can become very low, and the impregnation becomes more difficult. The many challenges to modeling flow behavior have served as the catalyst to much recent scientific research in this area. From the introduction, the most typically discussed challenges are:

- Permeability variation
- Fabric compressibility
- Dynamic viscosity
- Dual-scale flow
- Vacuum bag sealing of fabric surface

Each of these will be discussed in the following sections.

### 2.3.3 Permeability

One important application of the extension of Darcy's Law to RI flow modeling is that all preforms must be characterized by their permeability. Permeability expresses the ease with which a fluid flows through the reinforcement [49]. It is a function of preform architecture and porosity [28,77] and should be independent of other flow conditions (pressure gradient and viscosity). It lumps together all the complicated interactions that take place between the fluid and the fiber-preform structure [78].

Optimization of fill-time by changing the other variables in Darcy's Law (pressure gradient and viscosity) is limited by tooling, cure time and properties. But permeability can exhibit a large range through relatively minor changes to the preform [79]. Therefore, it is not only the most difficult variable to characterize in flow modeling, but also the most critical [78,80,81,82,83].

The permeability of an anisotropic preform material can be characterized by a tensor including the magnitudes of permeability in each of the nine component directions. Darcy's Law (Equation 2.3) then becomes [84]:

$$\begin{pmatrix} u_x \\ u_y \\ u_z \end{pmatrix} = -\frac{1}{\mu} \begin{pmatrix} K_{xx} & K_{xy} & K_{xz} \\ K_{yx} & K_{yy} & K_{yz} \\ K_{zx} & K_{zy} & K_{zz} \end{pmatrix} \begin{pmatrix} \partial P / \partial x \\ \partial P / \partial y \\ \partial P / \partial z \end{pmatrix} \quad (2.7)$$

Even in the case of anisotropic fabric media, the preform exhibits point symmetry in right angle directions (orthotropic) [10,85,86]. The flow from a point source then propagates as an ellipsoid (Figure 2.12). Thus, the permeability tensor can be diagonalized and the principle axes ( $x, y, z$ ) define its only three components:

$$\begin{pmatrix} K_{xx} & 0 & 0 \\ 0 & K_{yy} & 0 \\ 0 & 0 & K_{zz} \end{pmatrix} \quad (2.8)$$

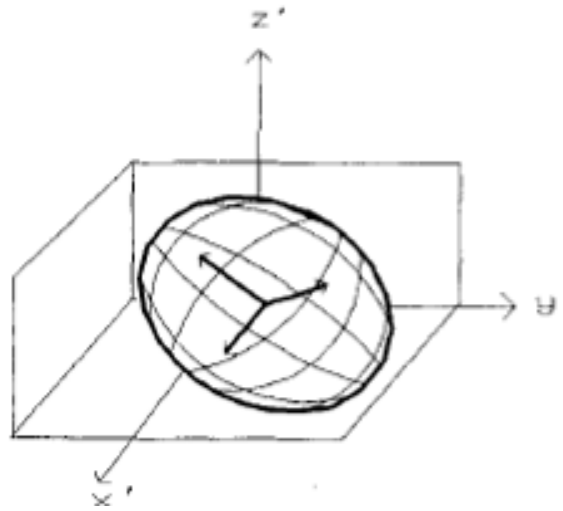


Figure 2.12 – Permeability tensor orientation in general coordinate system [86].

The orientation of the principle axes ( $x, y, z$ ) is often not intuitive. To relate a permeability tensor measurement to any anisotropic material requires knowledge of its orientation with respect to some general axis of the material (Figure 2.12). Trigonometric transformations allow the diagonalized tensor ( $\mathbf{K}$ ) to be related into any general coordinate system, often defined by the manufacturing machine or mold. For example, the  $0^\circ$  axis in general coordinates is often aligned to the stitching in a rolled non-crimp fabric.

When a flow experiment is performed, the flow lengths are measured with respect to the assumed general coordinate system, from which an effective permeability tensor ( $K_0, K_{90}, K_{45}$ ) is calculated [10,13]. This can be changed by matrix transformation back into the  $x, y, z$  axes of the actual permeability given the orientation angle  $\theta$  between each set of axes.

Another common simplification, especially in the earlier days of RI flow modeling and weaker computer processing resources, was to neglect the through-thickness (z-direction) permeability component [87]. This was rationalized by the fact that most composite parts resemble thin shells; the thickness is at least an order of magnitude smaller than the length or width. This was further supported by the experimental determination that the through thickness permeability is usually 1-2 orders of magnitude smaller than the in-plane components. Therefore, many modeling efforts neglected flow out of plane and averaged the properties through the thickness. Darcy's Law then further reduces to:

$$\begin{pmatrix} u_x \\ u_y \end{pmatrix} = -\frac{1}{\mu} \begin{pmatrix} K_{xx} & 0 \\ 0 & K_{yy} \end{pmatrix} \begin{pmatrix} \partial P / \partial x \\ \partial P / \partial y \end{pmatrix} \quad (2.9)$$

The flow ellipse lies at a single angle ( $\theta$ ) to the general coordinate system. In the case of isotropic media, the diagonal values ( $K_{xx}$ ,  $K_{yy}$ , and  $K_{zz}$ ) are all equal, and the equation simplifies to the 1D scalar flow case of Darcy's Law:

$$\frac{dL}{dt} = \frac{K\Delta P}{\phi\mu L} \quad (2.10)$$

This can easily be integrated with respect to time to yield:

$$L^2 = \frac{2K\Delta Pt}{\phi\mu} \quad (2.11)$$

where  $L$  is the length of the portion of the cavity already filled by the resin, and  $t$  is the filling time.

### 2.3.3.1 Experimental vs. Theoretical

Up until 20 years ago, the permeability of a fiber-reinforcement was customarily analyzed based on theoretical models developed for flow through porous media [88,89,90,91]. The most applied of these permeability-estimation expressions is the Kozeny-Carman equation [92,93]:

$$K = \frac{D_f}{C} \frac{(1-\phi)^3}{\phi^2} \quad (2.12)$$

where  $D_f$  is the diameter of a single fiber and  $C$  is an empirical constant for each material. These models considered an idealized unit-cell of the preform geometry to determine the micro-flow characteristics and then apply it across the entire fabric.

The fluid-fiber interactions in fiber reinforcements, however, have proven to be quite complex [94] and to exhibit statistical variation even in the same material [95,96]. These models often require extensive experimental work to determine required coefficients [97], and yet still produce permeability values that can vary 1-2 magnitudes from the experimental results [98]. Theoretical models also cannot consider the stochastic behavior (broad distribution) of permeability. The conclusion in more recent studies has been that experimental determination is the only accurate method to determine permeability [82, 95,99,100].

The industry's hope is that databases of permeability data will allow for simulation of materials without the need for experimentation. This is made possible by experimental characterization of the sensitivity of permeability to general trends in geometry variation [77].

The most promising source of theoretical permeability data is the Wisetex software developed at KU Leuven. The WiseTex software package [101,102] is an integrated textile pre-processor for the description of the internal geometry of textile structures based on a unit cell model. The modelling requires information of the internal geometry of the material, such as micrograph-measured thicknesses and widths of the tows after placement on the mandrel. The LamTex program in WiseTex then incorporates nesting effects into the ply interfaces. Calculations with FlowTex, based on Navier-Stokes equations (inter-tow) and the Brinkmann Equation (intra-tow), produce permeability data for the unit cell. The characterization work requirements for this modelling method are probably too much to apply to all industrial fabrics. But it generates a good understanding of the fabric structure and gives an estimate of permeability that can be used for validation of experimental data.

#### 2.3.3.2 Permeability measurement methods

Several procedures for gaining this data have been proposed, mostly involving the compaction of the reinforcement between two flat plates to a desired cavity thickness. A test fluid is then pumped into the mold at the injection gate, either by constant flow rate or constant injection pressure, and flow is established in the preform. Permeability components are derived from analytical solutions using the data achieved by monitoring the flow. Collected data can be injection pressure or flow rate histories, fluid pressures within the part, and progression of the fluid flow front.



The analytical methods to determine the permeability components from the experimental data have naturally become more complex as the experiments themselves have also become more complex. For the simplest case of 1D flow, Equation 2.11 is applied [103]. Once the pressure difference is measured, and the viscosity and porosity known, and the linear relationship between  $L^2$  and  $t$  established, then  $K$  is easily determined as the slope of that relationship.

Other models incorporate more complex flow modeling concepts and boundary conditions based on the experimental setup. The majority of reported techniques define the permeability tensor at a single  $v_F$  value, and must be repeated several times if permeability is required as a function of  $v_F$ . The data is then commonly fit to a power-law model [82,104]:

$$K = A_k v_F^{B_k} \quad (2.13)$$

where the parameters  $A_k$  and  $B_k$  are determined experimentally for a reinforcement.

All the proposed permeability measurement methods differ, and can be categorized, by the dimensionality of flow, which usually equates with the number of permeability components they analyze in a single test. Most methods fall under one of two categories: unidirectional flow (1D) or radial flow (2D) (Figure 2.13).

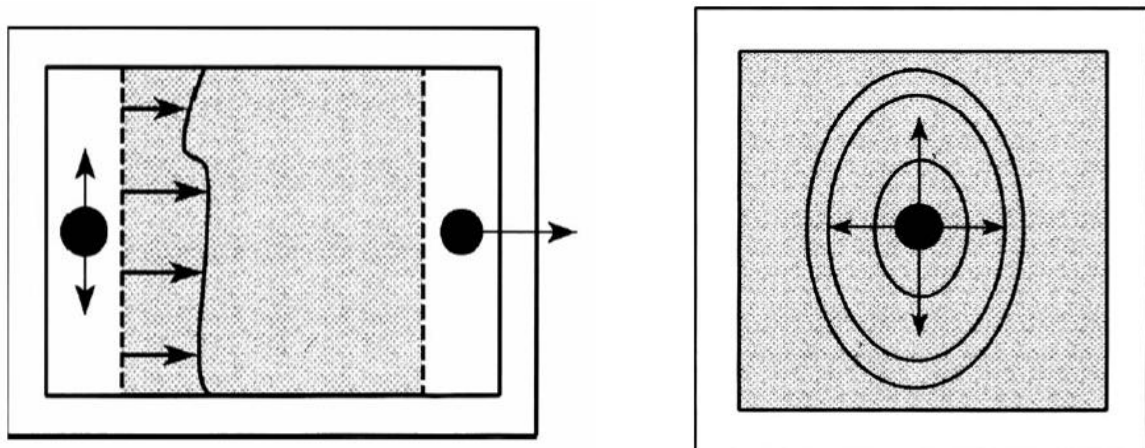


Figure 2.13 – Permeability experiment types: unidirectional flow (left); radial flow (right) [105].

### 2.3.3.2.1 Unidirectional experimentation

The first measurements of permeability were similar to Darcy's original experiments for 1D flow through sand. Such experimentation began using steady-state flow through an already saturated medium. The pressure difference is evaluated against the resultant flow velocity and the

permeability is easily calculated. Later on the 1D experiment was adapted for an advancing flow front through unsaturated media. The test fluid is injected from a short end of the sample and the flow-front position is measured and plotted as a function of time for calculation of the permeability. This latter method was assumed to be more genuine to the RI process, but it introduced many non-Darcy flow complications of micro-scale fluid-media interactions.

This method was initially applied to isotropic materials, where only one measurement was needed. A complication arose in the case of an anisotropic material, however. A 1D flow experiment can yield a value for the effective permeability ( $K_\theta$ ) in the direction of forced flow, assumed to lie at an angle ( $\theta$ ) to a principle axis. To calculate the 2D permeability components ( $K_{xx}$ ,  $K_{yy}$ , and  $\theta$ ) at least three experiments in different  $\theta$  flow directions (usually  $0^\circ$ ,  $90^\circ$ , and  $45^\circ$ ) need to be performed [57]. Given the three resultant effective permeabilities, the commonly applied in-plane approximate Darcy solution [106,107]:

$$K_\theta = K_{xx} \cos^2 \theta \left( 1 + \frac{K_{yy}}{K_{xx}} \tan^2 \theta \right) - \frac{\left( \frac{K_{yy}}{K_{xx}} - 1 \right)^2}{\frac{K_{yy}}{K_{xx}} \tan^2 \theta + 1} \quad (2.14)$$

is solved with the three resultant simultaneous equations.  $K_{xx}$  and  $K_{yy}$  are the major in-plane permeability tensor components and  $\theta$  is the angle between the x-axis of the permeability tensor and the axis of forced flow in the experiment. While this is only an approximate solution to Darcy's Law, it has been shown to agree with exact Darcy FEA analysis of an idealized geometry [86].

A useful simplification of the above solution is based on the inverse of the permeability tensor, called the resistance to flow ( $R$ ) [42]:

$$K_{xx} = \frac{1}{\frac{1}{2}(R_{xx} + R_{yy}) - R}, K_{yy} = \frac{1}{\frac{1}{2}(R_{xx} + R_{yy}) + R}, \theta = \frac{1}{2} \arctan \left( \frac{2 \cdot R_{xy}}{R_{xx} - R_{yy}} \right) \quad (2.15)$$

where the resistance components are:

$$R_{xx} = \frac{1}{K_0}, R_{yy} = \frac{1}{K_{90}}, R_{xy} = \frac{1}{K_{45}} - \frac{1}{2K_0} - \frac{1}{2K_{90}}, R = \sqrt{\frac{(R_{xx} - R_{yy})^2}{4} + R_{xy}^2} \quad (2.16)$$

Following is a history of significant advancements in unidirectional permeability experiments:

- The basic process was patented, where the permeability through a stack of felt was determined by measuring the pressure difference across the flow path [108].
- Method expanded to continuous aligned fibers [40].
- The permeabilities of a variety of fiber mats were measured and empirical solutions for the anisotropic flow were proposed [59].
- Constant pressure and constant flowrate experiments were compared, showing very little difference [57].
- Introduced an automated data acquisition system to the saturated flow 1D method [81].
- Measurement of the saturated permeability at several values of  $v_F$ , from a single preform sample, in one continuous experiment using a compression head [13].
- Use of gas instead of liquid as the permeant was suggested [109,110].

The most discussed disadvantage of 1D flow testing is its sensitivity to so-called race-tracking, i.e. the preferential flow of the fluid along the mold walls when the material sample does not perfectly fit in the mold cavity [27,111,112,113,114]. Race-tracking has been shown to easily cause errors in excess of 100% in permeability measurement experiments [115]. Fabrics are more susceptible to race-tracking than mats, due to the preferential flow orientation resulting from a set of aligned fiber beds [57]. The magnitude of race-tracking effects is unpredictable and unrepeatable [112]. But there are strategies to minimize it, such as using wider moulds [116,117], using a silicone sealant [118,119], or tacky tape on the material edge [105,120]. Methods to separately measure bulk and edge flow have also been developed to quantify the effect of race-tracking [111,114]. Permeability data can be independent of race-tracking if the bulk flow (away from the edges) is separated from the flow by the edges and studied independently [114].

A problem limited to only saturated flow experiments occurs when the initial mold filling leaves trapped air in the preform. This air expands and contracts during the course of the experiment, leading to apparent non-Darcy behavior and measurement errors as large as 50% [115].

#### 2.3.3.2.2 The multiple cavity parallel flow technique

Gebart and Lidström [42] developed a “multi-cavity unidirectional experiment”, where all three fabric orientation experiments needed to solve the 2D in-plane components are performed in a single experiment. The amount of fluid discharge over time in each of three or four cavities (each containing a different orientation fabric sample) is compared to a reference material with known

unidirectional permeability, thus allowing three effective permeabilities to be determined in comparison, and thus the in-plane permeability tensor. The exact values of the fluid viscosity, the temperature (if isothermal), and the injection pressure have no influence on the result as data only comes from mass flow rate comparison. This technique was optimized to reduce race-tracking by using an automated cutting system, silicon seals, and glass platens to visually check for the problem [46]. The method was applied in a repeatability study to a variety of materials with good results and has exhibited standard deviations within 10% [46,121], which is very favorable compared to the typical variation from other methods [27,115].

### 2.3.3.2.3 Radial experimentation

The disadvantages of the unidirectional method led directly to radial experimentation [122], where the resin spreads from the injection point outwards through an enclosed reinforcement towards the cavity walls. This eliminated race-tracking at least along the mold sides, because the fluid now spread continually through the reinforcement and the experiment ends as soon as the walls are reached (Figure 2.13). Adams, et al. [38,39] refined the radial methodology and proposed a solution for the in-plane permeability components and orientation from only one radial experiment using the history of the flow front progression. This cuts down on sample preparation time compared to 1D testing, as only 1 sample (not 3) is required, and the dimensional tolerance can be relaxed without the threat of race-tracking along the mold-sides.

For anisotropic materials, the flow propagates in an ellipse shape, thus naturally accommodating the effects of flow perpendicular to the principle flow direction. Figure 2.14 illustrates an example of the typical flow pattern for a plain weave and its orientation to the machine axis. During the experiment the flow emanates from a central port of radius  $b_t$ . The geometry of the flow ellipse ( $x$ ,  $y$ , and  $\theta$ ) is captured at intervals in time. Its orientation to the machine axis is easily measured visually. An iterative procedure then determines the permeability components as a transformation from the pre-defined general coordinate system.

For constant pressure infiltration in isotropic media, Equation 2.6 is solved as:

$$\frac{dR_f}{dt} = \frac{K\Delta P}{\phi\mu} \frac{1}{R_f \ln(R_f / R_0)} \quad (2.17)$$

The solution to this and its anisotropic equivalent has evolved to accommodate various experimental improvements [27,96,123,124].

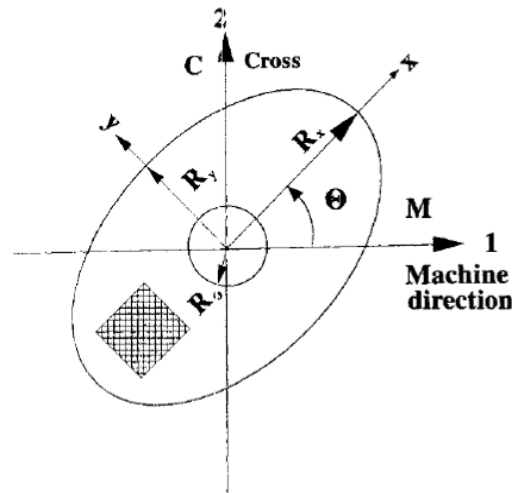


Figure 2.14 – Anisotropic (weave) flow pattern in radial experiment [60].

The radial equivalent of a compression-head based test has been developed for saturated in-plane testing [113]. But this technique showed low accuracy for  $v_F > 50\%$ . A combination of in-plane and 3D flow testing was also based on saturated radial testing, and showed similar low accuracy at high  $v_F$  [125]. Saturated radial testing is probably hampered by the dimensional accuracy needed to fit elliptically-cut fabric stacks to the mold.

A disadvantage of the radial method is that the material and the flow front have to be visible throughout the infiltration. Thus, one side of the mold is made of glass or an optically clear plastic such as acrylic. These transparent mold materials usually have a relatively low stiffness in comparison to the rest of the mold. The high resultant pressures of injection can thus lead to bending of the transparent mold-wall and a non-uniform cavity thickness. At a pressure of 3 bars, the deflection of a PMMA cover at the center of a large point-injection mold was observed to be about 30% of the cavity thickness [42]. Errors of 50% in permeability measurement have been attributed to mold deflection [115]. This problem is typically reduced by placing a metallic frame over the top of the transparent wall as reinforcement. But adding reinforcement obstructs the view of the flow front, creating a trade-off.

Another disadvantage is the radial method's reliance on a direct comparison of the experimentally observed wetted areas with a solution of the Darcy equation in cylindrical coordinates. This approach was found to be sensitive to the radius of the injection port [60, 126]. The nature of the Darcy solution assumes the injected flow rate as a point source - an approximation only valid when

the wetted area becomes large enough compared to the size of the injection port. A large mold is thus required to prevent misleading data. Other complications of point injection include the high pressure resulting from forcing the fluid through a small area, as well as fabric damage when cutting the hole. The fabric variation resulting from the combined effects of high pressure and fabric damage reduces the repeatability of permeability measurement, especially for smaller test rigs.

The transient radial flow behavior is sometimes not well behaved, even when far from the injection area, making data interpretation very difficult. This is because wetting effects become more complicated as the resin velocity slows down in 2D flow compared to 1D flow, especially as flow gets farther from the inlet (described in Section 2.3.6) [84].

The results from 1D and radial test methods have been compared [121,127]. The differences between the two have been attributed to mold deflection in the radial testing [42]. The anisotropy was found to be consistent even when the measured magnitude was not [107]. The differences between the two methods may be confined to experimental care, mold deflections, and wetting effects [107,128].

#### 2.3.3.2.4 Through-thickness permeability measurement

Most of the research cited up to this point has, as noted earlier, neglected through-thickness flow and averaged all flow characteristics into the in-plane dimensions. The principle reason for the lower permeability is assumed to be because most fibers, which resin can flow along, lie in the fabric plane [115].

The first call for transverse permeability values came due to inhomogenities in in-plane flow of thick parts due to the stacking of materials with different permeabilities [27,80,91,129,130]. Early attempts to evaluate the permeability of such a stack used a thickness-weighted average of the individual layer permeabilities [31]. But this approach was determined to allow too much error as it did not account for the transverse flow during the infiltration of a stack [45,131,132]. It was observed that as the resin front advanced faster in one layer than in an adjacent layer, that resin would seep up or down into the dry fibers of the adjacent layer.

$K_{zz}$  measurement has become especially popular in recent literature, as processes like VARI and RFI become more common in industry. Through-thickness flow is the most time-consuming path in

VARI/RFI, so industry has demanded tools to simulate it [13,64]. 1D saturated flow  $K_{zz}$  data was included in establishing a database of permeability data for the National Institute of Standards and Technology (NIST) [115].

The unique challenge with  $K_{zz}$  measurement is that the flow front is not as easily observed as with in-plane measurements, as the fabric itself, impedes observation. As visualization is not a problem with saturated 1D flow testing, various attempts at forcing 1D flow through the thickness have been published [133,134]. Some involve 1D flow in a compression cell, enabling continuous measurement of  $K_{zz}$  and compressibility at a range of  $v_F$  [91,135]. This latter method has been used with gas instead of liquids as the permeant [136]. [137] used a similar method to show a strong dependence between  $K_{zz}$  and the stitching density of non-crimped fabrics (NCF). The challenge of race-tracking in 1D  $K_{zz}$  testing was shown to be minimal with a high driving pressure [114]. Nevertheless, each of these methods suffers to an extent from the same weaknesses of in-plane 1D measurements and requires dedicated tooling.

As the permeability tensor may tilt away from even the z-direction machine axis, [86] extended the empirical model in Equation 2.14 to include  $K_{zz}$ , thus providing a model to determine all three components and their respective orientations. The previous system of three equations then becomes a system of six highly non-linear simultaneous equations to solve for six variables ( $K_{xx}$ ,  $K_{yy}$ ,  $K_{zz}$ ,  $\theta_x$ ,  $\theta_y$ , and  $\theta_z$ ), requiring at least six flow experiments. There are no experimental results reported in the study, however, underscoring the complexity of this approach. Thus, the common approach is to simplify the model by assuming  $K_{zz}$  is aligned with the z-direction machine axis. This then requires only four infusions to solve flow models for ( $K_{xx}$ ,  $K_{yy}$ ,  $K_{zz}$ , and  $\theta$ ).

The simplest method for through-thickness permeability characterization is by point-infusion into the top of a stack of material. As with the radial in-plane testing, all the permeability components can be determined from the flow dimensions of one experiment and race-tracking is not an issue for wetting flow. This method has been employed by various laboratories. The challenge of flow visualization in the z direction has been addressed by various flow monitoring methods: color changing in glass [138], ultrasound [139], MRI [140], X-ray radioscopy [141], or embedded sensors [58,126,142,143,144]. These methods all require expensive equipment. In addition, embedding sensors was shown to cause race-tracking and non-uniform flow [100,145,146,147].

The data analysis for point-infusion is a difficult task, as modeling Darcy's law for three principle directions is mathematically taxing. The resultant complex model must then be solved for three unknowns ( $K_{xx}$ ,  $K_{yy}$ , and  $K_{zz}$ ). Nedanov and Advani [148] presented a mathematical model to solve the variables given the flow geometry at the point the resin reaches the bottom of the mold in point-infusion. This method requires only a glass-bottom mold to see the moment of resin arrival and the in-plane flow radii at that moment. They showed that extracting the  $K$  components from this one point yielded results no different statistically from calculations based on multiple  $z_f$  flow front positions through time within the mould.

Non-intrusive transverse permeability studies have been aided by the practice of the inverse estimation method (IEM), where a full numerical solution model is setup with a guess of the permeability components, and then computer processing compares the solution with actual flow experimentation and iteratively changes the input permeability until the flow front progression history and pressure distribution converge upon the experimental data. This is then a combination of an experimental and a numerical solution. It relies on the validity of the simulation model, but eases the burden of complex experimental procedures [149,150,151].

All of the usual challenges to resin infusion for in-plane  $K$  measurement apply to  $K_{zz}$  as well. But dual scale wetting complications like capillary pressure are even more significant in  $K_{zz}$  flow than in 2D due to even smaller pressure gradients. To date, a universally accepted method for 3D permeability measurement has not yet been found [130].

### 2.3.3.3 Complex geometry

Although the permeability of many materials has been successfully characterized, a significant challenge to permeability testing remains the complexity of actual part geometries. Most  $K$  testing involves un-deformed material with flat geometry. This may be valuable as benchmark data. But if the overall goal is to help the RI industry, then the bends, thickness changes, and curves of parts demanded by industry must be addressed. RI simulation programs cannot account for such architectural effects on the flow behavior without permeability data for deformed media [152].

While it is evident that the pore structure and hence the permeability changes with any departure from ideal geometry, it is undesirable to have to test for the variation in permeability for every possible alteration. This is not only due to the repetitiveness of testing many permutations, but also due to the added complexity. Recent work has focused on general trends to predict the



changes to fiber architecture and flow performance based on a type of geometry feature [152,153,154,155,156].

This study does not treat upon the added complexities of fabric draping or any other geometrical manipulations, however. A fundamental understanding of the simplest geometry is the first priority. Its application to the complex geometries of actual industrial parts will be left to further investigation. This study deals exclusively with materials in their flat un-sheared state.

#### 2.3.3.4 Challenges to permeability measurement

Permeability measurements are not simple and are notorious in the literature for high variation. Also, comparing the measurements from separate laboratories for the same material has frequently shown conflicting data [57]. The challenges to  $K$  measurement are:

- Sensitivity to ever-present variation in local fabric porosities [82,88,115,157,158]. This is the case no matter how much care is taken in manufacturing and handling.  $K$  was reported up to three times higher due to these small geometry variations [159], and thus is difficult to measure with high precision. Often, the care taken in handling during permeability measurement is not the same as when the material is handled in the industry, resulting in different flow characteristics.
- $K$  is a non-linear function of the thickness of the fabric ( $h$ ), as mentioned above in RI deviations from Darcy flow. And the height varies with time for infusion under flexible tooling [100]. Thus comparing data requires precise quantification of the  $v_F$  for every test.
- Variation in  $v_F$  in the  $z$  direction. This results from micro-level fabric variation. All fabrics will be geometrically different at some point of magnification. Its effect has been shown to be negligible for autoclave-cured prepreg [160]. But meso-scale variation between layers has been reported for more complex fabrics [94] and is observed in a later section for the materials in this study.
- The often complex geometrical arrangement and inhomogeneous and anisotropic nature of modern textile preforms (described in Section 3) has complicated process modeling.
- $K$  is also dependent on the number of layers,  $n$ , in the preform stack and the geometry of the tows on either side of layer-interfaces. “Nesting” of tows, i.e. the sinking of fabric layers into each other occurs at ply-interfaces, thus changing the fabric architecture and decreasing  $K$  [130,161]. This effect is highest with parallel tows on either side of the

interface, and decreases as the angle between the tows increases to 90°. For low  $n$ , the top and bottom surfaces of the fabric stack are against either the rigid mold or a vacuum bag and thus have a different amount of nesting as the fiber-fiber interfaces. As  $n$  increases, the average degree of nesting increases as more fiber-fiber interfaces are added. At high  $n$ , the difference in nesting between different  $n$  is negligible [133].

- Permeability has demonstrated a high sensitivity to all kinds of minor disturbances in the experiments such as race-tracking, mold deflection, and incomplete saturation of the preform [84,98,105,148]. Standardization should be applied to experimental installation, data processing, and the measurement technique [57,115,121].

Although much experimental error in measurements can be limited by standardization, a high amount of error for measured values will always remain due to inherent variation in the material geometry. Carefully repeated practices still produced variation of 11 to 34 % in a round-robin study [121]. A minimum variation of 10 to 20 % has been suggested [27]. This implies a need for statistical analysis of the stochastic behavior of permeability [162].

Stochastic studies of the permeability have been aided by increased radial flow testing speed from automated data acquisition systems based on either digitization of video camera footage [148] or electrical sensor arrays [84,96]. Permeability measurement studies of up to 75 experiments of the same material at a single  $v_F$  showed high standard deviation (about 20%), but a normal distribution after elimination of the outliers [81,163]. Statistical analysis allowed the effects of various sources of experimental error to be compared. Fabric nesting was determined to be the most significant source to scatter in  $K$  [95].

Parametric studies of the data showed that for a sample set of only three to five measurements (as has been the case in many published reports), a large uncertainty remains concerning the mean [95]. A minimum of 20 measurements are necessary to come to within 10% of the expected population mean with a confidence level of 95%, and a minimum of 30 measurements is required to obtain a reliable estimate of the standard deviation [163]. These results came from studies of simple weave materials of 42 to 53 %  $v_F$ . In a recent stochastic study, the variation in permeability was shown to decrease with increasing  $v_F$  as the spacing becomes more regular [164]. So at least one flow modeling complication is made simpler with modern high-performance materials of  $v_F > 55\%$ .

Although it represents an unsolvable problem, the understanding of the stochastic nature of permeability can benefit the industry. Knowledge of the possible variation (normal distribution) of permeability enables the design of 'robust' molds and simulation software that takes this into account. When several such simulations ('Monte-Carlo' type) are performed, each time with one of the different possible permeabilities assigned, one can assess possible problem areas in the mold. The mold that is most insensitive to the variations in permeability can thus be designed [10,157].

#### 2.3.3.5 Summary of permeability measurement literature

Permeability measurement for the purpose of RI optimization still faces a number of challenges. The rules of application of permeability have become:

- Permeability measurement methods should have a high degree of standardization and automation, in the sample preparation, flow experiment, data acquisition, and data interpretation.
- All previously published permeability data must be evaluated with caution due to the many commonly practiced experimental errors as well as the high degree of random error inherent to micro-geometry variation.
- The wetting effects around the flow front must be understood to evaluate permeability independent of this in the RI process. This means that the micro-level interactions between the liquid and the preform material must be characterized.

#### 2.3.4 Compressibility

As mentioned in Section 2.3.3.4, in VARI flow the permeability of the fabric is not constant because of thickness changes due to the flexible vacuum bag (Figure 2.15). During infusion, the resin pressure ( $P_R$ ) develops a gradient across the flow length from atmospheric pressure ( $P_A$ ) to the vacuum pressure ( $P_V$ ). In infusions with a fixed cavity height (RTM), the thickness is forced to be constant. But in infusions under a flexible bag (VARI),  $h$  is not constant because the bag bends to balance the pressure gradient against the sum of  $P_R$  and the compaction pressure on the fibers ( $P_C$ ):

$$P_A - P_V = P_R + P_C \quad (2.18)$$

If the resin pressure follows a linear gradient as in RTM, the compaction pressure and thickness would look like the plot in Figure 2.16. As will be shown later, the resin pressure actually curls slightly due to small changes in resin velocity along the filled length.

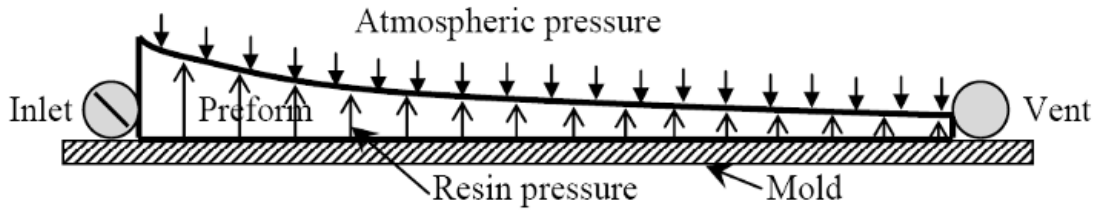


Figure 2.15: Thickness gradient development in RI under flexible tooling [24].

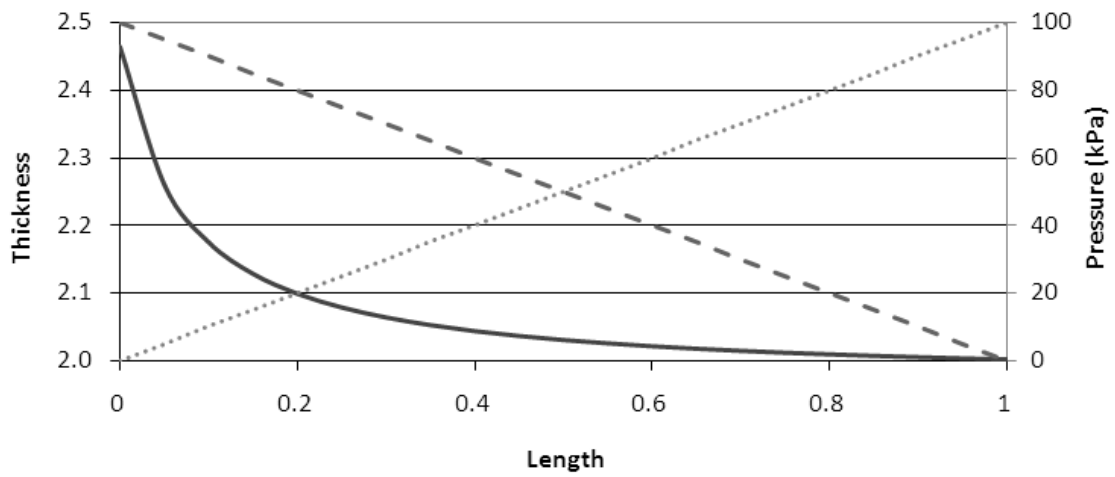


Figure 2.16: Relationship between thickness (solid),  $P_R$  (dashes), and  $P_C$  (dots) along the flow length.

$K$  is a function of  $\phi$ , or  $v_F$  by Equation 2.13. A 10% increase in  $K$  has been associated with every 1% change in  $v_F$  [42]. The porosity or  $v_F$  is in turn directly proportional to  $h$  by:

$$1 - \phi = v_F = \frac{nA_F}{h\rho_F} \quad (2.19)$$

where  $A_F$  is the areal weight (superficial density) of the fabric, i.e. the weight of the fibrous reinforcement per unit area,  $h$  is the thickness of the preform,  $n$  the number of layers in the cavity, and  $\rho_F$  the density of the fibers. The height,  $h$  is a nonlinear function of  $P_C$  [165,166]. The gradient  $dP_R/dx$  along the flow length is linear by Darcy's Law, and so  $dP_C/dx$  is also linear assuming a

constant  $P_A$ . With models  $K(h)$  and  $h(P_C)$  and the  $P_C$  gradient, the permeability  $K(x/x_f)$  can be determined for any point along the flow length ( $x_f$ ) [167,168].

The compressibility  $h(P_C)$  of a material is, like permeability, assumed to be a function of the fabric geometry, but also of the mechanical flexural properties on the micro- and meso-scale. The relationship  $h(P_C)$  changes as permeability does with the number of layers and fiber orientation at the ply-ply interface. This sensitivity to nesting requires that compressibility be characterized for different geometries and materials and lay-ups. The compressibility is somewhat random, as  $K$  is, due to micro level variation in geometry [107, 158]. Thus statistical analysis with repeats of each material is also required.

Note: a complication of compressibility in flow modeling is that compressibility can theoretically vary between the in-plane and through-thickness directions, as the fabric architecture is different. [169] reported that the surface area of a fiber stack did not change after compaction. This infers that all movement which occurs during compaction results in rearrangement by internal translation and rotation of the individual fibers and not by gross outward displacement. Thus, compressibility testing is not conducted in this study for in-plane deformation. It is assumed that the expansion in the in-plane direction is negligible as in [170].

#### 2.3.4.1 Thickness gradient

Resin pressure builds up across the entire part in infusion. This happens faster by the inlet than at the vent (Figure 2.15) [76,171]. Variation in thickness from one end of a part to the other results in lower  $v_F$  and lower associated mechanical properties at one end. This gradient is frozen into place by cure unless remedied.

The magnitude of the thickness gradient has been reported from 25% to 0 (insignificant gradient) [21,165,171,172]. Many studies have shown that the thickness gradient is most significant for low number of layers in the stack,  $n$  [133,169,173,174,175]. For high  $n$ , the stack is more rigid [43,176].

Using binders, debulking cycles [177], lower pressure differentials, applying vacuum to the pot after filling [178], resin bleeding, closing the inlet after filling [21], and using VAP membranes (Section 2.2.3.4) [23] have all been shown to reduce the gradient. An understanding of the compression response is required for flow simulation, as well as to optimize the process to minimize the pressure gradient using any of these methods.

Compressibility characterization of composite reinforcements was introduced in [91]. Most compressibility studies experiment with fabric compaction in a typical compression testing machine. Gas flow has been used [83]. Other methods have measured the fabric pressure response across the part *in-situ* during resin infusion using LVDT sensors [179], laser displacement [172] or Stereophotogrammetry [180]. This latter method produced excellent visualization of the full field thickness gradient.

Most of these studies modeled  $h(P_C)$  as some type of power law function. Many other empirical models for  $h(P_C)$  have been presented to fit the compressibility of non-power law fabrics [73,120,166,171,174,181,182,183,184,185,186]. Some of these models require extensive empirical modeling, having many parameters to fit. Analytical models for the compressibility have also been presented [187,188,189].

#### 2.3.4.2 Mechanisms

During VARI processing, a sequence of compaction and relaxation occurs in the textile. The uncompressed, dry textile is placed under vacuum and compacted to a high pressure (usually about 100 kPa) and  $v_F$ . It is held at that pressure ( $P_A$  acting on the bag) until the resin begins the infusion. That “hold” time is assumed to be longer than 1 minute in all cases, which allows the textile time enough to re-arrange its dry fibers under the pressure to “decay” or nest to an equilibrium higher  $v_F$ .

When the resin first arrives at a particular location, the lubrication of the fibers causes an immediate further increase in nesting and  $v_F$ . [166,172] showed how the thickness immediately drops when the resin flow front reaches a point in the textile, due to a higher compliance from rapidly-acting lubrication phenomenon. The thickness rises (and  $v_F$  decreases) thereafter as resin pressure relieves the compaction pressure (Equation 2.18). This “springback” of the preform depends not only on resin pressure but also on micro- and macrosaturation [166]. This cycle is illustrated in Figure 2.17.

After the part is completely infused, a relaxed vacuum pressure (such as 30 kPa) is often applied in industry to both the inlet and outlet to remove excess resin and decrease the thickness gradient that developed along the flow length. A resin pressure of 30 kPa means that the final compaction pressure on the wetted fabric is about 70 kPa.

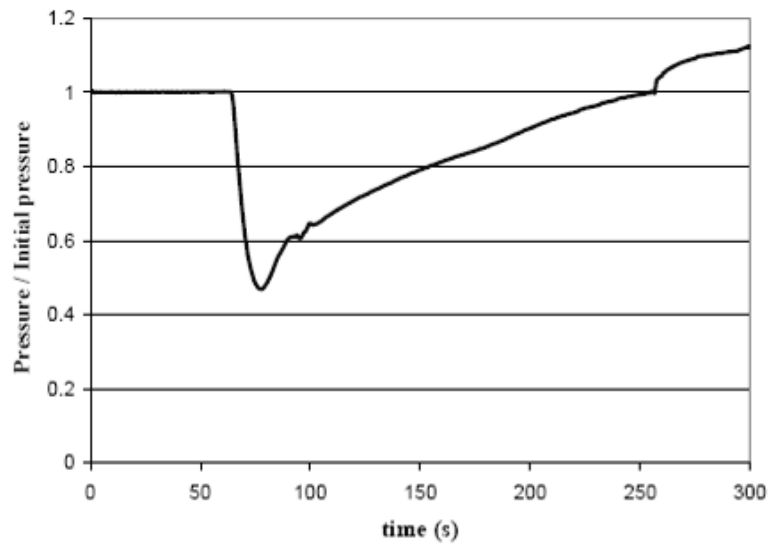


Figure 2.17: Typical development of preform thickness during VARI around time of resin arrival [166].

This extent of this cycle for any point in the fabric depends on its location in the mold (Figure 2.18). Close to the inlet, the fabric will undergo full unloading (expansion) from  $P_C = 100$  kPa (dry) to  $P_C = 0$  due to  $P_R$  reaching the atmospheric pressure applied to the pot. The post-infusion reduction of  $P_R$  to 30 kPa will cause a rapid compaction to 70 kPa. In contrast, by the vent, the fabric will remain at its dry full  $P_C$  throughout most of the infusion time. It undergoes lubrication when the flow front finally reaches that point.  $P_R$  remains low by the vent, so it experiences little relaxation until the entire part is relaxed by the post in-fusion pressure change of  $P_V$  to 30 kPa.

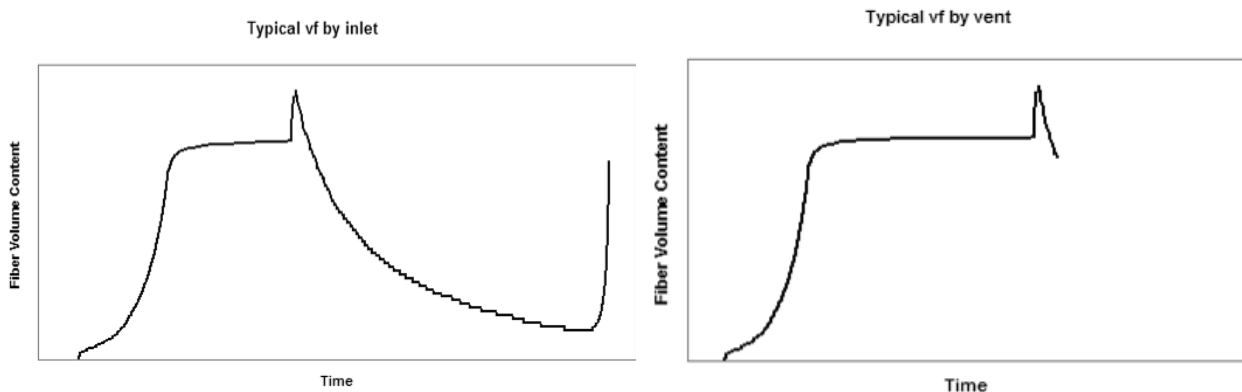


Figure 2.18: Typical  $v_F$  vs. time during VARI infusion.

### 2.3.4.3 Dry and wet differences

The compaction response of the fabric can be viewed as an array of springs. It has been shown that a wet fabric exhibits different compressibility when compared to a dry fabric due to reduction

of the fiber friction coefficient from lubrication (Figure 2.19) [44,181,190,191,192]. The dry compaction followed by both the dry and the wet release for a carbon NCF has been measured (Figure 2.20) [193]. This allowed demonstration of the difference in compressibility between the dry and wet release, and emphasized the importance of wet unloading modeling. This test would logically be most accurate to the VARI process. But this is a difficult test setup to achieve in practice – to monitor the thickness of the preform with accuracy, while it is under a vacuum bag and under pressure. An adequate setup for such an experiment requires something along the lines of full-field laser scanning [21,181] or digital speckle photography [194].

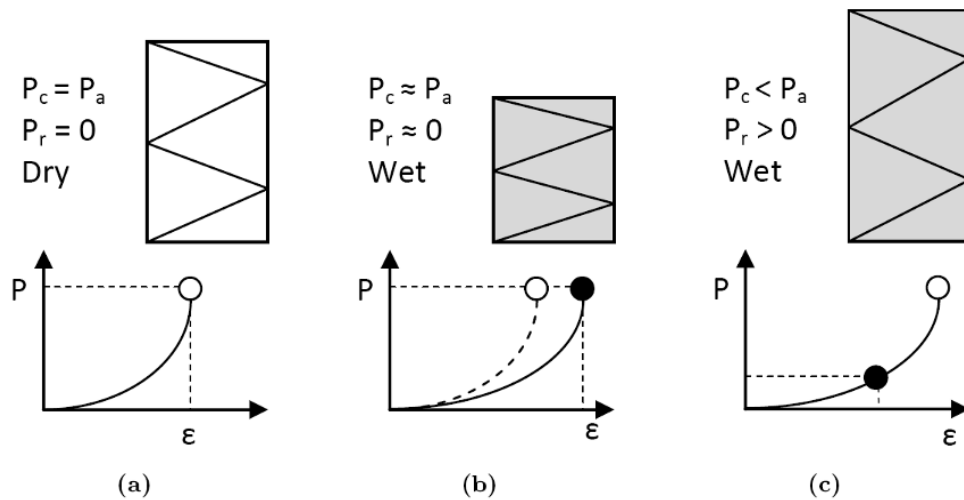


Figure 2.19: Compaction mechanism in VARI infusion [191]: (a) dry compaction, (b) wet compaction, (a) wet unloading (spring back).

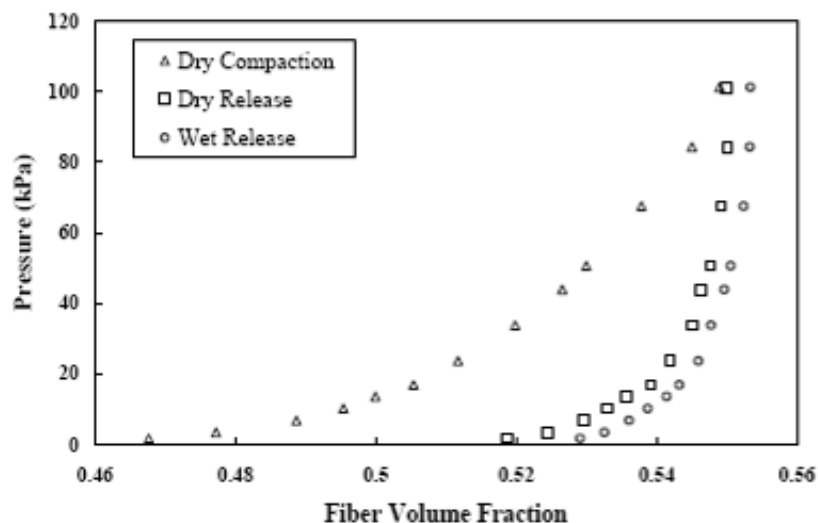


Figure 2.20: Dry compaction, followed by dry or wet relaxation of carbon NCF [191].



The wet compressibility's dependence on the choice of wetting fluid has been investigated. For the case of comparison between water and oil, both insignificant differences [174] and significant differences [52,177] have been reported. For flow studies, silicon oil was shown to achieve results close to those for ideal analytical solutions, suggesting that the surface chemistry interactions between silicon oil and carbon cause few complications [52]. Silicone oil is frequently used in porometry studies of carbon, and easily wets carbon fabric by capillary action without any external pressure (0° contact angle).

A VARI flow simulation code depends only on the compressibility of a fabric from the point the resin reaches it [187]. Therefore a model of the wet unloading from 100 kPa to 0 pressure and subsequent rapid compaction to 70 kPa is the target data that accounts for lubrication. As the rapid re-compaction occurs in a small portion of the fabric around the inlet, the wet unloading curve is the most important data in compressibility modeling for VARI simulation.

#### 2.3.4.4 Wet expansion modeling

A simple power law fit the first compaction data well, but only for the dry samples did it accurately fit the expansion curve. Many of the empirical compressibility models mentioned in Section 2.3.4 were attempted to fit with the compression data of the materials in this study. None of them fit the wet relaxation curves as well as the Grimsley model for wet expansion [191]. This is an empirical model to describe the wet expansion pressure response following dry compaction:

$$\varepsilon_w = a_w + b_w \left( \frac{P_C}{c_w + P_C} \right) \quad (2.20)$$

where the wet strain is defined as:

$$\varepsilon_w = 1 - \left( \frac{v_{F0}}{v_F} \right) \quad (2.21)$$

$v_{F0}$  in this case is the minimum initial fiber volume of the dry material before compaction, thus taking into account the viscoelasticity differences between dry and wet compressibility.

The Grimsley model has been successfully applied to carbon NCF materials similar to those in this study [104]. In another attempt apart from this study at coupling the multiple models of viscosity,  $K$ , and  $P_C$ , the Grimsley model was also used for a similar carbon NCF [69].

This study's approach to flow simulation incorporating the Grimsley model relies on two assumptions:

1. The wet unloading expansion curve is not significantly different when preceded by wet compaction as opposed to the dry compaction in the VARI process.
2. Instantaneous lubrication: the lubrication-induced increase in  $v_F$  at the point where the flow front first wets the fabric occurs rapidly enough (Figure 2.17) that one can assume the wet expansion curve to apply immediately and throughout a flow simulation without having to incorporate the transition from the dry curve to the wet curve.

#### 2.3.4.5 Viscoelasticity

It has been observed that the load to maintain a constant thickness reduces with time or alternatively, the thickness reduces with time for a constant load during a compaction test. Pressure drops of as much as 40% at the same thickness [91], and up to 3.8% thickness at constant pressure [195] have been observed. An equilibrium pressure or thickness can take up to 5min to be achieved [195], but most of the decay occurs within the first 10 seconds [91]. This viscoelastic behavior is attributed to the nesting-rearrangement of the tows during compaction. Viscoelasticity increases with lubrication [196], more layers [43,44], and slower compaction speed [197].

Various models to predict the pressure/thickness decay of fabric reinforcements were compared by [198]. A model for the pressure decay at constant thickness [43] can be used to extrapolate the theoretical thickness at a higher equilibrium pressure using the same fitted constants from a constant thickness experiment. This gives converted results as they would be in VARI where the pressure stays constant.

#### 2.3.4.6 Debulking cycles

Viscoelastic behavior has also been seen in the change of compressibility with subsequent cycles of compression/expansion (Figure 2.21). The compression and expansion curves are typically different for wet expansion, a hysteresis that changes the compressibility with each cycle [43,44,82]. [172,196,199,200] all showed that repeating this cycle shifts the compressibility to higher  $v_F$  at lower pressures, thus the name "debulking". More than 50 debulk cycles are required to provide an equilibrium compressibility [200,201]. But most of the fabric architecture changes happen during the first few cycles; little change in compressibility is subsequently seen [177,182]

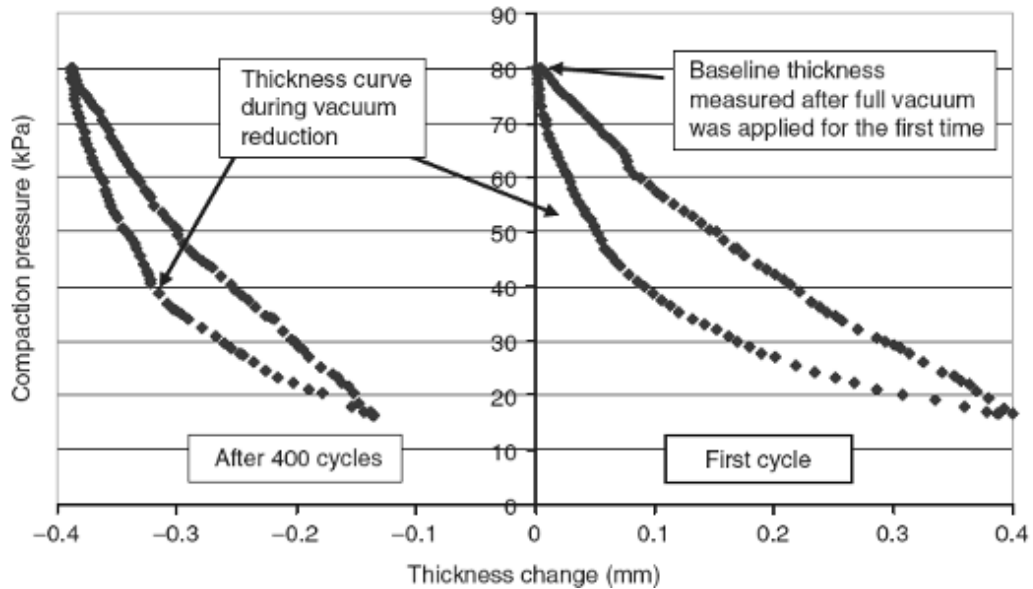


Figure 2.21: Thickness reduction during debulking for 24oz E-glass [201].

Successive cycles can reduce inter-tow space (resin rich areas), reduce void content, and increase the maximum  $v_F$  [177]. Debulking of the preform allows the  $v_F$  in VARI to approach that of prepreg materials. VARI processing starts with a dry fabric, which allows for the nesting-rearrangement of the dry fibers before infusion. Prepreg materials cannot implement this method of thickness reduction as they are already infused with resin before processing.

#### 2.3.4.7 Resin shrinkage

The thickness of an epoxy wetted fabric will change as the resin shrinks due to cure. This is assumed to only happen once the resin is gelled to the point that it cannot flow through the fabric anymore. This only happens then after an equilibrium pressure gradient (Equation 2.18) has been “frozen” into place. This shrinkage results in a decrease in the height and increase in the  $v_F$ . The magnitude of this effect must be calculated.

The shrinkage of a curing resin is difficult to measure. Most reported values estimate it as the “apparent shrinkage” from the difference between uncured and cured densities [8]. The RIM235R epoxy is based on a DGEBA (Bisphenol-A-Epichlorhydrin) epoxide. The cure shrinkage for similar DGEBA epoxy systems has been reported to be between 4 and 7 % [202, 203]. Assuming that the lengths of the fibers constrain resin shrinkage in the in-plane directions, all shrinkage of the epoxy only occurs in the thickness direction. This means that a maximum plausible reduction in epoxy thickness is 7%. But no shrinkage occurs in the carbon fibers, so the 7% max shrinkage must be

reduced by the fabric porosity. As with the volume fractions, an effective resin thickness  $h_R$ , can be defined:

$$h_R = h\phi = h - h_F \quad (2.22)$$

where  $h$  is the thickness of the preform, and  $h_F$  is the effective thickness of the fibers. As the volume of fibers does not change,  $h_F$  is also constant through the cure. If  $\beta_C$  is defined as the percentage decrease in resin thickness, then substitution of  $h_R$  for the uncured (1) and the cured (2) versions of Equation 2.22 yields:

$$\beta_C = \frac{h_{R1} - h_{R2}}{h_{R1}} = \frac{h_1 - h_2}{h_1 - h_F} \quad (2.23)$$

The fiber thickness  $h_F$  can be replaced with the product of the total height  $h$  and  $v_F$ , similar to the resin relationship in Equation 2.22. The ratio of the uncured  $v_F$  to the cured  $v_F$  is the inverse of the height ratio:

$$\frac{v_{F1}}{v_{F2}} = \frac{h_2}{h_1} \quad (2.24)$$

After substitution and re-arrangement of terms, the cured fiber volume ratio is:

$$v_{F2} = \frac{v_{F1}}{1 + \beta_C(v_{F1} - 1)} \quad (2.25)$$

This simple function implies that 7% shrinkage will only increase the fiber volume content by 2.2% of the uncured  $v_F$ . A  $v_F$  of 60% for instance, would only increase to 61.8% with 7% shrinkage.

### 2.3.5 Viscosity

Three things happen to a resin during cross-linking: 1) evolution of exothermic heat, 2) increase in viscosity, 3) resin shrinkage. The last phenomenon was discussed in Section 2.3.4.7. The viscosity in Darcy's Law (Equation 2.3) is frequently assumed to be constant for modeling simplicity. This assumption is safer when the time of testing is low, and the ambient temperature shows little fluctuation over that time. But in reality, the viscosity changes with both cure and exotherm.

The curing reaction, the exotherm, and the heat and mass transfer during a curing infusion all complicate viscosity modeling efforts. Various empirical models exist to predict the viscosity-time

relationship [204]. The majority of them are simple isothermal models of the curing effects on viscosity [171]. Most isothermal models are built around an exponential function of time:

$$\mu(t) = \mu_0 e^{Ct} \quad (2.26)$$

where  $\mu_0$  is the initial viscosity, and  $C$  is an empirically fitted constant. This can be determined fairly easily with a viscometer and a small amount of resin kept at the same temperature by a water bath or similar means.

There are fewer empirical models to predict non-isothermal viscosity [72,205,206,207,208,209]. As the temperature of the system fluctuates due to exotherm or ambient temperature ( $T_A$ ) fluctuation, the viscosity will change due to both changes in the cure rate and the temperature dependence. The temperature dependence can be understood by simple isothermal testing fit to the above equation. But the curing rate is more difficult.

The reaction conversion at any time  $\alpha(t)$  represents the fraction of available reactants that have already cured, changing from 0 at time of mixing to almost 1 when most curing has already been accomplished. The reaction rate,  $k_R(t, T)$ , is the change in conversion from one time step to the next and is a function of the temperature:

$$k_R(t, T) = \frac{\partial \alpha(t)}{\partial t} \quad (2.27)$$

where higher temperatures naturally result in higher reaction rates.  $\alpha(t)$  at any point in cure is then the sum of the  $k_R(t, T)$  contributions to the conversion for every time-step from mixing to  $t$ :

$$\alpha(t) = \int_0^t k_R(t, T) dt \quad (2.28)$$

Thus the conversion is a measure of the temperature history up to any point. The non-isothermal viscosity  $\mu(t, T)$  is a function of both  $\alpha(t)$ , representing the curing dependence, and  $\mu_0(T)$  which represents the temperature dependence. The latter variable,  $\mu_0(T)$  is the Arrhenius relationship between temperature and the initial viscosity (uncured) just after mixing of the resin:

$$\mu_0(T) = A_0 e^{\left(\frac{E_0}{RT}\right)} \quad (2.29)$$

$A_0$  and  $E_0$  are empirical constants for a given liquid and  $R$  is the ideal gas constant.

Of the published non-isothermal models, the model of Pichaud et al. (referred to in this work as the “Pichaud model”) seems to be the most straightforward approach [209]. At least three curves of empirical data are required: the  $\mu_0(T)$  curve, as well as at least two tests at different temperatures of the isothermal viscosity development  $\mu(t)$  at each temperature. With this data, the viscosity  $\mu[T,\alpha(t)]$  can be predicted at any temperature and conversion. This model will be discussed further in Section 4.5.

With such a model  $\mu(T,t)$  for different finite elements of resin, volume scattered throughout the resin pot and mold can be determined, given the temperature history for each of the finite resin elements. To determine the temperature distribution during the exothermic cure, modeling the concentration of heat in the center of the resin pot is required due to the associated heat transfer.

#### 2.3.5.1 Heat transfer

Heat transfer is the transfer of energy in the form of heat from a hotter object to a cooler object. This transfer happens spontaneously when two objects of different temperatures come in contact. It cannot be stopped; only slowed. This is known as the second law of thermodynamics or the Clausius statement.

Heat transfer occurs in three different pathways: conduction, convection, and radiation. For all cases of exotherm due to epoxy cure, the radiative heat transfer is insignificant compared to conduction and convection.

Conduction is heat transfer through a homogenous medium. On an atomic scale, heat transfer is made via excitation of free electrons and their subsequent movement to a location and status of less free energy. The inherent ability of a materials ability to transfer energy among these electrons is quantified as the thermal conductivity,  $k$ . Metals are good conductors due to the close proximity of freely moving electrons. As the density of a material decreases, so does the proximity of electrons, as well as the conductivity [210]. Thus liquids are worse conductors than metals, and gases are even worse than liquids. The 1D conductive heat transfer across a homogenous medium with constant conductivity  $k$  from one temperature to another ( $\Delta T$ ) is:

$$q = k\Delta T \frac{A}{L} \tag{2.30}$$

where  $L$  is the length between the two temperatures, and  $A$  is the cross-sectional area the heat goes through.

Heat convection describes the effects of gravity on fluids of changing density during heat transfer. When a surface comes into contact with a fluid (gas or liquid) of a different temperature, heat conduction warms or cools the fluid immediately adjacent to the surface. Heating a fluid makes it less dense, while cooling it does the opposite. The mobility of fluids allows gravity to move the heavier fluid around that of the lighter fluid. This is how warm air rises off a heated surface. The cooler, heavier air is constantly replacing the warmer air due to gravity, with the warmer air being pushed up in displacement. The cooler air warms as well when in contact with the surface, providing a continual rotation of the air. This rotation whisks heat away from the surface, thus accelerating the heat transfer from the surface in comparison to conduction-only transfer.

In the case of a curing resin pot, the exotherm-heated resin is conducting heat from the surface on all sides to air or water. For the sides and bottom of the resin body, this conduction happens through the pot walls (either stainless steel or paper). But as the walls are very thin, this added heat resistance is considered negligible. Furthermore, air or water is constantly rotating to displace lighter warmed air/water with heavier fluid, thus accelerating the heat transfer from the epoxy to the atmosphere.

When the air or water around the pot is moving, for example due to a fan, then this heat transfer is accelerated (“forced convection”). But the lab environment is controlled to minimize air movement, and so all convection is assumed to be “natural”.

The heat convection from a liquid to an infinite medium of gas is evaluated by the difference between the temperature of the liquid ( $T_L$ ) and the temperature of the infinite medium ( $T_\infty$ ), well away from the surface. The 1D conductive heat transfer,  $q$ , is modeled for constant temperatures through a surface area of  $A$  as:

$$q = h_c A (T_\infty - T_L) \tag{2.31}$$

where  $h_c$  is the rate of convection. This term is difficult to determine even in natural convection. It requires characterization of the conduction of each substance. The rate  $h_c$  from one substance to another is dependent on many parameters for the interface of that particular combination of

materials: temperatures, viscosities, and physical orientations. Some general models exist to predict  $h_c$  for ideal cases, but accuracy requires experimentation for each system analyzed [210].

In the case of a heated resin pot, the upper surface of the resin convects to air above it. Modeling this convection problem is complicated by unstable boundary layers caused by the plumes of warm air off the resin surface [211]. Modeling the conduction in a resin pot is difficult enough in itself.

As the typical container holding resin for infusion is cylindrical, the body of resin is shaped as a stubby cylinder. A model for both conduction and convection in a stubby (finite) cylinder is available. The dimensionless temperature distribution in a stubby cylinder can be approximated as the product of the distributions of an infinite cylinder and an infinite slab [210,212]:

$$\Theta = \frac{T(r, z, t) - T_\infty}{T_i - T_\infty} = [\Theta_{slab}] [\Theta_{cylinder}] \quad (2.32)$$

This is visualized in Figure 2.22. Each of the temperature distributions are derived from their separate solutions. The 1D Laplacian of the heat diffusion equation in Cartesian coordinates for an infinite slab of thickness  $h$  is:

$$\frac{\partial^2 T}{\partial h^2} + \frac{q_V}{k} = \frac{1}{\alpha_T} \frac{\partial T}{\partial t} \quad (2.33)$$

with its Laplacian in cylindrical coordinates for an infinite cylinder of radius  $r$ :

$$\frac{1}{r} \frac{\partial}{\partial r} \left( r \frac{\partial T}{\partial r} \right) + \frac{q_V}{k} = \frac{1}{\alpha_T} \frac{\partial T}{\partial t} \quad (2.34)$$

where  $q_V$  represents the volumetric heat generation from the exotherm and  $\alpha_T$  represents the thermal diffusivity of the material:

$$\alpha_T = \frac{k}{\rho c_p} \quad (2.35)$$

The specific heat at constant pressure of the material is denoted here as  $c_p$ .



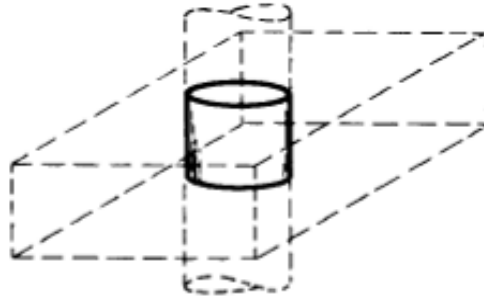


Figure 2.22: Heat transfer model for stubby cylinder as product of infinite slab and cylinder [210].

The solution to this model has been shown for the case of no exotherm, no convection, and where the boundary conditions are the same for both. But no solution is available to this model with either heat generation or heat convection, and it is beyond the author's abilities or resources at mathematical analysis to generate one.

Thankfully, the heat transfer in stubby cylinders has been shown to behave like a sphere [212,213], especially as the height of the cylinder approaches its radius. The shape of the cylindrical resin body in infusions through this study was done with cups/cans of the right size to make a particular mass of resin have nearly equal height and radius. This greatly simplifies the problem as only one dimensional variable, the radius, is examined.

The solution for heat transfer in a sphere is derived from the polar coordinates Laplacian of heat diffusion is:

$$\frac{1}{r^2} \frac{\partial}{\partial r} \left( r^2 \frac{\partial T}{\partial r} \right) + \frac{q_v}{k} = \frac{1}{\alpha_T} \frac{\partial T}{\partial t} \quad (2.36)$$

The solution to this has been presented for unsteady-state conduction with heat generation of a sphere into an infinite surrounding medium with the same properties [214]. For a sphere of radius  $R$ , the temperature  $T(t,r)$  at any time and point within the sphere at  $r$  from the center is:

$$T(t,r) = \frac{q_v \alpha t}{k} - \frac{q_v R^3}{2rk} \left[ F \left( \delta_1, \frac{t \alpha_T}{R^2} \right) - F \left( \delta_2, \frac{t \alpha_T}{R^2} \right) \right] \quad (2.37)$$

where  $F(\delta,t)$  is:

$$F(\delta, t) = \frac{4t^{3/2}}{3\sqrt{\pi}} e^{-\delta/4t} + \left(\frac{\delta}{3} - \sqrt{\delta}\right) \sqrt{\frac{t}{\pi}} e^{-\delta/4t} + \left[t + \frac{\delta}{2} - \sqrt{\delta}\left(t + \frac{\delta}{6}\right)\right] \operatorname{erfc}\sqrt{\frac{\delta}{4t}} \quad (2.38)$$

$\delta$  is defined as:

$$\delta_1 = \left(1 - \frac{r}{R}\right)^2, \delta_2 = \left(1 + \frac{r}{R}\right)^2 \quad (2.39)$$

This solution was later adapted for the case of the sphere (subscript 1) and medium (subscript 2) having different material properties [215]:

$$T(t, r) = \frac{q_v R^2}{k_1} \left\{ \frac{k_1}{3k_2} + \frac{1}{6} \left(1 - \frac{r^2}{R^2}\right) - \frac{2R\delta_1}{r\pi} \int_0^\infty \frac{\exp(-y^2 t \alpha_{T1} / R^2) (\sin y - y \cos y) \sin(ry / R)}{y^2 \left[ (\delta_2 \sin y - y \cos y)^2 + \delta_1^2 y^2 \sin^2 y \right]} \right\} \quad (2.40)$$

$\delta$  in this case is:

$$\delta_1 = \frac{k_2}{k_1} \sqrt{\frac{\alpha_{T1}}{\alpha_{T2}}}, \delta_2 = 1 - \frac{k_2}{k_1} \quad (2.41)$$

These models still incorporate no convection. Each of these solutions merited a separate journal publication. The incorporation of convection is once again beyond the author's abilities or resources. But these solutions can at least generate an all-conduction approximation of the temperature as a function of time and radius from the center of the sphere.

This allows the estimation of temperature history for a particular infinitely small body of resin at any location in the pot. Modeling the conductive heat transfer for a moving resin element could be done by evaluating all local temperatures at each individual time, and tracking the movement and change of environment as a resin element leaves the pot and goes through the inlet tube and then through the fabric in the mold.

The models described above for the temperature distribution and development, as well as the non-isothermal curing viscosity development, will be compared to experimentation to determine their applicability in flow modeling. It is assumed (and hoped) that high accuracy in flow modeling will not require convection modeling of heat transfer from the resin.

### 2.3.6 Dual-scale flow effects

An often-reported deviation of flow from Darcy's Law is a nonlinearity dealing with the flow rate ( $Q$ ) and the pressure gradient ( $\Delta P$ ). Darcy's Law dictates that a linear relationship should exist between these two parameters. The coefficient of proportionality (permeability divided by viscosity) should be a constant for a particular experiment when conducted in the same material and fiber geometry, assuming isothermal conditions or insignificant variation in viscosity. Some studies have confirmed this behavior over a range of flow rates [121,199].

But many authors have reported this to not be the case [47,48,51,80,91,216,217,218]. Darcy behavior may only be reasonably expected from a particular range of flowrates and injection pressures. It seems that at low flow velocities, either from low  $Q$  or low  $\Delta P$ , measured values of  $K$  decrease exponentially as  $Q$  or  $\Delta P$  decrease.  $K$  should be a function only of the fabric geometry however; it should not change with flow velocity. Something else is slowing down the flow.

The effects of shear between the flowing resin and the fibers have been blamed for the non-linearity. In this context, resins of the same viscosity, but different surface tensions or contact angles can exhibit different flow [48,51,219]. But the majority of literature on the subject of flow non-linearity discusses dual-scale wetting effect differences between saturated and unsaturated flow, especially in terms of the variable capillary pressure,  $P_{cap}$ .

The question if there is a difference between the permeability in flow with a moving front (wetting flow) and fully saturated flow without moving front (saturated flow) has been a matter of concern. A summary of the contrasting results in the literature is found elsewhere [220]. The deviations in the results by the two methods have been attributed to differences in experimental method or materials [220], pressure-induced movement of the fibers [47], surface energy effects at the micro level [199] and inclusion of air bubbles at the flow front [49]. The difference is usually explained however, by the longer penetration time in unsaturated flow due to the required wetting of tows [119,154,158,216,220,221].

This principle was demonstrated in a comparison of the pressure gradient over the length of the flow at low flow velocities (Figure 2.23) [29]. When the part is still not completely filled, the unsaturated pressure gradient is not linear. Only when the part fills does the saturated flow adopt the linear relationship assumed by Darcy. Thus unsaturated flow effects are in force throughout flow modeling [56].

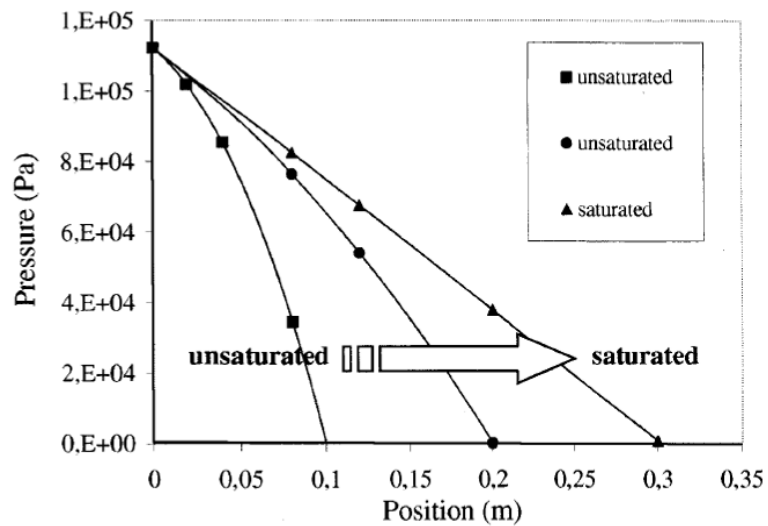


Figure 2.23: Non-linear pressure gradient at slow  $v$  during wetting flow [29].

At low flow velocities, “fingering” of the resin can be observed, where the flow front in the center of the tows lags behind the front in between the tows. This is especially evident in the case of stitched materials due to regularly spaced gaps; the fingering follows both the stitching and the inter-tow channels [222,223]. Figure 2.24 shows this phenomenon in a non-crimped fabric (NCF). This was proven to be the result of heterogeneity between inter-tow and intra-tow pore architectures [152,224]. The dual scale flow effects increase with the number of fibers in a tow [56,225].

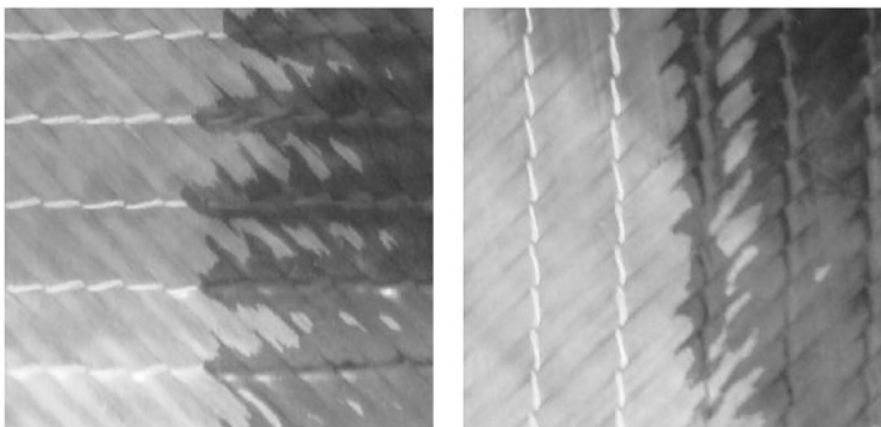


Figure 2.24: Flow fingering along stitching and inter-tow gaps: flow along (left), and perpendicular (right) to stitching [15].

This lag prevents the development of a sharp flow front during unsaturated permeability testing, and hence complicates permeability measurement. If the tows were impermeable, then flow would be faster along the inter-tow gaps and would be an ideal Darcian flow. But the resin is

drawn from the inter-tow gaps and into the dense fiber packing of the tows through capillary draw. This effectively slows the bulk flow of the fabric [56,224,226,227].

### 2.3.6.1 Dual-scale flow modeling

For RTM, it is agreed that the preform macro-structure is of primary importance due to higher flow velocities [40,53,54,105]. While it is the logical starting point for VARI modeling, the slower speeds may necessitate characterization of the micro-structure as well.

A sink term,  $S$ , has been used to describe a decrease in the resin velocity at the flow-front due to dual-scale effects [55,228,229].  $S$  is the volumetric rate of resin absorption by tows per unit volume, and is directly related to the ratio of intra-tow to inter-tow pore volume. The sink term was linked to the pressure loss caused by micro-structure flow [230,231], and is suggested to be a function of the capillary number [55].

Another approach to quantifying the effects of dual scale flow is by adding a new pressure term to Equation 2.18. The total pressure gradient in an infusion is the combined effects of applied pressure (inlet), vacuum pressure (vent), gravity and capillary pressure ( $P_{cap}$ ) [128,232]. In the absence of gravity, the pressure relationship across the vacuum bag for VARI including the  $P_{cap}$  term is:

$$P_A - P_V \pm P_{cap} = P_R + P_C \quad (2.42)$$

Previous papers have disagreed on whether the capillary pressure adds to the pressure gradient [232] or subtracts from it [128]. For 1D fibrous resin flow, the capillary pressure has been estimated as [232]:

$$P_{cap} = \frac{F}{D_f} \cdot \frac{1-\phi}{\phi} \cdot \gamma \cos(\theta_C) \quad (2.43)$$

where  $D_f$  and  $\phi$  are the diameter of a single fiber, and fabric porosity.  $\theta_C$  is the contact angle of the fluid on the fiber, and  $\gamma$  is the fluid's surface tension.  $F$  is the form factor for the alignment of the fibers to flow, being 4 for along the fibers and 2 for perpendicularity [233].  $F=3$  to 3.7 was determined for in-plane flow in a plain weave [234], while  $F = 1.8$  for z-direction flow [232].

Lower pressure [220], smaller contact angle, and higher  $v_F$  [8,54] have been shown to cause higher  $P_{cap}$ . In 1D infusions of a glass fabric and epoxy,  $P_{cap}$  was found to be as high as 37 kPa, or over 1/3

of ambient pressure [232]. This was reported for a  $v_F$  of 79%. At more typical  $v_F$  values to VARI, maximum  $P_{cap}$  values were slightly lower [8]. Except for very close to inlet, this greatly exceeds the applied pressure on resin.

Different techniques for contact angle measurement have been suggested [235,236,237]. The static contact angle for a typical epoxy on carbon has been reported to be 28.5° [53]. Slightly different results, 33° were measured for the dynamic contact angle, when the fluid is slowly moving [236]. This is assumed to be more accurate to flow modeling.

The effects of fluid velocity ( $v$ ) viscosity ( $\mu$ ) and surface tension on  $\theta_c$  are related to the capillary number, which is [235]:

$$Ca = \frac{\mu v}{\gamma} \quad (2.44)$$

$\theta_c$  is constant for low flow velocities at  $Ca < 10^{-6}$ . The relationship between static  $\theta_{CS}$  and dynamic  $\theta_{CD}$  contact angles has been modeled for low gravity and inertia as [238]:

$$\frac{\cos\theta_{CS} - \cos\theta_{CD}}{\cos\theta_{CS} + 1} = \tanh(4.96Ca^{0.702}) \quad (2.45)$$

Above a certain threshold in velocity,  $\theta_c$  has been shown to diverge into advancing and receding versions of the contact angle [237]. But for sufficiently low velocities, Equation 2.45 can be solved for the dynamic contact angle given the static contact angle and capillary number from Equation 2.44.

Another approach entails a modified version of Equation 2.44 included direct contact angle dependence [239]. Relating  $Ca$  directly to the Darcy flow parameters:

$$Ca = \frac{K\Delta P}{\gamma\phi L \cos\theta_c} \quad (2.46)$$

This allows for experimental determination of the contact angle given a typical 1D flow experiment.

There are a few studies in which wetting effects have been incorporated into flow simulation [228,240]. FEM simulation of dual scale flow has been modified to incorporate a 1d element at each node, representing the saturation of the tow. Thus two permeability values are required: one

for the bulk flow and one for the impregnation of the tows [224]. The relationship between the two can be calculated from the lead-lag length seen in flow-fingering (Figure 2.24). Another approach to dual-scale flow modeling is based on Darcy flow inside the tow, and Navier-Stokes flow in the inter-tow channels [241]. These remain mostly theoretical attempts.

### 2.3.7 Vacuum bag sealing of fabric surface

In a rigid mold setup such as RTM, the inter-tow gaps on the top and bottom surfaces of the fabric stack are assumed to be the least nested. Thus, the bulk permeability measured from flow monitoring in a rigid cavity incorporates this effect. In contrast, infusion under a vacuum bag may have some nesting of the top layer in a fabric stack due to vacuum suction of the bag into the inter-tow gaps.

A recent work suggested modifying the peel-ply permeability for bag sealing in simulation efforts of DM-based VARI [242]. Another recent study suggested that simulation of flow in the distribution media cannot rely on  $K$  measurements of the DM by itself, but requires *in-situ* evaluation under a vacuum bag due to the sealing [243]. The difference in fabric permeability however, between rigid cavity flow and VARI flow has not yet been quantified. This “bag sealing” of the top surface is assumed to be less significant as more layers are added to the stack.

### 2.3.8 Void prediction

The ability to predict void content is not an obstacle to accurate flow simulation. But attempts are being made to incorporate void prediction into flow modeling. This is due to the correlation of void size/distribution with processing parameters such as pressure or flow rate. As these are determined for each local area in the part, concurrent predictions can be made for the void content. Void content is usually quantified as the fiber content is, by the volumetric percentage of it in the final part,  $v_0$ . The value of  $v_0$  has shown to be strongly correlated with final part properties. Accurate prediction of voids in flow simulation therefore would be very beneficial to the industry in the context of design optimization. A brief overview of the literature on void characterization is presented here.

#### 2.3.8.1 Correlation between voids and properties

As already mentioned in Section 2.1.2, the presence of voids is highly detrimental to the resin-dominated properties of a composite material. These include shear and compression. A 2 to 10 %

decrease in properties for each 1% increase in  $v_0$  has been reported for all typical composite materials [Judd]. Experimental results for carbon and epoxy have shown that each 1% of increase in  $v_0$  results in a decrease of 7 to 8 % in inter-laminar shear strength (ILSS) [244,245], 10% in flexural strength, as well as lower impact strength, fatigue life, and surface quality [244].

Nevertheless, a critical value for  $v_0$  has been shown, where further decreases result in no further significant increase in properties. This critical value of  $v_0$  was shown early-on to be 3 to 4 % [246], but more recently to be 1% for carbon prepreg [247]. The correlation between  $v_0$  and mechanical properties relies on precise and accurate measurement of  $v_0$ . Perhaps as  $v_0$  measurement methods improve, further increases in properties even below 1%  $v_0$  will be reported. Measurement methods for  $v_0$  will be discussed in Section 2.4.2.

#### 2.3.8.2 Causes of voids

Voids in the final cured part have been attributed to entrapped air in the resin during mixing, leaks in the bag and connections, shrinkage of the resin, generation of volatile curing byproducts, and both inter-tow and intra-tow entrapped air.

High temperature curing epoxies give higher properties (such as glass transition temperature and modulus), but more volatilization. Volatile generation can be decreased thus with a resin that gels at low  $T$ , but at a sacrifice to the properties [11,248].

Entrapped air in the tows is due to the lower permeability in the tightly packed tow compared to the inter-tow gaps, making it difficult to remove small bubbles [249,250]. This is referred to as mechanical entrapment of voids – when some physical obstruction keeps the bubbles from being washed out of the system with resin bleeding. Not only tows, but the stitches in NCF materials show mechanical entrapment of voids [244].

This is combated in RI methods other than VAP by the practice of continually “bleeding” resin through the part after the flow front reaches the vent [67,251]. With time and continual flow, intra-tow voids follow the pressure gradient into the inter-tow gaps and are washed from the part. Partial but insufficient resin bleeding leaves most of the voids by the vent [252]. Bleeding can be expensive for large parts, and has at times shown little improvement in  $v_0$  [239].



Low viscosity [244] and vacuum assist [253,254,255,256] have been proven to assist in removing these trapped bubbles. But no amount of vacuum removes all of the bubbles entrapped in the typical tow structure [226,244,255].

Low vacuum may help with the out-washing of voids, but it also prevents the voids from being dissolved into the resin. Henry's Law states that a liquid's gas concentration at equilibrium increases linearly with respect to the pressure, and that the gas concentration at absolute vacuum is zero. This implies that any gas dissolved in the resin at ambient pressure will "outgas" into bubbles as the resin pressure  $P_R$  is decreased.

In RTM, Henry's Law is taken advantage of by the use of high pressure [247]. But for the inherent low pressures in VARI, this means that very little gas will remain dissolved in the resin if kept at full vacuum. The local resin pressure continues to increase as the flow front moves farther away from it. Thus, voids are naturally more common by the flow front [252] or towards the vent, and towards the tool surface (as opposed to the DM) because of the lower pressure there [244,257,258,259].

Resin "degassing" before infusion is a standard industrial practice for void minimization. Many air bubbles are deposited in the resin system upon mixing for cure initiation or other handling steps. The pot of resin is placed under the highest vacuum possible to outgas as many bubbles as possible and release them to the atmosphere via resin boiling. This greatly reduces the outgassing during subsequent vacuum application for infusion [260], especially when the pressure is set at slightly higher of a level as used during the degassing. This also increases the capacity of the resin to dissolve more bubbles at a given pressure, which are formed during flow [79].

A similar procedure regarding Henry's Law is also standard practice in the industry. Infusion happens at full vacuum until the part is filled; then both inlet and vent are equalized at half vacuum strength. This not only reduces the thickness gradient, but also dissolves many of the remaining voids back into the resin. But this decreases the average part  $v_F$  and adds cycle time.

### 2.3.8.3 Flow optimization for void minimization

Mechanical entrapment of intra-tow voids can be combated by increasing the fluid's ability for capillary scale movement. A higher capillary number  $Ca$ , either due to low contact angle or less

surface tension, aids in void out-washing. This decreases  $v_0$  [40,261,262,263] up to some critical value of  $Ca$  where no further minimization is seen [264].

$Ca$  is also increased by the flow velocity. Other researchers have shown that only large inter-tow “macrovoids” were minimized by increasing the flow velocity. But intra-tow “microvoids” actually increase in concentration with higher flow. There is a critical value of  $Ca$  where both are minimized [258,265,266]. This correlation between low  $Ca$  and lower intra-tow microvoids is at disagreement with the research in the previous paragraph.

This difference in size and location of voids is explained by the influence of dual scale flow. The resin flows faster in the inter-tow gaps at high pressures, but flows faster inside the tows due to capillary draw at low pressures. Bubbles are entrapped in the tows with the former, as they are not completely impregnated when the resin outruns them. Bubbles remain in the inter-tow gaps, however with the latter (low pressure). Capillary forces draw the resin into the fiber bundles and form voids between them [241,244,258].

Sample SEM micrographs in Figure 2.25 from another researcher at the author’s institution illustrate the difference between large inter-tow and small intra-tow voids [267]. In another study, the ratio of axial permeability to transverse permeability was shown to determine the size of the voids [268].

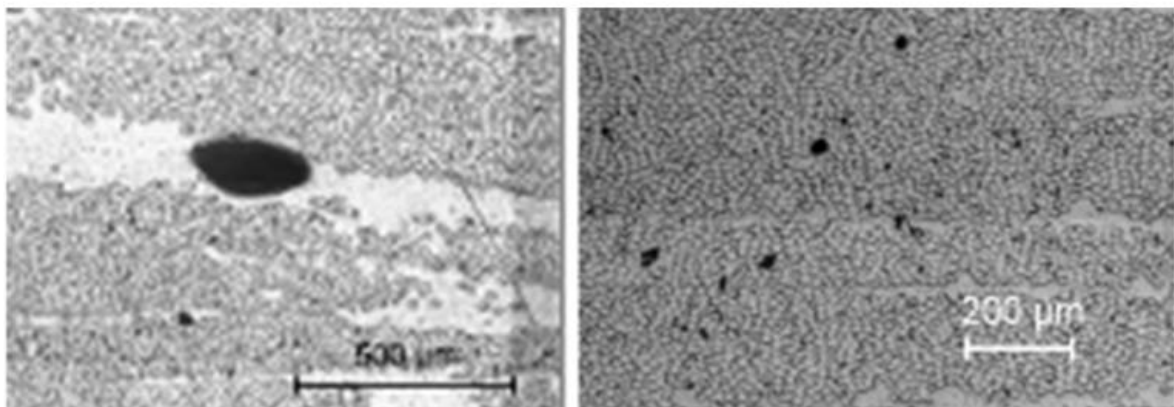


Figure 2.25: Comparison of large inter-tow (left) and small intra-tow (right) voids [267].

A host of void prediction models have been presented based on such correlations with processing parameters [262,265,266,268,269]. The PAM-RTM simulation program has implemented code to design an optimized infusion by varying the flowrate to keep  $Ca$  at its optimum value to minimize voids.

## 2.4 Final part characterization

As mentioned in the Introduction, the application of composite materials suffers from a lack of characterization data when compared to traditional materials like aluminum and steel. Part of this problem lies in the recent beginnings of composite materials. Aluminum and steel have been around for many more years, affording extensive properties databases. In contrast, carbon-epoxy composite materials have only been around for the last 30 years or so. But the tools to characterize these materials are still being developed as well. Improving characterization tools is assumed to be more worth the effort than characterization work by itself at the present moment.

The two most common metrics used to characterize a composite material are the fiber volume content ( $v_F$ ) and void content ( $v_0$ ). A review of both measurement methods for both is given here.

### 2.4.1 Fiber volume content measurement

Various methods for measuring  $v_F$  have been classified by standards organizations and/or used in the literature. They are:

#### *Mass measurement (ISO 14127-Method A)*

The mass of the preform is measured before infusion, and then after infusion as well. With component densities, the  $v_F$  of the carbon can be determined. But this is difficult when there are other solids in the component besides carbon and resin. The mass of stitching, binder, glass backing, etc., must also be known. These component masses are difficult to determine with accuracy. Also, the final part usually has non-uniform  $v_F$  along the edges due to compression. These parts are usually trimmed off to have a uniform part. This invalidates any measurement of the original preform mass.

#### *Thickness measurement (ISO 14127-Method B)*

The thickness is measured by any method with high accuracy. When the carbon fiber density and carbon areal weight are known, the  $v_F$  can be calculated from the thickness. This method only applies to materials that have experimentally demonstrated a uniform areal weight. The preform mass and dimensions should be measured before infusion, as with the last method, to ensure an accurate areal weight value.

#### *Solvent digestion (ASTM D 3171-99, DIN EN 2564)*

The epoxy is dissolved in concentrated sulfuric/nitric acid and hydrogen peroxide. A comparison of the weight of the sample before digestion, and after, gives the mass of fiber in that sample. Much care is required to keep all of the fibers together in the same place. And the PES (polyethersulfone) material in typical stitching threads has partial resistivity to these solvents. White streaks show up in the black carbon afterwards due to this, and add some non-carbon mass to the measurements.

#### *Combustion (ASTM D 2734-70, ASTM D2584)*

The resin is burned off of the fibers. Again, the  $v_F$  is determined from before-and-after mass measurements and the component densities. This has worked well for glass fibers, but is usually avoided with carbon fibers due to loss of some ash residue from the fibers.

#### *Microtoming: optical image analysis (no standards)*

Polished cross-sections of the sample are examined with light microscopy or scanning electron microscopy (SEM). Carbon fibers are ideally suited for light microscopy due to their opaqueness and light reflectivity when polished [270]. Epoxy resin is transparent and transmits incident light.

An image of the sample at 50x-1000x magnification is produced showing the ends of the fibers, oriented normal to the view. For the small area in this magnified picture, the fiber, resin, and void content are determined. This is considered a sampling of the component volume percentages for the entire part.

Two types of optical analysis methods are used to analyze binary digital images:

- Areal method: an image analysis program counts the number of black pixels compared to white pixels, thus determining the volume percent of each constituent. This relies on a gray-scale threshold to differentiate the various shades into fiber resin. Manual setting of this threshold hinders accuracy due to operator subjectivity. However, many algorithms are available to automate thresholding.
- Fiber counting method: each fiber is counted, usually with an image analysis program rather than manually. The radius of carbon fibers is tightly controlled by their manufacture. A  $v_F$  value is calculated by multiplying the cross-section area of a single fiber by the fiber count, and then dividing by the total area of the image.

Optical image analysis can examine spatial non-uniformities in the material, unlike all the previous methods. It also can characterize more about the fibers than their concentration, such as their position in relation to each other, degree of clustering, and size/shape of the fibers [271]. This is advantageous for textile modeling such as building meso-scale fabric models for theoretical predictions of behavior in programs like Wisetex (Section 2.3.3.1).

But both areal and fiber count methods are time consuming, and do not accurately represent the bulk material unless many measurements are made. Automated scanning methods are available to speed up the process, but difficult to setup for either accurate thresholding (areal method) or fiber delineation (fiber count method) across every image. A problem with the fiber count method is the image analysis software's interpretation of fibers completely in the image and fibers only partially in the image, due to location along an image-edge. The accuracy of the fiber counting method increases as the image magnification decreases. The fibers on the edges represent less of the total number of fibers in the image [160]. This also depends on an accurate measure of the average fiber cross-sectional area. In contrast, the areal method is more of a stand-alone measurement method, but requires very high quality images obtained at higher magnification to obtain accurate results [160]. Optical techniques are not yet covered by any standards organization, underlying the lack of precision or repeatability with such measurements.

One last method in the literature is nuclear bombardment with neutrons [272], but this requires much more dedicated capital investment than the other methods.

Hence, no technique is particularly applicable for all types of composites or characterization needs. Experimental error can still be further minimized for any of these methods. A recent round-robin study over 5 laboratories with simple glass weaves showed  $v_F$  measurement variances of 1.5 to 6.1 % [273].

#### 2.4.2 Void content measurement

##### *Density comparison (ASTM D2734)*

The density of the sample is measured before burning, digestion, or casting the sample in epoxy for  $v_F$  measurement. The density measurement method most used is liquid displacement [247]: ASTM D 792-66 (Specific gravity and Density of Plastics by Displacement). A sample is weighed in air and then in a liquid (usually water). The experimental density of the material is then

determined by the difference of the weights. A “no-void” theoretical density can also be calculated from the results of  $v_F$  testing by the rule of mixtures with each component. The difference between the measured and theoretical densities represents the amount of voids,  $v_0$ .

This method is prone to measurement error; it lumps the usual error in the preceding  $v_F$  measurement with the error of density testing of the composite. Carbon-epoxy composite materials show some water absorption, and their surfaces have an affinity for air bubbles which increase the buoyancy of the sample.

In comparison to other methods where voids are directly measured, this method gives an easily obtained bulk measurement of the void content without the need for many tests of the same sample. But as with the non-optical  $v_F$  measurements, it prevents one from characterizing any through-thickness gradients in the constitution of the sample. Optical image analysis is the best method when this is required. But for most applications requiring  $v_F$  and  $v_0$  data, the bulk average of the sample is more applicable and easier to obtain.

#### *Microtoming: optical image analysis (no standards)*

Over the last decade, the areal method in optical image analysis has been the most popular of  $v_0$  measurements [160,224,252,274,275]. A sampling of images representing the part is examined for the darkest areas signifying voids. As with areal  $v_F$  measurements, a gray-scale threshold must properly delineate the void areas. A study comparing  $v_0$  measurements by the density-comparison method and the optical image analysis showed the optical method to have greater accuracy as it is a direct measurement of the actual void [276].

#### *C-scan ultrasound*

Ultrasonic inspection is the most non-destructive used technique to detect defects [241, 245,247,274]. It is often used in tandem with the density comparison test for validation purposes. This is because ultrasonic scans cannot detect voids that have diameters of less than 1  $\mu\text{m}$ . For imaging of smaller voids, optical image analysis must be used [277].

Two other methods in the literature for  $v_0$  measurements are ultraviolet light [261] and high voltage insulation measurements [256].

Absolute void content is quite difficult to measure regardless of the technique used [276], as evidenced by the frequent quotation of negative void contents [278]. High variation exists in void measurement with each of these methods [160]. A portion of the variation is assumed to lie in the difficulty of accurately measuring void content for a composite material in bulk. A concentration of voids may be predicted to be either inter- or intra-tow based on processing parameters. But within either case, the location of voids is randomized, and much more random than the fiber structure. Void content has been reported to also vary in the through-thickness direction based on processing parameters [275]. For measurement methods based on small areas of the part, such as microtoming, this implies that results must be averaged over many measurements [279].

### 3 Materials

RI manufacturing usually involves laying 2D fabric layers into the mold before infusion. This is often preceded by extensive fabric preparation: cutting, stacking, and alignment to the mold geometry. RI has greatly benefited from advances in textile preforming. “Preforms” are often used to minimize production time. A preform is a stack of 2D fabric layers held together and shaped by some type of 3D element. Large and complex part-shapes can be assembled and held in place until resin injection and curing. Preforms provide other benefits: easy handling and placement, as well as control of fiber alignment, part thickness, and the fiber volume fraction. Rapid fiber placement and net shape preforming are essential needs of the aerospace industry as mentioned in the introduction, and have driven the innovation of the following modern high-performance textiles.

Most modern preforming techniques belong to one or more of three main categories: stitching, tackifying, or braiding. Each of these techniques is represented in this study in order to present an overview of permeability for the modern carbon fiber preforming industry. Thus far, the composite reinforcements characterized for flow modeling do not well represent the breadth of high-performance carbon fabrics available today.

Previous permeability studies of stitched materials have focused on glass fibers [280,281,282]. Tackifier permeability studies have examined only glass weaves [283,284], glass UD [280] and simple carbon weaves [285,286]. Braiding studies have all mentioned only glass [287,288,289].

Compressibility data is available for a slightly broader range of fabrics. Glass mats and weaves [43,91,126,179], glass NCF [70,180,282], carbon weaves [195,290], and recently Carbon NCF [193,204,291] have all been characterized.

Table 3.1 lists all the materials used in experimentation in this study.

#### 3.1 NCF

The combination of uni-directional placement of fibers in plies with consolidation of the preform by stitching (Figure 3.1) leads to an advantageous combination of properties, allowing an RI process resulting in full fiber modulus and strength in the part. Stitching has also shown the



potential to reduce the preform count for complex parts when compared to exclusively binder-preforming technologies [292].

Table 3.1 - Tested materials.

<i>Code</i>	<i>Type</i>
Baseline	Saertex S32CX00K stitched NCF, carbon HTS40 12K
NCF-6K	Saertex S32CX00K stitched NCF, carbon HTA5131 6K
NCF-Tri	Saertex S32CY35K triax stitched NCF, carbon HTS40 12K
T1(12)/T1(16)	TFP – $[0]_n$ , 12 or 16 plies, carbon 12K
T2(12)/T2(16)	TFP – $[(0/90)_n]_s$ , 12 or 16 plies, carbon 12K
T3(12)/T3(16)	TFP – $[0/0/0/90/0/0]_s$ or $[0/0/90/0/0]_3/0$ , carbon 12K
Bind.5%	Baseline NCF, 0.5% binder
Bind1%	Baseline NCF, 1% binder
Bind2%	Baseline NCF, 2% binder
Bind3%	Baseline NCF, 3% binder
Bind4%	Baseline NCF, 4% binder
Braid-B	Biax Braid, 6 ply, +/- 45°, carbon 12K
Braid-T	Triax Braid, 4 ply, +/- 45°, carbon 12K
Braid-S	Triax Braid, 4 ply, +/- 60°, carbon 12K, 24K standing fibers

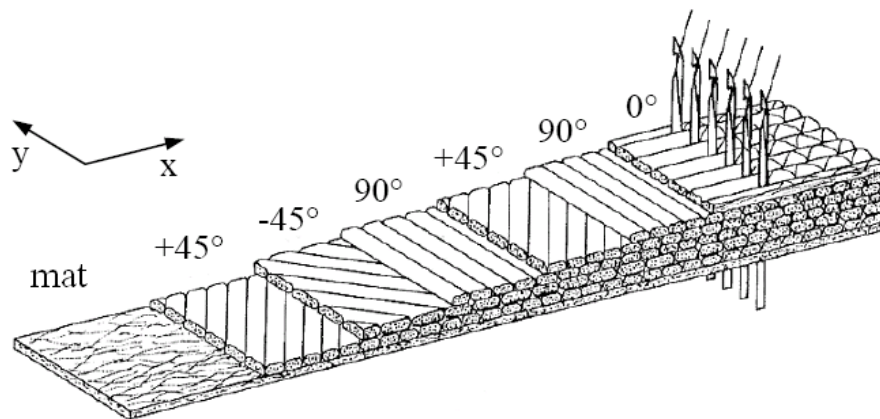


Figure 3.1 - Stitched non-crimp fabric from orientation of UD layers [293].

As a baseline material for the study a carbon non-crimp fabric (NCF) was chosen with an areal weight of  $540 \text{ g/m}^2$ , including 1.1% (by mass) of stitching (chain-stitched) (PES 74 dtex). The tows in this material are Toho Tenax E HTS40 12K. This material is presented as a standard for modern

high-performance textiles in the composites industry. Two other Saertex NCF's were studied: a similar fabric with HTA 6K tows to investigate the effects of sizing and tow fiber-count, as well as a Triax NCF to investigate the effects of fiber direction.

### 3.2 TFP

Tailored fiber placement (TFP) is a novel stitching-performing process that allows high design flexibility. It consists of laying individual tows wherever local reinforcement is desired, and holding them in place by stitching along the tow. The tow laying/stitch process has been automated with the use of industrial embroidery machines [294]. This process is capable of producing multi-axial reinforcements of many plies in thickness, with no wasted carbon fiber. With complex load geometries, TFP customization of tow orientation can be greatly beneficial, as demonstrated in Figure 3.2 for a loop connection.

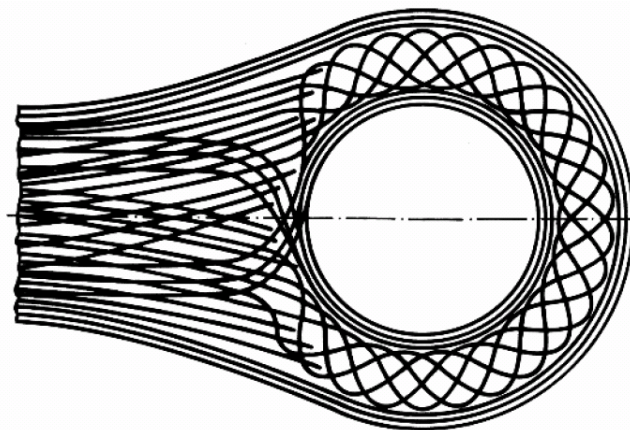


Figure 3.2 - TFP orientation of a loop connection [293].

A Tajima TLMX embroidery machine was employed to make several geometrical configurations of both 12-ply and 16-ply TFP samples. The configurations were (1) 0° UD, (2) 0/90 every other layer, and (3) 0/90 with only two or three 90° plies and the rest 0°'s. The fiber tows used in all samples are the same Tenax 12K tows as in the baseline NCF. A bottom layer of fiberglass cloth (106 g/m<sup>2</sup>) was used as a base for the stitches. The tows were spaced every 4mm and fixed with a zigzag-stitch (lock-stitch) using PES (Serafil 200/2) thread.

### 3.3 Binders

Tackifying consists of binding fabric together with polymeric materials, referred to as tackifiers (or binders). These are resins that are solid at room temperature but can melt easily upon heating [295]. During cooling, the tackifier resolidifies to hold the fabrics in shape.

The binder can be applied to the fabric either by dissolving the binder into a solvent and then spraying it on the fabric, distributing a powder binder on the fabric, or laying a veil between plies [295]. While the spray method provides the most uniform coverage, it also introduces health issues and the need for solvent removal and recovery. Powders are easily available but require the most care to distribute uniformly. Veil materials provide a good compromise between the two. A polyamide adhesive veil, Spunfab PA1541, with an activation temperature of 104-116°C, was used in this study.

While typical binder amounts have been reported as 4 to 7 % by mass of the reinforcement [285,295], in-house experience with this particular binder has shown that anything higher than 4% makes the preform “boardy.” Beyond this, as reported in [295] for overly-high binder amounts, the stiff fabric requires a high resin injection pressure because of less pore volume available in the preform. Thus, samples were prepared with 1, 2, 3, and 4% binder by mass. Plies of the binder veil were equally distributed between the plies of the same carbon NCF used as the baseline.

Controlled application can be done with the use of infrared lamps or ovens, but a simple iron was used here as in [286]. A Teflon® coated fiberglass release separator film was employed in the ironing process. To aid in consolidation and uniform distribution of the binder, the preforms were then vacuumed to 30 kPa and heated to 110°C for 90 minutes.

### 3.4 Braids

Two-dimensional braiding machines offer the ability to make both self-standing, thin, hollow preforms as well as reinforcement over-braided on any shape. This process has proven to be a cost effective method of producing preforms with a low waste rate. The integrated fabric architecture of braided structures also implements excellent crash behavior. The simplest braiding configuration produces biax tows at a process-determined angle with the feed direction. UD tows

("standing") can be fed through the biax tows to make a triax braid. Multiple layers can be braided on top of each other to increase the reinforcement thickness.

For this study a 2D braider (Herzog) with 176 carriers and 88 standing yarns (Figure 3.3) was employed to make biax and triax braids at a +/- 45° angle, with the same carbon tows as in the baseline NCF material. Some triax samples were also prepared with 24K tows as the standing fibers, and +/- 60° braid angle of the 12K braided tows. The braids were cut open lengthwise to get a flat material for testing.



Figure 3.3 - Herzog 2D braider.

### 3.5 Fiber volume content calculation

The  $v_F$  is a commonly used metric to describe composite materials (Section 2.1.1). A clarification of  $v_F$  is necessary with these high-performance modern carbon textiles: whether the  $v_F$  is a measure of total volume of fiber, or just carbon. For braids, this is no difference. But for the others, non-carbon solids are present:

- Stitching in NCF
- Stitching and binder in NCF
- Stitching and glass base layer in TFP

Similar to resins, it is assumed that each of these non-carbon solids have insignificant mechanical properties when compared to the carbon. Therefore, as the aim of this study is to correlate design parameters to final mechanical properties, all fiber volumes will be measured as the volume percentage of only carbon. As the permeability has probably been reported with fiber volumes both with non-carbon solids and without, the in-plane permeability  $K_{XY}$  will be calculated with both to quantify the difference.

The porosity  $\phi$  of a fabric is the inverse of the  $v_F$ , which would include all non-carbon materials with the empty space by this approach. It is recognized that flow through empty space is different from flow within binder, polyester stitching, or glass fabric. But it has been proven that each of these materials has permeability at least an order of magnitude higher than the carbon fibers in this study. Thus, their inclusion with the empty space in porosity is assumed to be more appropriate to these materials than otherwise.

The  $v_F$  is related to the preform thickness by Equation 2.19, which can be modified to include the mass of the fibers  $M_F$ :

$$v_F = \frac{M_F}{A \cdot \rho_F \cdot h} \quad (3.1)$$

where  $A$  is the in-plane surface area of the stack. Incorporating non-carbon solids into this calculation means the mass is the total weight of the dry preform,  $M_D$ , and  $\rho_F$  must be adjusted for non-carbon densities by the rule of mixtures. To only include carbon in the calculation, the total dry mass ( $M_D$ ) must be lowered by the ratio of areal weights (only-carbon,  $A_F$  / all-solids,  $A_D$ ), and  $\rho_F$  is now the density of pure carbon fiber:

$$v_F = \frac{M_D}{A \cdot \rho_F \cdot h} \left( \frac{A_F}{A_D} \right) \quad (3.2)$$

The areal weight is the mass of dry material divided by its surface area. With the exception of the 6K NCF, all other materials in this study consist exclusively of Toho Tenax –E HTS40 F13 12K 800 tex carbon tows, with a fiber density of  $1760 \text{ kg/m}^3$ . This density is published by Hexcel, and was verified by the author's own density tests. The 6K NCF consists of Toho Tenax –E HTA40 E13 6K 400tex carbon tows. The two yarn types differ by fiber count and sizing:

- HTS40 = 12,000 fibers/tow, 1.0% PUR sizing

- HTA40 = 6,000 fibers/tow, 1.3% epoxy sizing

Despite the differences, the HTA40 tows also have a fiber density of 1760 kg/m<sup>3</sup>. So this fiber density is applied throughout this work. The average areal weight, AF for all these materials is listed in Table 3.2.

Table 3.2 - Areal weight of tested materials.

<i>Material</i>	<i>A<sub>F</sub> (kg/m<sup>2</sup>)</i>
Baseline; NCF-6K; Bind1%; Bind2%; Bind3%; Bind4%	0.534
NCF-Tri	0.817
Braid-B	0.536
Braid-T	0.735
Braid-S	0.777
T1(12); T2(12); T3(12)	2.400
T1(16); T2(16); T3(16)	3.200

## 4 Modeling experimentation

### 4.1 VARI benchmark infusions

[Note: the experimentation described in this section was performed in tandem with Holger Ahlborn and Mohab ElGhareeb. As they worked on this in pursuit of degrees, these results are presented in their individual theses as well [15,296].]

The success of flow simulation is measured by its agreement with experiments. Thus, experimental infusions were performed for a selection of the materials listed in Section 3. The flow front progression over time was recorded, to serve as the benchmark for comparison with simulation efforts. A brief description of the infusions is given in this section. Efforts to simulate these infusions will be presented in a later section, after modeling of each of flow phenomena has been accomplished.

For the benchmark infusions, VARI processing was chosen for the excellent visibility associated with the vacuum bag. The flow was forced in an approximate 1D direction through the fabric by placing an omega inlet tube directly on top of the fibers at the short end of a 150 x 200 mm<sup>2</sup> fabric stack (Figure 4.1). The tube is filled quickly by the resin, and then seeps down almost uniformly into the fibers. DM (distribution media) was not used to accelerate in-plane flow so that the differences in the fabrics could be ascertained. DM was used, however, to attach the vacuum vent tube to the last 20 mm along the length and at the bottom of the fabric stack. Once the resin flow front reaches 180 mm in length along the bottom of the part, it reaches this DM and the experiment is concluded.

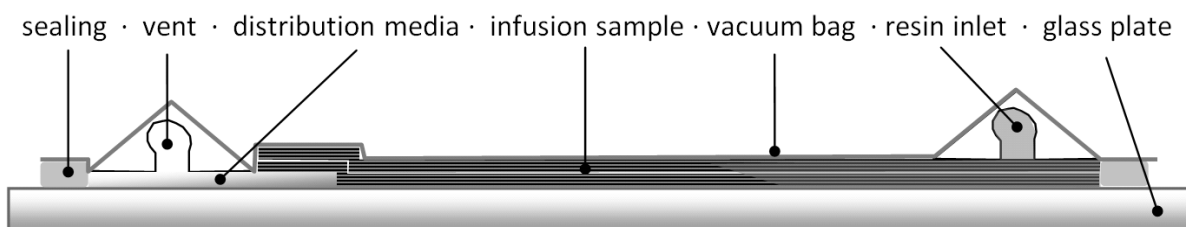


Figure 4.1 - Lay-up sequence for VARI benchmark test infusions.

To monitor through-thickness differences in flow, the infusions were conducted on a thick glass plate. The glass was held between two rotatable mirrors as shown in Figure 4.2. The mirrors were turned at the appropriate angle to allow a camera to see both the top and bottom of the fabric. A timer and ruler were placed on the top of the glass to enable time and flow front length measurements for each image captured by the camera.

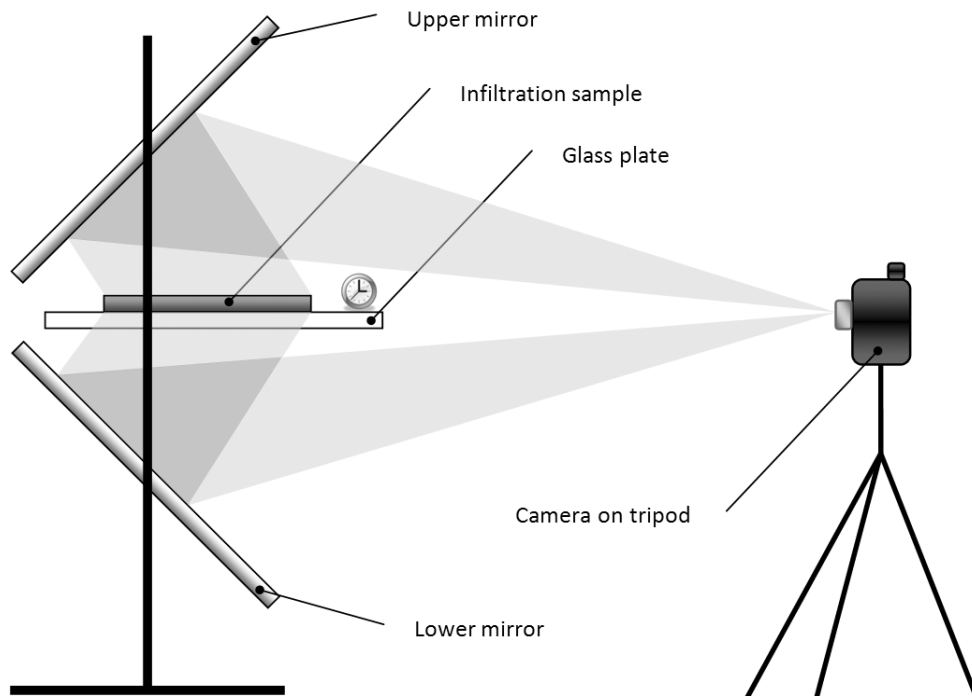


Figure 4.2 - Experimental Setup for In-plane flow front monitoring.

As mentioned in Section 2.1.2, Hexion Epikure RIM 235 was the curing epoxy system used in all curing infusions in this study. For the first VARI infusion tests, the hardener RIM235H was used. This was found to cure a little too quickly for complete infusion of a 200 mm length of the baseline NCF, so the balance of infusions were performed with a mix of 1/3 RIM235H and 2/3 RIM236H. The mix of 235H and 236H takes around 24 hours to fully cure at room temperature. The mix was formulated to cure as quickly as possible, yet still be able to fully infuse a 200 mm long part of the above-mentioned reinforcement without the use of DM before gelling.

After mixing the resin and hardener, the epoxy was degassed for 5 minutes at 500 to 1000 Pa. The vacuum pressure in the mold was set slightly higher, 3kPa, to minimize voids. After infusion began, digital photos were captured every couple of seconds initially, and every few minutes towards the end of the infusion. An example image is shown in Figure 4.3, where the flow fronts for four samples, both top and bottom, are clearly seen. The experiment was concluded the moment the



flow front reached the DM bottom or when there was no more significant flow. Afterwards, both the resin pot at the inlet, and the vacuum vent were connected and set to a pressure of 30 kPa to reduce the thickness gradient and achieve a regular  $v_F$ . The samples remained at this pressure for 24 hours of curing before demolding.

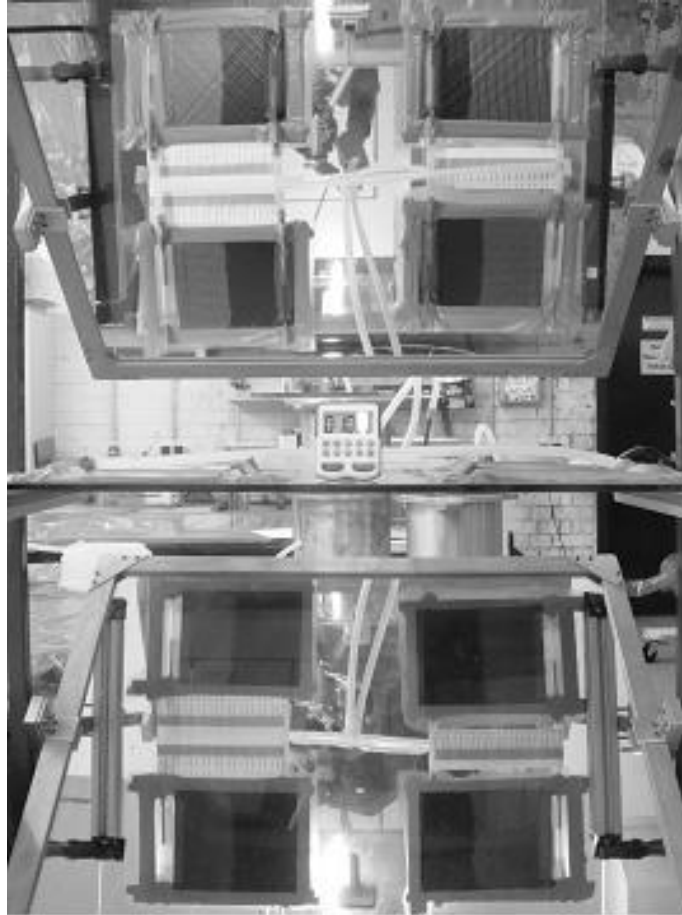


Figure 4.3 - Example captured Image of VARI flow fronts.

Samples were cut and laid in a variety of ply numbers,  $n$ , and orientation. The orientation of forced flow was either  $0^\circ$ ,  $90^\circ$ , or  $45^\circ$  to the:

- stitching (in the case of NCF),
- mandrel direction (in the case of braids),
- top layer's tow direction (in the case of TFP).

The materials included in the benchmark VARI infusions and the lay-up and orientation of each sample is listed in Table 4.1. For each repeat, the temperature was recorded at the beginning of infusion for the purposes of later viscosity modeling. All infusions were drawn from a resin pot of approximately 400 grams.

Table 4.1 - VARI benchmark tested materials.

<i>Sample ID</i>	<i>Material</i>	<i>Layers</i> (n)	<i>Repeats</i>	<i>T (°C)</i> 1/2/3
Baseline-4 (0)	Biax 12K NCF [(+/-) <sub>2</sub> / (-/+) <sub>2</sub> ]	4	2	24/27
Baseline-4 (90)	" [(+/-) <sub>2</sub> / (-/+) <sub>2</sub> ]	4	2	24/27
Baseline-4 (+45)	" [(+/-) <sub>2</sub> / (-/+) <sub>2</sub> ]	4	2	23/23
Baseline-6 (0)	" [(+/-) <sub>3</sub> / (-/+) <sub>3</sub> ]	6	2	23/23
Baseline-8 (0)	" [(+/-) <sub>4</sub> / (-/+) <sub>4</sub> ]	8	2	23/23
NCF-Tri (0)	Triax 12K NCF [(+/-) <sub>2</sub> ]	2	1	24
NCF-Tri (90)	Triax 12K NCF [(+/-) <sub>2</sub> ]	2	1	24
NCF-6K	Biax 6K NCF [(+/-) <sub>4</sub> ]	4	2	24/24
Braid-B	Biax Braided	4	2	24/24
Braid-T	Triax Braided	3	2	24/24
T1(12)	TFP – [0] <sub>12</sub>	1	3	24/24/24
T2(12)	TFP – [(0/90) <sub>3</sub> ] <sub>5</sub>	1	1	24
Bind1%-110 (0)	Baseline+1% binder	4	2	27/27
Bind2%-110 (0)	" +2% binder	4	2	24/24
Bind1%-110 (90)	" +1% binder	4	2	23/23
Bind2%-110 (90)	" +2% binder	4	2	23/23

#### 4.1.1.1 Results

A detrimental phenomenon to flow modeling was often seen in the VARI experiments without DM in this study: that of resin pooling under the vacuum bag by the inlet. As the flow moves slowly through the low-permeability fabric, the resin pressure continues to push against the vacuum bag by the inlet. Eventually, the fabric by the inlet no longer conforms to the thickness of the cavity and the bag peels away from it. This causes race-tracking over the top and means that flow front progression monitoring is no longer a valid measure of the fabric permeability. This phenomenon was more prevalent with lower flow velocity. Through trial and error, this phenomenon was found to be effectively prevented by placing the tacky tape borders immediately against the fibers. This takes some care however; some infusions still succumbed to resin build-up as the resin velocity slowed down with flow length. Thus, flow front progression data was only recorded before this occurs.

Due to other edge effects in some cases, the flow front was not always a straight line perpendicular to the flow. The portion of the flow front that seemed least perturbed by edge effects was recorded as the flow progression.

The omega inlet piping was placed with the resin inlet line ~15 mm from the end of the fabric. The omega tube was also cut to only extend across 120 to 130 mm of the 150 mm part width. Thus, the flow from the inlet must fill the corners around this, the rear 15 mm, and flow through the thickness of the bottom of the fabric under the inlet before it can assume true 1D flow. Thus, flow front measurements for the first 5 minutes do not represent 1D flow.

Due to resin gelation, there was no more significant flow in any of the fabrics after ~100 minutes of infusion. Given a total of 15 minutes for mixing, degassing, and setup, this equates to a total of about 115 minutes (about 2 hours) of flow from the point of first contact between resin and hardener. The resin remaining in the pot seemed to be more viscous at this point than in the mold. This signifies that the reaction exotherm in the pot where surface area to volume ratios are smaller has increased the curing rate faster than in the mold.

In all NCF materials, 0° flow was significantly faster than 90° flow. This is demonstrated in Figure 4.4, where the flow front progression for both orientations is illustrated. In most tests, there was a very small lag in flow length on the bottom compared to the top. The lag was so small that it was difficult to quantify, even for the thickest materials. This lag decreased with time and both top and bottom fronts were approximately equal for flow > 50 mm from the inlet.

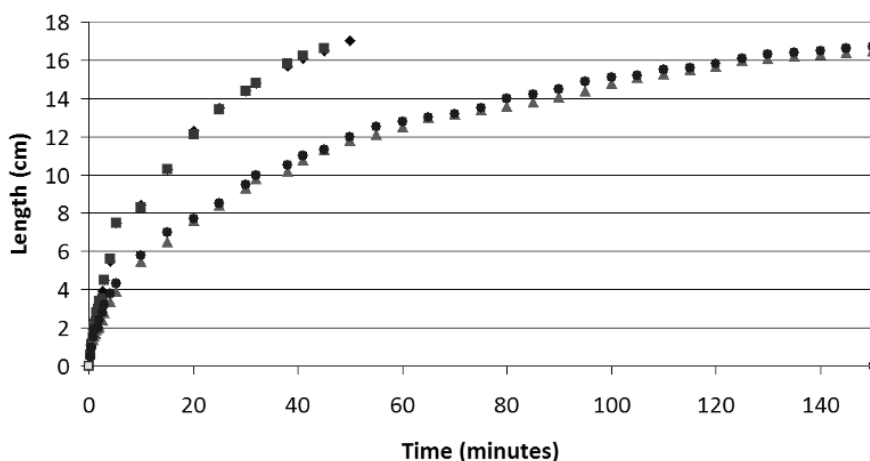


Figure 4.4 - Flow front progression for baseline NCF: 0° flow (◆: top, ■: bottom) and 90° flow (▲: top, ●: bottom).

For purposes of benchmarking for later comparison with simulation, the time to reach the milestones of 100 and 160 mm in flow length were tabulated. Top and bottom times were averaged for each test, and then averaged across repeats of each material. The results are presented in Figure 4.5 for the non-bindered materials. Standard error bars are included; no error bars denotes no repeats. 100 minutes was noted above as the time after which no significant flow was seen. Therefore the maximum time in Figure 4.5 is set at 100 minutes. The fastest infusions happened in the triax braid and the TFP materials. The slowest happened in both of the 90° oriented samples. The flow in the NCF-triax 90° sample never reached the 160 mm mark.

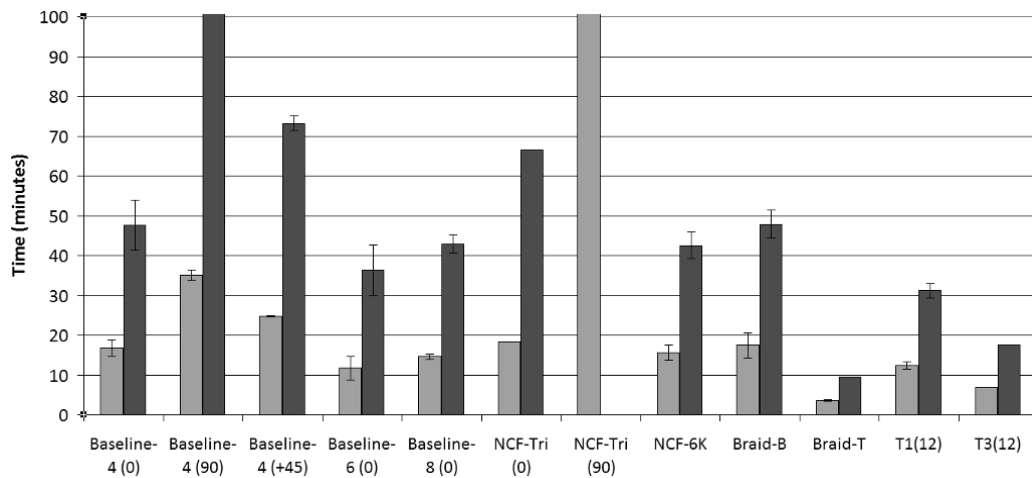


Figure 4.5 - Time to milestone lengths of 100 mm (light) and 160 mm (dark).

Figure 4.6 shows the results for bindered materials compared to the baseline non-bindered standards. The flow was generally slower in the bindered samples, thus no time maximum is placed on the graph for the sake of comparison. Not much difference was seen for the 1% 0° test.

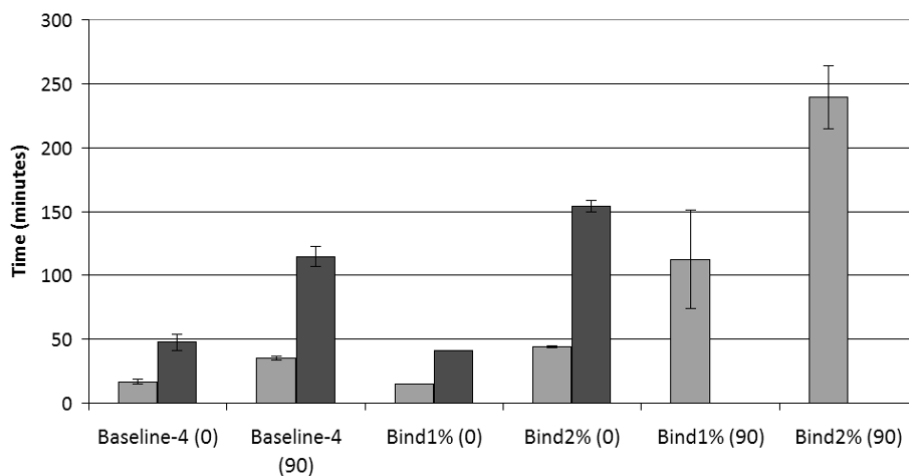


Figure 4.6 - Time to milestone lengths for bindered materials: 100 mm (light) and 160 mm (dark).

Note that the binder for all the samples in this study was applied at 110°C as described in Section 3. An increase in fiber sealing by the binder was observed in a parallel study, which decreased the flow velocities in all cases from the data presented here [15].

## 4.2 In-plane permeability characterization

The in-plane permeability was determined by the multiple cavity parallel flow technique (Section 2.3.3.2.2) for many of the fabrics listed in Section 3. The materials tested, and their orientation and ply number are listed in Table 4.2.

Table 4.2. Tested materials for in-plane permeability.

Code	Type
Baseline	Biax stitched 12K NCF, [+45/-45] <sub>6</sub> ,
NCF-6K	Biax stitched 6K NCF, [+45/-45] <sub>6</sub>
NCF-Tri	Triax stitched 12K NCF, [+45/0/-45] <sub>4</sub>
T1(12)/T1(16)	TFP – [0] <sub>n</sub> , 12 or 16 plies
T2(12)/T2(16)	TFP – [(0/90) <sub>n</sub> ] <sub>s</sub> , 12 or 16 plies
T3(12)/T3(16)	TFP – [0/0/0/90/0/0] <sub>s</sub> or [0/0/90/0/0] <sub>3</sub> /0
Bind1%	Baseline, [+45/-45] <sub>6</sub> , 1% binder
Bind2%	Baseline, [+45/-45] <sub>6</sub> , 2% binder
Bind3%	Baseline, [+45/-45] <sub>6</sub> , 3% binder
Bind4%	Baseline, [+45/-45] <sub>6</sub> , 4% binder
Braid-B	12K Biax Braid, 6 ply, +/- 45°
Braid-T	12K Triax Braid, 4 ply, +/- 45°
Braid-S	12K Triax Braid, 4 ply, +/- 60°, 24K standing fibers

### 4.2.1 Test fluid

Many binders are designed to dissolve in the matrix during infusion, which changes the rheology of the fluid [297]. The hydrophobic paraffin oil used as the test fluid should not dissolve to any significant extent the relatively polar polyamide binder at room temperature. Thus viscosity changes were assumed to only be caused by ambient temperature variation. The temperature during every experiment was measured and used to model an effective viscosity given the known

permeability of a reference capillary system (described below). This in turn allowed a theoretical calculation of the permeability given an effective viscosity and pressure difference. This theoretical value was compared with the measured value only as a quality check to ensure there were no significant deviations which would indicate a calculation error.

The viscosity data was fit to the exponential model in Equation 2.26, modified for temperature dependence (instead of time). The resulting model is shown in Figure 4.7.

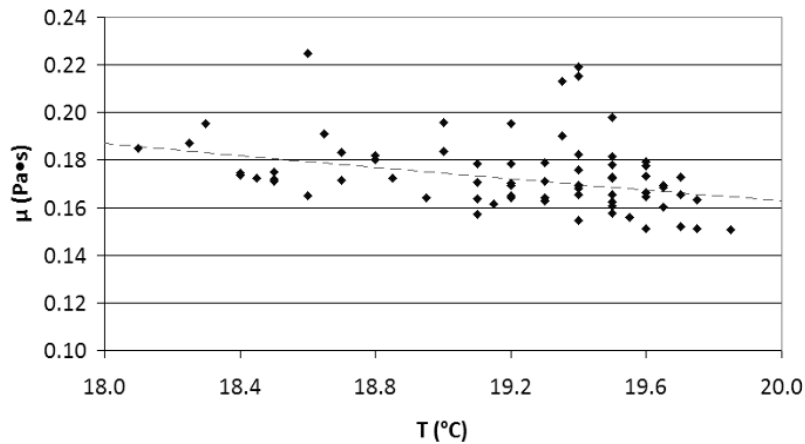


Figure 4.7 - Viscosity model for paraffin oil.

#### 4.2.2 Equipment

The test equipment used is located at the Swerea SICOMP facility in Piteå, Sweden, and is shown in Figure 4.8. An 80 mm thick acrylic mold was used as the mold top, and reinforced by 18 bolts spread along 3 steel bars. The pressure applied to the oil to drive the flow was set at 100 kPa, which has proven to be low enough to minimize mold deflection but high enough to minimize capillary effects. Silicone sealant is used to define the edges of the mold against the sample edges. Samples were cut at a size of 300 x 150 mm<sup>2</sup> from an automated cutting machine to achieve high precision and thus minimize race-tracking. The reference material used to calculate the sample material permeability data is a system of 5 capillary tubes with known permeability.  $K$  for the capillary tubes is from the Hagen-Poiseuille Equation:

$$K = \frac{r^2}{8} = \frac{(0.3\text{mm})^2}{8} = 1.125 \cdot 10^{-8} \text{m}^2 \quad (4.1)$$

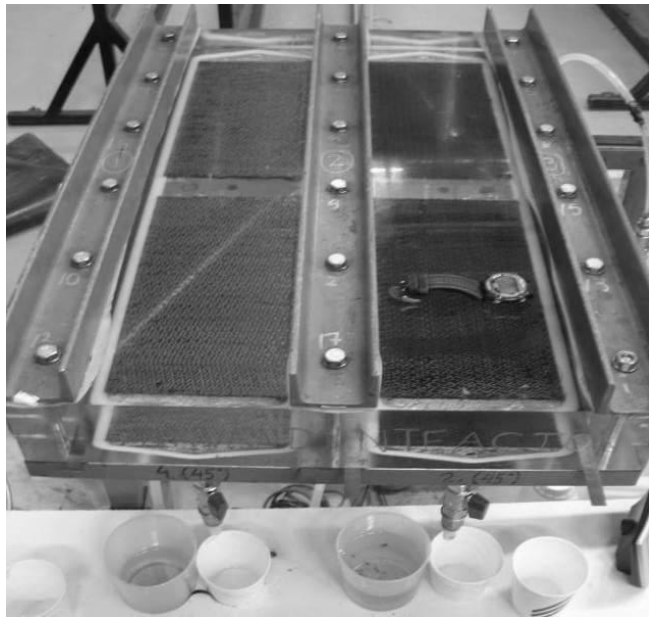


Figure 4.8 - Multi cavity parallel flow permeability measurement setup.

The experimental fiber volume fraction was controlled via sample thickness by the use of metal thickness gauges to separate the steel mold from the acrylic cover. For each sample set the unsaturated flow front was monitored to generate the wetting permeability at an initial thickness. Once all samples were saturated, the mass of extruded fluid was measured for each sample and reference over an arbitrary time period, and compared to the reference's known permeability. In this way the saturated permeability was measured. The fluid injection was then suspended and some thickness gauges removed to decrease the thickness (increasing the fiber content). The flow was then reestablished to steady state and another saturated permeability measured. This was repeated to achieve the permeability at up to four different fiber volume contents for each sample.

The chosen initial thickness was determined by the lowest fiber volume of interest for that material. The highest fiber content tested was either determined by the limit of interest, or by the onset of mold-sealant problems due to too high of compression pressure.

Effective permeabilities were calculated at each of these fiber volumes for material of each sample in the  $0^\circ$ ,  $90^\circ$  and  $45^\circ$  directions. Each material at each orientation was repeated to get from 2 to 5 values for statistical purposes.

### 4.2.3 Results

The weight of each sample was recorded with a Mettler Toledo scale to the hundredth gram. The small variations in repeat sample mass led to variation in fiber volume fraction. An adjustment using the Kozeny-Carmen equation (Equation 2.12) was made to yield the permeabilities of repeats at the same fiber volume fraction ( $v_F = 0.55$ ) to enable direct comparison between materials. Although the validity of adjusting the fiber volume to such a great degree to achieve absolute permeability data in this way is questionable, a comparison with such data can be useful. Figure 4.9 presents this comparison.

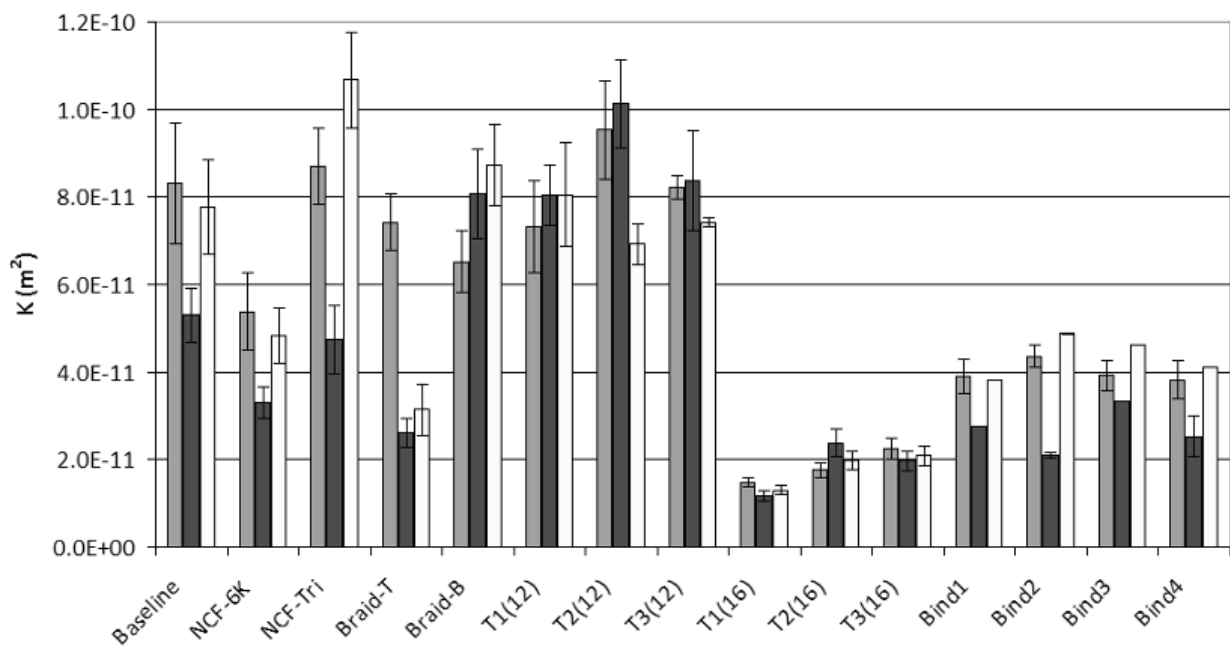


Figure 4.9 - K: all materials adjusted to  $v_F = 0.55$  (gray:  $K_0$ ; black:  $K_{90}$ ; white:  $K_{45}$ ).

Figure 4.9 represents calculations done with only-carbon based  $v_F$ 's. The same data was calculated using  $v_F$ 's based on all solids (including glass and stitching). By including all solids, the areal weight is increased, but the fiber density is decreased. The latter effect has a greater influence, as this showed to lower the  $v_F$ , and hence increase the K values at a given  $v_F$ . The increase (%) in  $K_0$  by material is shown in Figure 4.10.

With nothing but carbon, the braids obviously have no change in K. The NCF materials, with some stitching, show a 6 to 9% increase in  $K_0$ . Binded NCF, with the addition of binder veil material to the mass, show a greater increase, from 18 to 32% (from 1 to 4 % binder by mass). The TFP materials, with a layer of glass and many stitches show increases of up to 240%. These



percentages are similar for the  $K_{90}$  and  $K_{45}$  values. It is thus critical in reporting permeability values to also report the basis of  $v_F$  calculation for any preform material stabilized with non-carbon substances.

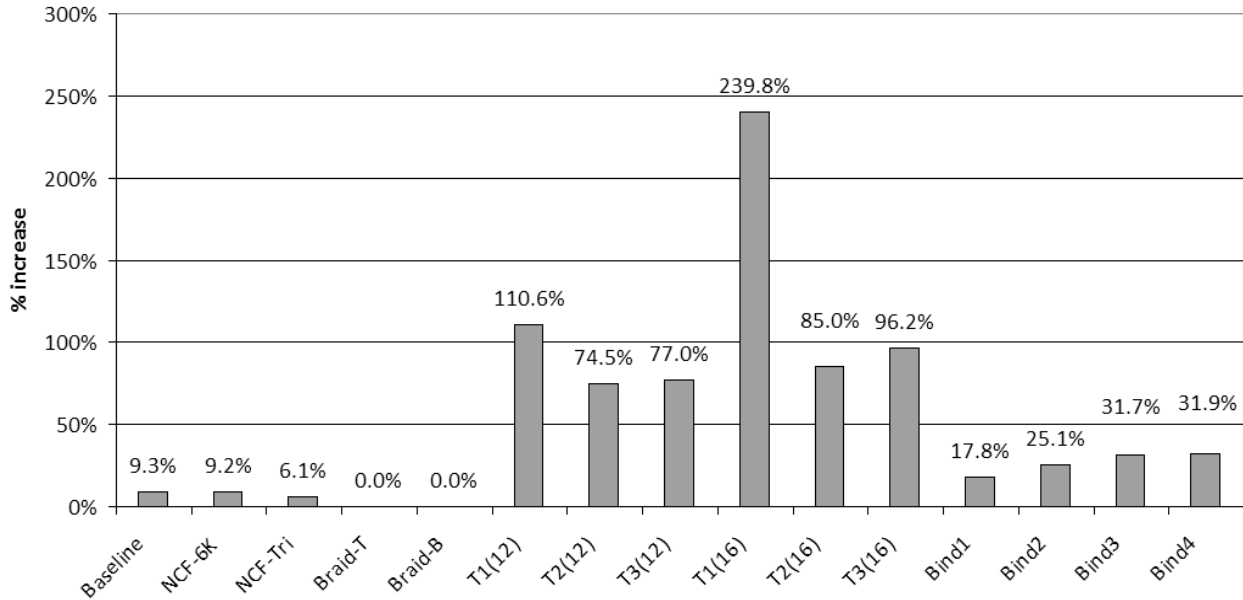


Figure 4.10 - Increase in  $K_0$  at 55%  $v_F$  by including all solids in  $v_F$  calculations.

Note that permeability results base on all-solids calculations were presented in [298,299]. With subsequent work on correlating modeling to final mechanical properties, the approach of only considering carbon was implemented since then. Only carbon will be considered in all remaining  $v_F$  calculations in this study.

Following the coordinate transformation method in Equation 2.15 the principal values and direction of the in-plane permeability tensor were determined from the resultant effective permeabilities (Figure 4.11).

#### 4.2.3.1 Darcian flow validation

The flow progressions in the unsaturated tests were all fit to Equation 2.11 to check for Darcian flow. All samples exhibited high straightness in a plot of time versus the square of the flow front progression distance. The example of the baseline NCF material is shown in Figure 4.12.

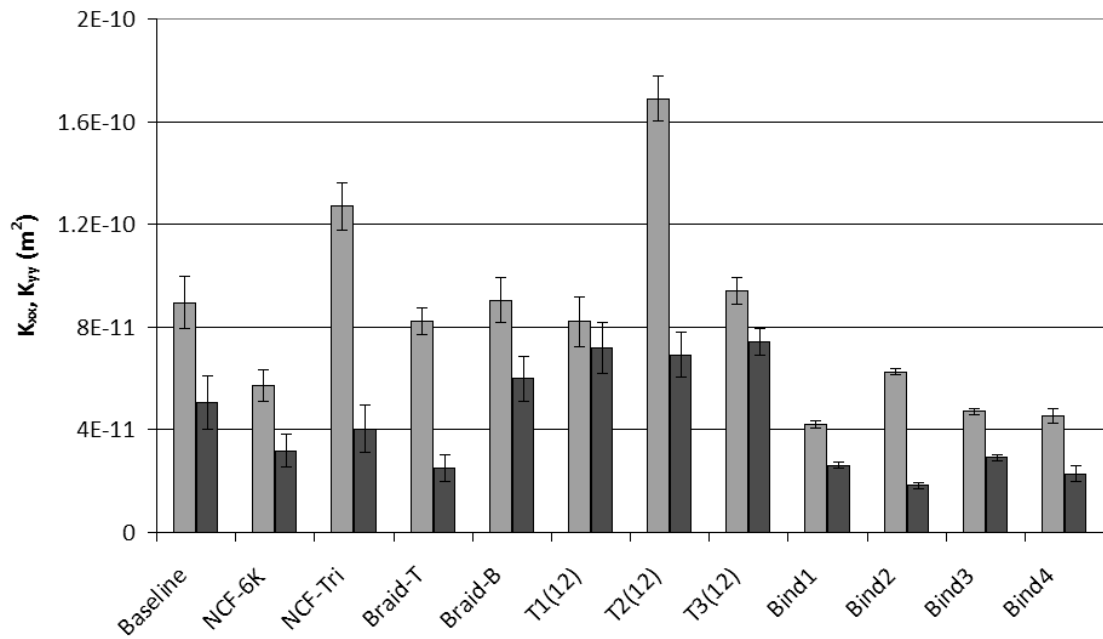


Figure 4.11 -  $K_{xx}$  (light) and  $K_{yy}$  (dark) for  $K_{xy}$  tests, adjusted to  $v_F = 0.55$ .

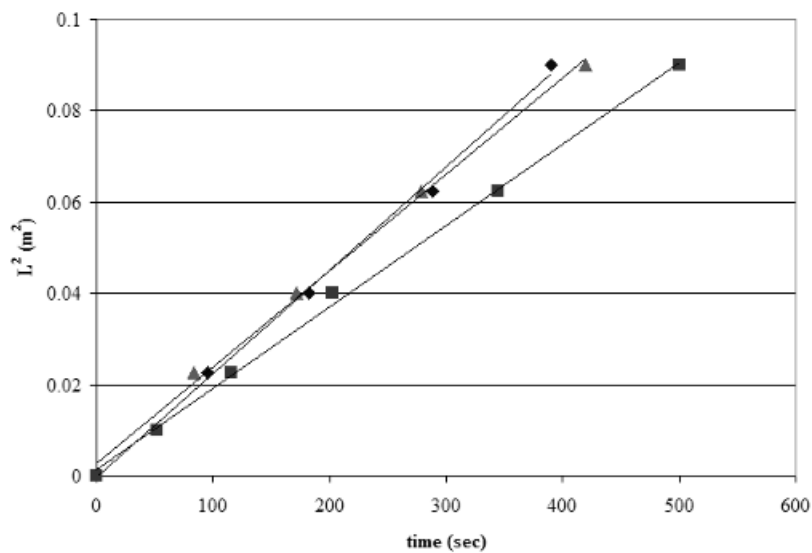


Figure 4.12 - Darcian Flow Behavior: Baseline NCF ( $\blacklozenge$ : 0,  $\blacksquare$ : 90,  $\blacktriangle$ : 45).

#### 4.2.3.2 Non-crimped fabric

The effective permeability measurements for the baseline fabric are presented in Figure 4.13. A power-law model seems to adequately model the decrease in permeability with increasing  $v_F$ . Although the  $K_{45}$  and  $K_0$  directional permeabilities seem very close to each other,  $K_{90}$  is about 30% lower. This can be explained by the stitching orientation – which runs along the 0 direction and parallel to the 90 direction. [300] showed that flow is enhanced in the direction of the stitches, and thus would increase the permeability in the 0 direction.

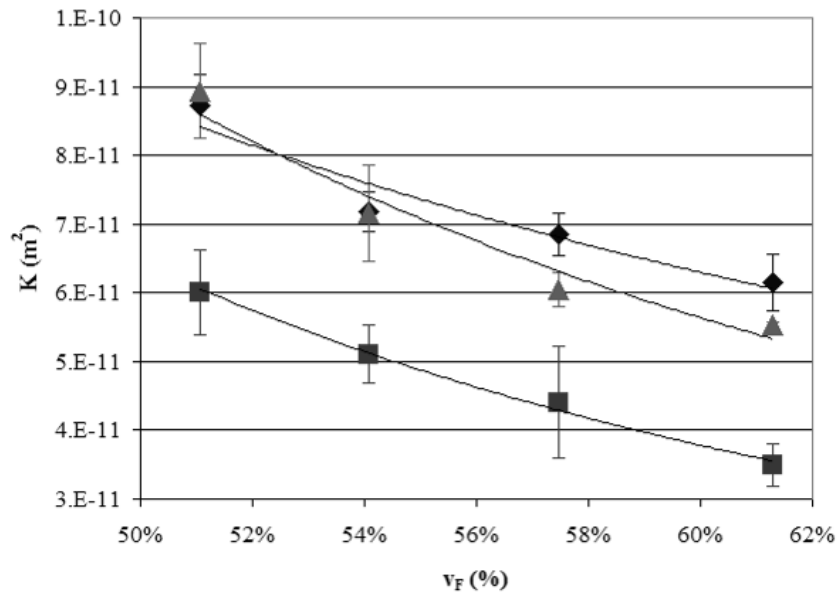


Figure 4.13 - Effective permeability: baseline NCF (◆: 0, ■: 90, ▲: 45).

When transformed to the principle permeability components (Figure 4.14), the baseline material shows an orientation between 14 and 25°. This falls in between the stitching and 0 direction. The slight off-axis orientation may be from different spacing of the tows in one of the directions from the chain-stitch eyelet double thread's larger bulk than the stitching on the other side of the ply, thus enhancing flow in one direction. A similar difference in inter-tow spacing has been reported for carbon [101] as well as glass NCF's [280]. The difference between  $K_{xx}$  and  $K_{yy}$  is once again ~30 to 40%.

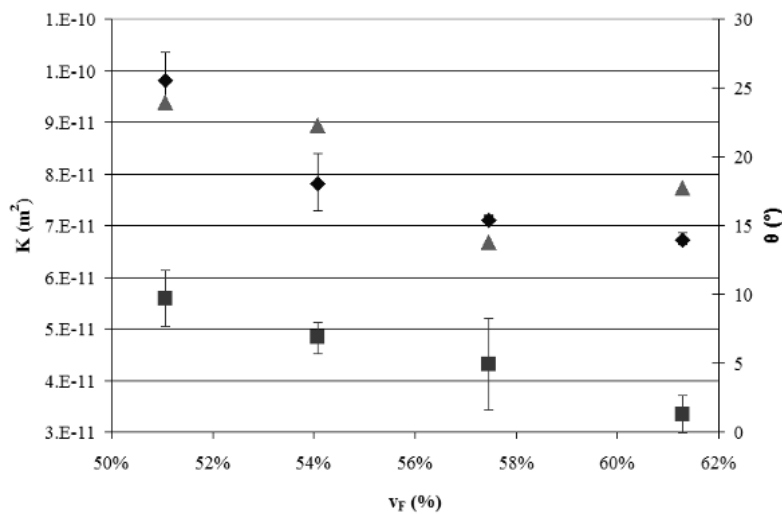


Figure 4.14 - Principle permeability components: baseline NCF (◆:  $K_{xx}$ ; ■:  $K_{yy}$ ; ▲:  $\theta$ ).

Figure 4.15 shows a comparison of  $K_0$  for the three NCF materials. The 6K fabric showed a ~30% decrease in the axial permeability from the baseline's 12K-tow fabric. Shih and Lee [286] reported a similar decrease in permeability from 12K to 6K, and attributed it to binder-like effects of consolidation.

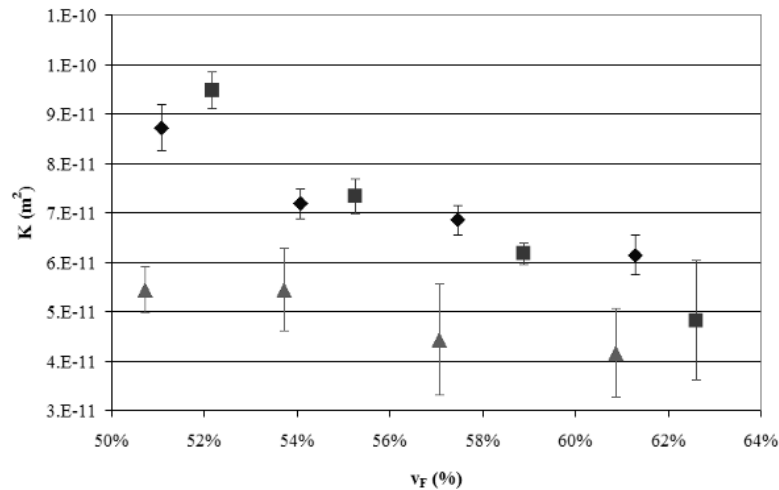


Figure 4.15 -  $K_0$  (◆:Baseline; ■: NCF-Tri; ▲: NCF-6K).

The NCF-triax material shows similar permeability to the baseline material. An increase would be supposed from the addition of axial fibers for flow enhancement. But, although the triax NCF has the same number of tow-layers (4 plies x 3 tow-layers) as the biax NCF (6 plies x 2 tow-layers), there are 4 ply-interfaces between the stitching as opposed to 6 for the biax NCF. The number of layers is higher, which may result in enhanced flow along the interfaces between plies [280], and outweighs the enhancement of the axial tow addition.

#### 4.2.3.3 TFP

The properties of a fabric made solely from TFP should be similar to a stitched NCF material of similar architecture. In this case, both the NCF and some of the TFP have 12 layers of tows (the NCF has two layers of tows in each of the 6 biax plies). Other than the base layer of glass, one particular difference is the concentration and type of stitching.

The NCF baseline has a chain-stitch around each of the 6 plies, whereas the TFP has 12 layers of lock-stitches. In the case of the TFP, the lock stitches were made around all the existing tows; the first layer is stitched around one tow, the second layer is stitched around the first and second layers of tows, and the 12<sup>th</sup> ply's stitches go around all 12 layers of tows. Thus, the underside of the base glass fabric is saturated with stitch thread-loops, similar to a random mat ply.

Figure 4.9 shows similar permeabilities between the NCF materials and the 12-ply TFP's. But the 12 ply TFP's are 4-6x higher permeability than the 16 ply TFP's. Interestingly, the glass bottom layer with thousands of stitches remained partly dry in all of the TFP samples throughout testing. Figure 4.16 shows the TFP samples turned over just after taking off the acrylic lid for a set of tests. Only the ends of the bottom layer by the inlets and vents are infiltrated by oil. The flow prefers to travel through the upper tow layers. This may be due to the greater concentration of stitching in the lower layers, as the bottom layer is stitched over 12 or 16 times in each place. The high number of stitches would compact the lower layers more than the upper ones. This would also explain the much greater  $K$  in the 12 ply samples, as they have many less stitches in the lower plies.

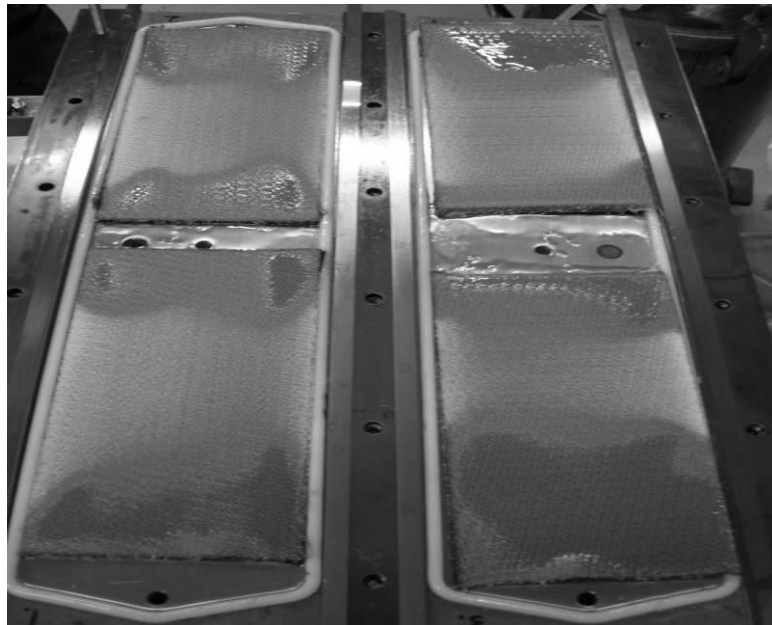


Figure 4.16 - Partly dry undersides of TFP samples.

For both 12 and 16 layer samples, it seems that  $K_0$  and  $K_{90}$  are not significantly different (quasi-isotropic). The only difference apparent between the different layer configurations is that  $K_{45}$  seems to slightly decrease (in the 12 ply layers) in relation to the other  $K$ 's as more  $90^\circ$  layers are added. Although a slight difference, this may be from the ply interfaces being less free for non-axial travel as parallel tows are added, both guiding the non-axial flow to the  $90^\circ$  direction, as well as causing more inter-ply crimping.

#### 4.2.3.4 Binded NCF

The effect of binders was seen immediately during permeability testing. The majority of samples had problems with channeling over the top and just below the acrylic top (Figure 4.17).

Complications of this type have been reported for too-high fiber contents where the permeability is too low for the experiment to work [280]. [286] reported the need to pre-compress tackified samples to a thickness slightly larger than the target thickness so that the preform can still be further compressed during testing and avoid this type of race-tracking. Although care was placed in consolidating the binders with just enough heat and pressure, it seems that many had no more capacity to compress away from the side walls and up against the acrylic top. This made the samples seem slightly too wide for the cavity.

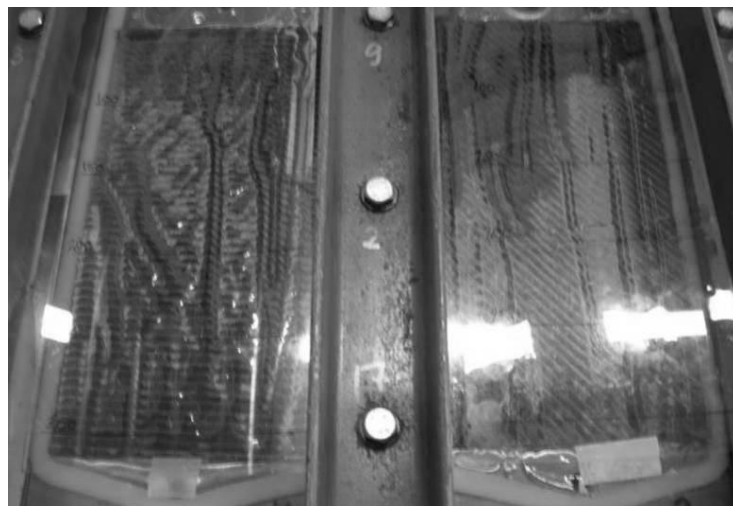


Figure 4.17 - Channeling on top layer in tackified materials.

The data that was collected showed a ~50% decrease in the effective permeability values of the non-tackified NCF, no matter what the amount of binder (Figure 4.18). Similar results were seen for tackified glass materials where the addition of any binder made a quick drop in the permeability, but further binder amounts caused minimal further influence [284].

The presence of binder has been universally shown to greatly affect the permeability, albeit in different ways. [283] showed that binder application greatly reduces the fabric permeability. This was attributed to a reduction either in channeling or the effective porosity of the preform. The location of the binder was shown to be important; both type of binder application and performing conditions can influence whether the binder will penetrate within fiber tows or remain on the layer surface. When the binder remains outside the tows, the permeability decreases as the binder

concentration is increased, and this is attributed to blockage of the inter-tow channels [284,285,286].

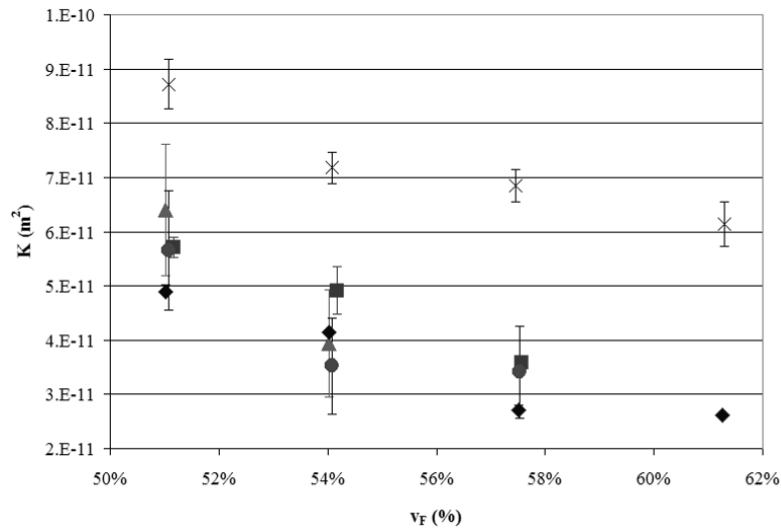


Figure 4.18 -  $K_0$ : Tackified NCF ( $\diamond$ : bind1,  $\blacksquare$ : bind2,  $\blacktriangle$ : bind3,  $\bullet$ : bind4,  $\times$ : non-tackified NCF).

The effects of binder entry into the intra-tow gaps are not as clear. [285] saw an increase of over 5x in permeability by adding a binder through solvent application into the tows, and attributed it to solvent shrinkage of the tows by capillary effects, leaving large inter-tow gaps, and not dependent on the binder itself. Other researchers also saw a strong increase in permeability as intra-tow binder concentration was increased until a maximum was achieved, followed by a decrease [286]. The increase in permeability was attributed to the binder itself consolidating the fibers of each tow, thus increasing the inter-tow gaps or preventing tow deformation during compression [301]. The decrease at high concentrations was explained by reaching a tow saturation point and further binder remaining outside the tows.

Based on previous findings and these results, it would appear that the binder was melted enough to effectively fill the inter-tow-spaces, and still leaving some binder in between the plies. Further experimentation will attempt to clarify this by trying out various consolidation heats and pressures.

#### 4.2.3.5 Braids

Little work exists in the literature on the evaluation of the permeability of braided fabrics. [302] argued that a braid is more permeable than a similar woven fabric due to inherent higher porosity. And [280] showed that weaves were more porous than NCF's due to the crimp of the tows. Thus it

can be inferred that braids should have greater permeability than NCF's. But in this case, the braids show similar permeability values to the NCF's.

The biax braid material exhibits relative isotropic permeability. [287] also reported a quasi-isotropic permeability tensor for 45° biax glass. It is generally agreed that the 0° (axial/mandrel feed direction) and 90° (rotational) directions coincide with the principle permeability components in all braid configurations, i.e.  $\theta = 0$  [287,289,302], although no previous work is known in which the permeability of triax braids is discussed.

Understandably, the standing fibers enhance axial flow, and  $K_0$  is ~3x greater than  $K_{90}$  or  $K_{45}$ . This confirms the previous report of increased K from alignment of the fibers with the flow [174]. This is especially true at low fiber volume contents (Figure 4.19), showing greater isotropy as  $v_f$  increases.

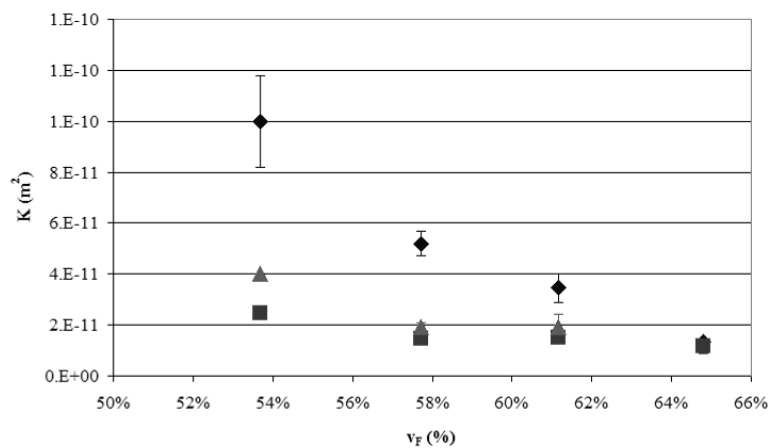


Figure 4.19 - K: braided triax (♦: 0, ■: 90, ▲: 45).

The “Braid-S” material, with 24K standing tows, and 60° braiding angle, appears to be slightly less permeable than the normal triax braid (Figure 4.20). But the differences are slight. The increase of the braid angle from 45° was suggested to both reduce [288] and increase [287] the tow spacing. But further research is required to make any conclusions on braid angle in braided materials.

#### 4.2.4 Validation of results

The permeability of the baseline material was also measured in a separate study [77]. At a  $v_f$  of 57%,  $K_0$  was reported there to be ~9e-11  $m^2$ . Interpolation of the power law curve from this study predicts  $K_0 = 6.9e-11$  which is very close given the usual variation in K measurement.



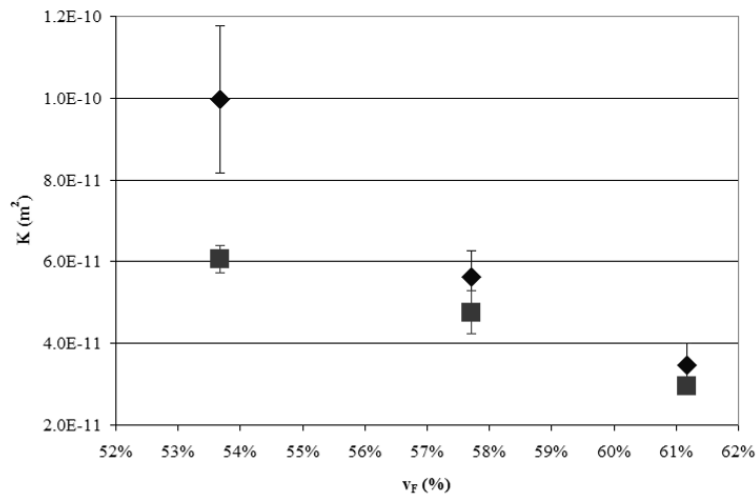


Figure 4.20 -  $K_0$ : braided triax materials (◆: Braid-T, ■: Braid-S).

For comparison purposes, the permeability of the biax braided material was simulated with WiseTex, LamTex and FlowTex (Section 2.3.3.1). A unit cell model developed for the biax braid at a  $v_F$  of 0.57 (Figure 4.21), resulted in a theoretical permeability of about  $7e^{-11}$  ( $m^2$ ) which is comparable to the average experimental value at that  $v_F$  of  $\sim 6e^{-11}$ . Further work is intended to develop similar models for the triax braid as well as the stitched materials.

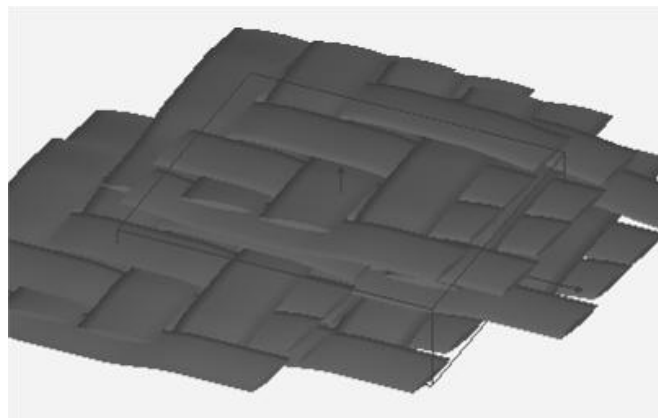


Figure 4.21 - Wisetex/Lamtex model of biax braided fabric stack.

#### 4.2.5 Saturated vs. unsaturated comparison

Figure 4.22 shows all sample configurations compared between the permeabilities resulting from saturated testing and the initial wetting experiment. The permeabilities shown are only for the initial  $v_F$  with each material, and are exhibited to show how the two testing techniques compare for each material. As seen, the greatest differences between the two are with the 12 layer TFP samples. They also have the highest relative permeabilities across materials. The higher saturated permeability in this case is attributed to dual-scale flow effects, which will be discussed in a later

section. Most of the other materials show good agreement between saturated and unsaturated testing results.

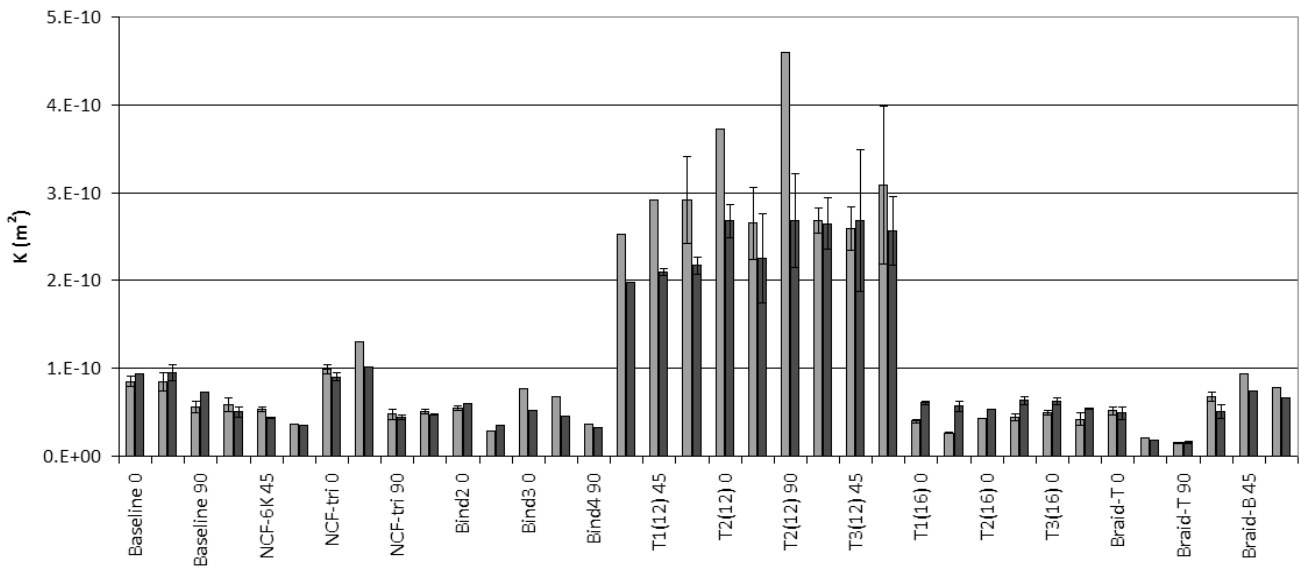


Figure 4.22 - Saturated vs. wetting permeability (light = saturated, dark = wetting).

#### 4.2.6 Summary of in-plane permeability characterization

The multi-cavity parallel flow technique for permeability measurement has proven to be applicable to the permeability measurement of various modern carbon textiles. The number of ply interfaces seems to have a strong influence on the permeability as well. Various tow orientations produced little difference in TFP samples, but the number of layers drastically changed the packing of the lower layers and thus the permeability. Great care must be exerted to control the consolidation process when applying binder to samples for permeability measurement. With only a little consolidation of binder into the inter-tow spaces, the permeability decreases significantly. The numerical prediction of biax braid permeability produced comparable results to the experimental and prompts further attempts with the other materials. Unsaturated permeability data seems to be comparable to saturated data at least at high fiber volume contents.

Each of the materials' permeability components were fitted to the power law in Equation 2.13. All the fitted constants  $A_k$  and  $B_k$  are presented in Appendix 1.

### 4.3 Through-thickness permeability

To gain a better understanding of 3D flow, as this is the norm in industry, 3D flow experiments were also conducted. The through-thickness permeability ( $K_{zz}$ ) was measured by point-infusion into the top of a stack of material, as discussed in Section 2.3.3.2.4. This type of  $K_{zz}$  measurement was employed in this study regardless of the complexity of data analysis, as this method seemed most related to the other modeling efforts in this work and is simple enough to be repeated in any lab. To further simplify the required tooling, and due to the focus on VARI for the remainder of this work, a vacuum bag was employed.

#### 4.3.1 Materials and experimental procedure

Table 4.3 lists the infusions performed; the materials are a selection of the list in Section 3. The lay-up column lists the number of plies and their orientation. The length and width of the stack was determined by guessing the minimum dimensions of flow when the resin reached the bottom of this number of plies. This was determined by inputting best guesses for  $K_{zz}$ , into a 3D flow simulation in PAM-RTM. The size used was 100 x 160 mm<sup>2</sup> for NCF, 100 x 100 mm<sup>2</sup> for braids and TFP.

The 16 plies of 12K NCF in each stack had stitching oriented either all in the same direction, or with 2 of the 15 ply-interfaces having a 90° change in stitching orientation. It was noticed that some of the older 12K NCF (~18 months old) seemed to be less stiff than newer 12K NCF material (~4 months old). To test for any differences, a stack of new NCF was also tested.

$K_{zz}$  values for chain-stitch NCF's like the baseline fabric have been reported to be 5x higher for flow from the side with 1 stitch thread when compared to flow from the eyelet side of the chain stitches [204]. Due to this reported morphology difference, care was taken in all infusions to keep the eyelet side on the bottom to eliminate any  $K$  variation from this.

$P_A$  ranged from 935 to 955 mbar, and  $P_V$  was held at ~30mbar. The pressure difference between  $P_A$  and  $P_V$  is listed in Table 4.3. The final height of the preform was measured with calipers after the resin had cured and the part was demolded. The porosity  $\phi$  (inverse of  $v_F$ ) was determined from the measured height and the areal weight by Equation 2.19:

$$v_F = \frac{n \cdot A_F}{\rho_F \cdot h} \quad (4.2)$$

The  $\phi$  (and  $v_F$ ) is assumed constant throughout the experiment for modeling simplicity.

Table 4.3 – Infusions for  $K_{zz}$  measurements.

<i>ID</i>	<i>material</i>	<i>layup</i> (top to bottom)	<i>hardener</i>	$\Delta P$ (Pa)	<i>Avg T</i> (°C)	<i>Avg <math>\mu</math></i> (Pa·s)	<i>final h</i> (mm)	$\phi$
z1	Baseline	[0] <sub>16</sub>	235H only	90900	22	0.2601	8.30	0.415
z2	Baseline	[0] <sub>8</sub> / [90] <sub>4</sub> / [0] <sub>4</sub>	235H only	91910	21.2	0.2743	8.25	0.396
z3	Baseline	[0] <sub>16</sub>	235H only	92920	22.9	0.2382	8.25	0.412
z4	Baseline	[0] <sub>16</sub>	235H only	92920	23.6	0.2341	8.55	0.432
z5	Baseline (new)	[0] <sub>16</sub>	235H only	91910	23.3	0.2343	8.00	0.393
z6	Bind4%	[0] <sub>18</sub>	mix	93223	22	0.2997	9.45	0.422
z7	NCF-6K	[0] <sub>14</sub> / [45] <sub>2</sub>	235H only	91910	23.1	0.2369	7.95	0.389
z8	Braid-B	[±45° tows] <sub>16</sub>	235H only	91910	22.4	0.2775	7.60	0.359
z9	Braid-T	[±45° tows] <sub>8</sub>	mix	93425	21.9	0.2797	6.30	0.470
z10	Braid-S	[±60° tows] <sub>10</sub>	mix	93223	22	0.2838	7.70	0.427
z11	T1(12)	[0] <sub>12</sub> ×3	mix	93122	22	0.2749	8.35	0.510
z12	T2(12)	[(0/90) <sub>3</sub> ] <sub>5</sub> ×2	mix	93223	22.2	0.2699	5.80	0.530
z13	T3(12)	[0/0/0/90/0/0] <sub>5</sub> ×3	mix	92415	21.7	0.2791	8.55	0.522
z14	T3(16)	[0/0/90/0/0] <sub>3</sub> /0	mix	92415	21.7	0.2776	3.95	0.540

A resin amount of 80 to 90g was mixed for each separate infusion, and degassed for 5 minutes before infusion. The RIM 235R system was used, with either the 235H hardener, or the mix of 33% 235H and 67% 236H. The mix is the same as used in the majority of the VARI experiments in Section 4.1. 235H alone was used for some of the infusions, as 236H was not available.

Also listed in Table 4.3 is the average ambient temperature measured from start of infusion to the end of the experiment. An average viscosity for the infusion was determined with the viscosity model discussed later in Section 4.5 for isothermal cure at this average ambient temperature, at half of the total experiment time (average time). The assumption of neglecting the reaction exotherm, as done for the VARI experiments in Section 4.1, is even safer in this case for the following reasons:

- Resin mass was always under 100g, instead of 400g
- The maximum experiment time was 50 minutes, and only 2 cases were over 30 minutes, with the majority being under 15 minutes. This is lower than the 30 to 60 minutes or more for the VARI infusions in Section 4.1.
- Ambient temperature exhibited a lower range and lower average: max  $T_A$  was 23.6°C and minimum was 19.9°C.

The viscosity model from Section 4.5 allows calculation of the isothermal viscosity prediction at any time and ambient temperature for the 235H/236H mix resin system. This modeling is not done for the 235H (alone) system, which should have slightly different cure kinetics. To increase the accuracy of the  $K_{zz}$  characterization, an approximate viscosity development curve was generated for the 235H system for any  $T_A$ . This approximation is the source of the average viscosity listed in Table 4.3 for the 235H infusions. Details of this approximation are found in Appendix 2.

In each experiment, resin was infused from the pot (at  $P_A$ ) through a tube of length  $L_t$  and radius  $b_t$ , through a small whole cut in the vacuum bag, and out onto the top of the fabric stack (Figure 4.23). A mirror was positioned under the glass mold to watch for arrival of the resin on the bottom of the stack. The experiment ends as soon as resin is seen to be touching the bottom. The radii of the half-ellipsoid are measured then, with:

- $r_x$  and  $r_y$  equal to the major and minor axis, respectively, of the ellipse seen on the top through the bag,
- $r_z$  is the height of the preform.

In Figure 4.23, the right-hand image shows more wetting of the bottom than the first point of contact. The first point of bottom wetting is easily detected by the human eye, but not possible to demonstrate with a photo. The bars seen over the infusion were set up to hold the inlet tube in a vertical position, but do not exert any pressure on the fabric.

The in-plane flow was measured at time intervals before the resin touched the bottom. And the flow was continued for a short while after this point, with the flow ellipse measured on both the top and bottom of the stack at different time intervals. But the focus of the experiment was the point of resin touching the bottom, and so this is the effective end of the experiment. Any flow after this point is not a perfect ellipsoid anymore, as it is constrained by the glass mold bottom. Flow before this point has the usual  $K_{zz}$  measurement problem of observing the through thickness flow front position.

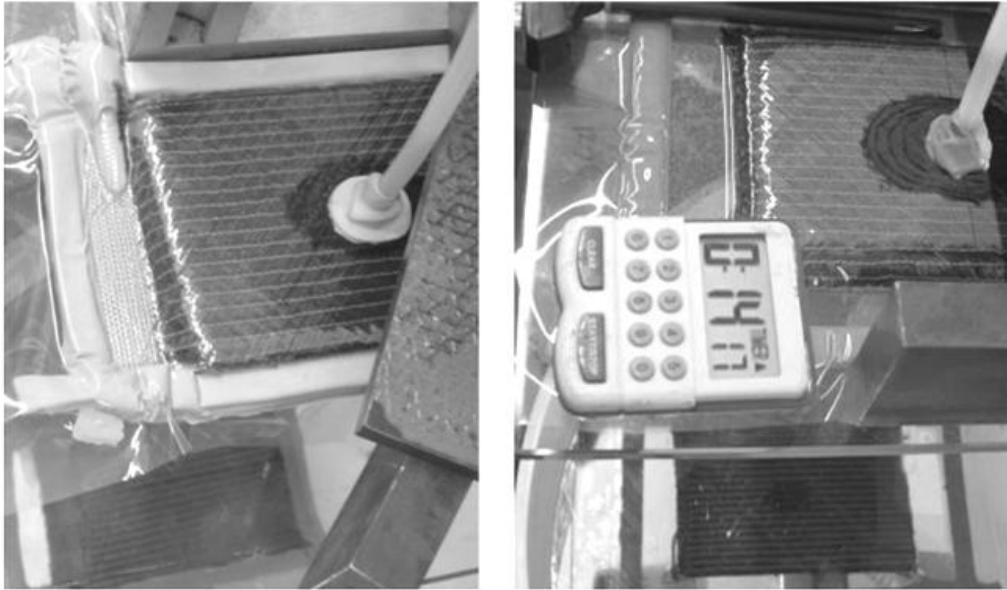


Figure 4.23 - (L) Infusion setup for  $K_{zz}$  measurements, (R) demonstration of experiment end.

Nedanov and Advani [148] monitored the resin flow into the mold and deduced the ellipsoid shape from the in-plane dimensions at each time interval. But they concluded that this was difficult to do with accuracy and that equal precision was obtained by only considering the last point, where the resin is visually observed to touch the bottom. This greatly simplifies the experimentation procedure, as only one set of dimensions and time is needed, and this can all be observed by in plain sight.

The point of resin reaching the bottom for each experiment is listed in Table 4.4. The final height from Table 4.3 (setup data) is repeated here, labeled as  $r_z$ , for comparison of dimensions. As in the VARI benchmark tests,  $\theta$  is the angle between  $r_x$  and the:

- top layer's stitching (in the case of NCF),
- mandrel direction (in the case of braids),
- top layer's tow direction (in the case of TFP).

For the biax braid and TFP2 infusions, the in-plane flow was approximately isotropic ( $K_{xx} = K_{yy}$ ), so pheta was difficult to characterize (Figure 4.24). The high permeability of the TFP materials made the times much shorter than the other materials. This was particularly the case with TFP3-16, where the wet-through was seen almost instantaneously, when the in-plane flow was about the dimensions of the tacky-tape seal (Figure 4.25).

Table 4.4 -  $K_{zz}$  experiments: final ellipsoid shape and time (\* = ~isotropic in-plane).

<i>ID</i>	<i>material</i>	<i>t</i> ( <i>s</i> )	<i>t</i> ( <i>min</i> )	$r_x$ ( <i>mm</i> )	$r_y$ ( <i>mm</i> )	$r_z$ ( <i>mm</i> )	$\theta$ ( $^\circ$ )
z1	Baseline	1125	18.8	35.5	24.25	8.30	5
z2	Baseline	900	15.0	36.5	21	8.25	4
z3	Baseline	750	12.5	34.25	22.25	8.25	4
z4	Baseline	1350	22.5	45	27.25	8.55	4
z5	Baseline (new)	990	16.5	30.5	19	8.00	4.5
z6	Bind4%	2310	38.5	38	29	9.45	2
z7	NCF-6K	930	15.5	34.5	22.75	7.95	2
z8	Braid-B	3000	50.0	32.75	31.5	7.60	NA*
z9	Braid-T	540	9.0	32.5	27.5	6.30	1
z10	Braid-S	1050	17.5	32.5	29.5	7.70	6
z11	T1(12)	315	5.3	24.75	23.5	8.35	2
z12	T2(12)	150	2.5	16	15.25	5.80	NA*
z13	T3(12)	150	2.5	22	20.5	8.55	28
z14	T3(16)	5	0.1	5	5	3.95	1

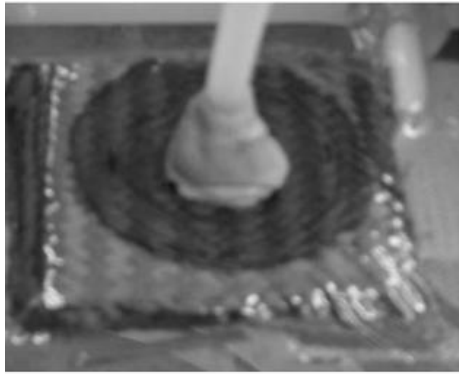


Figure 4.24 - Isotropic  $K_{xy}$ : Biax Braid.



Figure 4.25 - Rapid wet-through: TFP3-16.

#### 4.3.2 Data analysis

As mentioned in Section 2.3.3.2.4, most laboratories employing the point-infusion method solve for  $K_{zz}$  by the inverse estimation method. This consists of iterations of flow simulation by guessing permeability values until the flow front geometry and times match the point-infusion experiment.

[148] suggested a mathematical solution to flow front geometry analysis that involves solving Darcy’s law for an isotropic hemisphere with embedded conversions for anisotropic permeabilities. Both of these methods, with some adaptation/optimization, were applied to the data in this study. A constant fiber volume content is assumed in both cases for simplicity’s sake (neglecting the resin pressure gradient’s affect on fiber compression). This assumption is discussed and applied again in Section 5.6.

#### 4.3.2.1 Inverse estimation with PAM-OPT

Both a fine mesh (for accuracy) and a coarse mesh (for computation speed) were generated for PAM-RTM, for the stack of fabric for the first test, “z1” (Figure 4.26). The inlet is defined by face elements in blue. Due to symmetry, a quarter mesh was used, with edges corresponding to the principle permeabilities. The size was chosen to encompass the maximum  $r_x$  and  $r_y$  values from all  $K_{zz}$  experiments. The 2D shell elements model was first constructed for each, and then extruded to 14 layers of tetrahedral, for an aspect ratio,  $\lambda$ , of:

$$\lambda = \sqrt{\frac{K_{xx}}{K_{zz}}} = \frac{\text{length}_x}{\text{length}_z} = \frac{0.0025}{0.000589286} = 4.24 \quad (4.3)$$

This is only an approximate  $\lambda$ , as the length in the  $x$  and  $z$  direction is not constant in the principle directions  $x$  and  $z$  for tetrahedra. Square or cube elements are not supported by PAM-RTM’s non-conforming element approach. Extrusion to prismatic elements results in inaccurate simulation when infusing on the top layer. Tetrahedra elements were thus the only working possibility.

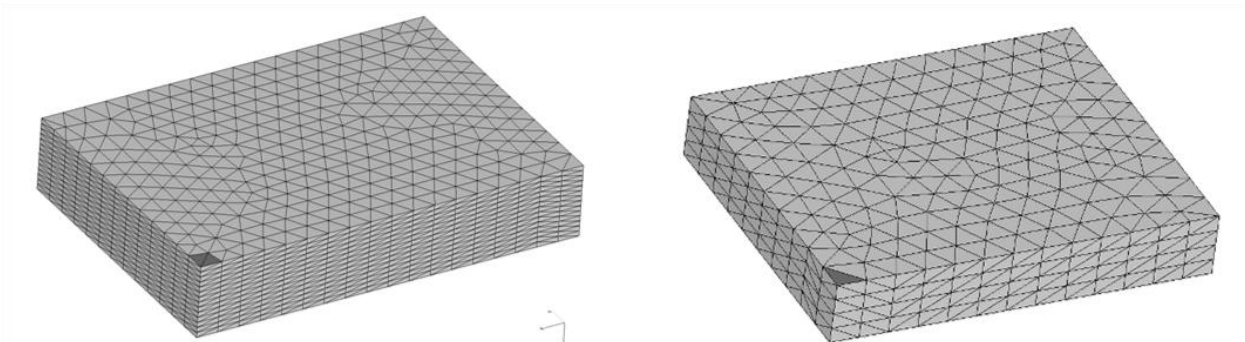


Figure 4.26 - Fine (L) and coarse (R) mesh models in PAM-RTM for  $K_{zz}$  test z1.

$K_{xx}$  and  $K_{yy}$  from the in-plane measurements in Section 4.2 were input into the coarse mesh (Figure 4.26, right-hand), along with a guess  $K_{zz}$  value. The simulation was manually run several times with different  $K_{zz}$  values chosen intuitively until the geometry matched the flow ellipsoid at the



experiment's end. These same numbers were input into the fine mesh (Figure 4.26, left-hand) and simulated to best show this geometry (Figure 4.27). Unfortunately, the time to reach this moment was low compared to the experimental time. To get all three permeabilities to match the geometry at the right time was deemed too time-consuming for manual optimization.

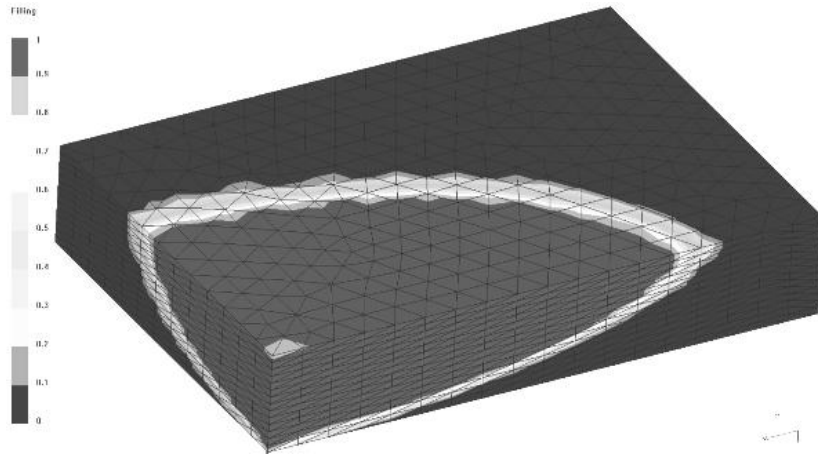


Figure 4.27 - PAM-RTM flow simulation showing proper ellipsoid geometry with guess permeabilities.

PAM-OPT is a program that can call PAM-RTM repeatedly and optimize the input variables to achieve a goal using various best-fit algorithms. To solve this simulation for all three permeabilities, a multi-objective function is used to minimize the error between the goal time and the times in each of the three directions based on the guesses for the permeabilities. The application of PAM-OPT to flow simulation is new practice. The developers of both PAM-RTM and PAM-OPT at ESI directly assisted the author with developing this application, as it is hoped that this can one day be an industrial resin infusion design tool.

The objective function used is a typical sum of the squares of the error (SSE):

$$SSE = (t_G - t_x)^2 + (t_G - t_y)^2 + (t_G - t_z)^2 \quad (4.4)$$

where  $t_G$  is the target time (goal), and  $t_x$ ,  $t_y$ , and  $t_z$  are the times to reach the target radii,  $r_x$ ,  $r_y$ , and  $r_z$  recorded at the experiment end. Guess values and upper and lower bounds were chosen and implemented in the PAM-OPT code.

The first major challenge was how to have PAM-OPT know when the flow arrives at the target ellipsoid geometry. The first attempt involved the “.fil” output file in PAM-RTM, which is a list of each element in the mesh by ID#, each with 2 times listed: for first contact with the liquid, and for

complete saturation. One must find the element ID# in the mesh at each target radius, and then specify in the PAM-OPT code to look in this file and find this number. This had two drawbacks:

- Neither the time of first liquid contact nor complete saturation for an element perfectly describes the time of resin arrival at a particular point in that element.
- The format of the “.fil” file seems to change from run to run, making it hard to call the right number.

The next attempt involved the pressure\_sensors.dat output file. Sensors can be placed at points within the mesh corresponding to the target radii. The pressure\_sensors.dat file then lists the resin pressure ( $P_R$ ) at each sensor at every time increment of the simulation. After some work at trial and error, the code was successfully modified to find the time for each sensor when pressure was at  $P_V + 1$  Pa. The first  $P_R$  value above  $P_V$  should signal the arrival of resin at that point. Again, two problems were apparent with this approach:

- In PAM-RTM the pressures through the simulation are computed in the middle of faces for 3D simulation. A sensor on a node at the outer edge of an element can register negative pressures for the first few time increments as the middle of the element begins to fill.
- As the time increments are not infinitely small, the first pressure registered above 0 is around a few thousand Pascals above  $P_V$ , so PAM-OPT attempts to iterate backwards to where the difference is only 1 Pa. This induces a degree of guessing and limits the accuracy.

The next attempt involved the Filling\_Threshold.dat file, which outputs the location coordinates of each sensor along with the exact time the flow arrives there (Figure 4.28). Interpretation of this file is tricky as it lists each sensor in order of resin arrival. In other words, the x-direction sensor may be either the first, second, or third row of data depending on the permeability guesses. With some trial and error, the PAM-OPT code was successfully adapted to look for the time in the fourth column corresponding to the maximum value in the first column (x coordinate) for the x sensor, and so on for the other two sensors. Note this only works when sensors are placed at locations with only 1 non-zero coordinate, (x,0,0) for instance.

```
: column 1 to 3 : sensor position (x, y, z)
: column 4 : time (s)
0.00000E+000 2.40000E+001 0.00000E+000 1.28140E+002
3.46154E+001 0.00000E+000 0.00000E+000 9.27376E+002
0.00000E+000 0.00000E+000 8.14000E+000 1.08114E+003
```

Figure 4.28 - Example “Filling\_Threshold.dat” output file from PAM-RTM with three sensors.

The Gradient optimization algorithm was first employed. Gradient-based fitting was not expected to work with three design variables due to the infinite number of local minimums for such a problem. But it is the simplest and quickest algorithm, so it was employed to ensure that PAM-OPT was reading the filling times correctly.

The next algorithm used was the Adaptive Response Surface Method (ARSM). Optimization was more successful with this method, optimizing the  $K$  values to get times close to the target ( $t_G$ ) in two of the directions, but not the third. The “Genetic Algorithm” method was then employed as a last attempt. The maximum iterations was set at 30, which took six hours of computation time on the author’s laptop. Yet the results were not satisfactory;  $t_x$  was 53% higher than  $t_G$ , while  $t_z$  and  $t_y$  were 14 and 6% lower than  $t_G$  respectively.

After much time and energy trouble-shooting the model, it is the author’s suspicion that the problem of flow simulation with three variables is too difficult for the current version of PAM-OPT. It is hoped that future work with this method will be more successful. The final genetic algorithm script in PAM-OPT is included in Appendix 3.

#### 4.3.2.2 Isotropic transform solution

Nedanov and Advani [148] presented a mathematical model to solve for the three permeabilities based on their geometrical mean. Solving the Darcy flow in three directions is enabled by transforming the point-injection permeability tensor of an anisotropic medium into an isotropic-type permeability scalar:

$$K = \sqrt[3]{K_{xx} K_{yy} K_{zz}} \quad (4.5)$$

The shape of this effective flow is then hemispherical instead of a half-ellipsoid, and can be solved in polar coordinates for the pressure gradient with respect to the radius from the inlet. The flowrates for the inlet tube, expanding hemisphere in an isotropic medium, and Darcy flow in an isotropic medium are set equal to each other:

$$Q = \frac{\pi b_t^4}{8\mu L_t} (P_A - P_I) = \frac{\partial r}{\partial t} 2 \cdot \pi \cdot r^2 \cdot \phi = \frac{K}{\mu} \frac{2 \cdot \pi \cdot r \cdot b_t}{(r - b_t)} P_I \quad (4.6)$$

where  $r$  is the isotropic flow radius,  $b_t$  is the inlet tube radius, and  $L_t$  is the length of the inlet tube.

After non-dimensionalization of the variables, rearrangement, and integration, a system of three equations is generated to solve for the three permeabilities by minimization of each. The inputs are the dimensions of the flow half-ellipsoid at  $t$ , where  $t$  is the time the flow touches the bottom of the mold. This solution was implemented in Mathcad (Figure 4.29). A solver block with the “Find” function resulted in values consistent with those reported in the publication with a Maple code.

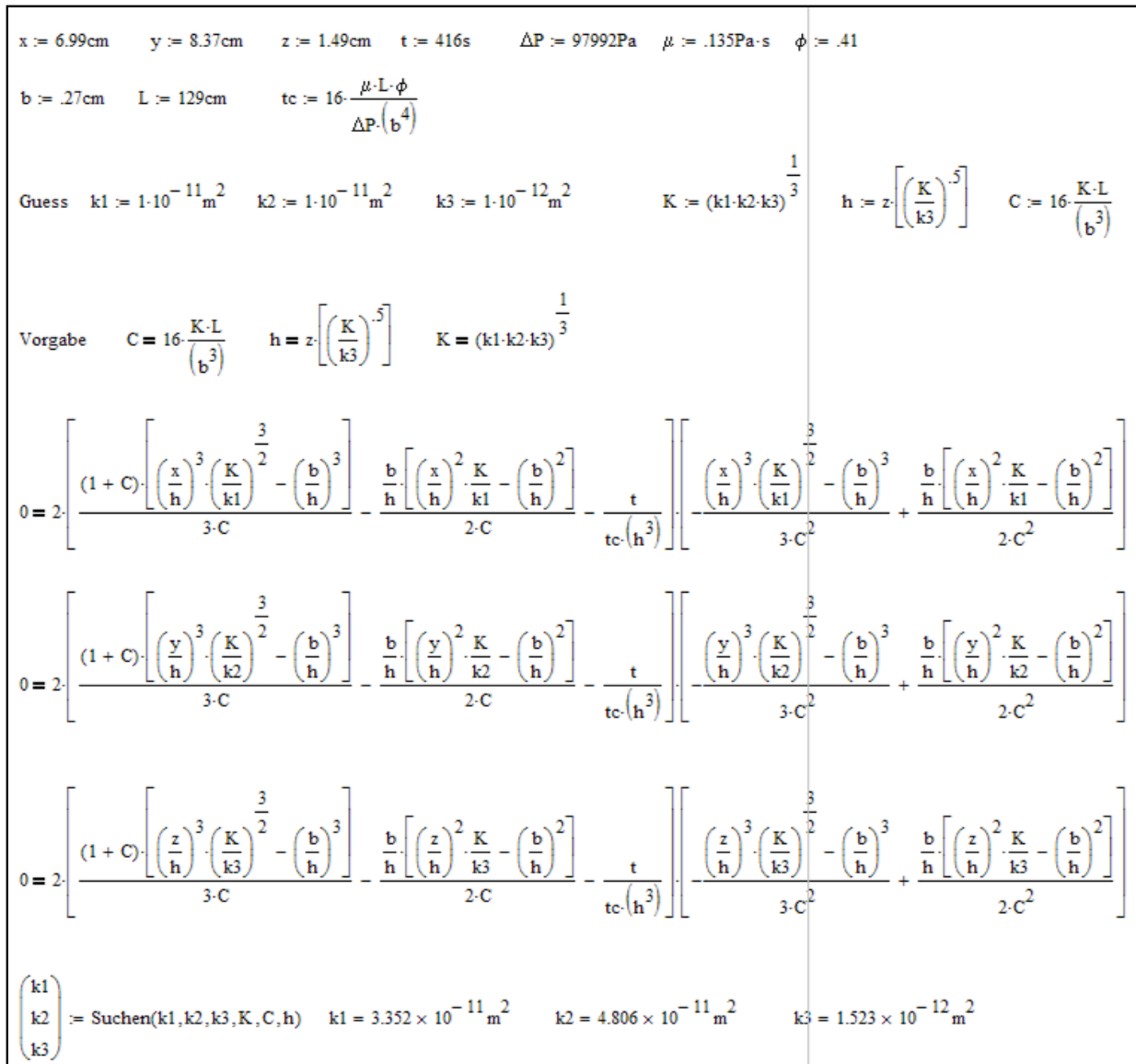


Figure 4.29 - Mathcad solution based on isotropic transformation solution.

The data from the “z1” and “z2” tests was input into this same model. Unfortunately, attempts at solving the data from this study’s experimentation resulted in no logical solution:

- solutions would only appear upon many iterations of the initial guess permeabilities
- The solutions were very sensitive to the initial guess

- None of the solutions were believable permeability values

Trying the various functions in Mathcad: Minerr, Find, Minimize, and Root (all at various TOL levels) proved unfruitful in every instance. A sample code to implement this solution in Maple is included in [148]. But attempts to implement this code in either Matlab or Maple produced no viable solution as well.

#### 4.3.2.3 Ratio simplification

It is intuitive that there must be some direct relationship between each permeability component and the corresponding flow length component. In 1D Darcian flow, the pressure gradient along the flow, when normalized by the total length of flow at a particular instant in time,  $P_R [x/L(t)]$  should be equal at any time. In other words, any point half way between the inlet and the flow front will always have the same  $P_R$ , regardless of the time or position of the flow front. It is assumed that this is the case in 3D Darcian flow as well; the pressure gradient in any of the three principle directions aligned with the flow-ellipsoid, when normalized by total flow length, should be equal at any time:

$$\frac{dP}{d[x(t)/x_f(t)]} = \frac{dP}{d[y(t)/y_f(t)]} = \frac{dP}{d[z(t)/z_f(t)]} \quad (4.7)$$

This is best illustrated in a flow simulation; Figure 4.30 shows the pressure gradient calculated in PAM-RTM for flow with the same geometry as the “z1” test (quarter symmetry). The extent of each color threshold extends proportionally to the radii of the flow front in each principle direction.

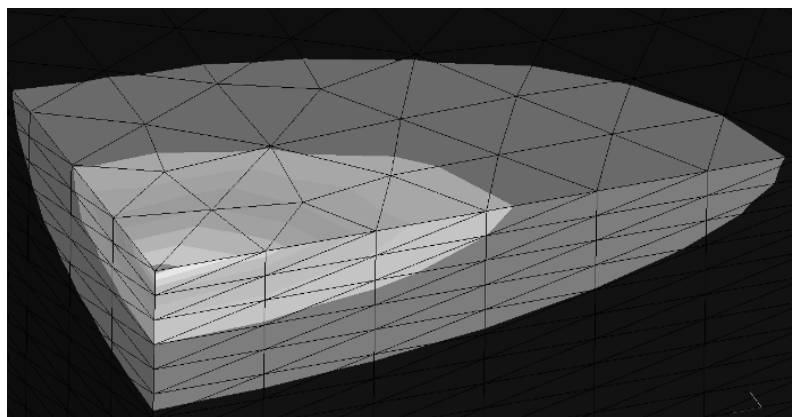


Figure 4.30 - Pressure gradient in 3D point-infusion.

This considers the 3D flow as three different “effective” 1D flows in each of the principle directions. The pressure gradient ( $\Delta P$ ) driving the resin from the atmosphere to the vacuum is not all available in any of these 1D “effective” flows, as it must be distributed in all directions in a 3D flow. Hence, with lower pressure gradients, each 1D “effective” flow will be slower than true 1D flow with the same  $P_A$  and  $P_V$ .

Even though the pressure gradients are lower than in true 1D flow, they are equal with this assumption. So if one compares the “effective” 1D flow in two of the principle directions by the 1D Darcy solution (Equation 2.11), these pressure gradients will cancel out. As we are assuming constant viscosity and porosity, the relationship between permeability must only be dependent on the square of the ratio of flow lengths. For example, the relationship between  $K_{xx}$  and  $K_{zz}$  is:

$$\frac{K_{xx}}{K_{zz}} = \frac{\left( x_f^2 \left( \frac{2 \cdot \phi \cdot \mu}{(dP/dx) \cdot dt} \right) \right)}{\left( z_f^2 \left( \frac{2 \cdot \phi \cdot \mu}{(dP/dz) \cdot dt} \right) \right)} = \left( \frac{x_f}{z_f} \right)^2 \quad (4.8)$$

The same relationship has already been applied to in-plane radial permeability testing [27, 96]. In 3D flow, this applies to all directional ratios:

$$\frac{K_{xx}}{K_{zz}} = \frac{x_f^2}{z_f^2}, \frac{K_{yy}}{K_{zz}} = \frac{y_f^2}{z_f^2}, \frac{K_{xx}}{K_{yy}} = \frac{x_f^2}{y_f^2} \quad (4.9)$$

This assumption was verified with the datasets published by Nedanov and Advani [148] with the isotropic transformation solution. The last point in the data set from Tables 2 and 3 in their publication, and the last point from their Appendix data are listed in Table 4.5 along with the permeability component solutions. The ratios between flow lengths were calculated, and then between permeabilities. A theoretical ratio between permeabilities was calculated from the square of the length ratios in each case, and compared to the published solution for each K component. The maximum deviation between the two is 7.4%, and only 1.4% for  $K_{zz}$ . This is within the typical standard deviation of in-plane permeability measurements, and the confidence interval for  $K_{zz}$  measurements in this publication is over  $\pm 100\%$ . So this error is deemed acceptable.

This affords a great simplification to the solution; two of the permeability variables can be eliminated ( $K_{xx}$  and  $K_{yy}$ ) by setting them equal to  $K_{zz} (L_{xy} / L_z)^2$ . If in-plane K data has already been obtained, then one can solve directly for  $K_{zz}$ . If in-plane K data has not yet been obtained, or merits

insufficient confidence, one can solve for  $K_{zz}$  with the simplified isotropic transformation solution, and then calculate the in-plane values from the ratios and size of the ellipsoid at experiment's end.

Table 4.5 - Ratio simplification solution applied to Nedanov and Advani data [148].

	<i>Table 2,3: only last point (m)</i>			<i>Appendix: only last point (cm)</i>		
	<i>x</i>	<i>y</i>	<i>Z</i>	<i>x</i>	<i>y</i>	<i>z</i>
<i>L:</i>	6.99	8.37	1.49	8.97	8.06	1.48
<i>K:</i>	3.66E-11	4.93E-11	1.54E-12	5.114E-07	4.145E-07	1.405E-08
	<i>x/y</i>	<i>x/z</i>	<i>y/z</i>	<i>x/y</i>	<i>x/z</i>	<i>y/z</i>
<i>L/L:</i>	0.835	4.691	5.617	1.113	6.061	5.446
<i>K/K:</i>	0.742	23.766	32.013	1.234	36.409	29.513
<i>K/K (theoretical) :</i>	0.697	22.008	31.556	1.239	36.733	29.658
<i>% error (K<sub>th</sub>-K)/K:</i>	-6.1%	-7.4%	-1.4%	0.4%	0.9%	0.5%

Simplification of the solution is as follows. The isotropic permeability reduces to a function of the ellipsoid shape and the one variable:

$$K = K_{zz} \left( \frac{r_x \cdot r_y}{r_z^2} \right)^{2/3} \quad (4.10)$$

The non-dimensionalized isotropic flow radius for the z-component direction reduces to 1:

$$\bar{r}_{ff} = \frac{r_z}{(r_x r_y r_z)^{1/3}} \left( \frac{K_{zz} \left( \frac{r_x \cdot r_y}{r_z^2} \right)^{2/3}}{K_{zz}} \right)^{1/2} = 1 \quad (4.11)$$

Only one error function is needed instead of three. Mathcad's "Root" function can solve this without the need for a separate function for minimization of error. This simplified solution as implemented in Mathcad is seen in Figure 4.31 for the case of the "z2" test.

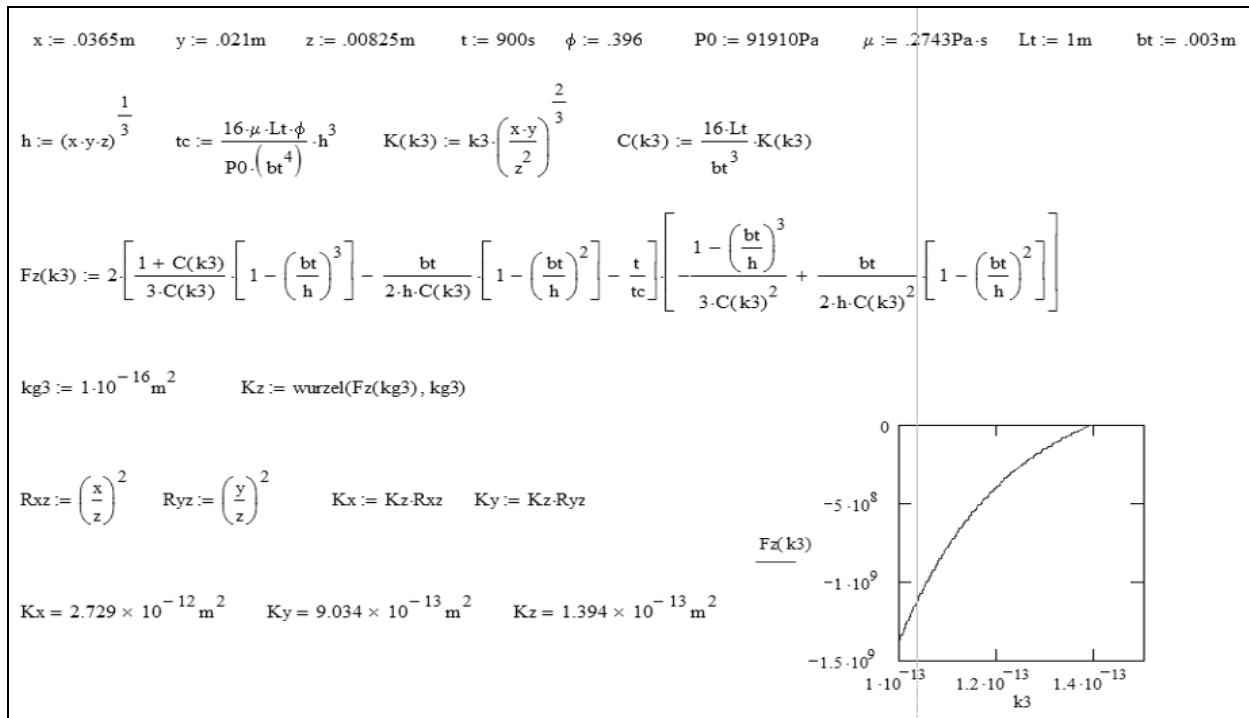


Figure 4.31 - Mathcad solution for ratio simplification of isotropic transformation solution.

The length of the inlet tube ( $L_t$ ) was between 800 and 1100 mm, but this range proved to be insignificant to permeability calculation. Changing the variable  $L_t$  from 1100 mm to 0.001 mm resulted in a change of only 0.1% for  $K_{zz}$ . A length of 1 meter is therefore assumed for all data analysis.

#### 4.3.3 Results

Table 4.6 lists all three resultant permeability components from the ratio simplified solution and the assumed fiber content. The five baseline  $K_{zz}$  values were normalized by the Kozeny Carman equation (Equation 2.12) to their average  $v_F$  (59.0%). The normalized average  $K_{zz}$  was  $1.235 \pm 0.134 \text{e-}13 \text{m}^2$ . The variation in baseline  $K_{zz}$  data was surprisingly small; standard error over the five repeats is  $\pm 9.3\%$ .

Table 4.6 - Point-infusion resultant permeability components.

ID	material	$v_F$	$K_{xx}$ ( $\text{m}^2$ )	$K_{yy}$ ( $\text{m}^2$ )	$K_{zz}$ ( $\text{m}^2$ )
z1	Baseline	0.585	2.188E-12	1.021E-12	1.196E-13
z2	Baseline	0.604	2.729E-12	9.034E-13	1.394E-13
z3	Baseline	0.588	2.570E-12	1.085E-12	1.491E-13
z4	Baseline	0.568	3.161E-12	1.159E-12	1.141E-13



z5	Baseline (new)	0.607	1.279E-12	4.963E-13	8.799E-14
z6	Bind4%	0.578	1.637E-12	9.534E-13	1.012E-13
z7	NCF-6K	0.611	1.990E-12	8.653E-13	1.057E-13
z8	Braid-B	0.641	6.632E-13	6.136E-13	3.572E-14
z9	Braid-T	0.530	4.081E-12	2.922E-12	1.534E-13
z10	Braid-S	0.573	2.182E-12	1.798E-12	1.225E-13
z11	T1(12)	0.490	4.067E-12	3.666E-12	4.629E-13
z12	T2(12)	0.470	1.991E-12	1.808E-12	2.616E-13
z13	T3(12)	0.478	6.368E-12	5.529E-12	9.617E-13
z14	T3(16)	0.491	6.806E-13	6.806E-13	4.247E-13

Without  $v_F$  normalization, the new 12K material seemed a little low compared to the others. But it also compressed to the highest  $v_F$ . Thus  $v_F$  normalization placed it within the range of the rest of the baseline data. A supplemental in-plane permeability experiment as per the methods in Section 4.2 proved that the newer 12K NCF material does indeed have an in-plane  $K_{xx}$  and  $K_{yy}$  of about 1/3 (34%) of the older material. Whether this is due to a different sizing in the new material, or deterioration of the sizing over time, this emphasizes the high degree of permeability variation in otherwise seemingly similar materials.

For comparison purposes, all  $K_{zz}$  results were normalized to 55%  $v_F$  by the Kozeny Carman equation. Results are shown in Figure 4.32.

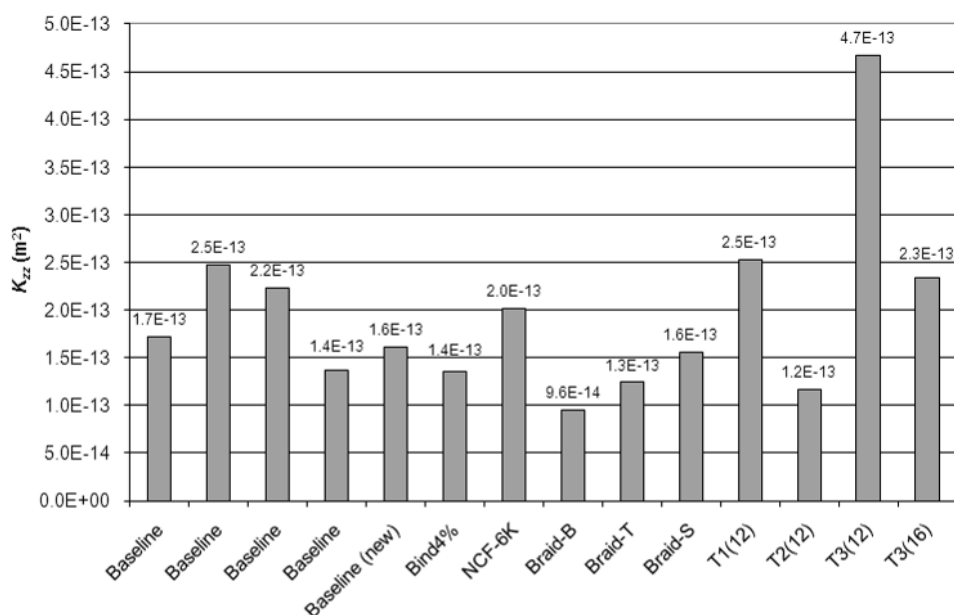


Figure 4.32 -  $K_{zz}$  by infusion, normalized to 55%  $v_F$ .

The 6K NCF was roughly equal in  $K_{zz}$  to the baseline material. The bindered NCF was on the low end of the baseline range; about 77% of the baseline average. This shows only a slight hindrance by the binder, which may be overshadowed by the through-thickness stitching facilitation of through-thickness flow.

The biax braid had the lowest  $K_{zz}$ . The long time to experiment end (50min) means that the viscosity development is compounding the slower flow. The braids have no through-thickness stitching as do all of the NCF's and TFP's, which results in lower relative  $K_{zz}$  [303]. The triax braids are higher; probably due to the increased undulation caused by the standing tows.

The TFP's show higher  $K_{zz}$  values and higher variation than the other materials due to the high stitch density and incorporation of glass fabric (the base layer) into the stack. The measured  $K_{zz}$  was shown to be sensitive to the flow length for low flow lengths, in both UD testing [91] and point-infusion [126]. This was attributed to flow disturbance near the inlet, an effect mitigated as flow distances itself from the inlet. The two lowest of the TFP's, TFP2 and TFP3-16 both had the lowest thicknesses of the study, so there may be significant flow perturbation by the inlet as described in [126,304]. As in [96], the material was examined in all tests for signs of deformation around the inlet, and no visible deformation was observed. But the tacky-tape seal hides the area of fabric immediately around the inlet. And the tows are more loosely held into place in TFP than in NCF's.

The orientation of the flow ( $\theta$ ) was compared from  $K_{xy}$  testing to  $K_{zz}$  testing (Figure 4.33). This comparison was only made for anisotropic materials, and where  $\theta$  was calculated in the  $K_{xy}$  testing. For the in-plane testing,  $\theta$  was chosen from the  $v_f$  closest to that of each  $K_{zz}$  test. The angles match well for the TFP materials, although the NCF materials'  $\theta$  is 10 to 15° farther from the machine stitching axis in the in-plane testing. This may be explained by the significant difference in ply count for the two test methods: 6 layers in  $K_{xy}$  testing and 16 layers in  $K_{zz}$  testing. A reduction in anisotropy with increasing number of plies has been previously reported and is explained by an increase in interface gap flow [300].

The similarity of the flow orientations shows repeatability in both experiments. Comparison of the in-plane permeability values will be addressed in a later section as the capillary pressure and other variables are assumed to cause significant deviations in between the two (Section 5).

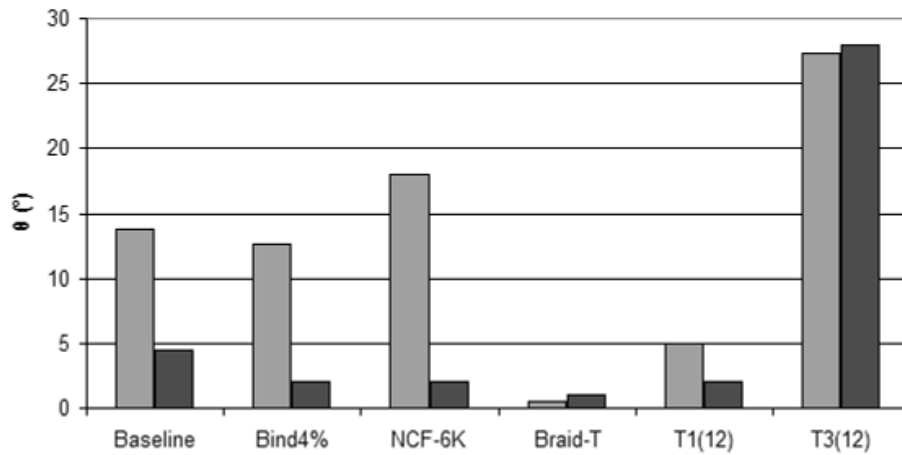


Figure 4.33 - Comparison of  $\theta$  obtained from  $K_{xy}$  testing (blue) and  $K_{zz}$  testing (red).

#### 4.3.4 Validation by variable variation

Interestingly, the solution is the same for any guess in Mathcad of  $K_{zz}$  lower than the solution, so a guess of a low extreme for the permeability ( $1e-16 \text{ m}^2$ ) is used in all cases. Only in cases of high  $K$  (TFP), does this low guess return imaginary number solutions;  $1e-15$  works then.

Any guess slightly higher than the solution also works. But some threshold value is reached as the guess increases past the solution, where the wrong solution is produced by the “Root” function. This signifies a small local minimum in error at the correct solution.

This was illustrated by varying  $K_{zz}$  (and the in-plane  $K$ 's by the ratios) around the solution for the “z2” infusion (baseline). The square root of the square of the error function  $F_z$  (SRSE- $F_z$ ) was plotted in Mathcad against  $K_{zz}$  for a range of  $1e-13$  to  $1e-11 \text{ m}^2$  (Figure 4.34). One can see the local minimum for the solution, and that the curve begins a continual decrease in error towards 0 at  $K_{zz}$  values above this. This peak is extremely small; iterative approaches could easily pass by it and never even see it without very high resolution. And this is probably why solving simultaneously for the 3 variables is so difficult.

To clarify this local minimum, each of the three  $K$  values was varied from the solution while keeping the other two at their solutions. Figure 4.35 illustrates the sum of the squares of the residuals (SSE) for varying each  $K$  value independently. One can see that  $K_{zz}$  by itself actually has a true minimum. But  $K_{xx}$  and  $K_{yy}$  are the ones with the small local minimum.

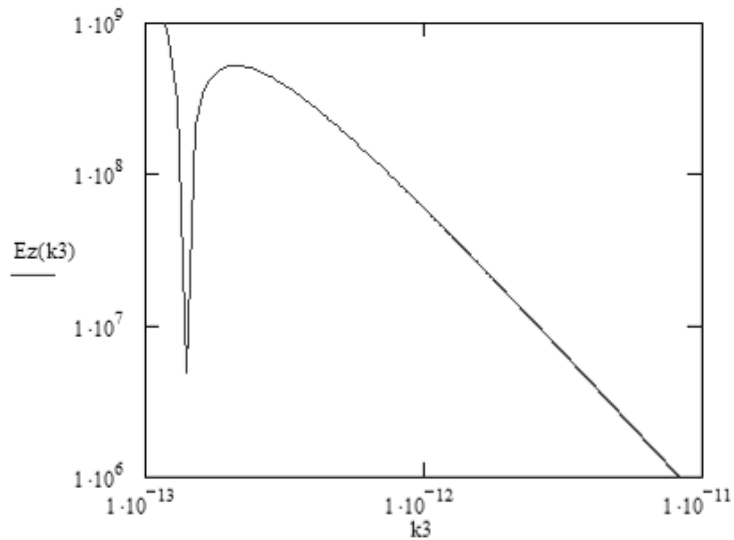


Figure 4.34 - Local error minimum for  $K_{zz}$ .

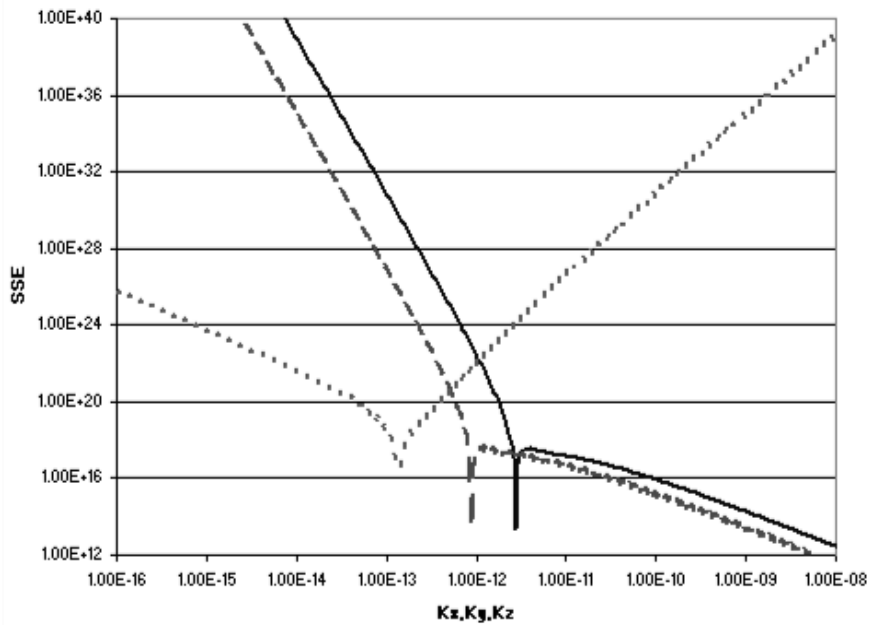


Figure 4.35 - SSE for variation of each variable independently around the solution (solid = varied  $K_{xx}$ , dash = varied  $K_{yy}$ , dot = varied  $K_{zz}$ ).

Both  $K_{xx}$  and  $K_{yy}$  were simultaneously varied then, holding  $K_{zz}$  to its solution.  $K_{xx}$  was varied by 50 values equally spaced around the solution, and 50 similar iterations of  $K_{yy}$  were evaluated at each of the 50  $K_{xx}$  iterations, for 2500 total iterations. The SSE at each of these values is plotted in Figure 4.36 as a function of  $K_{yy}$ . Each of the vertical blue lines represents the variation of  $K_{xx}$  at that value of  $K_{yy}$ . One can still see a small local minimum at the solution and that this local minimum will eventually be surpassed with higher values of both variables.

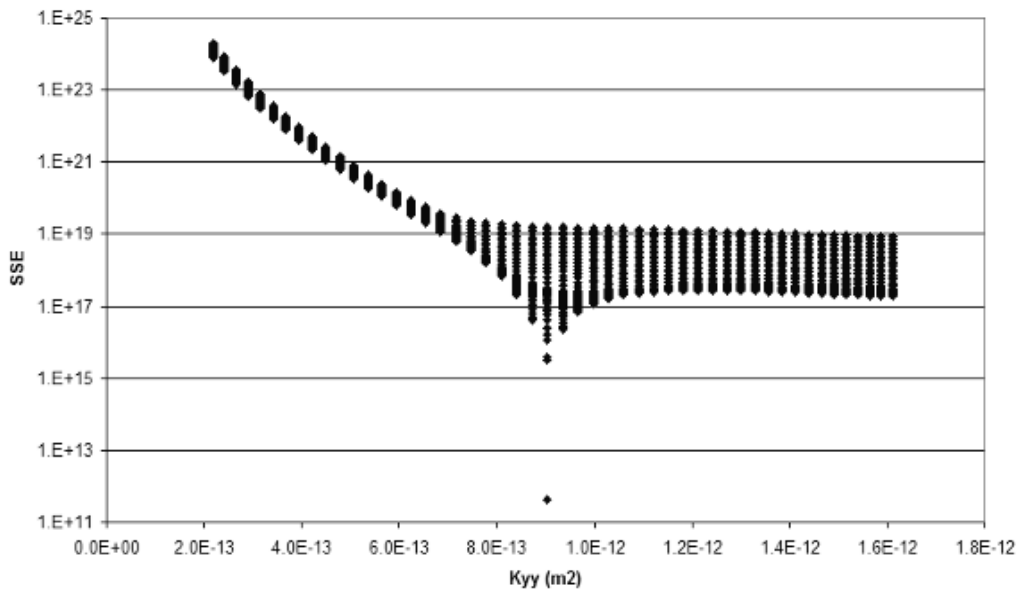


Figure 4.36 - SSE for simultaneous variation of  $K_{xx}$  and  $K_{yy}$  around local minimum.

At high values for both (Figure 4.37), no other local minimums were seen as both variables were increased beyond the range seen in Figure 4.36. SSE continues to converge on 0 as the values are increased. The lowest  $K_{yy}$  value to achieve a lower SSE than the local minimum is  $8.77\text{e-}11 \text{ m}^2$ . But this is only when  $K_{xx}$  is the highest in its variation range, at  $1.95\text{e-}10 \text{ m}^2$ . This permeability value for  $K_{xx}$  is considered too high for this material when compared to the literature, in-plane testing in this study, or any experimental infusions. So any permeability values higher than this are unrealistic, and lower SSE values than the local minimum can be disregarded.

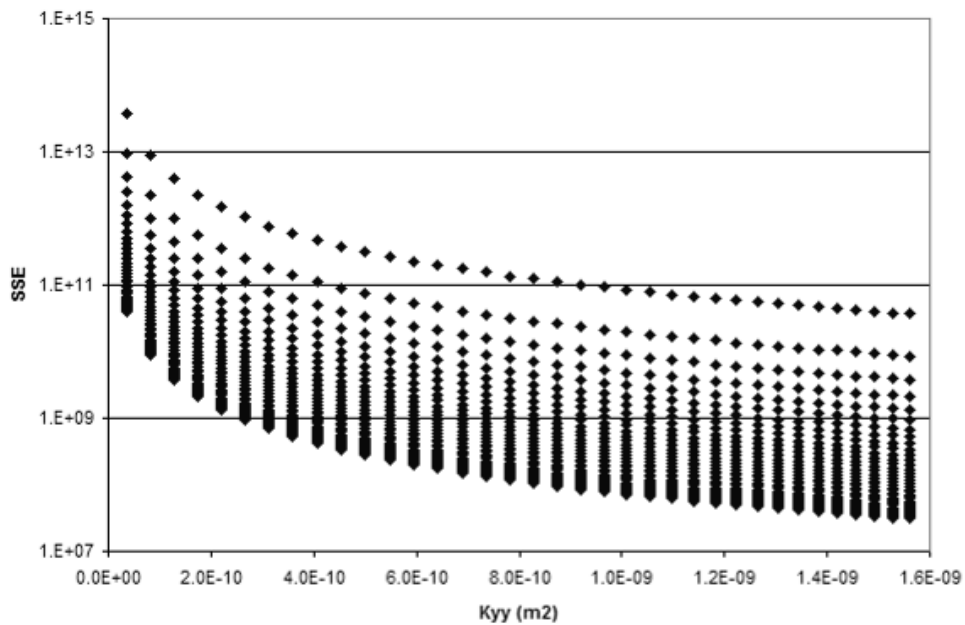


Figure 4.37 - SSE for simultaneous variation of  $K_{xx}$  and  $K_{yy}$  at high values.

Although  $K_{zz}$  is at a true minimum when varied independently, it was also varied simultaneously with the in-plane permeabilities to see if the SSE could be decreased with a different value of it as well as for  $K_{xx}$  and  $K_{yy}$ . The local minimum in Figure 4.36, again with a range in  $K_{xx}$  and  $K_{yy}$  values, was observed to move to the right (increasing  $K_{yy}$  at local minimum) as  $K_{zz}$  was increased. The SSE at that minimum was seen to increase exponentially as  $K_{zz}$  either increased or decreased from the solution (Figure 4.38).

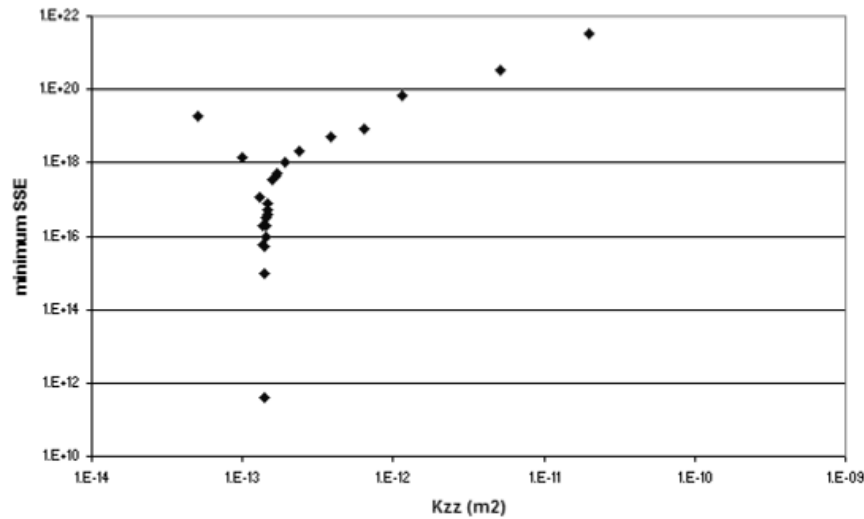


Figure 4.38 - SSE at local minimum vs.  $K_{zz}$  for simultaneous variation of all three  $K$ 's.

The ratio simplification solution has thus been validated to produce the same local minimum as in simultaneous variation of all three variables. Due to its much simpler approach and application, it is presented as the optimum method for  $K_{zz}$  measurement analysis.

#### 4.3.5 Validation by numerical simulation

Because the problem has become much simpler with only one design variable, PAM-OPT was again attempted to fit the flow data to  $K_{zz}$ . A new code was produced that set  $K_{xx}$  and  $K_{yy}$  equal to  $K_{zz}$  times the respective ratios for each iteration of  $K_{zz}$ . The ARSM algorithm successfully fit  $t_z$  to within 0.2% of  $t_G$  at  $K_{zz} = 3.35e-13$ . This permeability is 2.4x higher than the mathematical solution.

A separate simulation in PAM-RTM was run with the mathematical solution ( $K_{zz} = 1.394e-13$  and ratios). The resultant  $t_z$  was 2155 s. This is 2.4x the  $t_z$  from the mathematical solution. Seeing this multiple twice suggested another crossover to 1D Darcian flow basics. As the pressure gradient, porosity, and viscosity are assumed constant, the times could be assumed to be inversely proportional to the permeability at any length. Modifying Equation 2.11:

$$\frac{K_{zz1}}{K_{zz2}} = \frac{t_{z2}}{t_{z1}} \quad (4.12)$$

Thus if the goal  $t_G$  is 900 s and the initial guess of  $K$ 's gives  $t_z = 2155$  s, then the target permeability value ( $K_{zzG}$ ) is:

$$K_{zzG} = \frac{t_z}{t_G} K_{zz} = \frac{2155}{900} 1.394 \cdot 10^{-13} m^2 = 3.338 \cdot 10^{-13} m^2 \quad (4.13)$$

A new simulation run with this  $K_{zz}$  value, and new  $K_{xx}$  and  $K_{yy}$  values adjusted in the same way does in fact result in  $t_z = 900$  s. This validates the application of 1D flow principles to this 3D point-infusion. It also means that PAM-OPT or other optimization algorithms are unnecessary in the case of one design variable and unconstrained flow. In this case, one guess permeability value for  $K_{zz}$  results in a time that can be scaled to any target time by hand calculation. Note that for industrial settings, where flow is constrained by the mold walls for complex shaped parts, this will not apply and software such as PAM-OPT could be useful even in a 1-variable design problem.

Visual inspection of the flow pattern in PAM-RTM with time fitted to 900s shows that the geometry appears to be accurate to the target ellipsoid shape (Figure 4.39). But  $t_x$  and  $t_y$  are significantly larger than  $t_z$  in the Filling\_Threshold.dat file. Quantified,  $t_x$  is 26% higher than  $t_z$ , and  $t_y$  is 124% higher than  $t_z$ .

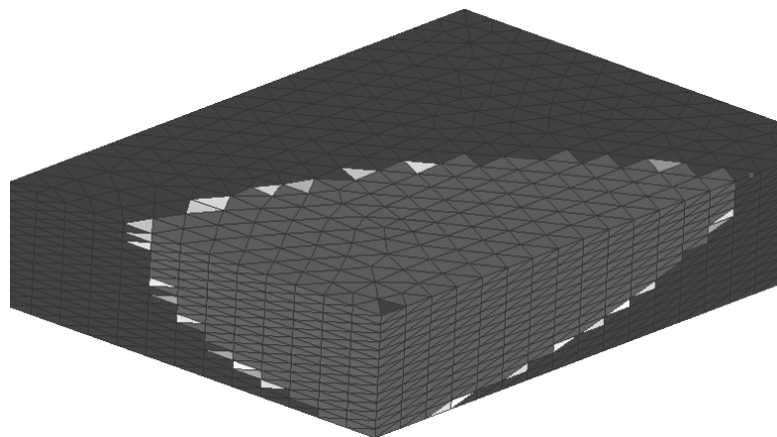


Figure 4.39 - PAM-RTM simulation with  $t_z$  manually fitted to 900 s.

So the simulation in PAM-RTM produces slower flow than the mathematical solution, and the times are not quite the same. These discrepancies between the mathematical solution and simulation are thought to be due to three causes:

- The mathematical solution incorporates pressure loss over the inlet tube, and PAM-RTM does not. But this was already determined to be an insignificant factor in permeability calculation.
- Choice of a finite node in the mesh that is closest to the target radii – no node exists at the exact location. And as the length deviates from the target, permeability and times deviate by the square of the residual in length. So a tiny error in length measurement makes a big difference in time.
- The aspect ratio ( $\lambda$ ) of tetrahedra is inherently wrong for anisotropic media. With non-constant element lengths in any direction, the accuracy of fill times will be decreased in simulation. It is suspected that the  $t_y$  values are inherently higher than  $t_x$  because the average length along the  $y$  axis of the tetrahedra elements is not any lower than the average length along the  $x$  axis. As the flow is slower due to lower  $K$ , they should be smaller.

#### 4.4 Compressibility characterization

[Note: a portion of the experimentation described in this section was performed in tandem with Holger Ahlborn and Mohab ElGhareeb. As they worked on this in pursuit of degrees, these results are presented in their individual theses as well [15, 296].]

The linear pressure gradient in Darcy's Law predicts  $P_R$  along the flow length from  $P_A$  to  $P_V$ . The validity of this linear pressure gradient was tested by three VARI infusions with baseline NCF samples of different lengths along a 1D forced flow direction. An embedded pressure sensor measured the resin pressure  $P_R$  on the bottom of the fabric stack. The location of the sensor along the flow length  $x$  was normalized by the total flow length  $x_f$  and recorded. The pressure for that normalized location should be equal to the predicted  $P_R$  at that normalized location for the same pressure gradient. The pressure at the sensor at the moment the fabric filling is finished is presented in Figure 4.40 along with the predicted pressure gradient for normalized length along flow,  $x/x_f$ .

The closeness of fit is as good as can be with only 3 observations. The compaction pressure can then be predicted for any position along the flow length from the  $P_R$  via Equation 2.18. Deviations due to these dual-scale effects (Section 2.3.6) will be discussed later. In Section 4.2 the in-plane



permeability was modeled for any  $v_F$ . The  $v_F$  is related to the thickness of the preform ( $h$ ) by Equation 2.19. To incorporate thickness changes into flow simulation (Section 5.1), the relationship between  $h$  and the compaction pressure  $h(P_C)$  remains undetermined.

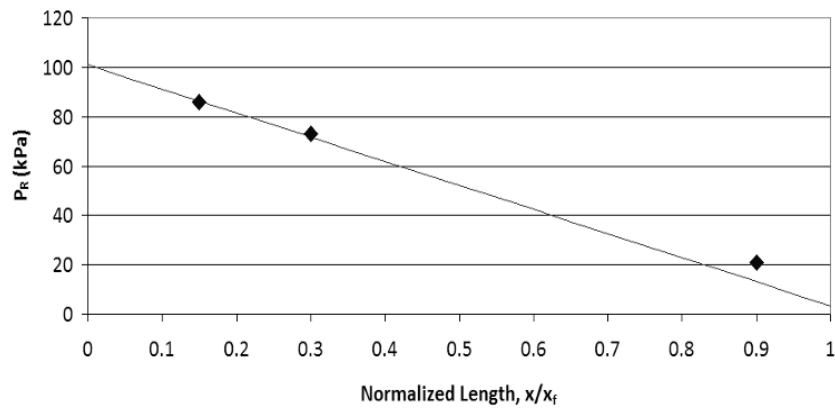


Figure 4.40 - Comparison of Darcian linear  $P_R$  gradient and experimental  $P_R(x/x_f)$  for normalized length along flow.

#### 4.4.1 Experimental procedure

Experiments to characterize most of the materials listed in Section 3 were performed. The number of plies ( $n$ ), ply-to-ply interface orientation, and the amount of binder for the bindered samples is listed in Table 4.7. A nylon mesh distribution media (DM) was also tested (by itself) for compression response. An areal weight of  $0.117 \text{ kg/m}^2$  was measured for each ply of DM, and a density of  $1100 \text{ kg/m}^3$ .

All of the NCF samples were laid-up with parallel stitching. Most were prepared with mirror symmetry of the tow orientations, making the tows perpendicular to each other across ply-to-ply interfaces at every interface except the middle. This is the same configuration used for all the VARI infusion experiments in Section 4.1. Some baseline samples, Baseline-4A, were laid up asymmetrically (A=asymmetric) around the middle plane, with all interfaces having perpendicular tows. Some other baseline samples, Baseline-4L and -8L, were laid up with tows in parallel (L=lined up) across every ply-to-ply interface to see if nesting was promoted in this way.

Samples were cut to  $100 \times 100 \text{ mm}^2$ . Both dry and wet samples were tested. Some samples were wetted by soaking them in rapeseed oil and excess oil was removed by lightly touching with paper towels, similar to [195]. The other wet samples were laid in silicon oil until complete wetting

occurred. Silicon oil was chosen for its excellent wetting of carbon fibers (Section 2.3.4.3) (Figure 4.41). The selection of fluids is listed in Table 4.7 by the abbreviations R (rapeseed) and S (silicon).

Table 4.7 - Materials and lay-up for compressibility testing.

<i>Sample ID</i>	<i>Material</i>	<i>Layers</i> (n)	<i>Replicates</i>		<i>Fluid</i> R / S
			<i>Dry</i>	<i>Wet</i>	
Baseline-2	Biax 12K NCF [(+/-) / (-/+)]	2	2	1	R
Baseline-4	" [(+/-) <sub>2</sub> / (-/+) <sub>2</sub> ]	4	5	4	R / S
Baseline-4A	" [(+/-) <sub>4</sub> ]	4	2	2	S
Baseline-4L	" [(+/-) / (-/+)] <sub>2</sub>	4	1	1	R
Baseline-6	" [(+/-) <sub>3</sub> / (-/+) <sub>3</sub> ]	6	1	1	R
Baseline-8	" [(+/-) <sub>4</sub> / (-/+) <sub>4</sub> ]	8	1	1	R
Baseline-8L	" [(+/-) / (-/+)] <sub>4</sub>	8	1	1	R
Baseline-10	" [(+/-) <sub>5</sub> / (-/+) <sub>5</sub> ]	10	1	1	R
NCF-6K	Biax 6K NCF [(+/-) <sub>4</sub> ]	4	4	2	R / S
NCF-Tri	Triax 12K NCF [(+/-) <sub>2</sub> ]	2	4	3	R / S
Braid-B	Biax Braided	4	4	2	R / S
Braid-T	Triax Braided	3	4	2	R / S
Bind1%-4	Baseline NCF + 1% binder [(+/-) <sub>2</sub> / (-/+) <sub>2</sub> ]	4	4	3	R / S
Bind.5%-4	Baseline NCF + 0.5% binder [(+/-) <sub>2</sub> / (-/+) <sub>2</sub> ]	4	2	2	R / S
T1(12)	TFP – [0] <sub>12</sub>	1	4	2	R / S
T1(16)	TFP – [0] <sub>16</sub>	1	1	1	S
T2(12)	TFP – [(0/90) <sub>3</sub> ] <sub>5</sub>	1	4	4	R / S
T3(12)	TFP – [0/0/0/90/0/0] <sub>5</sub>	1	2	2	R / S
DM-1	Distribution Media - nylon mesh	1	1	1	R
DM-5	Distribution Media - nylon mesh	5	1	1	R

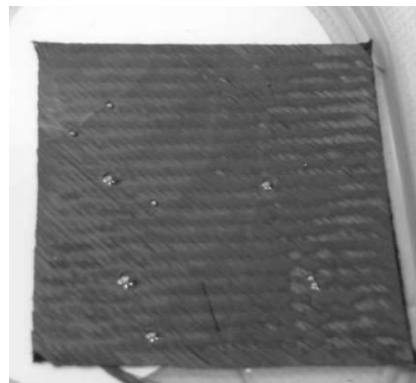


Figure 4.41 - Thorough wetting of carbon fabric by silicon oil.

Testing was done using a Schenck Trebel testing machine to monitor the pressure response (Figure 4.42). An attached extensometer monitored the thickness throughout the testing.

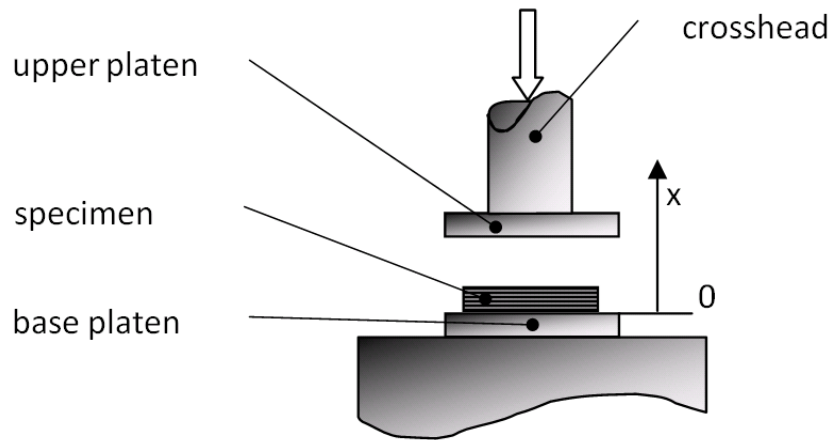


Figure 4.42 - Test Setup for Compressibility Measurement.

The viscoelasticity of carbon fabrics suggests that the compression response would depend on the speed of compaction [44,91]. Although the speed of compaction has a negligible effect on the dry compression (elastic), the wet relaxation is dependent on the speed (viscoelastic) [43,305]. Very low speeds show more viscoelasticity than high [176]. Slow speeds were chosen for the wet relaxation, to match the time it takes for the resin pressure to move through the cavity.

The testing cycle was chosen to mimic the preform compression in VARI (Section 2.3.4.2). An initial compaction was conducted at 0.5 mm/min to 100 kPa. A subsequent holding-step was controlled in one of two ways:

1. For the rapeseed oil-wetted samples and all dry samples, the cross-head was held there (constant thickness) to allow pressure decay to reach an equilibrium pressure. This is the simplest method, as a testing machine naturally records the pressure at a cross-head position or constant rate of movement.
2. For the silicon oil-wetted samples, the pressure was maintained at 100 kPa by manually toggling the compression on/off until an equilibrium thickness was reached. This is more difficult to implement as the pressure changes rapidly, and so the pressure in each test fluctuated around 100 kPa in actuality. Some type of digital controller might minimize the fluctuation. But it was usually kept within  $\pm 5$  kPa (5%). This method is more accurate to the VARI process as the atmosphere exerts a constant  $P_A$  on the bag and rearrangement of fibers continues to decrease  $h$ .

After the holding-step, the fabric was unloaded (expansion) at a rate of .2 mm/min until there was no significant pressure response. A 2<sup>nd</sup> compaction to 100 kPa was then performed, allowed up to 1 minute in a holding-step, followed by relaxation, followed by a third compaction to 100kPa, followed by a final minute-long holding-step. The typical experimental  $P_c(t)$  profile for each type of holding-step is shown in Figure 4.43. The difference between the unloading curves following the holding step at constant  $P$  (decreasing thickness) and constant thickness (decreasing  $P$ ) is assumed to be negligible.

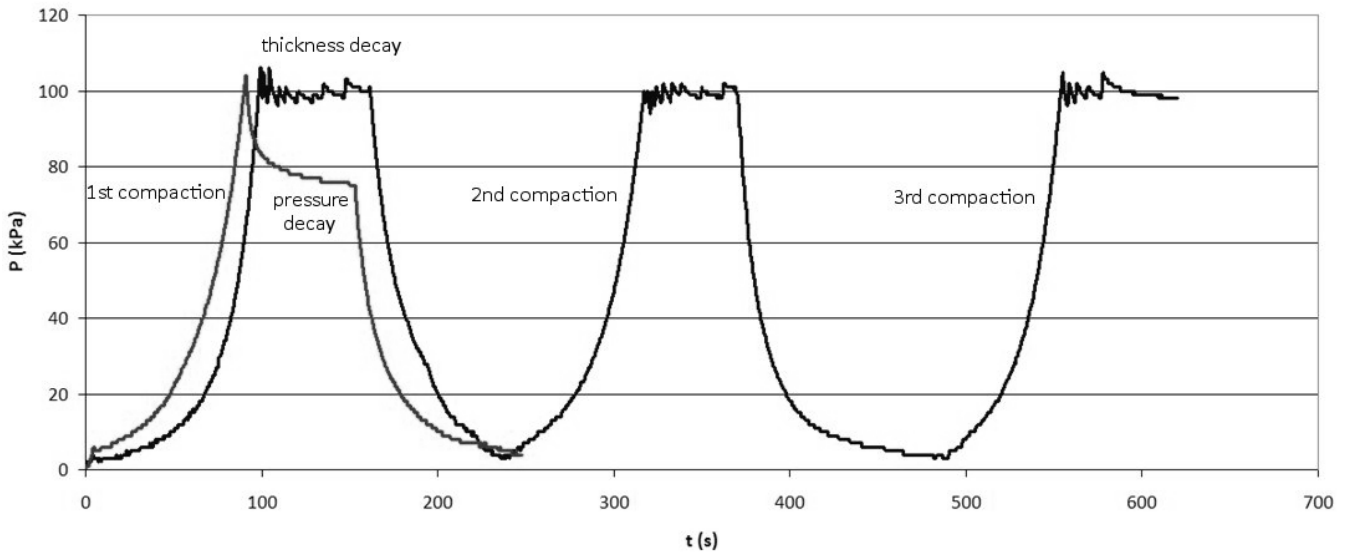


Figure 4.43 - Example  $P(t)$  graph for compressibility study (baseline wet): constant pressure at hold (dark), constant thickness at hold (light).

It is difficult to pinpoint the exact point where the pressure response becomes greater than 0. Difficulties with measuring the initial  $v_f$  at low pressures with accuracy or precision have been reported elsewhere [291]. The average thickness over all measurements recorded at 2 kPa was assumed as the initial thickness of the sample in this study. It is also difficult to determine where the pressure response ends, i.e. when the sample no longer pushes back on the cross-head. Thus, the average thickness for measurements at 2 kPa was again assumed, this time as the final thickness in expansion.

#### 4.4.2 Results

The pressure on the dry samples during expansion fit fairly well to a power law function of the  $v_f$ . The wet samples' pressure did not. A comparison between the two and their best power law fits is given in Figure 4.44. A power law does not adequately describe the high rigidity at the higher  $v_f$

values. As most of the preform is at the highest levels of  $v_f$  during infusion, this is the most important degree of compaction for flow modeling.

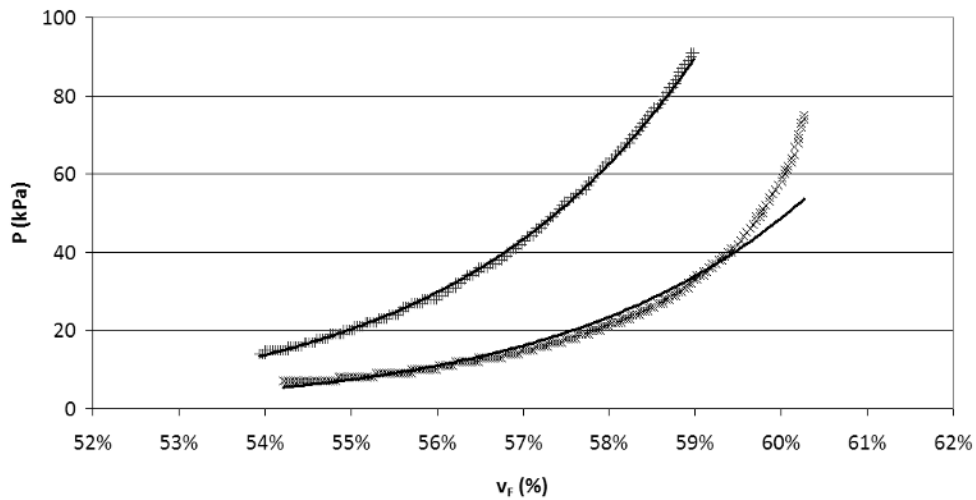


Figure 4.44 - Baseline 4 layer symmetric in relaxation: wet (x) and dry (+), and power law fits to each (black).

Figure 4.44 also illustrates the pressure response difference between dry and wet fabrics. The wet samples show much less rigidity (more compliance), requiring less pressure to get to the same fiber volume as the dry sample.

As mentioned in Section 2.3.4.4, the Grimsley model for wet expansion is used in this study's compressibility modeling. A perfect fit for the wet 4-layer baseline expansion is shown in Figure 4.45, in contrast to that of the power law for the same data in Figure 4.44. As flow simulation should only rely on the wet expansion of fabrics, modeling of the compression (decreasing thickness) is not reported here, only the expansion. The Grimsley model only requires one value from the dry fabric: the initial dry fiber content  $v_{F0}$ . This is measured in dry compression by the height of the preform at the moment of first pressure response. Thus, most reported data in this study will be from testing of the wet fabrics.

Three modes of compression were defined for textile reinforcements [170]. Initial linear preform compaction is primarily due to the reduction of pores and gaps among the fibers and yarns, while a third linear mode is dominated by the bending deformation of yarns. In between is exponential compaction from a combination of the two. These three modes can be seen in Figure 4.45, where the very highest pressures are crossing over into the third mode of linear compression response.

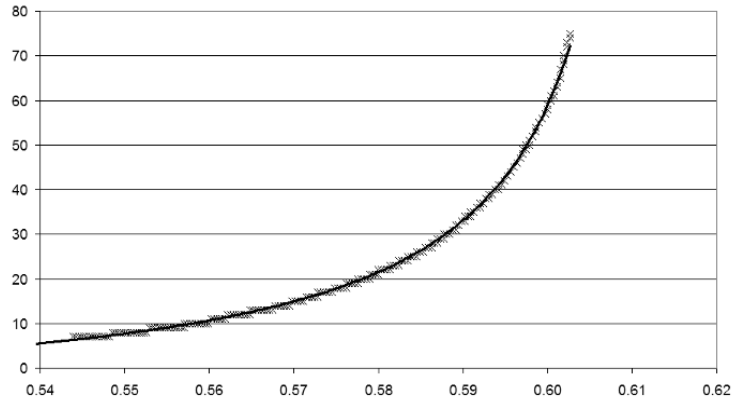


Figure 4.45 - Grimsley model fit of wet relaxation for baseline 4-layer stack: experimental (x) and model (solid line).

The characterization data collected includes:

- Fitted constants for the Grimsley model for each wet expansion cycle.
- Viscoelasticity:
  - Change in maximum  $v_F$  (at 100 kPa) and minimum  $v_F$  through the debulking cycles.
  - Characterization of the pressure/thickness decay from beginning to end of hold time.

The Grimsley wet-expansion model was fitted to the first and second wet expansion curves for each material. If Equation 2.20 and 2.21 are combined and solved for the  $v_F$ , a model is generated with these constants to predict  $v_F$  at any local  $P_C$  in flow simulation:

$$v_F = \frac{v_{F0}}{1 - \left[ a_w + b_w \left( \frac{P_C}{c_w + P_C} \right) \right]} \quad (4.14)$$

To compare the compression response of each material, the modeled  $v_F$  was calculated at a nominal  $P_C$  of 100kPa for each.

#### 4.4.3 Fluid differences

Comparison between the two wetting fluids shows consistently lower predicted  $v_F$ 's for rapeseed-oil wetted samples. Figure 4.46 shows the  $v_F$  at 100 kPa for all the materials where tests were done with both fluids. The  $v_F$ 's for the silicon oil experiments are the average of all replicate tests for that material along with standard error bars. The rapeseed-wetted experiments (no replicates for each) predicted  $v_F$ 's from 8 to 20 % lower than the silicon-wetted ones.

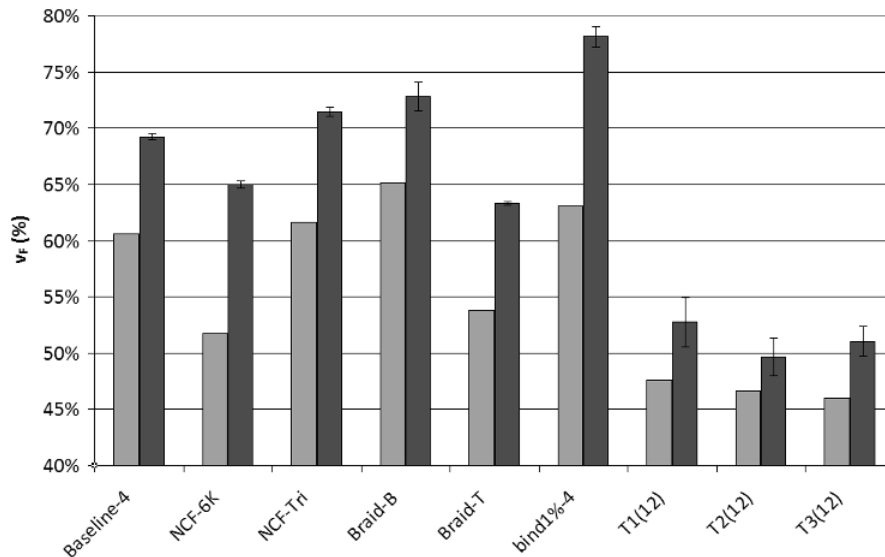


Figure 4.46 - Predicted  $v_f$  at 100 kPa for rapeseed-wetted (light) and silicon-wetted (dark) samples.

This implies higher rigidity in the rapeseed-wetted samples. This is most likely due to incomplete wetting of the fabric. The rapeseed oil, with contact angles on carbon of greater than 0 cannot fully wet every air pocket in the timeframe of the experimentation. The silicon oil has wetted the fabric significantly more and the increased lubrication and lower surface tension allows the fibers to re-arrange more into a very compact fabric. This was evidenced by the significantly higher  $v_f$ 's in the silicon-wetted samples at every milestone of the test cycle. For example, the measured  $v_f$  at the first instance of 100 kPa in the first compaction for rapeseed wetted baseline-4 was 60%, but 67% for a silicon wetted sample.

The goal of resin infusion is complete wetting, which would suggest that the silicon-oil wetted data is more applicable to RI flow modeling. But all  $v_f$  values for that data seemed very high compared to typical values for RI.

This was confirmed by a set of validation VARI infusion experiments to confirm the maximum and minimum  $v_f$ 's, corresponding to maximum and minimum  $P_C$ , respectively. Four different 100 x 100 mm<sup>2</sup> baseline NCF stacks ( $n = 4$ ) in the default symmetric lay-up were infused with the 235R/236R mix epoxy.  $P_V$  was 3 kPa and  $P_A$  was 99.5 kPa (dry  $P_C = 96.5$  kPa) during the infusion. Once filled, vacuum pressure was applied to the resin pot in 2 of the four lay-ups, to equalize the entire part thickness to the  $v_f$  at the max  $P_C = 96.5$  kPa. The other two infusions, once filled, were opened to the ambient air by making a small incision in the vacuum bag. This allowed the material to expand back to  $P_C = 0$ .

For the infused samples at ambient pressure, the thicknesses at both inlet and vent should correspond to the minimum  $v_F$ ,  $P_C = 0$  in the first wet expansion curve. The two samples kept at full vacuum pressure should have thicknesses corresponding to:

- By the vent: the first wet expansion curve at 96.5 kPa (after thickness decay), as no resin pressure has increased the thickness along the expansion model curve.
- By the inlet: the second wet expansion curve at 96.5 kPa (after thickness decay), as resin pressure has relaxed the saturated fabric to  $P_C = 0$ , then full vacuum was applied to the vent, compressing it a second time.

Thus, the samples at full vacuum should measure in thickness somewhere between these two predictions. The difference between these two predictions is only 1%  $v_F$ , so the average was calculated and applied to the full vacuum samples.

Light microscopy was used to optically measure the thickness along the length of each infused part at every 2mm. The choice of this procedure will be described later in this work (Section 6.1). To compare the cured thicknesses to the uncured wetted thicknesses, Equation 2.25 was used to correct the wetted  $v_F$  to its cured equivalent given an assumed 6% shrinkage. A comparison of the predicted values to the experimental values is given in Figure 4.47. The experimental measurements showed very little variation, as evident by the small error bars.

For the maximum pressure conditions, the rapeseed-wetted prediction is very close to the experimental result. The silicon oil wetted sample shows a higher  $v_F$ . For the minimum pressure conditions, the experimental results were much lower than either of the predictions. As already mentioned, low pressures are difficult to model due to the difficulty of picking up the first pressure response with the testing machine. But the rapeseed wetted prediction is closer in this case as well.

This must imply that the resin wetting of the fabric in VARI follows phenomena more similar to the rapeseed oil wetting than the silicon oil. The void content is minimized in an optimized VARI process, but never removed [244]. The contact angle for epoxy on carbon has been shown to be higher than zero [236], thus not as good as a wetting fluid as silicon oil. The higher surface tension ( $\gamma$ ) of DGEBA epoxy (47 mN/m) and organic oils such as rapeseed oil (~30 mN/m) when compared to silicon oil  $\gamma = 16$  to 19 mN/m) may contribute to this [237, 306].



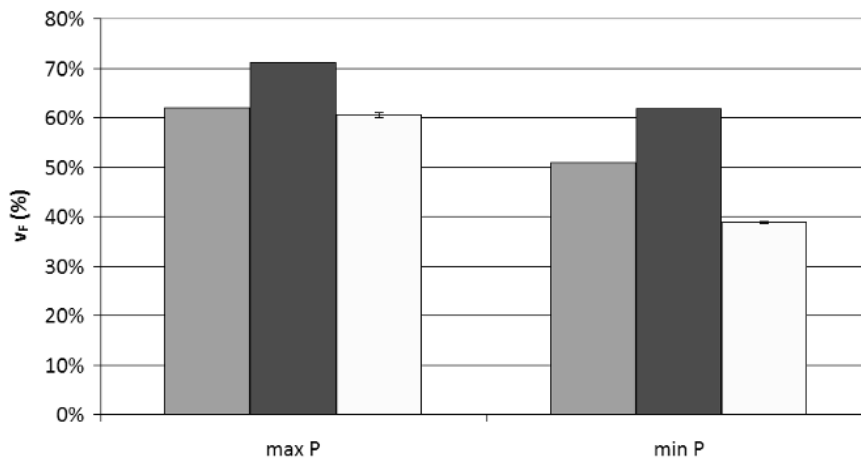


Figure 4.47 - Comparison of predicted and experimental  $v_F$  for max  $P$  (96.5kPa) and min  $P$  (0): rapeseed-wetted (gray), silicon-wetted (black), and experimental (white).

Both compressibility models were then compared to the measured  $h$  from the VARI infusions in Section 4.1. The thickness  $h$  was measured at regular intervals along the part length by optical microscopy.  $P_V$  for these infusions was 3 kPa, and  $P_A$  was  $\sim 100$  kPa, resulting in a max  $P_C = 97$  kPa. Vacuum pressure of 30 kPa was applied post-filling to both the vent and the resin pot after infusion (max  $P_C = 70$  kPa). If the resin viscosity remains sufficiently low, the thickness of the part should be equalized to this  $P_C$ . The resin was gelling rapidly before most parts were filled. The middle of each part thus ended up being slightly thicker than the ends where the vacuum pressure was applied. The resin was too viscous to fully distribute the pressure. The maximum difference in the calculated  $v_F$  from the middle to the ends was about 5%  $v_F$ .

The ends at 70kPa were compared to the model predictions. The average  $v_F$  was calculated from all  $h$  measurements along the first 25% of the part length (by inlet) and second 25% part length (by vent) and compared to the compressibility model's prediction for this  $P_C$ . The preform by the inlet has undergone full unloading and then subsequent compaction to 71 kPa (2<sup>nd</sup> wet compression). By the vent it has only been unloaded from 98 to 71 kPa (first wet expansion).

Results are shown in (Figure 4.48). A slightly lower fiber volume was measured in all cases by the vent. This is most likely due to the higher speed of compression not allowing the fibers to re-arrange as they do during the slow movement in expansion. In all cases but 2, the rapeseed-oil based model seemed to fit the experiments better. For the NCF-6K and the triax braid, the silicon oil model fit better. Whether this is due to wetting differences or experimental error during those tests, this suggests using the rapeseed model in all but these 2 fabrics for flow modeling efforts.

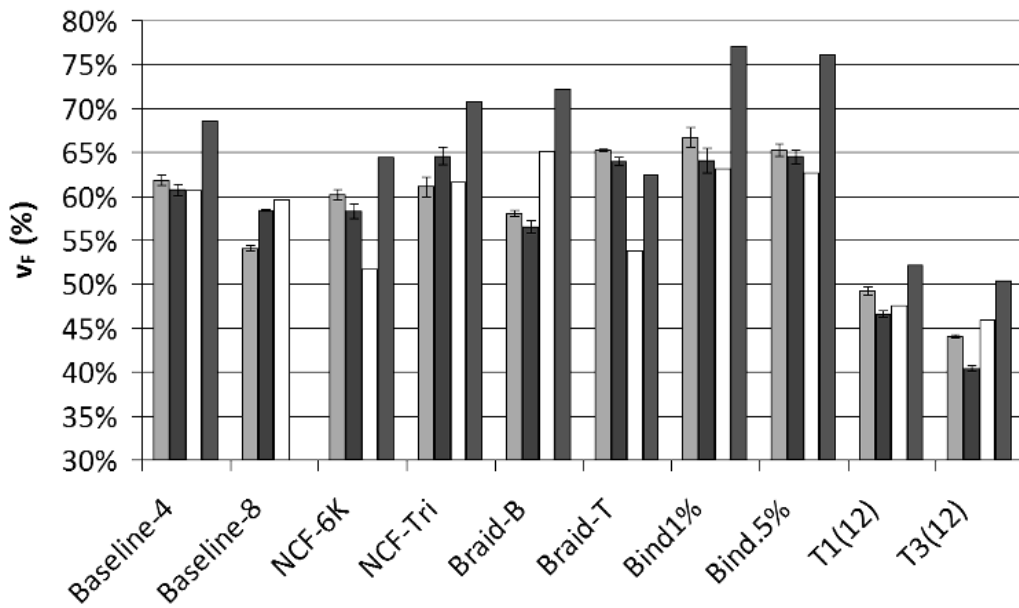


Figure 4.48 - Measured and predicted  $v_F$  at 70 kPa (light gray: measured by inlet, black: measured by vent, white: rapeseed model, dark gray: silicon model).

#### 4.4.4 Comparison of materials

All of the fitted constants for the Grimsley expansion model for each material, and for both rapeseed-oil samples and silicon oil samples are listed in Appendix 4. The predicted  $v_F$  at 100 kPa, wetted with rapeseed oil, for each material from these constants is shown in Figure 4.49.

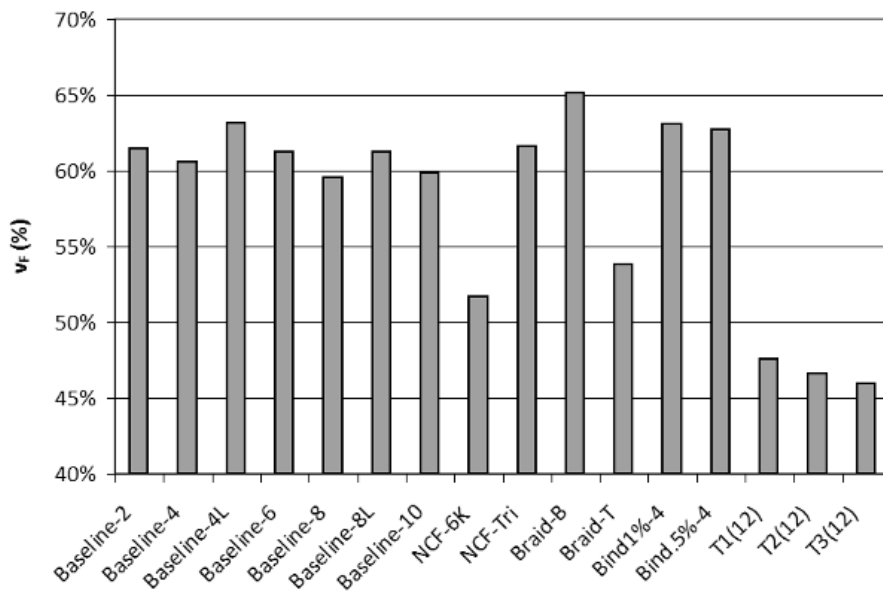


Figure 4.49 - Average by material of predicted  $v_F$  at 100 kPa for rapeseed-wetted samples.

Averaged constants for both the first and second expansion cycles for the silicon oil wetted samples were calculated as well. The predicted  $v_F$  at 100 kPa from these averaged constants is shown in Figure 4.50. Note that the calculated  $v_F$  from applying the model to the average constants is no different from the averaged  $v_F$  from models based on each replicates' constants. No error bars denotes no replicates for that sample. Note that the Grimsley model constants for the second expansion model are based on the minimum strain in the second expansion, but the initial dry  $v_{F0}$  is taken from the uncompressed fabrics. The  $v_{F0}$  value for a once compressed-and-relaxed fabric would be more accurate. But this showed little effect on the goodness of fit for the second expansion.

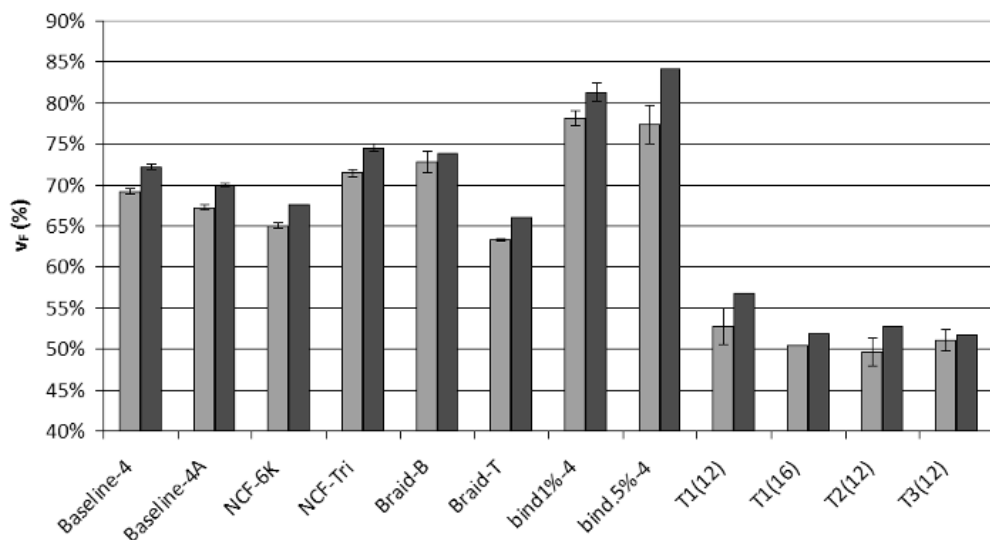


Figure 4.50 - Average by material of predicted  $v_F$  at 100 kPa for silicon-wetted samples: first expansion (light), second expansion (dark).

Comparing Figures 4.49 and 4.50, trends were similar between the two wetting methods. The T1(12) material, with all parallel tows, shows a slightly higher maximum  $v_F$  than the other T2(12) (all perpendicular) or T3(12) (some perpendicular). This indicates another expected increase in nesting due to aligned tows. Perpendicular tow arrangements should be more compliant (less stiff) than aligned tow arrangements [168,175]. But aligned fibers allow for more nesting, thus more re-arrangement and a higher maximum  $v_F$ . This is similar to the difference between the more compliant dry fabric and the stiffer, but higher nested wet fabric (Figure 4.44).

The TFP materials naturally showed low  $v_F$  values due to the carbon-only basis of calculation and the high amount of glass and stitching present. Similarly, adding binder to the material increased the compacted thickness (and lowers the  $v_F$ ) due to the addition of non-carbon binder material.

But the binder decreased the fabric compliance by impeding tow re-arrangement. This outweighs the increase in thickness and a shift in the curve towards slightly higher  $v_F$ 's was seen in comparison to the non-bindered NCF (discussed further in [15]). This is evident in the very high maximum  $v_F$ 's in both Figures. Similar effects of binder application have been reported [285]. As with the in-plane permeabilities, there seems to be little difference in compressibility between different amounts of binder.

Note that the bindered NCF's must be compacted during preforming to apply and consolidate the binder [15]. This implies one more dry debulking cycle than the non-bindered materials. The compression response and subsequent hysteresis observed in these measurements corresponds to the second compression cycle and not the first as in the other materials. This probably contributes to the increase in max  $v_F$  from unbindered NCF's.

Upon examination of all baseline materials, a few distinctions are seen (Figure 4.51). First, the rapeseed oil-wetted stacks of different layers showed some dependence of the predicted  $v_F$  at 100 kPa on  $n$ . But despite the variation around  $n$ , all the rapeseed oil-wetted stacks were consistently lower in the predicted  $v_F$  at 100 kPa than the silicon oil-wetted stacks of four plies. All observations were lumped within each liquid treatment and a  $t$ -test for difference in the mean between rapeseed-wetted samples and silicon-wetted samples confirmed a 100% probability of difference at a 95% confidence level.

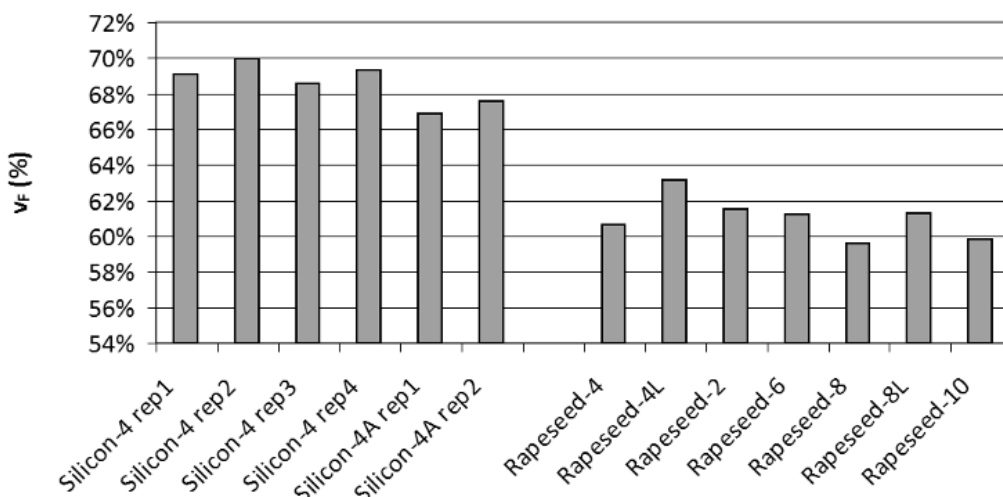


Figure 4.51 - Predicted  $v_F$  at 100kPa pressure for all baseline samples (“rep” = replicate).

The effect of ply-to-ply interface orientation was investigated by comparing the Baseline-4L and Baseline-8L samples against their default lay-up counterparts. The default lay-up for the baseline

material has the middle interface with parallel tows, but the other interfaces have perpendicular tows. The aligned samples (-4L and -8L) have the tows across every interface in parallel. This is thought to facilitate nesting in compression. Figure 4.52 shows a comparison of the default and aligned configurations. In both cases, the slight increase in  $v_F$  agrees with increased nesting.

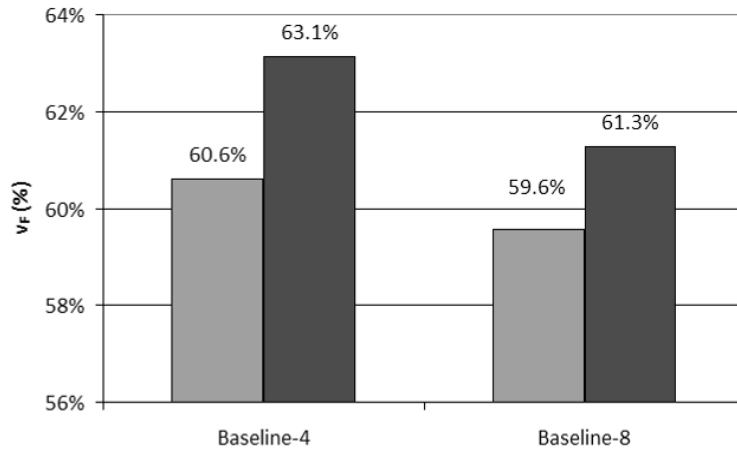


Figure 4.52 - Predicted  $v_F$  at 100 kPa for symmetric lay-ups (light) and asymmetric lay-ups (dark).

A slight increase in rigidity was seen with increase of  $n$  from 2 to 10, as previously reported [43,176]. Figure 4.53 shows the  $v_F$  at 100 kPa for each of the oil-wetted Baseline samples of default lay-up orientation. The Pearson Correlation Index was calculated to statistically quantify the relationship between  $n$  and the predicted  $v_F$ . The resultant value of -0.818 indicates a strong inverse relationship (-1 being a perfectly linear inverse relationship). Both number of plies and alignment of interface tows only result in a difference of less than 3%  $v_F$  for this tested range of  $n$ .

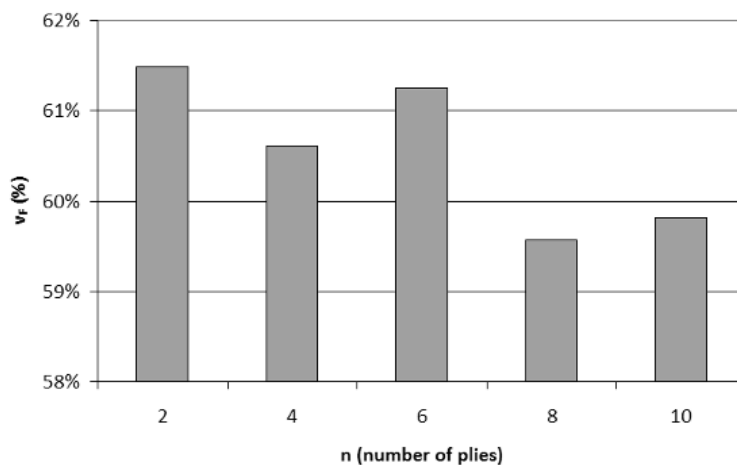


Figure 4.53 - Comparison of  $v_F$  at 100kPa for number of plies (baseline rapeseed-wetted).

Examination of the two asymmetric baseline samples (“-4A”) in Figure 4.51 shows slightly lower  $v_F$  than the default symmetric lay-ups (“-4”). This makes sense as the only difference between the two is that the asymmetric lay-ups have all interfaces with perpendicular tows. The default lay-ups have all but the middle interface with perpendicular tows. The one layer of parallel tows enhances nesting by a slight amount. A  $t$ -test for the difference in means gives 93% probability at the 95% confidence level, a statistically significant difference.

The compression response of the distribution media showed similar curves to the fabrics. The increase of layers from 1 to 5 resulted in a less rigid response however, opposite to the above trend. The Grimsley model provided a good fit to the DM as well (Figure 4.54).

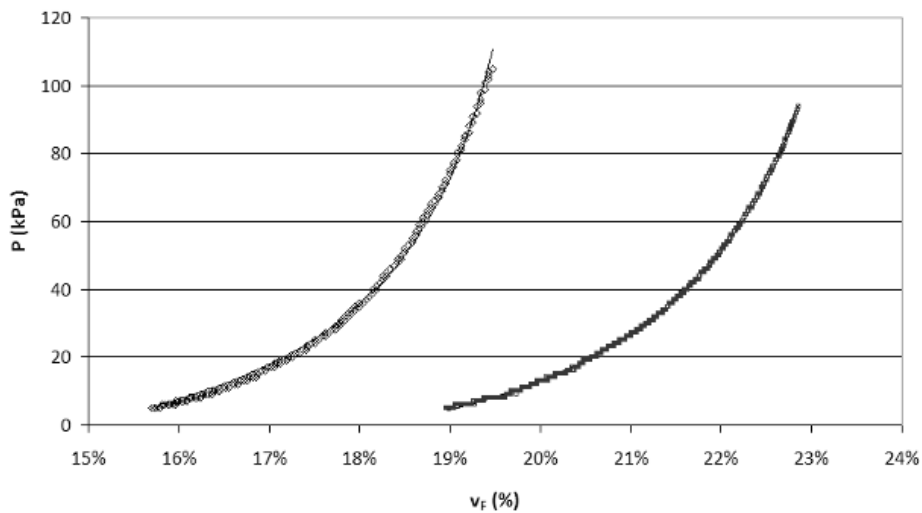


Figure 4.54 - Pressure response of DM: 1 layer (left) and 5 layers (right), with Grimsley model for each (solid lines).

#### 4.4.5 Viscoelasticity

The materials in Figure 4.50 exhibit viscoelastic behavior in that the  $v_F$  at maximum pressure has increased from the first compression cycle to the 2<sup>nd</sup>. To clarify, Figure 4.55 shows the hysteresis over the first three wet compression/relaxation cycles for a silicon-wetted triax braid.

The viscoelasticity of these materials was quantified by comparing the difference from initial minimum  $v_F$  before compaction, to the minimum  $v_F$  after expansion. The percentage increase in minimum  $v_F$  for each sample wetted with silicon-oil is shown in Figure 4.56. Many of these carbon fabrics exhibited a 50% increase in minimum  $v_F$  after the first compaction-unloading cycle. While the second cycle showed subsequent increases of only ~10%. Note that this metric is a direct

comparison of the minimum  $v_F$ 's, which as stated earlier, is difficult to measure with accuracy in a testing machine.

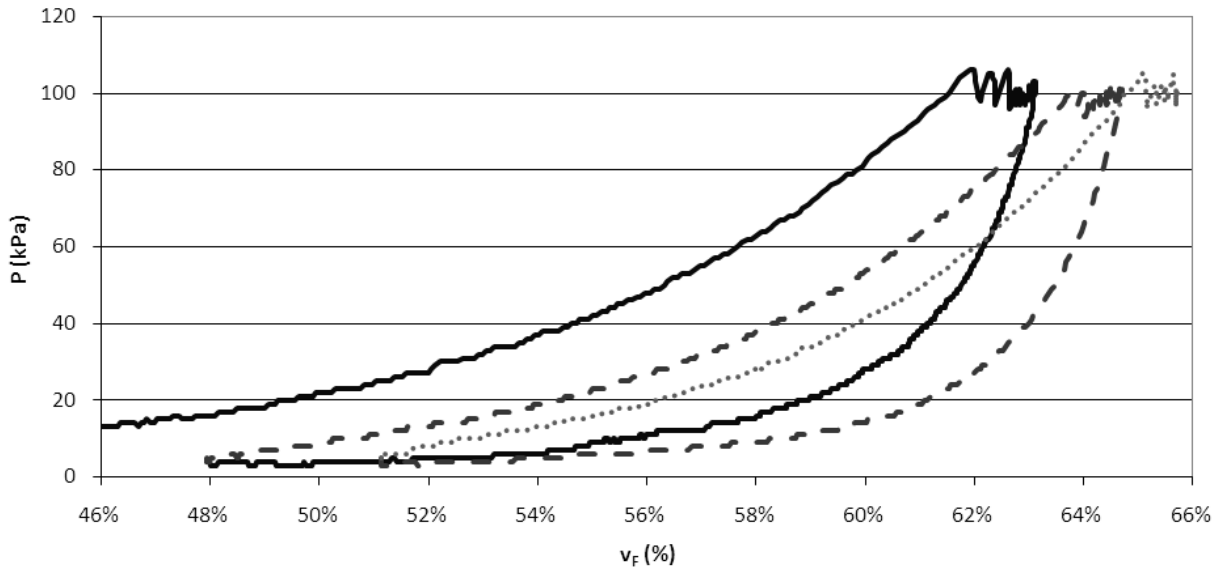


Figure 4.55 - Viscoelastic  $v_F$  of triax braid: 1<sup>st</sup> cycle (solid), 2<sup>nd</sup> cycle (dashes), 3<sup>rd</sup> cycle (dots).

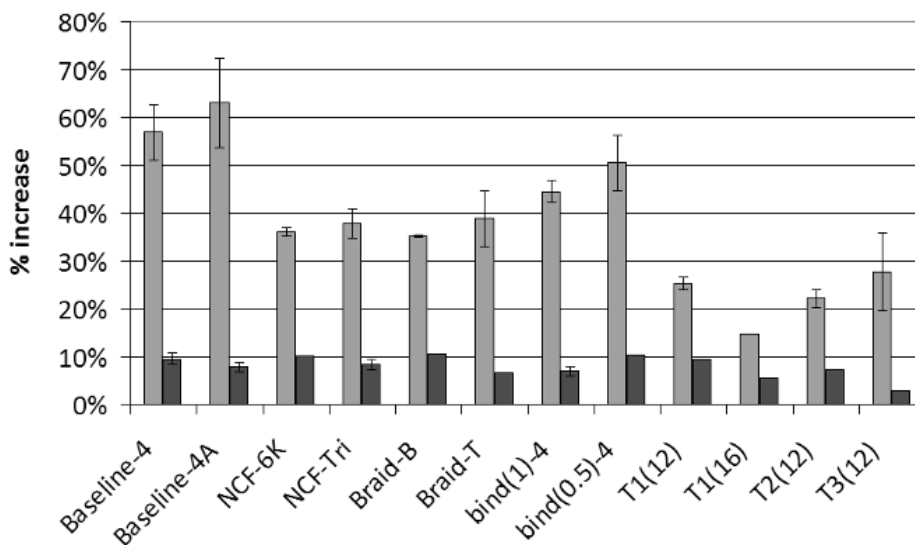


Figure 4.56 - Viscoelasticity in compaction/expansion cycles: % increase in  $v_F$ -min (light: 1<sup>st</sup> cycle, dark: 2<sup>nd</sup> cycle).

Another metric of the viscoelasticity is the change in thickness during the thickness decay of the constant-pressure holding-steps. This metric should be more precise than the last, as it relies on measurements of thickness at high pressures. The viscoelasticity was quantified by comparing the percent increase in  $v_F$  over the time of the holding-step for the silicon-oil wetted samples (Figure 4.57). As reported elsewhere [177,182], the change in thickness quickly decreases with each cycle

for all materials. The thickness change for first holding-step of 3 to 5 % for the both braids compares well with 3.4 to 3.8 % reported for the similar architecture of carbon weaves [195]. There seems to be an inverse relationship between the compliance of the fabric and the degree of decay. The most compliant materials (TFP's and braids) show the lowest decay while the stiffest (bonded NCF) show the highest.

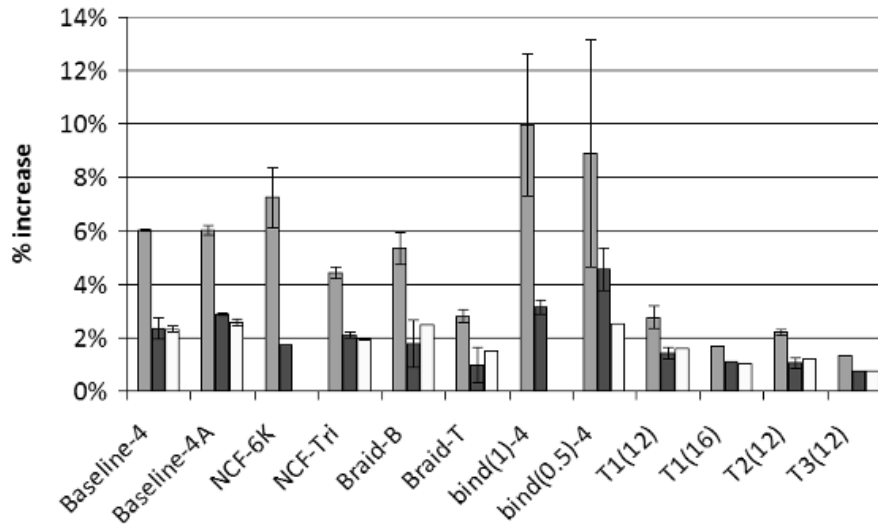


Figure 4.57 - Thickness decay: % increase in  $v_F$  (gray: 1<sup>st</sup> cycle, black: 2<sup>nd</sup> cycle, white: 3<sup>rd</sup> cycle).

Note that debulking cycles while wet instead of dry (as is customary) should result in a different hysteresis. It is assumed that the lubrication in wet fabrics assists in the debulking fiber re-arrangement, thus magnifying the effects of debulking. Therefore, this data covers a greater span of degree of debulking given the same amount of cycles, although it cannot be applied as an absolute value for industrial dry debulking.

#### 4.4.6 Maximum fiber content

A number of the samples were rapidly compressed to 5 MPa after the recorded compression and relaxation cycles. This was to determine the maximum possible  $v_F$  with all fibers nested to the maximum degree (Figure 4.58). A critical pressure where no further  $v_F$  increases can be achieved has been reported [45,80]. Some samples were measured close to 100%  $v_F$ ; it seems that some extra movement of the cross-head is being detected even when the sample itself cannot become any thinner. But the average of ~80 to 85 % is a logical maximum  $v_F$  given hexagonal packing limits.



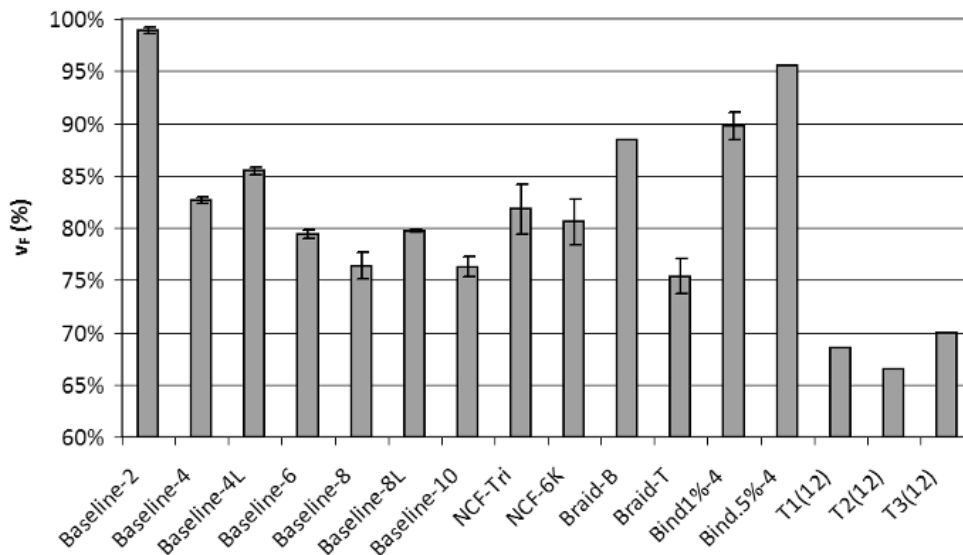


Figure 4.58 - Maximum  $v_F$  at 5 MPa pressure.

#### 4.4.7 Model validation

A 250 mm long TFP1 sample of 12 layers was infused with the RIM235 mix epoxy in VARI 1D flow along the aligned UD tows. This material was specifically chosen for its high permeability compared to the other materials. This was to minimize the dual scale effects from low flow velocity. The resin was continually bled through the part until it cured, so that the full VARI pressure gradient would be “frozen” into place. The  $v_F$  was measured along the flow length of the cured part at 1 mm intervals except for a gap in the middle from sample cutting. The results are presented in Figure 4.59 along with the rapeseed model for this material, corrected for 6% cure shrinkage (as per Section 2.3.4.7). The low pressure area by the inlet seems to be slightly over-estimated for  $v_F$ , probably due to the precision problems at low pressure. But otherwise, the model seems to fit well.

Two baseline NCF stacks (200 mm, 4 layers) were also infused in the same way, with flow forced along the stitching. The gradient was again frozen into place by bleeding resin until cured. The experimentally determined  $v_F$  at regular 4 mm intervals along the flow length, as well as the rapeseed model prediction corrected for 6% cure shrinkage are presented in Figure 4.60.

Again, the fit is good near the vent. But the area by the inlet is over-estimated. In this case, however, this was due to resin pooling under the vacuum bag by the inlet, as described in Section 4.1. The baseline fabric has a lower permeability than the TFP material, and thus was more susceptible to this phenomenon.

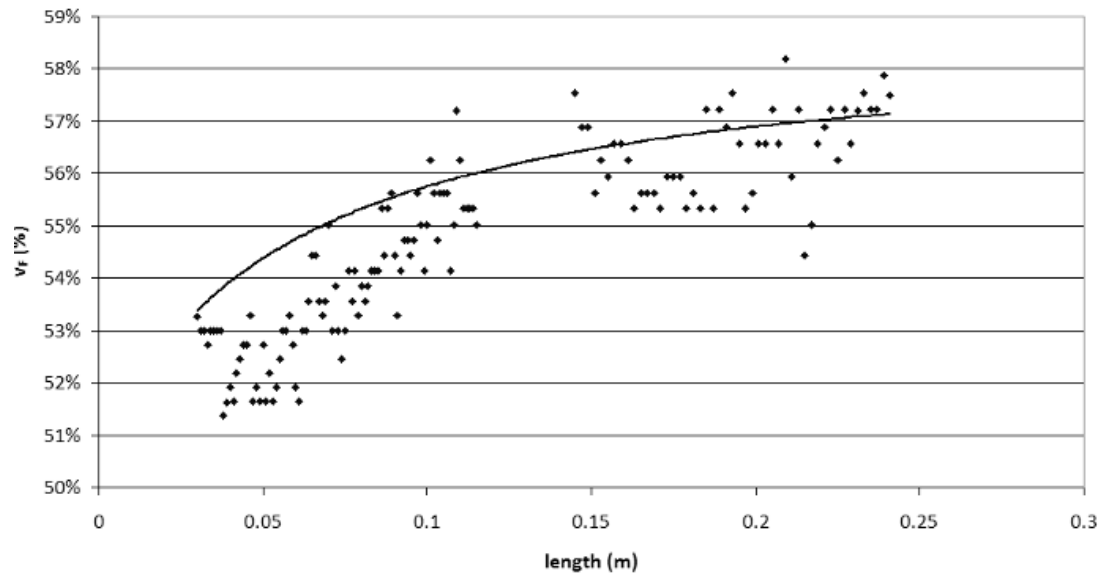


Figure 4.59 - T1(12) VARI  $v_F$  gradient along length (◆) and prediction model (solid line).

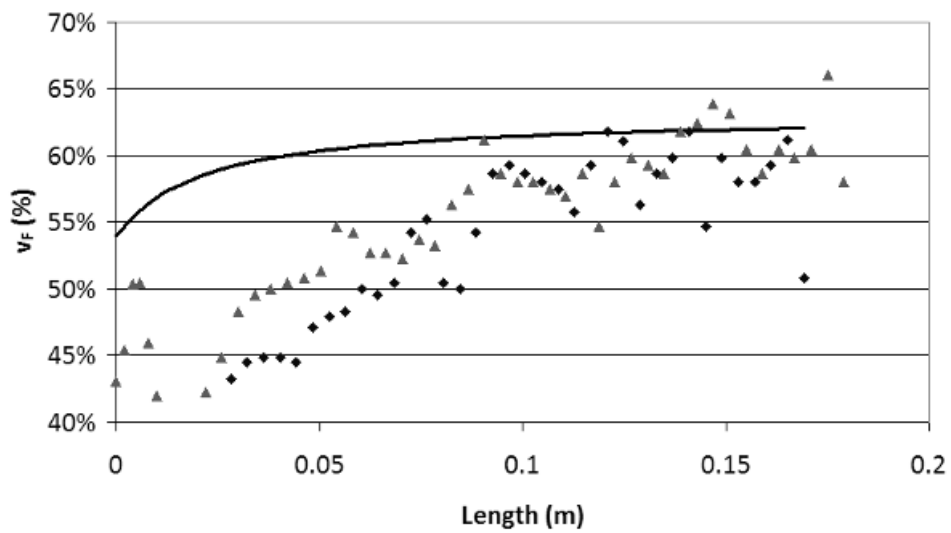


Figure 4.60 - Baseline NCF VARI  $v_F$  gradient along length (◆: replicate 1, ▲: replicate 2) and prediction model (solid line).

## 4.5 Viscosity characterization

### 4.5.1 Non-isothermal curing model

The characterization of the dynamic viscosity of a curing epoxy is discussed in this section. The first step in modeling viscosity is to characterize the relationship between the temperature and the

uncured viscosity of the epoxy,  $\mu_0$  (just after mixing). The applicable range of temperature for the room temperature curing RIM235 system is assumed to be 25 to 40°C. Hexion has provided data for  $\mu_0$  over this range for epoxies based on both RIM235H and RIM236H. As described earlier, a mix of hardeners was used in the epoxy systems used in the majority of infusions in this study. This hardener mix was 33% RIM235H and 67% RIM236H. The RIM235R has a slightly higher amine value, thus causing a higher curing reaction rate.

The  $\mu_0$  data for each separate hardener fit well to the Arrhenius model for temperature dependency (Equation 2.29). This is done by converting the temperatures to Kelvin, and then graphing the inverse of  $T(K)$  against  $\ln(\mu_0)$ . The slope of this line is  $E_0/R$  and the intercept is  $\ln(A_0)$ . With the two separate Arrhenius models,  $\mu_0$  for each was interpolated at various temperature increments over this range. The pairs of viscosity at each temperature were converted into the viscosity of the mix using the Refutas Equation [307]. The viscosity blending number (VBN) is calculated for each component by:

$$VBN_i = 14.534 \ln[\ln(\nu + 0/8)] + 10.975 \quad (4.15)$$

The kinematic viscosity ( $\nu$ ) is the dynamic viscosity ( $\mu$ ) divided by the density ( $\rho$ ). The densities of each resin system were also provided by Hexion. Then the VBN of the mix is:

$$VBN_{mix} = [x_A \cdot VBN_A] + [x_B \cdot VBN_B] \quad (4.16)$$

$x_i$  is the mass fraction of each component; 0.33 for 235H and 0.67 for 236H. The viscosity  $\mu$  of the mix is:

$$\mu = \rho \exp \left[ \exp \left( \frac{VBN_{mix} - 10.975}{14.534} \right) \right] - 0.8 \quad (4.17)$$

This was done for each pair of values. The resulting  $\mu_0(T)$  curve for the mix is shown in between the component viscosities in Figure 4.61.  $A_0$  for the Arrhenius fit to the mix curve is  $5.343e-10$  Pa·s, and  $E_0$  is 49169 J/mol.

The Pichaud model for non-isothermal viscosity at any temperature and reaction conversion is [209]:

$$\frac{\mu(T)}{\mu_0(T)} = \left( \frac{\alpha_{gel}}{\alpha_{gel} - \alpha} \right)^{A_C + \alpha B_C} \quad (4.18)$$

$\alpha_{gel}$  is the critical conversion at gelation and is determined by DSC experimentation. A value of 60% was assumed for the critical conversion at gelation, based on reported values for epoxies with similar reaction mechanisms [208,209]. The parameters of the critical exponent,  $A_C$ ,  $B_C$ , are linearly related to the temperature and are determined by error minimization fitting to isothermal curves for at least two different temperatures.

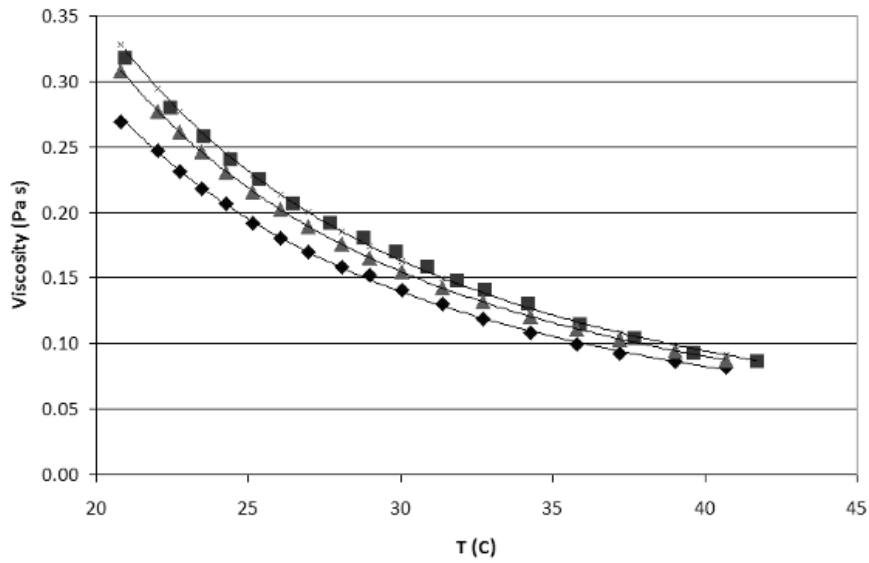


Figure 4.61 –  $\mu_0(T)$  for 235H (◆) and 236H (■), model for 235H/236H mix (▲), and Arrhenius models for each (solid lines).

The second-order autocatalytic model predicts the reaction rate at any time as:

$$\frac{d\alpha}{dt} = \frac{1-\alpha}{2-\gamma_K} (k_0 + k_1\alpha) [2\beta(1-\gamma_K) + \gamma_K\beta^{\gamma/2}] \quad (4.19)$$

The effective reaction rates  $k_0$  and  $k_1$  are functions of the reaction rates of a series of reaction mechanisms associated with DGEBA epoxy systems. They are also related to the temperature by an Arrhenius function.  $\gamma_K$  is the ratio of the secondary to primary amino hydrogens' rate constants. For similar amines as was the case with the RIM235 system, this was approximated to be 0.8. The ratio  $\beta$  is the molar concentration of unreacted amine divided by the concentration of cured epoxy. This expresses the availability of reactants; higher concentrations of amine speed up the reaction. It is inversely related to the reaction conversion by:

$$\alpha = \frac{1}{2 - \gamma_K} (2 - \beta - \gamma_K + \gamma_K \beta - \beta^{\gamma_K/2}) \quad (4.20)$$

EADS Innovation Works provided data for a 25°C isothermal cure of the resin mix. Hexion provided data for the 40°C isothermal viscosity development of each hardener 235H and 236H. The 40°C isothermal curve for the mix was again generated with the Refutas Equation (Equation 4.16). Each isothermal  $\mu(T)$  curve was fit to an Arrhenius model. The viscosity at regular intervals of 200 s for both isothermal curves was interpolated from this data and is shown in Figure 4.62.

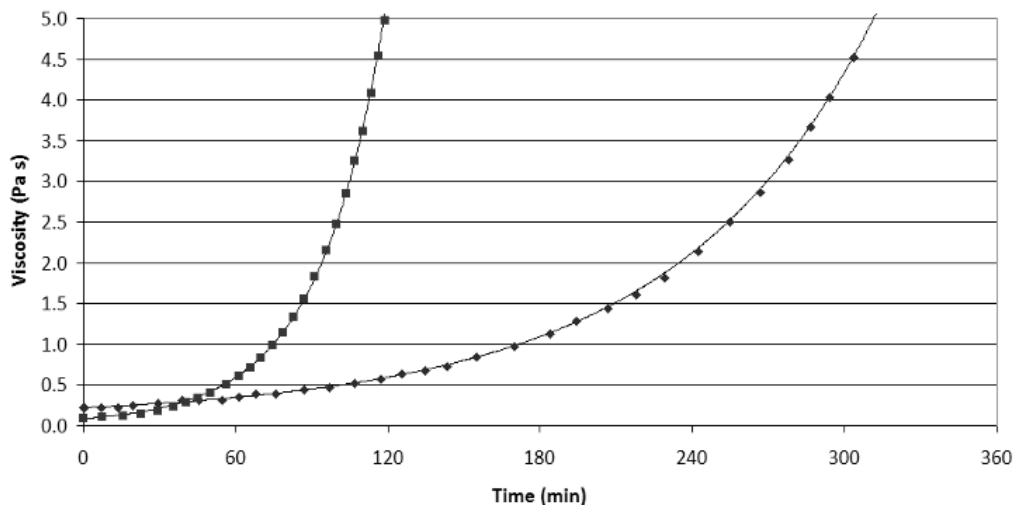


Figure 4.62 –  $\mu(T)$  for isothermal viscosity development at 25°C (♦) and 40°C(■); and  $\mu(T,\alpha)$  model fit (solid lines).

Equation 4.18 was then fit to these two profiles, by minimizing the combined sum of the squares of the residuals from both models. Guess values for  $k_0$ ,  $k_1$ ,  $A_C$ ,  $B_C$  were taken from the literature. These were optimized to fit Arrhenius functions of the temperatures in the case of  $k_0$  and  $k_1$ , and as linear functions of the temperatures in the case of  $A_C$ ,  $B_C$ . The results of the model are shown superimposed on each isothermal experimental curve in Figure 4.62. The parameters for the fits of these four variables are listed in Table 4.8.

Table 4.8 - Pichaud model fit parameters.

$A_{K0}$ (1/min)	$E_{K0}$ (J/mol)	$A_{K1}$ (1/min)	$E_{K1}$ (J/mol)	$A_C$ slope (1/K)	$A_C$ intercept -	$B_C$ slope (1/K)	$B_C$ intercept -
1.00E+07	-5.69E+04	1.00E+08	-7.00E+04	0.1142	-30.30	-0.2649	87.64

The ability of this model to predict non-isothermal viscosity development is demonstrated by modeling a change from a 25°C isothermal cure to a 40°C isothermal cure at 180 minutes after cure initiation (Figure 4.63). At 180 minutes,  $\alpha$  is 0.00222 from the 25°C cure. This same value is transposed to the 40°C cure by the Pichaud model, and subsequent curing proceeds at the new accelerated reaction rate of the 40°C cure. There is an initial drop in viscosity when switching to 40°C from the heat-thinning of the epoxy, but it rises quickly thereafter. Looking at the change in  $\alpha$  in Figure 4.63 (right hand side), changing to 40°C at 180 minutes transforms the  $\alpha$ -profile into the 40° iso curve, transposed over in time by about 120 minutes.

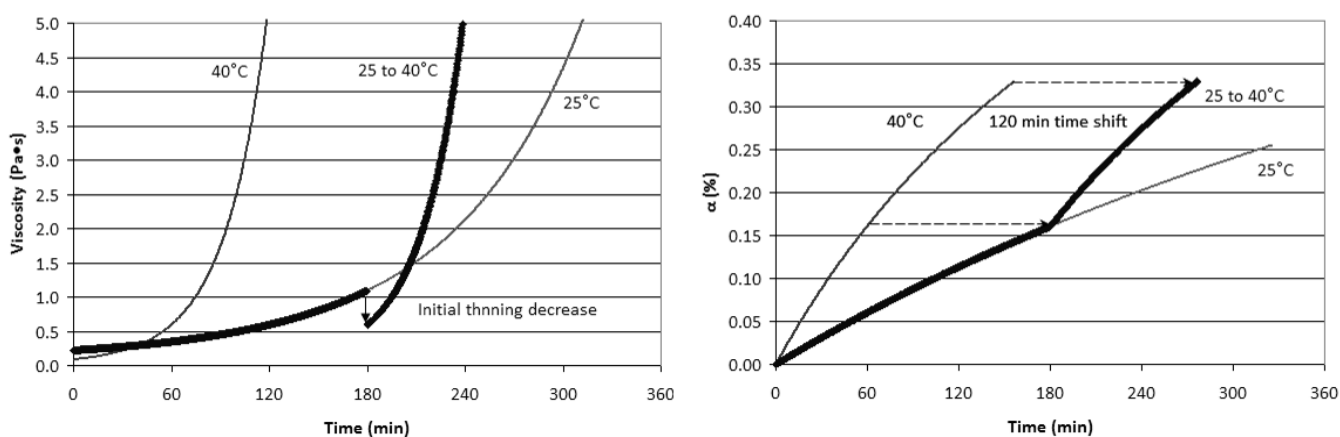


Figure 4.63 - Predicted viscosity for switch from 25° to 40°C, compared to isothermal cure.

#### 4.5.2 Model validation

In order to verify this model’s prediction of viscosity development, the viscosity of the resin at specific locations in the resin pot had to be measured over time. Measuring the viscosity of an epoxy during infusion in-situ can be difficult to implement [308]. With typical laboratory viscosity measurement equipment, it can be difficult to test a small portion of resin from a specific location, at rapid enough of a rate to follow the quick cure of a room-temperature curing resin.

A simple version of an Ostwald viscometer test was performed using 3 mL squeeze-droppers, with a small hole made in the finger-squeeze area. This hole allows the test-fluid to escape the dropper by gravitational pressure, instead of staying in the dropper until being manually squeezed out. A finger can cover the hole when drawing the test-fluid into the dropper by squeezing and then releasing the squeeze area. The regularity of this air-hole’s diameter was controlled by using the same small screw to turn a hole into the side.

Except for the earliest sampling times after mixing, when the viscosity was fairly constant, a new dry dropper was used at each subsequent viscosity sampling. The dropper was filled with resin from right next to the location of the “middle” thermocouple (and next to the “side” thermocouple for a few tests). The time for the liquid to fall from the 2.5 mL level to the neck at the taper was timed. Assuming constant test-fluid volume and gravity, the kinematic viscosity of the fluid is proportional to the time elapsed to drop the same height. Neglecting the change in density of the resin over these temperature ranges, the dynamic viscosity is then proportional to the fall-time as well. Thus, the ratio of the dynamic viscosity at any time compared to an initial time can be determined.

A 200 gram water-insulated pot of epoxy and a 100 gram air-insulated epoxy were monitored with for temperature by placing thermocouples in the center of the resin body, as well as at the inside pot wall (Figure 4.64). The Pichaud model was used to predict the viscosity based on the temperature history recorded at each thermocouple by a digital recorder sampling every second.

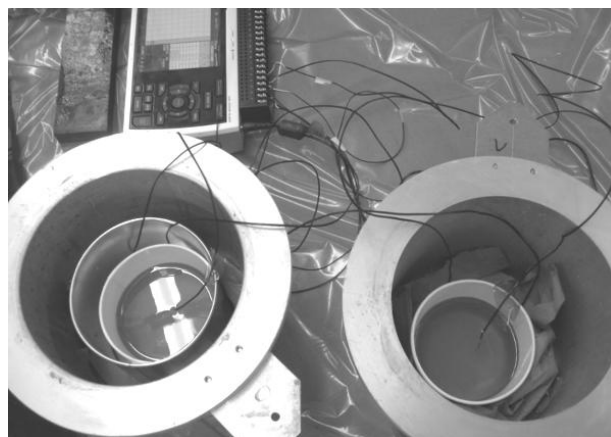


Figure 4.64 - Recording temperature profiles during cure for 200 grams (water-insulated, left) and 100 grams (air-insulated, right) of epoxy.

Figure 4.65 shows the logarithmic-scale viscosity development of both pots, normalized by their initial viscosity, compared to the normalized viscosity predicted by the model. These profiles are for the thermocouple at the middle of the resin. Note that the first viscosity sampling was done 8 minutes after mixing in both cases, so the predicted viscosity is the viscosity at time  $t$ , divided by the viscosity at a time of 8 minutes. Excellent agreement can be seen, thus validating the model for non-isothermal viscosity development. As water has a higher heat conductivity than air, the water-insulated pot shows a more gradual viscosity development. This is due to the higher temperature sustained, despite the larger mass and exotherm. At later times, the viscosity of the

fluid is changing very rapid, and the time to run the viscosity sampling is high. So the viscosity of the fluid can be significantly different at the beginning of the test when compared to at the end. Thus, the time of the test was adjusted to the median time between beginning and end, and error bars are added to show the time range of the test.

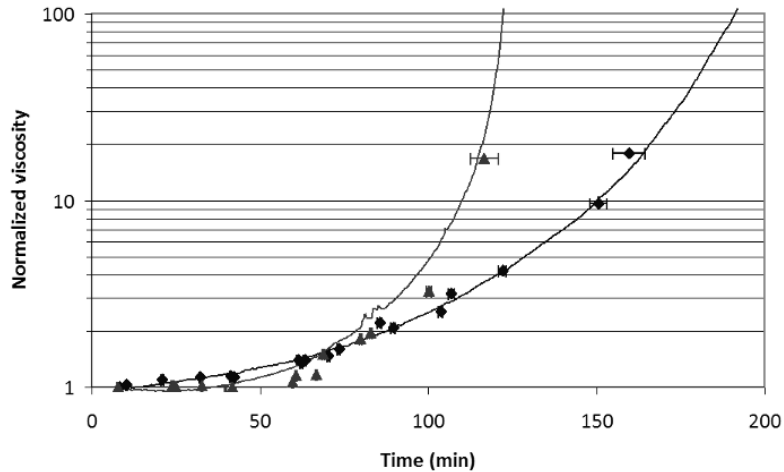


Figure 4.65 - Measured (◆,▲) and predicted normalized viscosity ( $\mu/\mu_0$ ) for curing epoxy: 200g water-insulated (dark ◆), 100g air-insulated (light ▲).

Figure 4.66 shows the 100 gram air-insulated viscosity, comparing the data for the middle thermocouple to the few measurements taken at the pot-side thermocouple. The “side” tests verify the slower viscosity development of the resin there as compared to the middle due to heat loss through the pot wall. Figures 4.67 shows a closer look at the low-viscosity (up to 2 Pa·s) data, as most infusion flow happens at viscosities below this threshold. Again, excellent agreement between the model and the measurements is seen.

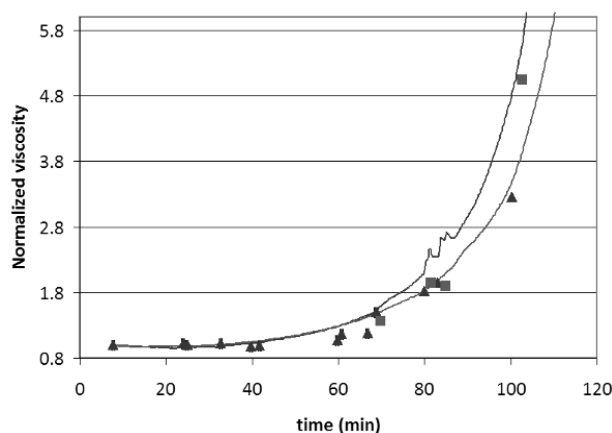


Figure 4.66 - Measured (▲,■) and predicted normalized viscosity ( $\mu/\mu_0$ ) for 100g air-insulated epoxy: middle (dark ▲), pot-side (light ■).



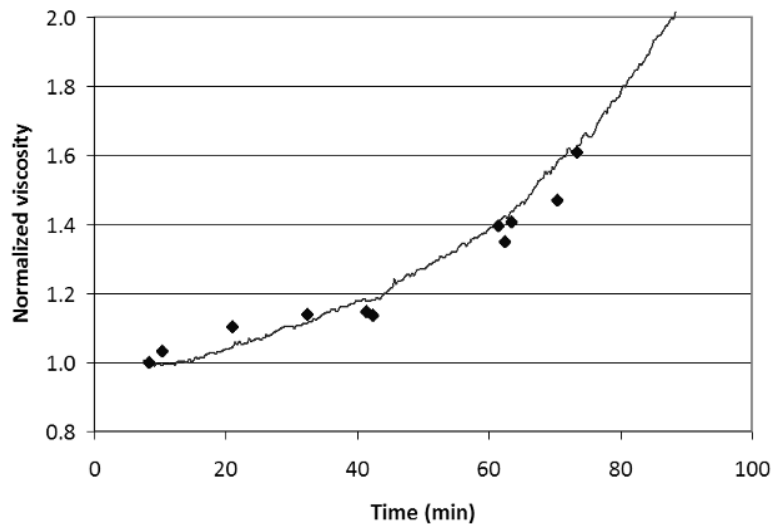


Figure 4.67 - Low viscosity development for 200g water-insulated epoxy: measured ( $\blacklozenge$ ) and predicted ( $\mu/\mu_0$ ).

#### 4.5.3 Temperature distribution modeling

Now that a model for  $\mu(T,t)$  is established, all that remains for viscosity prediction is a model for the temperature  $T(t)$  for the resin. As the resin sits in the pot, this varies for each location due to heat transfer. As the resin moves from the pot to and through the mold during infusion, the temperature history of each infinitely small body of resin predicts the resin conversion of that resin element during its movement. This is complex in application, especially when considering the change in volume of the resin pot as it empties or the change in thickness in the mold due to the pressure gradient on a vacuum bag.

To gain an experimental understanding for comparison, a variety of curing experiments were performed, where the temperature at various locations was monitored. This proceeded as above in Figure 4.64, only with more thermocouples, and sometimes concurrent to an infusion out of the pot. Table 4.9 lists the curing configurations tested. The epoxy was placed in either a paper cup or stainless steel can, which was then placed in a large aluminum vacuum pot typical of industry. Some resin cups were placed in a larger can containing water as a cooling medium. Others used wadded paper towels for small air pocket insulation. Some of the resin amounts stood still throughout the test, while others were drawn out in infusion to come to a lower final mass in pot.

The tests allowed to stand still showed the power of the curing exotherm. Figure 4.68 shows the temperature profile for the dry-insulated epoxies as well as their wet-insulated equivalents. For all

resin mass amounts, the temperature shows autocatalytic acceleration of the exotherm in a very step spike at 100 to 140 minutes. The rapid fall afterwards is due to heat transfer cooling of the epoxy after the reactants have been effectively used up.

Table 4.9 - Temperature monitoring experiments for epoxy cure.

<i>Mass (g)</i>	<i>Insulation</i>	<i>Pot material</i>	<i>Movement</i>
100	dry	paper	stand
200	dry	paper	stand
200	dry	paper	infuse to 0g
200	wet	paper	stand
210	dry	paper	stand
210	wet	paper	stand
300	dry	paper	stand
300	wet	paper	stand
400	dry	paper	stand
400	dry	paper	infuse to 50g
400	dry	paper	infuse to 175g
400	wet	paper	infuse to 60g
400	dry	steel	stand

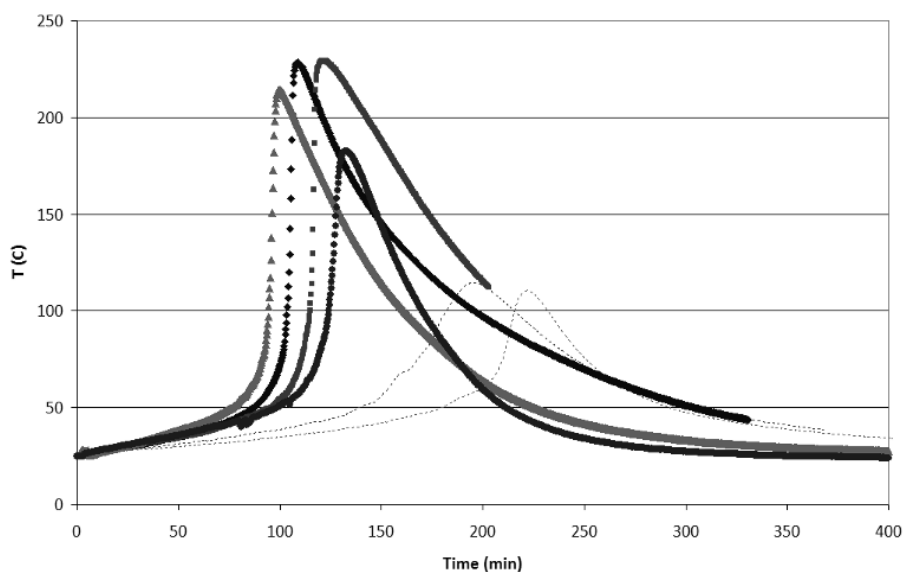


Figure 4.68 - Air insulated T development for resin middle: 400g (◆), 300g (■), 200g (▲), 100g (●), and water-insulated 300g (left-dashes) and 200g (right-dashes).

It is assumed that a higher resin mass will cause this acceleration faster and sooner due to more available heat of reaction. Variations in ambient temperature are thought to cause the slight discrepancies in measurements from these assumptions. The water-insulated infusions show later- and much slower temperature spikes due to the higher heat transfer from the resin.

The final color of the cured epoxy is indicative of the mass and insulation type. The color ranged from a light blue-green for low mass and water-insulation to a dark brown for high mass and air-insulation (Figure 4.69). This would indicate that the decomposition temperature of the epoxies has been reached somewhere around the height of the air-insulation peak at 200°C. Obviously, this amount of exotherm cannot be tolerated in industry. The exotherm is limited in practice by infusing the resin before this spike, to a cooler mold where the auto-catalyzation is limited, or by using a slower curing system or temperature.



Figure 4.69 - Comparison of color of cured still epoxy.

An infusion involves the following temperature modeling complications:

- Decreasing mass in pot and corresponding decreasing exotherm
- Unsteady state and anisotropic: must characterize the temperature distribution in pot for any mass and time
- Heat transfer model for the pot: unsteady-state stubby cylinder with conduction tensor, convection off the top and volumetric heat generation (exotherm).

This latter problem, as described in Section 2.3.5 is simplified into the unsteady-state conductance in a sphere with exotherm.

To make the problem of temperature modeling approachable, the analysis of this problem is organized by examination of each location of resin during infusion.

The temperature along the inlet tube was measured in one of the above mentioned tests. A thermocouple placed at the middle of the 1m tube length only showed a rise of 2°C during

infusion. A thermocouple on the tube right by the mold entrance only rose 1.5°C. Note that the conductive heat resistance of the tube wall differentiated these thermocouple readings from the resin's true temperature. But the heat absorbed by conduction across the tube walls was thought to be insignificant due to the thinness of wall. This was validated by a theoretical study into heat transfer across the tube wall. The thermal resistance of the silicone inlet tube is calculated for a cylinder, per 1 meter length of the cylinder, by:

$$\text{Resistance}_{t,\text{cylinder}} = \frac{\ln(r_o/r_i)}{2\pi k} = \frac{\ln(7.75\text{mm}/6.25\text{mm})}{2\pi(1\text{m})(149\text{W}/\text{m}\cdot\text{K})} = 0.00022908 \frac{\text{K}}{\text{W}} \quad (4.21)$$

The low resistance means a low temperature gradient will exist across the tube walls given a heat transfer across it. Over 4 kilowatts of heat transfer would have to occur to create a temperature difference of at least 1° between the resin and the outer tube wall (where the thermocouples were placed). In all temperature measurements in the pot during resin infusion experiments, the maximum temperature rise was 7.7°C over ambient. Note that this only applies to these infusions, with small amounts of resin (< 400g) in the pot. The maximum mass flow-rate recorded for any of the infusions was 7 g/s. If the resin in the tube was actually still at this maximum temperature, instead of the  $\Delta T = 1.5^\circ$  recorded, a gain of 6.2° would have to occur over the wall thickness. At the maximum resin mass flow-rate this would require a heat transfer of:

$$\dot{Q} = \dot{M} c_p \Delta T = \left(7 \frac{\text{g}}{\text{s}}\right) \left(1600 \frac{\text{J}}{\text{kg}\cdot\text{K}}\right) (6.5\text{K}) = 69.4\text{W} \quad (4.22)$$

This is obviously not nearly enough to cause a significant temperature difference across the tube wall of length 1 m. Therefore, tube wall conductive resistance will be neglected, and the resin temperature can be assumed to be equal to the temperature on the outer tube wall.

Temperature differences are even lower in the mould. The resin temperature was measured for 4 VARI infusions with thermocouples placed on the bag. The maximum  $\Delta T$  registered for all was only 1.75°C. The thickness of the vacuum bag is much thinner than the inlet pipe wall, so the thermal resistance of the bag is considered to be negligible as well.

The low temperatures for the bag sensors suggest that heat convection to the atmosphere dominates in such a thin part. Figure 4.70 shows the typical setup for the infusion tests. In general, thin components made in aluminum molds (high conductivity) will tend towards the isothermal

case. In contrast, thick components in molds made of composite materials such as GFRP (lower conductivity) will tend towards the adiabatic case (perfect insulation) [8,27].

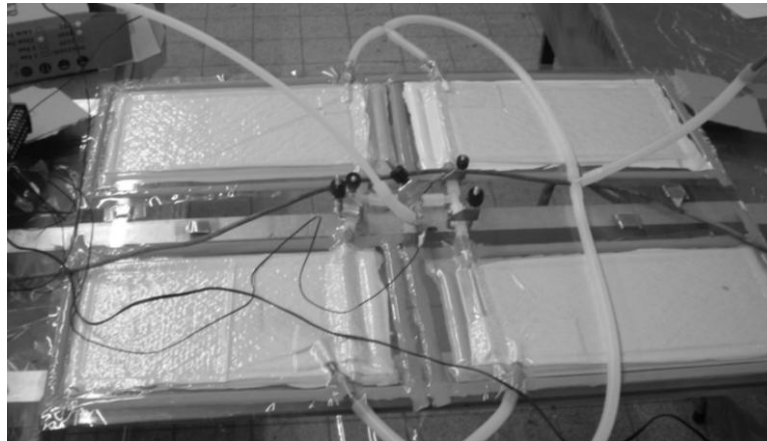


Figure 4.70 - Typical mold setup for infusion temperature profiling tests.

Thus, since the temperature of the resin in the tube (measured at the outer wall) shows temperature gradients of less than  $2^{\circ}\text{C}$  over ambient, it is assumed that the tube and everything afterwards (including all of the mould) is isothermal, with  $T \sim T_A$ . All efforts on temperature profiling for viscosity modeling will focus on the resin pot.

For resin in the pot, the exotherm heat build-up is decreased by both convection and conduction. Convection occurs as warmed air or water on the outside of the pot (all sides) rises and cooler fluid replaces it. Conduction moves the heat from the warmer center to the cup walls.

A resin-element leaves the pot with a certain reaction conversion  $\alpha$ , then passes through the tube and into the mold. The assumption made of isothermal environment in the tube and mold means that the reaction rate from this point is shifted to isothermal cure at ambient temperature throughout that resin-elements movement.

As an infused 400 gram water-insulated pot was typical to the VARI experiments in Section 4.1, the temperature profiles for this test are most applicable to flow modeling. Those experiments began infusion around 15 minutes after mix (cure-initiation), and were all done (either filled or gelled) within a maximum of 165 minutes after infusion-initiation (3 hours total from mixing). Most of the experiments were filled within 1 hour of infusion (75 minutes after mixing).

Figure 4.71 shows the temperature at ambient, the end of the tube in the pot, the middle of the pot, and on the vacuum bag by the inlet for the 400g water-insulated test. The end of the tube is

eventually warmer than the pot middle due to the resin level dropping below the suspended thermocouple during infusion. The rise in temperature for either the middle or tub-end would look more like the wet curves in Figure 4.68 were it not for the decrease of mass in the pot due to infusion. The tube end shows a maximum  $T = 31.7^{\circ}\text{C}$  at about 100 minutes. This is a 5.7 degree maximum  $\Delta T$  over ambient ( $T_A$ ). In comparison, the temperatures on the bag surface never reach more than 1.5 degrees above  $T_A$ .

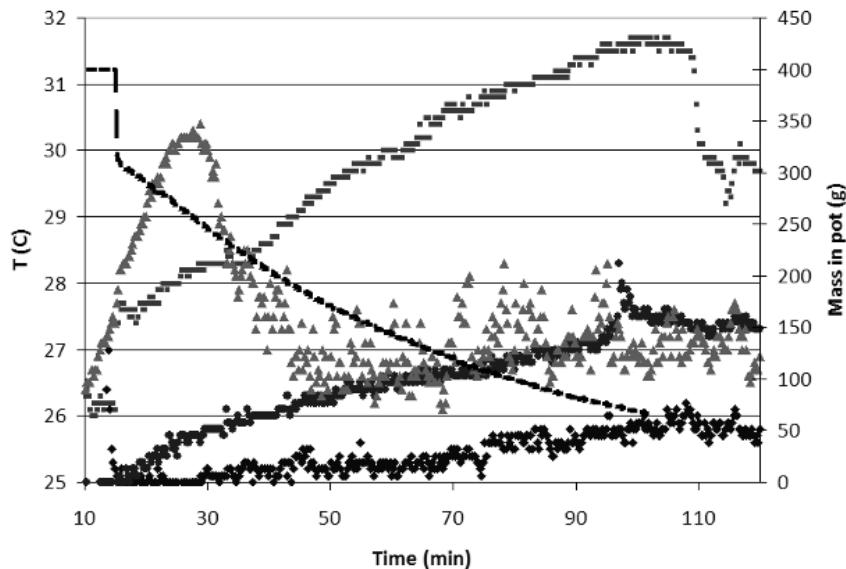


Figure 4.71 - Temperature during infusion: ambient ( $\blacklozenge$ ), tube-end in pot ( $\blacksquare$ ), pot-mid ( $\blacktriangle$ ), bag by inlet ( $\bullet$ ), and mass in pot (dashes).

The other temperature monitoring tests (Table 4.9) showed similar trends. The highest temperature gradient between pot and ambient was  $7.7^{\circ}\text{C}$ , and the bag was usually only about a degree higher than ambient.

#### 4.5.4 Theoretical temperature distribution

The temperature profile at the tube-end and middle was compared to a theoretical prediction of the temperature distribution over the first 15 minutes via the sphere models in Equations 2.37 and 2.40.

For this prediction model, a number of assumptions need to be made:

- Constant  $k$  (conductivity) – which should be alright for infusions with such small  $\Delta T$ .
- The conductivity of the epoxy =  $0.21 \text{ (W/m}\cdot\text{K)}$ , reported by multiple sources for similar epoxies [309,310]

- The cure reaction rate  $da/dt$  for the first 15 minutes is linear and approximately equal for both tube-end and middle. This was confirmed in the Pichaud model calculations of the reaction rate.
- The heat capacity,  $c_p$  for cast epoxy at 25°C is 1.35 (J/kg·K) [309]. But having it almost completely uncured implies more available hydrogen bonding, which causes a higher  $c_p$ . An approximation of 1.6 for the  $c_p$  resulted in the best model fits.

The results of prediction models for both constant properties in the surrounding medium (Eq. 2.37) and different properties (Eq. 2.40, water and epoxy) are presented along with the experimental measurements of the temperature change ( $\Delta T$ ) for a water-insulated resin-pot in Figure 4.72. The model shows little difference from changing the properties of the surrounding medium from epoxy to water. The most significant physical property differences between these materials are that the  $k$  and  $c_p$  for water are 3x higher than those for the uncured epoxy. For the tube-end measurements, the slope is more level (less temperature change) than either prediction although the non-homogenous medium has a more accurate slope. This indicates that heat loss through the water is slightly better predicted with the higher thermal diffusivity.

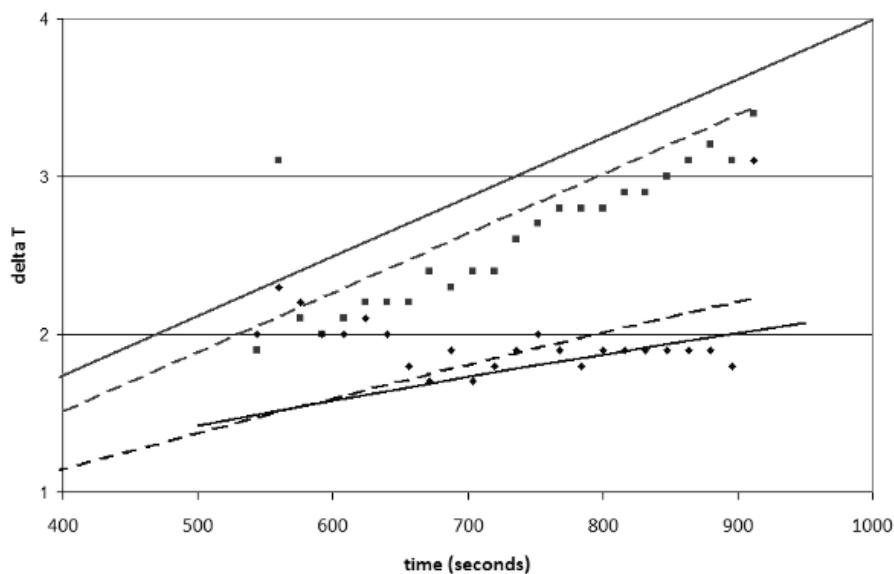


Figure 4.72 - Water-insulated  $\Delta T$  at middle (light, top) and tube-end (dark, bottom) with prediction for homogenous medium (dashed lines) and differing medium (solid lines).

The model of temperature distribution in the pot during cure based on an unsteady-state sphere without convection seems to produce good results. The lower  $\Delta T$  at the pot-middle compared to

prediction is thought to be due to the convective heat loss not present in this model, especially from the top of the resin to the air.

Some of the VARI infusions in Section 4.1 were done with 400g resin pots insulated with air. The same sphere model was again compared to the temperature measurements at pot-middle and tube-end for an air-insulated resin pot. The model predicts higher temperature gradients when the surrounding medium is set to the material properties of air (Figure 4.73). The experimental temperature gradients in this case are significantly less than both predictive models. The non-homogenous model, using the properties for air in the medium, over predicts more than the homogenous model. Air is a poor conductor and has much less diffusivity than water. So an all conduction model would treat it more adiabatically than with a water medium. But convection seems to play a greater role here. Air is an easier medium for convection due to its low viscosity compared to liquids. Convection is taking the heat out faster than the conduction-only model can account for.

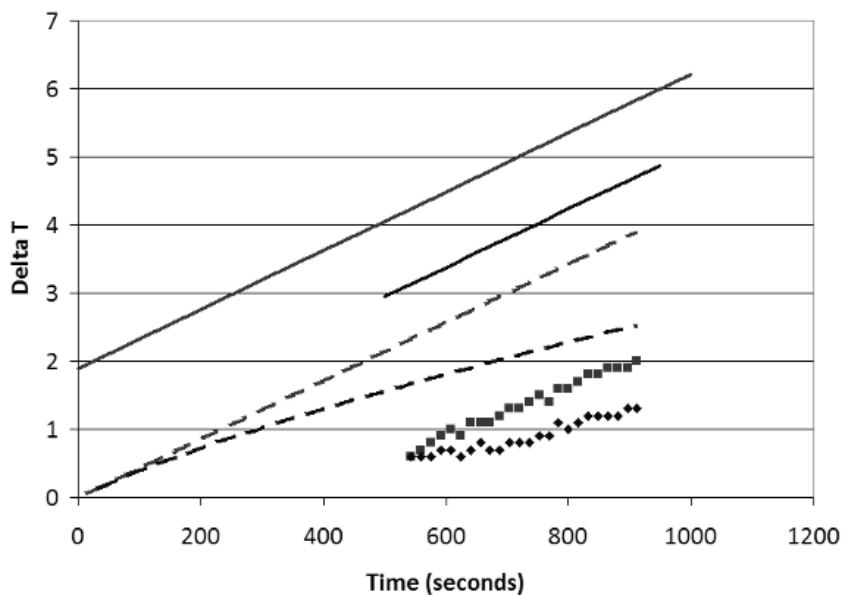


Figure 4.73 - Air-insulated  $\Delta T$  at middle (light, top) and tube-end (dark, bottom) with prediction for homogenous medium (dashed lines) and differing medium (solid lines).

#### 4.5.5 Summary: sensitivity to exotherm

Regardless, the temperature gradients in the resin pot were surprisingly low for all experiments. For the case of the water-insulated test in Figure 4.71, one can assume that the temperature at any location in the infusion system at any given time must lie somewhere between the maximum



temperature in the pot at that time, and the ambient at that time. A “max/min” study was performed to see the viscosity’s sensitivity to this  $T$  variation. The Pichaud model was applied to both the ambient temperature history data, as well as the temperature data at the tube-end. The predicted viscosity at different time intervals for each is listed in Table 4.10.

Table 4.10 - Comparison of maximum and minimum predicted viscosities.

<i>Time (min)</i>	<i>Max <math>\mu</math> (Pot tube-end)</i>	<i>Min <math>\mu</math> (Ambient)</i>	$\Delta\mu$	<i>% increase</i>
15	0.2130	0.2445	-0.0315	-12.87%
30	0.2337	0.2712	-0.0375	-13.83%
45	0.2636	0.3014	-0.0378	-12.54%
60	0.3042	0.3471	-0.0430	-12.38%
120	0.7883	0.5916	0.1967	33.25%
180	2.0748	1.1357	0.9391	82.68%

Results show that through the first hour of infusion, the viscosity at the highest possible temperature is still lower than the minimum ( $T_A$ ). This implies that the accelerated curing due to exotherm has not yet over-powered the heat-thinning effect on the viscosity. By the second and third hours, the viscosity is finally higher at the maximum temperature due to cure. But the resin inlet was closed off at about 60 minutes, so none of this resin makes it to the mold. This suggests that the exotherm does not significantly effect the curing over the fill times in flow modeling for this case.

This trend follows industrial practice. The mold has to be filled before curing becomes a significant effect on the viscosity. Thus, the resin in the pot should be at a higher temperature, and lower viscosity than the resin already in the mold (assumed to be at  $T_A$ ). The accelerated curing should not outweigh the temperature thinning of the resin until the filling is being slowed by gelation.

Table 4.10 represents an over-estimation of the differences in viscosity for most of the resin involved in the infusion. Most flow happens in only the first few minutes. For resin leaving the pot at 20 minutes after mixing, the temperature profile is the same as for  $T_A$  as per the assumption of isothermal environment in the tube and mold. The model predictions were again compared for the case of switching the resin middle profile from measurements to the ambient temperature profile at 20 min (Table 4.11).

Table 4.11 - Comparison of predicted viscosities for maximum  $T$  to 20 minutes.

<i>Time</i> (min)	<i>Max <math>\mu</math></i> Pot tube-end	<i>Min <math>\mu</math></i> Ambient	$\Delta\mu$	% increase
15	0.2130	0.2445	-0.0315	-12.87%
30	0.2754	0.2712	0.0042	1.55%
45	0.3063	0.3014	0.0049	1.64%
60	0.3530	0.3471	0.0059	1.70%
120	0.6034	0.5916	0.0118	1.99%
180	1.1608	1.1357	0.0251	2.21%

Results in Table 4.11 show that the heat-thinning effect over the first 20 minutes is still evident. But with temperatures the same afterwards, the slight difference of ~2% in viscosity over 3 hours is due to the difference in curing rates for only the first 20 minutes. In flow modeling, a 2% increase in viscosity equates to only a 2% increase in time to fill.

Table 4.12 lists the change in reaction conversion ( $\alpha$ ) instead of viscosity, for the same model of switching to ambient at 20 minutes. This quantifies the difference independent of the temperature thinning. The percent increase in  $\alpha$  only 6.57% after the first 15 minutes, which is mitigated at later times as the rate increase is the same after 20 minutes.

Table 4.12 - Comparison of predicted reaction conversions for maximum  $T$  to 20 minutes.

<i>Time</i> (min)	<i>Max <math>\alpha</math></i> Pot tube-end	<i>Min <math>\alpha</math></i> Ambient	$\Delta\alpha$	% increase
15	0.0166	0.0156	0.0010	6.57%
30	0.0329	0.0309	0.0020	6.58%
45	0.0478	0.0459	0.0020	4.29%
60	0.0624	0.0605	0.0019	3.15%
120	0.1177	0.1161	0.0017	1.44%
180	0.1669	0.1655	0.0015	0.89%

This was also the case for the dry 400g infusions: the predicted viscosity at the maximum temperature in the pot is lower than at ambient through the first hour. The curing exotherm even in more of an adiabatic case has little effect on the viscosity compared to the temperature dependence.

This implies that a great simplification can be made to the viscosity model: that of approximately isothermal curing at an average ambient temperature. The viscosity is still changing due to cure, but without the auto-catalyzation by exotherm incorporated in the model. For reasons of simplicity, this is a usual simplification in dynamic viscosity models for flow modeling. This approach has been validated for VARI elsewhere as well [171].

A range of 18 to 28°C covers the ambient temperature range for all the infusions performed in this study. Figure 4.74 shows the predicted isothermal viscosity development at temperatures of 18, 20, 22, 24, 26, and 28°C over the first hour after mixing. The coolest temperature results in the higher viscosities over this time range, while the warmest results in the lowest viscosity. As one can see, curing effects are not significant enough at these temperatures and times to overcome the heat-thinning effects on temperature dependence. The accelerated reaction rate for the 28°C cure is about to cause the viscosity to overtake the 28°C cure's viscosity. But very little change in the gap between the viscosity curves is seen for the lower temperatures.

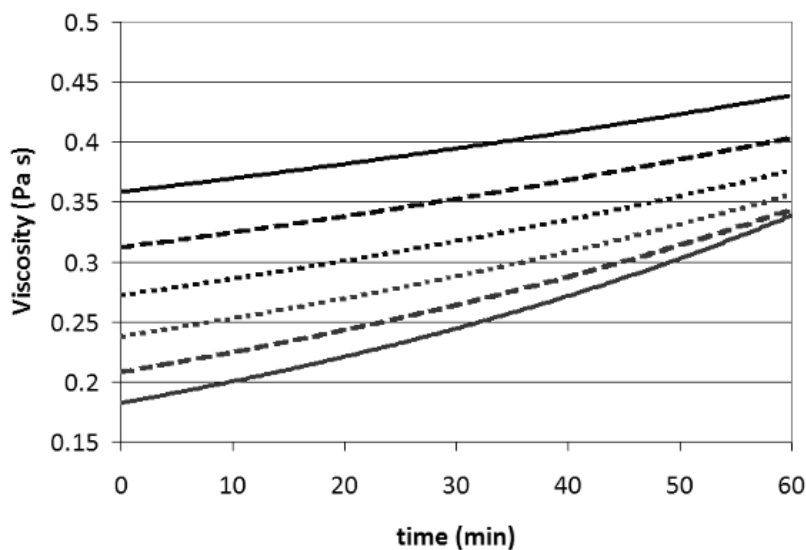


Figure 4.74: Predicted isothermal viscosity development- dark/top: (18°: solid, 20°: dashed, 22°: dotted); light/bottom: (24°: dotted, 26°: dashed, 28°: solid).

These isothermal viscosity profiles were each fit to exponential functions of time:  $\mu(t) = A_V \cdot \exp(B_V \cdot t)$ . The constants for each isothermal temperature are shown in Figure 4.75. The constant  $A_V$  represents the initial viscosity, which drops with increasing temperature. The constant  $B_V$  represents the rate of increase, and increases with increasing temperature.

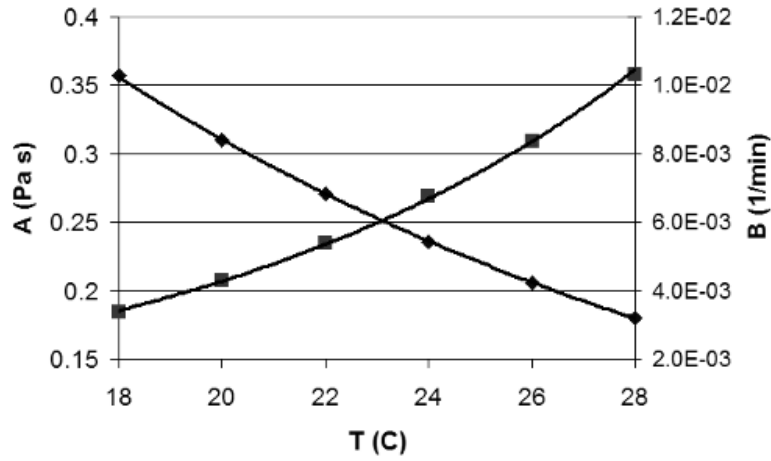


Figure 4.75: Viscosity fit constants -  $A_V$  (◆) and  $B_V$  (■).

The constants themselves were also fit to exponential functions of the temperature. Thus, the viscosity at any time (in minutes) and average isothermal temperature (in °C) is modeled by:

$$\mu(t, T) = A_V(T) \exp[t \cdot B_V(T)] = [a_A \exp(b_A T)] \cdot \exp\{t \cdot [a_B \exp(b_B T)]\} \quad (4.23)$$

where  $a_A = 1.2169$  (Pa·s),  $b_A = -0.068287$  (1/°C),  $a_B = 7.643e-6$  (1/s), and  $b_B = 0.11164$  (1/°C). This model will be used in later flow modeling in this study.

## 4.6 Pressure gradient characterization

As discussed in Section 2.3.6, the pressure gradient for slow flow velocities may not be linear over the flow length. The pressure gradient must then be modeled for each experiment case in this study to aid in accurate flow modeling. To aid in this, each possible source of pressure loss is discussed here.

The pressure drop from gravity is assumed negligible in the case of all infusion experiments in this study as the resin pot was always placed at the same height as the mold. In other applications, a gravity term would be added to the pressure loss, equal to the product of the fluid density, gravitational acceleration, and the change in height.

#### 4.6.1 Inlet pipe pressure loss

The Isotropic Transformation Solution used for through-thickness permeability calculations in Section 4.3 incorporates the pressure loss over the inlet pipe to account for the case of significant pressure loss there. The Reynolds number for the fluid flow is a function of the fluid velocity:

$$\text{Re} = \frac{2v\rho b_t}{\mu} \quad (4.24)$$

For  $\text{Re} < 2320$ , the flow is laminar. The highest possible Reynolds number is calculated by examination of the maximum possible values. The initial viscosity  $\mu_0$  at 25°C of the epoxy mix was measured to be 0.2235 Pa·s. All recorded temperatures during the VARI,  $K_{xy}$ , and  $K_{zz}$  experiments were below 25°C, so  $\mu_0$  should never be lower than this (inverse with temperature). The first recorded flow velocity in the VARI infusions was usually around 0.0001 m/s. An even higher guess of 0.01 m/s is assumed to cover the highest initial flow velocities at smaller time gradients. A resin density for the hardener mix (235H and 236H) of 1108 kg/m<sup>3</sup> was determined from ROM (rule of mixtures) from published data by Hexion for the separate components. The radius of all piping used was 3mm. These values result in a maximum Re of ~0.3. Thus laminar flow can be assumed for all VARI infusions in this study.

For laminar flow, the pressure drop across  $L_t$  of a cylindrical pipe is:

$$\Delta P = \frac{64 L_t \rho}{\text{Re} 4b_t} v^2 \quad (4.25)$$

After substitution and rearrangement of terms:

$$\Delta P = \frac{8L_t \mu}{b_t^2} v \quad (4.26)$$

For a tube of length of 1 m (the average in all flow experiments), the application of the above maximum values results in a pressure drop of ~3 kPa. The flow velocity at most times, however, is less than 0.0001, which results even for very high viscosities in  $\Delta P < 1$  kPa. Thus the pressure drop across the pipe is insignificant to the flow in this study.

#### 4.6.2 Pressure differences for dimensionality

As also mentioned in Section 4.3, the pressure gradient driving the resin from the atmosphere to the vacuum is not all available in any 1D direction for the case of 2D or 3D flow. It must be distributed in all directions in a 3D flow. Hence, with lower pressure gradients, each 1D “effective” flow will be slower than true 1D flow with the same  $P_A$  and  $P_V$ .

A summary of predictions for  $P_R$  over the flow length in any 1D direction for all dimensionalities was given in [126]. If  $P_I$  is the inlet pressure,  $b_t$  is the inlet tube radius, and  $x_f$  is the length of the flow front in that direction, then:

$$P_R(x)_{1D} = P_I \frac{x_f - x}{x_f - b_t} \quad (4.27)$$

$$P_R(x)_{2D} = P_I \frac{\ln(x/x_f)}{\ln(b_t/x_f)} \quad (4.28)$$

$$P_R(x)_{3D} = P_I \frac{x_f \cdot b_t}{x_f - b_t} \left( \frac{1}{x} - \frac{1}{x_f} \right) \quad (4.29)$$

A comparison of the predicted resin pressure gradients for  $P_I = 100$  kPa along a non-dimensionalized flow length for each of these models is given in Figure 4.76.

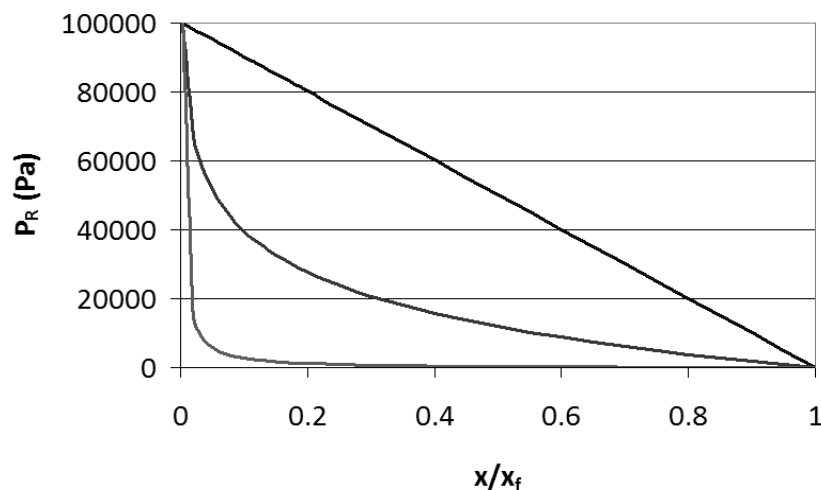


Figure 4.76 - Predicted resin pressure gradients in 1D direction for 1D (right-most), 2D (middle), and 3D (left-most) flow.

By this model, the case of 3D hemisphere flow in the  $K_{zz}$  point-infusion experiments will have a very low  $P_R$  for the majority of the flow length. This is one reason why the point-infusions have such slow flow rates compared to the 1D-flow in the  $K_{xy}$  testing in Section 4.2. The other reason is thought to be the heightened influence of capillary pressure in point infusions.

#### 4.6.3 Capillary pressure

With a room-temperature curing epoxy and no distribution media, the flow will be relatively slow, and will continue to slow down even further with time due to cure. As discussed in Section 2.3.6, the effect of capillary pressure is inversely proportional to resin velocity. At most industrial infusion velocities it is insignificant, but this may not be the case in the VARI and  $K_{zz}$  experiments in this study.

The low flow velocity due to the low  $P_R$  in 3D flow suggests that capillary pressure is most significant in the  $K_{zz}$  infusions compared to the other forms of flow in this study. As a matter of fact, capillary effects have been analytically shown to be significant over any flow length for spherical point infusions [126].

For any case of significant capillary pressure during resin infusion, the pressure gradient across the system must be modified by a term for capillary pressure,  $P_{cap}$  according to Equation 2.42. The pressure gradient over the length of the flow in the case of constant  $P_{cap}$  would be  $\Delta P = P_A - P_V \pm P_{cap}$ . The capillary pressure however, cannot be constant due to its dependence on flow parameters such as resin flow velocity, which change throughout the infusion. Thus,  $P_{cap}$  must be evaluated at each time, as well as at each local position along the flow length, just as the permeability, viscosity, and porosity must be.

For the simplest case of 1D flow,  $P_{cap}$  is a function of the porosity and the contact angle per Equation 2.43. At any particular time for position  $x$  along the flow, the capillary pressure is:

$$P_{cap}(x) = \frac{F}{D_f} \cdot \frac{1 - \phi(x)}{\phi(x)} \cdot \gamma \cos[\theta_C(x)] \quad (4.30)$$

The pressure gradient across the system then also becomes a function of  $x$ :

$$\Delta P(x) = P_A - P_V \pm \frac{F_c}{D_f} \cdot \frac{1 - \phi(x)}{\phi(x)} \cdot \gamma \cos[\theta_C(x)] \quad (4.31)$$

This assumes a constant surface tension, form factor, and fiber diameter. The surface tension has been reported for DGEBA epoxy at room temperature by multiple sources to be about 0.047 N/m [311]. Due to the low variation in resin temperature for the times of significant flow, this will be assumed to be constant despite any temperature dependence. The fibers are the same for all the carbon used in this study, reported by Toho Tenax to have a fiber diameter of 7  $\mu\text{m}$ . As was done in another study of 3D fabrics [126],  $F_C = 3$  is assumed here for in-plane flow as a middle value between all of the previously reported values mentioned in Section 2.3.6.1. This is supported by the report of  $F_C = 3$  to 3.7 for in-plane flow in a plain weave [234].

For the case of a rigid mold, the porosity in Equation 4.31 would also be constant, and  $\Delta P$  would only vary with the contact angle  $\theta_C$  along the flow length. But as the benchmark infusions were VARI, the porosity's dependence on flow position due to compression under the vacuum bag must be incorporated.

As mentioned in Section 2.3.6.1,  $\theta_C$  is the static constant contact angle for low capillary numbers,  $Ca < 10^{-6}$ . This would remove the position dependence of Equation 4.31 and greatly simplify flow modeling. To test this, Equation 2.44 was combined with the Darcy equation for flow velocity (Equation 2.10) with each parameter evaluated at position  $x$  along the flow length:

$$Ca = \frac{K(x)\Delta P(x)}{\gamma x \phi(x)} \quad (4.32)$$

The baseline NCF fabric (Section 3) was chosen for the test case. The models in this study for the permeability (Section 4.2) and compressibility (Section 4.4) were applied for a 250 mm long 1D infusion along the stitching ( $0^\circ$  general axis).  $P_A$  was assumed to be 100 kPa and  $P_V = 0$ . By the inlet, where flow is very fast, the capillary number takes on very high values, such as 3.8 for  $x = 0.1$  mm. By the vent ( $x = 250$  mm), with full vacuum compaction,  $Ca = 1.3\text{e-}3$ . If we assume a capillary pressure of 30 kPa (equal to the maximum reported  $P_{cap}$  for a similar system [8]), the capillary number drops to  $9.3\text{e-}4$ . This is still significantly higher than the limit of  $10^{-6}$ . Therefore, the static contact angle cannot be used in Equation 4.31.

The dynamic contact angle  $\theta_{CD}$  must be applied. This can be calculated by Equation 2.45 from the capillary number and the static contact angle. The static contact angle,  $\theta_{CS}$  is assumed to be  $28.5^\circ$  as reported for a similar epoxy on carbon [53]. Solving for  $\theta_{CD}$  at any length  $x$ :



$$\theta_{CD}(x) = \arccos\left[\cos\theta_{CS} - (\cos\theta_{CS} + 1)\tanh\left(4.96(Ca(x))^{0.702}\right)\right] \quad (4.33)$$

Evaluating Equation 4.31 becomes tricky as the compaction pressure is modified by  $P_{cap}$ . In evaluating the dynamic contact angle  $\theta_{CD}$ , the capillary number in Equation 4.33 includes the porosity term as well (Equation 4.32), which is dependent on  $P_{cap}$ . This entails dependence of the resulting  $P_{cap}$  on itself. The wet fabric is very stiff, however, and so incorporation of  $P_{cap}$  in its evaluation may not be significant.

To test the dependence of inclusion of the capillary pressure in evaluation of itself, the same test case from above was applied, that of 250 mm 1D infusion along the stitching of baseline NCF. A decrease in velocity due to capillary pressure was assumed. At 20 mm along the flow (by the inlet),  $P_A - P_R = 8000$  Pa. Equation 4.30 evaluated at this  $\Delta P$  results in  $P_{cap} = 9.4$  kPa. If Equation 4.30 is substituted into the  $P_{cap}$  term of the pressure gradient (Equation 4.31) in evaluation of the porosity in Equation 4.31 and the pressure gradient in Equation 4.32, the newly evaluated  $P_{cap}$  is 10.0 kPa. This results in a further reduction of the pressure gradient of  $10.0 - 9.4 = 0.6$  kPa. The difference in flow rates is assumed to be insignificant for a reduction of the pressure gradient by 0.6 kPa. Similar evaluation by the vent results in  $P_{cap} = 27.3$  kPa when no  $P_{cap}$  is included in its own evaluation, and  $P_{cap} = 26.9$  kPa when it is. This would also result in an insignificant difference between flow rates.

This was verified in Mathcad by plotting the capillary pressure for its evaluation independent of itself, and with one substitution of Equation 4.30 in itself for all evaluations of the pressure gradient in Equation 4.31. Figure 4.77 shows the results; no significant difference in  $P_{cap}$  is seen. Thus, Equation 4.30 can be evaluated with the pressure gradient of  $(P_A - P_V)$ , and is not dependent on itself.

With this same test case, the dynamic contact angle for conditions by the vent ( $x = 250$  mm) is  $37.8^\circ$ . This implies less effective wetting than would be the case with a static fluid, as  $\theta_{CD} > \theta_{CS}$ . By the inlet, at  $x = 10$  mm,  $\theta_{CD}$  is over  $85^\circ$  implying a very low degree of effective wetting. The maximum capillary pressure for this test case is the value reported above by the vent:  $P_{cap} = 27.3$  kPa. In 1D flow, the fluid velocity is directly proportional to the pressure gradient. Given  $P_A - P_V = 100$  kPa, if this gradient is reduced by 27.3 kPa, the fluid velocity will be 27.3% slower at that point. Capillary effects are thus deemed significant at least by the vent.

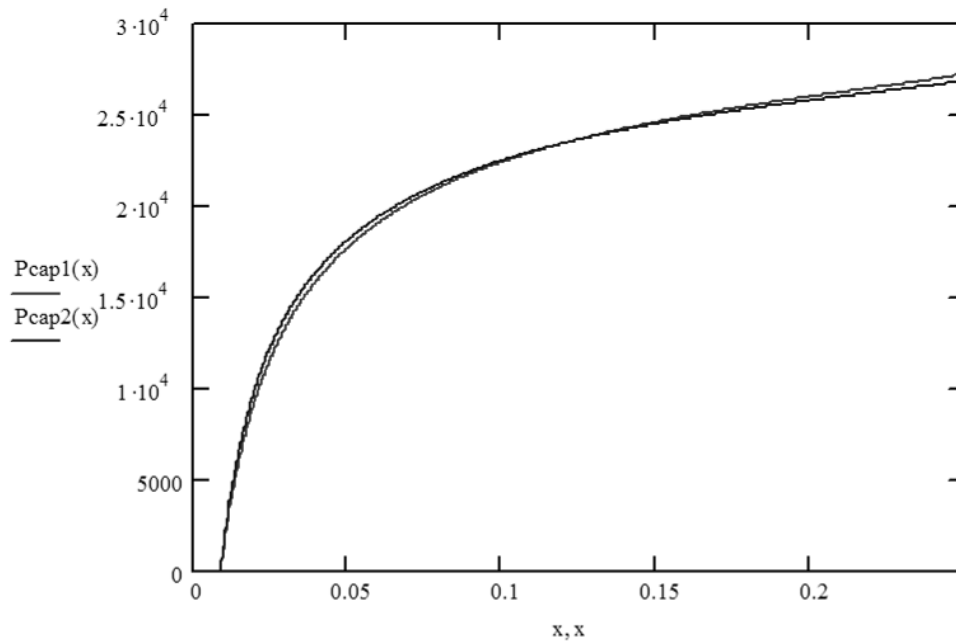


Figure 4.77 - Comparison of capillary evaluation: independent of itself (light), with one substitution of Equation 4.30 in Equation 4.31 (dark).

#### 4.7 Vacuum bag sealing of tows

As mentioned in Section 2.3.8, a possible complication of flow modeling is the sealing of the top layer fabric tows by suction of the vacuum bag. This phenomenon is assumed to be the most insignificant of any of the possible complications discussed as it only deals with the top layer of tows in the fabric stack.

To test this, two infusions were made with the two layers of the baseline NCF at  $P_V=3\text{kPa}$ . The default vacuum bag used in all other tests was used in one infusion. A much more compliant (less stiff) plastic bagging material was used in the other, thinking that it would be sucked into the tows easier. RIM235 resin was infused in each, and the pressure gradient from  $P_A$  to  $P_V$  was frozen into place by bleeding until cure.

Figure 4.78 shows optical micrographs of samples cut from the infusion with the compliant bagging material after curing. These images were taken by the vent (upper image) and by the inlet (lower image). In both cases, no significant sealing of the top fiber tows can be seen. It is assumed that the resin cured in the shape the vacuum bag was during infusion, and this shape is seen to be

relatively flat along the top. No evidence was seen of the bag conforming to the inter-tow gaps in these samples or in the samples with the stiffer bag. Thus, this is deemed to be an insignificant effect on the bulk permeability.

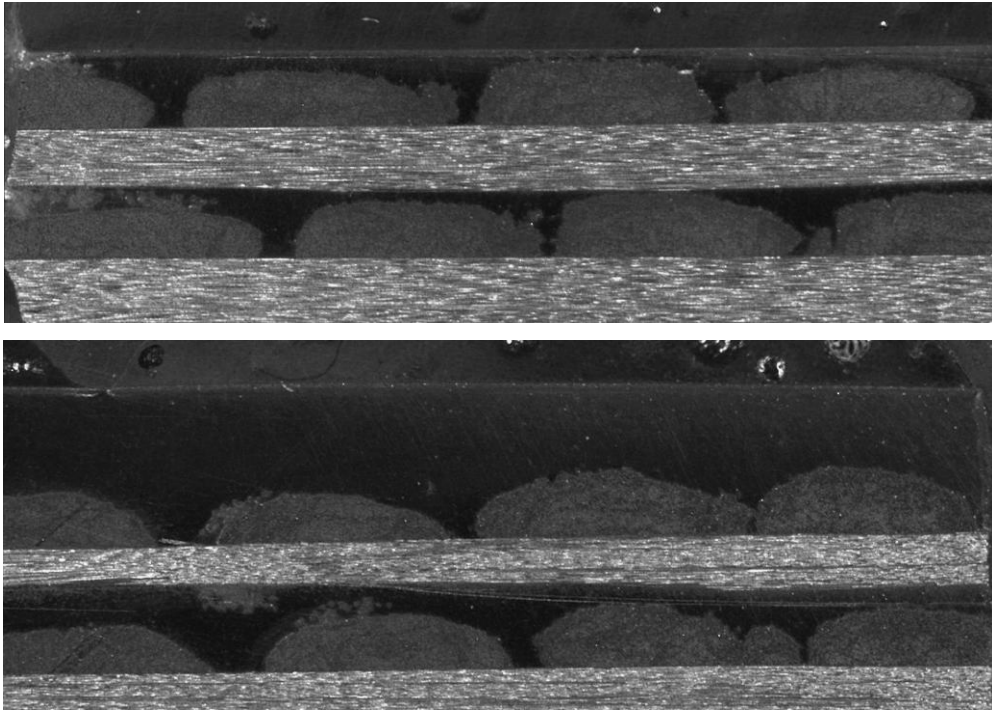


Figure 4.78 - Comparison of vacuum bag sealing for high pressure (top) and low pressure (bottom).

## 5 Coupled model solution results

Here the combination of all models in one coupled model is presented. The 1D Darcy Equation for the velocity across the 1D flow length  $dx$  is proportional to the pressure gradient over that  $dx$ :

$$\frac{dx}{dt} = \frac{-K}{\mu \cdot \phi} \cdot \frac{dP_R}{dx} \quad (5.1)$$

All of these variables have been discussed and modeled. To find a solution to the coupled model, the variables must be set in terms of either  $x$  (position) or  $t$  (time). In this paper, the pressure gradient, permeability, and porosity are evaluated for both  $x$  and  $t$ . The viscosity, as discussed in Section 4.5.5, will only be evaluated for  $t$  (homogeneous viscosity at any given time). Organization of Equation 5.1 by variables yields the two sides to be integrated:

$$\frac{-\phi(x,t)}{K(x,t) \cdot (dP_R / dx)} dx = \frac{dt}{\mu(t)} \quad (5.2)$$

The right side can be integrated with respect to time. For a constant viscosity, the right side simply yields the filling time divided by the viscosity. The integration for a linear dependence on viscosity was demonstrated in another study [312]. For the exponential dependence suggested earlier with Equation 4.23, the right side yields:

$$\int_0^t \frac{dt}{A_V \exp(tB_V)} = \frac{1}{A_V B_V} - \frac{1}{A_V B_V \exp(tB_V)} \quad (5.3)$$

If the left side of Equation 5.2 is  $C$ , then one can solve for the fill-time  $t$ :

$$t = \frac{1}{B_V} \ln \left( \frac{1}{1 - CA_V B_V} \right) \quad (5.4)$$

The difficulty of evaluating the left side ( $C$ ) of Equation 5.2 greatly varies for the different levels of model-complexity. For simulation neglecting the compressibility and capillary pressure,  $C$  is easy to evaluate. This implies a constant pressure gradient. Neglecting inlet effects, assuming the injection pressure is equal to the ambient pressure, and adding a term for non-negligible vacuum pressure to Equation 4.27, the local pressure becomes:

$$P_R(x) = \frac{x}{x_f} (P_V - P_A) + P_I \quad (5.5)$$

Differentiation of Equation 5.5 yields the constant pressure gradient for a given flow length:

$$\frac{dP_R}{dx} = \frac{1}{x_f(t)} (P_V - P_A) \quad (5.6)$$

For no compressibility and the assumption of incompressible media, the fiber content, porosity, and permeability are all constant throughout the mold. The equation of continuity (Equation 2.5) then implies that the velocity is constant throughout the mold at a given time. The velocity can then be evaluated as the change in flow front with time. Thus, after substituting the pressure gradient from Equation 5.6, the left side (C) can be integrated with respect to the flow front position:

$$C = \int_0^{x_f} \frac{-\phi \cdot x_f}{K \cdot (P_V - P_A)} dx_f = \frac{\phi \cdot x_f^2}{2 \cdot K \cdot (P_A - P_V)} \quad (5.7)$$

Combining this with a constant viscosity yields the simplest 1D Darcy solution (Equation 2.11).

To incorporate capillary pressure into this model, a closed form solution is no longer possible to evaluate C. As mentioned in Section 2.3.6.1, the capillary pressure has been said to both increase [232] and decrease [128] the available pressure gradient. As discussed in [258], and mentioned in Section 2.3.8.3, the resin flows faster in the inter-tow gaps than inside the tows for high pressures, and vice-versa for low pressures. Perhaps this would explain the contradicting effects of capillary pressure on the overall resin pressure gradient. The draw of capillary pressure may decrease the resin velocity when the flow is faster in the inter-tow gaps than within the tows, and increase the resin velocity for the opposite case when the flow in the tows is faster than outside of them. As the infusions in Section 4.1 have very slow flow compared to typical industrial infusions, it is thought that an increase in the pressure gradient due to capillary pressure is more probable than vice-versa, thus increasing the velocity. The pressure gradient is then a function of the instantaneous flow length and capillary pressure. Adding the capillary pressure to Equation 5.6 yields:

$$\frac{dP_R}{dx} = \frac{1}{x_f(t)} \left[ P_V - (P_A + P_{cap}(t)) \right] \quad (5.8)$$

The opposite case, where the capillary pressure diminishes the pressure gradient will also be treated.

Still neglecting compressibility means that the equation of continuity still holds true; the velocity is constant throughout the mold at any particular time. The capillary pressure is then evaluated only for time by Equation 4.30:

$$P_{cap}(t) = \frac{F}{D_f} \cdot \frac{1-\phi}{\phi} \cdot \gamma \cos[\theta_{CD}(t)] \quad (5.9)$$

Equation 4.32 was expressed with a general 1D pressure gradient that was integrated over the length of the filled regime. If this is changed to a local pressure gradient, the instantaneous capillary number becomes:

$$Ca(t) = \frac{1}{\gamma} \cdot \frac{K}{\phi} \cdot \frac{dP_R}{dx} \quad (5.10)$$

Combining this with Equations 4.33, and 5.1, the dynamic contact angle for any time is a function of the instantaneous flow velocity and viscosity:

$$\theta_{CD}(t) = \arccos \left[ \cos \theta_{CS} - (\cos \theta_{CS} + 1) \tanh \left( 4.96 \left( \frac{\mu(t)}{\gamma} \cdot \frac{dx}{dt} \right)^{0.702} \right) \right] \quad (5.11)$$

As discussed in Section 4.6.3, the capillary pressure need not be included in the pressure gradient when evaluating  $dP_R/dx$  in Equation 5.10. But a better method is to solve for the flow velocity,  $dx/dt$  in Equation 5.1, by substituting the pressure gradient with Equation 5.8, then the capillary pressure with Equation 5.9, then the dynamic contact angle with Equation 5.11:

$$\frac{dx}{dt} = \frac{K}{\phi \cdot \mu(t) \cdot x_f(t)} \left( P_A - P_V + \frac{F}{D_f} \cdot \frac{1-\phi}{\phi} \cdot \gamma \cos \left[ \arccos \left[ \cos \theta_{CS} - (\cos \theta_{CS} + 1) \tanh \left( 4.96 \left( \frac{\mu(t)}{\gamma} \cdot \frac{dx}{dt} \right)^{0.702} \right) \right] \right] \right) \quad (5.12)$$

This then evaluates the capillary pressure without the need for such a simplification. This equation is too complex to solve for  $dx/dt$ , but can be evaluated using a simple bisection method.

The flow front progression is incrementalized by  $dt$ . The time and flow front length are initialized by setting  $t = 0$  and  $x_F = 0$ . The velocity is evaluated for that  $dt$ , and  $x_F$  is advanced by  $dx$ . For the case of constant viscosity, the velocity must be evaluated for the instantaneous  $x_F$  at each time step. To add the  $\mu(t)$  viscosity model in Equation 4.23, the velocity must be evaluated at each  $dt$  for both the instantaneous viscosity and  $x_F$ .

To model a flexible mold with compressibility of the fabric, the assumption of homogeneous velocity (Equation 2.5) no longer holds true. This is because variation of the mold height requires a small through-thickness flow velocity which upsets the flow balance (Figure 5.1).

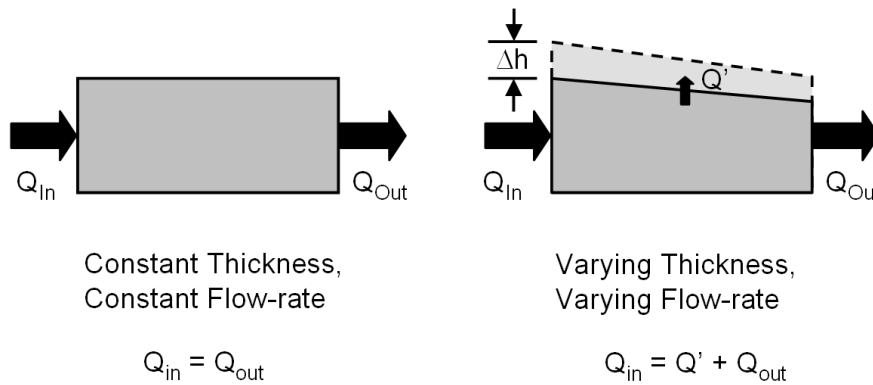


Figure 5.1 – Conservation of mass in rigid mold (left) vs. under flexible cover (right) [313].

A modified equation for conservation of mass was proposed in [190]:

$$\frac{\partial h}{\partial t} = -\frac{\partial}{\partial x}(u \cdot h) \quad (5.13)$$

For non-homogeneous velocity, the pressure over the filled regime is no longer a linear function of position, i.e. the pressure gradient is no longer linear. It must be evaluated along the length of the filled region. For 1D flow, and substituting Equations 2.3 and 2.4 into Equation 5.13:

$$\frac{\partial h}{\partial t} = -\frac{\partial}{\partial x} \left( \frac{-K \cdot h}{\mu} \cdot \frac{\partial P_R}{\partial x} \right) \quad (5.14)$$

A method to evaluate the pressure gradient for such a system was proposed by Modi [313]. This method involves non-dimensionalization of the position  $x$ :

$$\alpha_X = \frac{x}{x_F} \quad (5.15)$$

Equation 5.13 can then be written as (derivation in [313]):

$$0 = \frac{d^2 P_R}{d\alpha_X^2} + \left[ \frac{1}{K} \cdot \frac{dK}{dP_R} + \frac{(\phi + \alpha^2)}{h \cdot \phi} \cdot \frac{dh}{dP_R} \right] \cdot \left( \frac{dP_R}{d\alpha_X} \right)^2 \quad (5.16)$$

The shooting method is used to convert this boundary problem into two initial value problems by replacing the second order equation (Equation 5.16) with two first order equations:

$$0 = \frac{dI}{d\alpha_X} + \left[ \frac{1}{K} \cdot \frac{dK}{dP_R} + \frac{(\phi + \alpha^2)}{h \cdot \phi} \cdot \frac{dh}{dP_R} \right] \cdot (I)^2 \quad (5.17)$$

$$\frac{dP_R}{d\alpha_X} = I \quad (5.18)$$

Both of these equations must be discretized by time ( $dt$ ) and position ( $d\alpha_X$ ). For a particular time step, the local properties are calculated at  $\alpha_X = 0$ , where the inlet boundary condition specifies that the resin pressure is the ambient pressure,  $P_R = P_A$ . An initial guess is made for the pressure gradient ( $dP_R/d\alpha_X$ ) at this position. The compaction pressure,  $P_C$  at  $\alpha_X$  is calculated by simply subtracting the local resin pressure,  $P_R$  from the ambient pressure,  $P_A$ . The fiber content is a function of the compaction pressure by the Grimsley model. Evaluating this (Equation 4.14) as a function of  $\alpha_X$  gives:

$$v_F(\alpha_X) = \frac{v_{F0}}{1 - \left( a_w + b_w \left( \frac{P_C(\alpha_X)}{c_w + P_C(\alpha_X)} \right) \right)} \quad (5.19)$$

The porosity is simply the inverse of the local  $v_F$ . The permeability is a function of  $v_F$  by power law fitting (Equation 2.13):

$$K(\alpha_X) = A_K [v_F(\alpha_X)]^{B_K} \quad (5.20)$$

The height is evaluated by rearrangement of Equation 4.2:



$$h = \frac{n \cdot A_F}{\rho_F \cdot v_F} \quad (5.21)$$

The derivative terms for permeability and height in Equation 5.16 are then:

$$\frac{dK}{dP_R} = \frac{-v_{F0} A_K B_K b_w c_w}{(c_w + P_C(\alpha_X))^2 \left(1 - a_w - \frac{b_w P_C(\alpha_X)}{c_w + P_C(\alpha_X)}\right)^2} \left( \frac{v_{F0}}{1 - a_w - \frac{b_w P_C(\alpha_X)}{c_w + P_C(\alpha_X)}} \right)^{B_K - 1} \quad (5.22)$$

$$\frac{dh}{dP_R} = \frac{b_w c_w}{(c_w + P_C(\alpha_X))^2} \left( \frac{n \cdot A_F}{\rho_F \cdot v_{F0}} \right) \quad (5.23)$$

A new  $P_R$  for the next  $\alpha_X$  is calculated, and the local properties again computed at that  $\alpha_X$ . As detailed in [313], the Euler method or a 4<sup>th</sup> order Runge-Kutta method can be used for the discretization of Equations 5.17 and 5.18. Reported results showed no significant difference between methods, or for discretization with 100 nodes or 1000 nodes. Thus, Euler-based discretization with 100 nodes is sufficient [313].

The pressure,  $P_R$  at the last node ( $\alpha_X = 1$ ) is the output of this discretization. It varies with the initial guess for the pressure gradient at the inlet. The resin pressure at the last node must equal the vacuum pressure,  $P_V$ . Thus, the initial guess is modified to meet this requirement. A secant method of optimization is better here than a bisection method, for its benefits in calculation speed as this requires a number of iterative evaluations the entire pressure field.

The resulting pressure field is constant over time when analyzed in terms of the non-dimensionalized position (Equation 5.15) [70,173,313]. This is because the pressure distribution at an early short flow length is essentially the same as for a later, longer flow length, only stretched out across the new flow length. Thus, the pressure field only has to be solved once. The local pressure gradient at the flow front determines the flow front velocity. As that local pressure gradient is constant at any time, Darcy's Law can be integrated to find the fill time given that effective pressure gradient:

$$\int \frac{dt}{\mu(t)} = \frac{L^2 \phi}{2K(-dP_R / d\alpha_X)} \quad (5.24)$$

where  $K$ ,  $\mu$ , and  $\phi$  and the pressure gradient are all evaluated at the flow front ( $P_R = P_V$ ). The left side of this equation is evaluated as specified earlier for either a constant viscosity or the exponential viscosity function.

No attempts at incorporation of both capillary pressure and compressibility into one flow simulation were found in the literature. Although [173] outlines a strategy to incorporate compressibility along with a sink in flow for dual scale effects, no actual simulation results are presented for the combination. This underlies the difficulty of this type of coupled simulation, as well as the difficulty in characterizing pressure gradients to validate a modeling strategy.

In this study, a coupled model is presented and applied to flow simulation. This is then the first known attempt at flow simulation with such a coupled model. It is based on location discretization (based on the compressibility model), as well as time discretization (based on the capillary pressure model). It is assumed that the only change in velocity with position is due to change in mold height as the flexible cover rises. Thus the only change in the non-dimensionalized pressure gradient with location is also due to the bag, and Equation 5.16 still applies. The pressure distribution for the first time step is thus calculated in similar fashion. The pressure gradient and flow front velocity are calculated, and a new flow front position determined for the next time step.

After the first time step, wetting effects are incorporated. The capillary pressure is a function of the capillary number. Combining Equations 5.8 and 5.10, one can see that it is dependent on the flow front length, and thus the time:

$$Ca(t) = \frac{K}{\gamma\phi x_f(t)} [P_V - (P_A + P_{cap}(t))] \quad (5.25)$$

The capillary pressure theoretically modifies the total available pressure gradient (Equation 2.42), and both increases and decreases to the pressure gradient will be examined. The balance between the resin pressure and compaction pressure is determined by this available pressure gradient. This is the difference between ambient and vacuum for no capillary pressure. Adding capillary pressure thus requires fitting the compressible pressure field so that the final node's resin pressure ( $P_R$  at  $\alpha = 1$ ) is equal to the vacuum pressure plus or minus the instantaneous capillary pressure (evaluated with properties at the flow front). This is illustrated in Figure 5.2, where the simulated pressure field across a short flow length in the Baseline NCF is simulated. The black line is the linear pressure gradient for no compressibility or capillary pressure. The red dashed line is the pressure

gradient from adding compressibility modeling as outlined above. The characteristic “hump” was also seen in [313,314], due to the dynamic mold height. The dotted lines are from coupling both compressibility and capillary pressure models, with  $P_{cap}$  adding to the available pressure gradient (bottom dotted) and diminishing it (top dotted). The curves are essentially the same as the compressibility-only curve (dashes), but tilted towards a different final pressure.

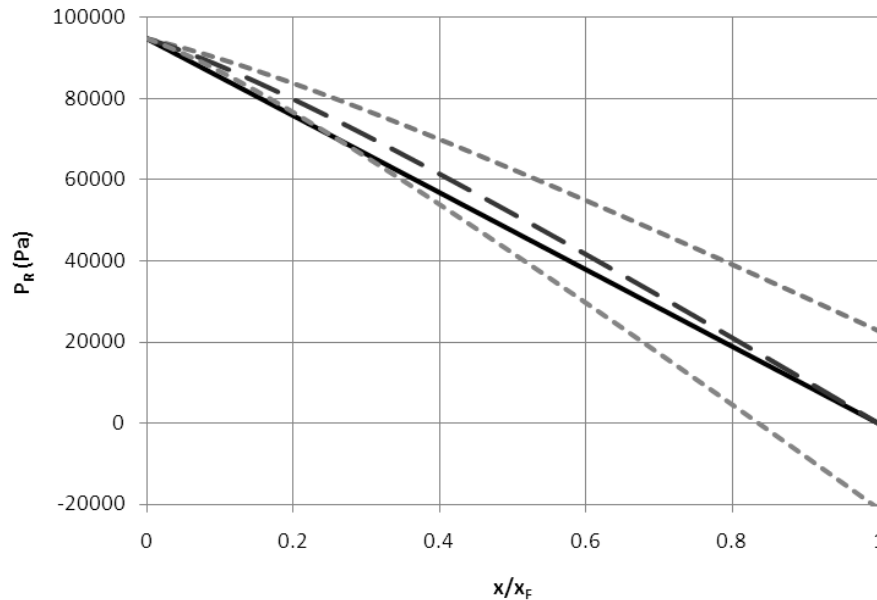


Figure 5.2 – Predicted pressure field: no compressibility or  $P_{cap}$  (solid),  $P_{cap}$  adds to available pressure (bottom dotted),  $P_{cap}$  diminished available pressure (top dotted).

Once the pressure gradient at the flow front is known, the resulting instantaneous velocity determines the next flow front position. The non-dimensionalized pressure gradient is related to the dimensionalized version by:

$$\frac{dP_R}{dx} = \frac{1}{L} \cdot \left( \frac{dP_R}{d\alpha_X} \right) \quad (5.26)$$

Combining this and Equation 5.1 for a discretized flow length movement over  $dt$  gives the incremental flow distance to add to the previous time step’s front position,  $x_{F0}$ :

$$x_F = x_{F0} + \frac{-K}{x_F \phi \mu(t)} \cdot \left( \frac{dP_R}{d\alpha_X} \right) dt \quad (5.27)$$

The new flow front position can be evaluated by rearrangement of terms and the quadratic equation:

$$x_F = \frac{1}{2} \left( x_{F0} + \sqrt{x_{F0}^2 - 4 \left( \frac{K}{\phi \mu(t)} \cdot \left( \frac{dP_R}{d\alpha_x} \right) dt \right)} \right) \quad (5.28)$$

The following time steps repeat this procedure of computing the pressure field for an adjusted available pressure gradient, and then calculating the movement of the flow front.

Figure 5.2 implies that these models for the capillary pressure predict a large drop or rise in the pressure as one moves from the resin at the front to the air on the other side of the front. The prediction of significant differences in the pressure on either side of the flow front makes these results questionable. A more accurate model may be some combination of addition and subtraction effects to the available pressure gradient to achieve the vacuum pressure at the flow front. This would entail changes to the velocity other than from cover movement though. The conclusion seems to be that the capillary pressure can significantly affect the pressure gradient, but how this happens is too much of theoretical conjecture at this point. Further experimentation is needed to establish these mechanisms.

A code for MATLAB, in which the fill times for all the possible combinations of these models is included in Appendix 5.

## 5.1 Sensitivity of results to each model

All modeling constants (including rapeseed oil wetted compressibility) and properties were input for the Baseline NCF in 1D flow along the stitches, at 24°C and  $P_A - P_V = 100$  kPa, to a length  $x_f$  of 250 mm. With the simplest model (no coupling), the time to fill was 473s. This was then compared to more complex combinations of the separate models to show the sensitivity of the flow prediction to each model. The variations were coded by the following acronyms (K = permeability; V = viscosity; C = compressibility; P+ = capillary pressure, increasing the available pressure; P- = capillary pressure diminishing pressure):

- K: constant  $\mu$  (for  $t = 0$ ), constant  $h$  ( $P_C = P_A - P_V$ ), and  $P_{cap} = 0$ , Equation 2.11
- KV: constant  $h$  and  $P_{cap} = 0$ , exponential  $\mu(t)$ , Equation 5.4
- KC: constant  $\mu$  and  $P_{cap} = 0$ , solve pressure field, Equation 5.24
- KVC:  $P_{cap} = 0$ , solve pressure field,  $\mu(t)$ , Equations 5.4 and 5.24
- KP- / KP+: constant  $\mu$  and  $h$ ,  $P_{cap}$  included in velocity evaluation, Equation 5.12

- KVP- / KVP+: constant  $h$ ,  $P_{cap}$  included,  $\mu(t)$ , Equations 4.23 and 5.12
- KCP- / KCP+: constant  $\mu$ ,  $P_{cap}$  included, solve pressure field, Equation 5.28
- KVCP- / KVCP+:  $\mu(t)$ ,  $P_{cap}$  included, solve pressure field, Equations 4.23 and 5.28

The results of predicted fill times for the baseline-0°, 250 mm infusion, as well as 500 mm, and their equivalents for baseline-90° flow and T1(12)-0° flow are listed in Table 5.1. One can see that longer length and the lower permeability of the 90° tests result in greater differences between the modeling combinations. The effect on fill time for adding the exponential viscosity model increases with the time to fill as the viscosity slows things down. The compressibility models make steeper pressure gradients at the last node than a linear gradient, thus increasing the velocity, and decreasing the fill times. The “P+” models show significant decreases in fill times as the velocity is magnified. The “P-” models show an even greater change in the fill time, in the opposite direction. Table 5.2 illustrates this, where the fill times for the K and all “P+” and “P-” models are shown.

Table 5.1 – Fill time comparison between model coupling combinations.

<i>Infusion</i>	<i>L</i>	<i>Fill time (s) for coupled models</i>								
		<i>K</i>	<i>KV</i>	<i>KC</i>	<i>KVC</i>	<i>KP+</i>	<i>KVP+</i>	<i>KCP+</i>	<i>KVCP+</i>	<i>KVCP-</i>
baseline 0	250 mm	473	486	421	431	386	394	351	358	557
baseline 0	500 mm	1998	2261	1769	1971	1588	1748	1436	1564	2720
baseline 90	250 mm	789	825	674	700	636	659	559	577	911
baseline 90	500 mm	3154	3886	2695	3205	2520	2957	2203	2527	4438
T(1)-12 0	1 m	2184	2502	2051	2328	1921	2161	1812	2024	2765

Table 5.2 – Fill time comparison between capillary pressure model coupling combinations.

<i>Infusion</i>	<i>L</i>	<i>K</i>	<i>Fill time (s) for coupled models</i>							
			<i>KP+</i>	<i>KP-</i>	<i>KVP+</i>	<i>KVP-</i>	<i>KCP+</i>	<i>KCP-</i>	<i>KVCP+</i>	<i>KVCP-</i>
baseline 0	250 mm	473	386	620	394	642	351	540	358	557
baseline 0	500 mm	1998	1588	2718	1748	3238	1436	2348	1564	2720
baseline 90	250 mm	789	636	1048	659	1114	559	866	577	911
baseline 90	500 mm	3154	2520	4247	2957	5752	2203	3502	2527	4438
T(1)-12 0	1 m	2184	1921	2539	2161	2984	1812	2380	2024	2765

To compare the effect of the individual models on the fill time, the fill time for the “K” model was compared to the fill time for each 2-model combination. The percentage change in fill time for each is tabulated in Table 5.3.

Table 5.3 – Increase in predicted fill time by addition of independent models.

<i>Infusion</i>	<i>L</i>	<i>% Increase in fill time</i>			
		<i>K-KV</i>	<i>K-KC</i>	<i>K-KP+</i>	<i>K-KP-</i>
baseline 0	250 mm	2.7%	-11.0%	-18.4%	31.1%
baseline 0	500 mm	13.2%	-11.5%	-20.5%	36.0%
baseline 90	250 mm	4.6%	-14.6%	-19.4%	32.8%
baseline 90	500 mm	23.2%	-14.6%	-20.1%	34.7%
T(1)-12 0	1 m	14.6%	-6.1%	-12.0%	16.3%

The capillary pressure modeling and compressibility modeling have the least effect for the TFP material. The higher flow rates in the TFP due to the significantly higher permeability is the probably cause for this.

For the short length results ( $L = 250$  mm), the viscosity model is the least significant factor for the fill time. The compressibility is the next least significant factor for those short lengths and the smallest factor overall for the longer lengths. Afterall, the thickness differences for a flexible cover are confined mostly to the inlet half of the mold [180] due to the exponential character of the compressibility. Previous attempts at coupling compressibility modeling reported only 10 to 20 % differences and concluded that the sacrifice of computing time was not worth it [70,187]. The differences here are 6 to 15 % for these materials and these lengths, which falls within this range.

The most significant result from this sensitivity study is the significance of capillary pressure modeling in these flow predictions. Table 5.4 lists the % increase in fill time when each model combination without  $P_{cap}$  modeling is modified to include  $P_{cap}$  modeling. This suggests that for the slow flow in modern fabrics with low porosity, capillary pressure can be significant.

Of course, industrial practice commonly uses distribution media to speed up the process. But the slow flow will still happen through the thickness with DM. Hence this applies to any flow modeling for these fabrics.

Table 5.4 – Increase in predicted fill time by addition of capillary pressure model.

Infusion	L	% Increase in fill time					
		K-KP+	K-KP-	KV-KVP+	KV-KVP-	KVC-KVCP+	KVC-KVCP-
baseline 0	250 mm	-18.4%	31.1%	-16.7%	35.7%	-24.3%	17.8%
baseline 0	500 mm	-20.5%	36.0%	-12.5%	62.1%	-21.7%	36.1%
baseline 90	250 mm	-19.4%	32.8%	-16.5%	41.2%	-26.9%	15.5%
baseline 90	500 mm	-20.1%	34.7%	-6.2%	82.4%	-19.9%	40.7%
T(1)-12 0	1 m	-12.0%	16.3%	-1.1%	36.6%	-7.3%	26.6%

As mentioned in Section 4.2.4, permeability testing was conducted in a separate study for the baseline material [77]. The unsaturated wetting permeability  $K_0$  in that study was reported to be 70% of the saturated permeability. Fill time is inversely proportional to the permeability, thus this equates to a 30% increase in unsaturated fill times compared to those for saturated testing. This difference can be logically attributed to the elimination of the pressure loss from capillary pressure once all the tows are fully saturated. And the 30% increase in time compares favorably for the baseline material predictions when adding capillary pressure in Table 5.4.

The baseline test case was simulated in PAM-RTM for validation of the model for baseline 0° flow. A fine mesh was generated with constant size triangle shell elements, and then scaled down in the 90° direction to have an  $x$ - $y$  aspect ratio  $\lambda = 0.75$ , approximately equal to  $(K_0/K_{90})^{1/2}$  (Figure 5.3). For the “K” case, the time to reach 250 mm was 468 s. This compares well with the 473 s for “K” in Table 5.1.

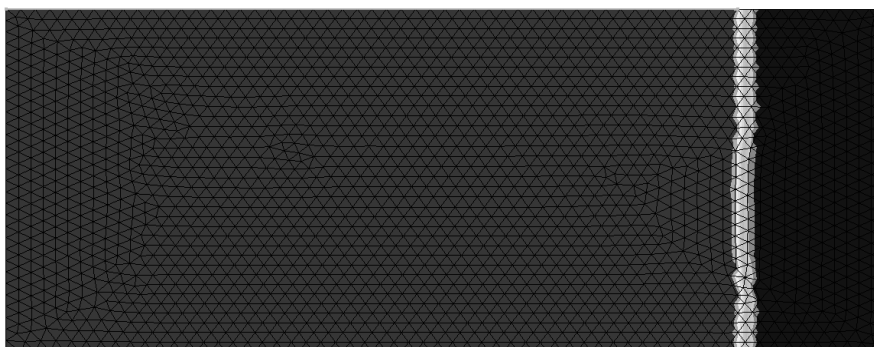


Figure 5.3 – PAM-RTM mesh with aspect ratio for  $(K_0/K_{90})^{1/2}$ .

## 5.2 Comparison with VARI experiments

The baseline material was infused in the benchmark VARI testing in Section 4.1. Two tests were done for the 0° flow; the first was at an initial  $T = 24^\circ\text{C}$ , and the second was at an initial  $27^\circ\text{C}$ . It took 55 min to reach the 160 mm mark at  $24^\circ\text{C}$  and 40 min at  $27^\circ\text{C}$ . The coupled 1D flow model vastly underpredicts this, however. The “KVCP+” model predicts 2.5 minutes, and the “KVCP-” model predicts less than 4 minutes at to 160 mm at  $24^\circ\text{C}$ . At  $27^\circ\text{C}$ , nearly identical fill times are predicted. Clearly, either the modeling data is not accurate to this material/infusion, or something slowed the flow down in the VARI testing that is not accounted for in the 1D coupled model. The experiments show lower fill times for the higher temperature, thus the viscosity exotherm has not yet become significant.

The experimental results for the square of the length are plotted against the time in Figure 5.4 for the  $27^\circ\text{C}$  baseline  $0^\circ$  and  $90^\circ$  infusions. Darcy-type flow should show linearity for such a plot. One can see that at 40 minutes, a “droop” in the profiles is seen, presumably due to the accelerating reaction rates of the curing. This increases the viscosity more and more with time and “drags” the flow. Assuming about 15 minutes between first contact of resin components, this gives about an hour of time after mixing before significance of curing, which agrees with previous findings in this study. But the plots before this time show fairly linear character. It is doubtful that this late effect of viscosity is causing the great discrepancy between experimental results and predictions.

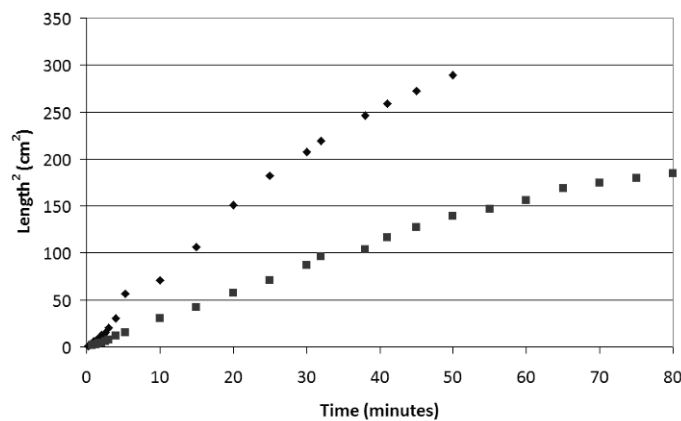


Figure 5.4 - VARI infusion  $L^2$  vs.  $t$ , 0 to 80 min (◆:  $0^\circ$  flow, ■:  $90^\circ$  flow).

A closer examination of the same profiles at low times (0 to 5 min) shows an initial “sagging” in the profile (Figure 5.5). Linear fits of the data to this point, forced through the origin clarify the curve to the profiles. This droop in the flow profile could be caused by the geometry of the inlet, or some initial loss in pressure.



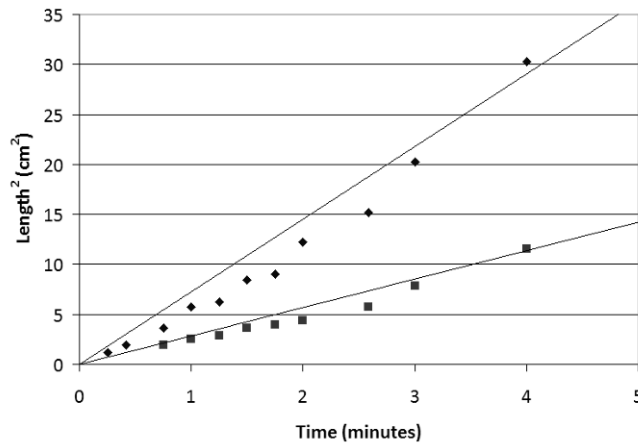


Figure 5.5 - VARI infusion  $L^2$  vs.  $t$ , 0 to 5 min (◆: 0° flow, ■: 90° flow).

### 5.3 Complex flow dimensionality

As mentioned in Section 4.1, the omega tube for the VARI infusions was placed on top of the preform and only over ~125 mm of the total 150 mm width of the preform. Thus, it has to fill in the through thickness direction to the bottom of the preform, and to the back and sides of the omega tube before it can assume true 1D flow towards the vent at the other end. As discussed in Section 4.6.2, any dimensionality besides exclusive 1D flow will result in lower pressure gradients in any flow direction as the pressure must be spread in multiple directions.

This flow geometry is neither 1D, nor perfectly radial, nor perfectly spherical due to mold constraints. Thus it is difficult to model analytically. FEM based methods can simulate such a flow [150]. A simulation of this flow geometry, including orientation of the inlet, was performed for 3D tetrahedral in PAM-RTM. A view of the under-side of the preform, directly below the omega tubing shows a complex wetting pattern to fill in all of the corners (Figure 5.6). Note: due to symmetry, this is a half-mesh of the part width, thus this model splits the omega tube inlet in half at its middle. The more wetted corner of Figure 5.6 corresponds to the middle of the part as the omega tube extends to the end of the mesh there.

Even late into the infusion, the pressure gradient is not linear by the inlet, although it is fairly linear through most of the length. This is seen again in the PAM-RTM simulation pressure output (Figure 5.7), where the different shades of blue and green correspond to  $P_R$  (resin pressure) isobars. Under the inlet, the isobar is still curved, but it is more and more linear along the flow length.

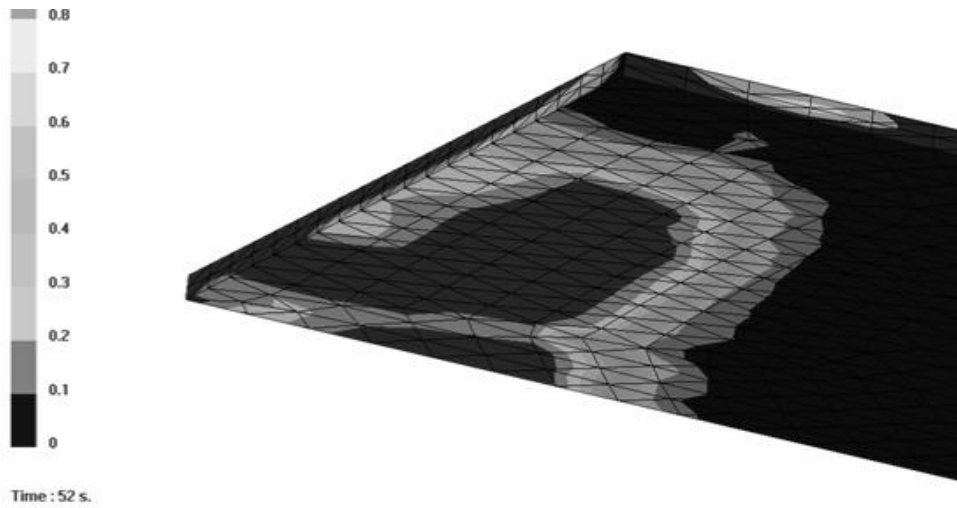


Figure 5.6 - PAM-RTM 3D simulation of VARI infusion: resin filling at 52 s.

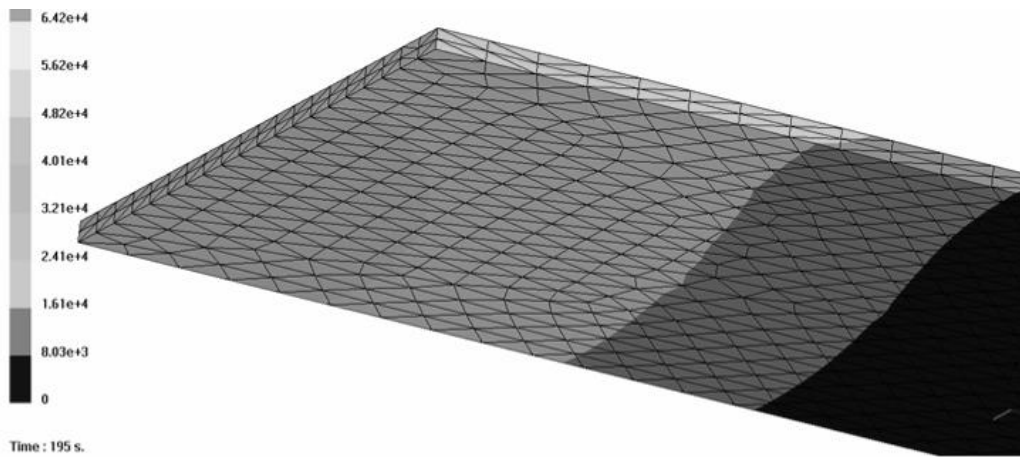


Figure 5.7 - PAM-RTM 3D simulation of VARI infusion:  $P_R$  at 195 s.

The above 3D model in PAM-RTM was evaluated with the non-constant isothermal viscosity model at 24C, constant thickness and  $P_{cap} = 0$ . These are the conditions for the “KV” test from above.  $K_{xy}$  data was used from the results of experimentation in Section 4.2. A guess value of  $1e-13$  m<sup>2</sup> was used for  $K_{zz}$ . Experimental data from Section 4.3 was not used for  $K_{zz}$  as it has not yet been adjusted for  $P_{cap}$  and viscosity. The aspect ratio was set as close as could be with tetrahedral to the square root of the permeability ratios. For 0° flow,  $t_{16}$  was ~600 s. For the same model implemented in shell elements (no z-direction flow), with the same inlet geometry,  $t_{16}$  was only 210 s. This 2D shell model was then modified so that the inlet nodes extended along the entire width of the part. This in essence makes it 1D flow. The time to 160 mm further dropped to ~195 s.

The 1D coupled solution “KV” test for equivalent flow modeling numerically resulted in  $t_{16} = 207$  s. This is in between the 1D and 2D PAM-RTM simulation results, which are very close to each other. Thus, the difference between inlet across the entire width, and only 80% of the width is not very significant. The coupled model presented here shows good agreement with PAM-RTM simulation results for strictly in-plane flow.

By adding the 2 mm of part thickness to the flow dimensionality in PAM-RTM however,  $t_{16}$  is increased by 3x (210 s to 600 s). As seen in Figure 5.7, the pressure isobars resemble 1D flow along the length of the part as the flow gets farther from the inlet. But there is a lag between the flow front on the bottom and the flow front on the top as the through-thickness flow must wet the bottom before 1D flow can be achieved, and  $K_{zz}$  is lower than  $K_{xy}$ . This lag has been verified in experiment and shown to dissipate away from the inlet [138, 46]. [315] reported the lag length to be linearly dependent on  $n$  (ply count). The lag can be very short and difficult to characterize however, as seen in the minimal top to bottom flow differences in Section 4.1.

Another way to quantify the difference between this constrained 3D and exclusive in-plane flow is by performing experimental infusions with forced in-plane flow. The  $K_{xy}$  testing in Section 4.2 had forced in-plane flow, but this was for a rigid cavity. In a VARI environment, forced in-plane flow could theoretically be achieved by placing an inlet runner along the entire thickness at one end of the fabric (instead of on top).

Various supplemental VARI infusions were performed with the omega tube inlet placed so that the inlet runner covered the entire end of the preform (Figure 5.8). It proved slightly difficult to place the tube in a way that the inlet channel would stay around the entire end. To facilitate this, the omega tube inlet channel was widened with a razor (Figure 5.9).



Figure 5.8 – Omega tube placement to cover the end of the fabric stack (L: top, R: bottom).

In a head-to-head comparison of 2-ply NCF-6K 90° flow infusions with omega tubing on the top, and omega tubing around the end, placement of the inlet around the end resulted in significantly faster flow. Figure 5.10 shows the time and flow length history for each, both monitored on the

top of the mold and bottom. Again, any flow lag between the top and bottom was difficult to measure. But the bulk flow rates were very different. For the inlet on top,  $t_{16} = 104.6$  min, and for the inlet around the end,  $t_{16} = 48.8$  min. This is under half of the time, confirming that the pressure loss for through-thickness flow is significant.

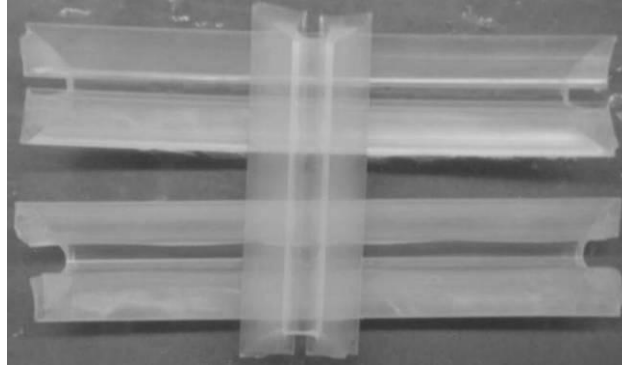


Figure 5.9 – Unmodified omega top (top) and with widened inlet channel (bottom).

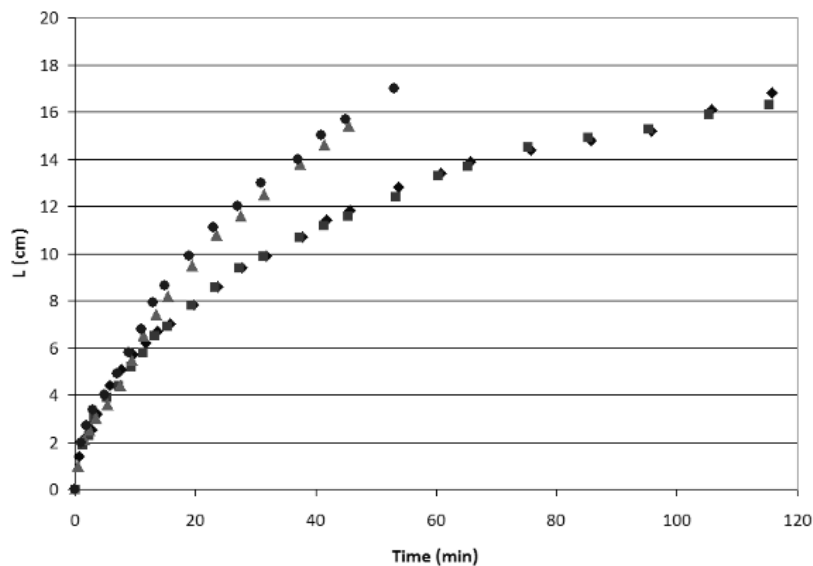


Figure 5.10 – Comparison of NCF-6K 90° flow: inlet on top of fabric (◆: top, ■: bottom) and inlet around end of fabric (▲: top, ●: bottom).

Table 5.5 lists the experimental and predicted values for  $t_{16}$  for various baseline 4 layer 0°-flow infusions. The first two rows are from the VARI infusions in Section 4.1. The second two rows are results from supplemental infusions comparing the inlet placement location. As the temperature was different from infusion to infusion, the viscosity plays a significant role in differences in  $t_{16}$ . Thus, each infusion is compared to the coupled model prediction by the ratio of  $t_{16}$ . The model incorporates the temperature dependence of viscosity; the differences between experimental and theoretical  $t_{16}$  should be independent of the viscosity changes.

Table 5.5 – Comparison of experimental and predicted  $t_{16}$ .

$T(^{\circ}C)$	$\Delta P$ (kPa)	Inlet	Experimental $t_{16}$	Predicted $t_{16}$	Experimental $t_{16}/$
			(min)	(min)	Predicted $t_{16}$
24	93.5	top	55.3	4.220	12.44
27	95.5	top	39.9	3.450	11.31
22	94.0	top	62.9	5.048	12.46
22	94.0	end	52.4	5.048	10.38

Once again, there is a significant decrease in  $t_{16}$  by moving the inlet from the top to the end. But the experimental  $t_{16}$  in this case is still almost 10 to 11 times that of the predicted time. This inlet placement may still not be resulting in total 1D flow due to local compaction of the fabric at the end by the omega tubing. It seems however, that the through-thickness flow can only account for a portion of the flow differences; something in addition is also slowing the flow.

#### 5.4 Other possible sources of flowrate reduction

Some other possible causes of the slower experimental flowrate are discussed here:

##### *Under-predicted capillary pressure*

The application of the dynamic contact angle from Equation 4.33 in predicting  $P_{cap}$ , instead of the static contact angle implies reduced wetting due to flow velocity. Equation 4.33 is based on empirical constants for similar materials, but may not be accurate to this situation. Substitution of lower contact angles in Equation 4.30 to predict the capillary pressure would result in higher  $P_{cap}$ . For the 1<sup>st</sup> baseline 0°-flow infusion, the predicted value for  $P_{cap}$  at the flow front at 160 mm rises from 23.6 kPa to 27.2 kPa for such a change. Substituting  $\theta_{CS}$  for the contact angle in the “KVCP-“ model increases  $t_{16}$  for this case from 4.22 min to 4.78 min. This is an increase of 13%, which could contribute to the slower flow in experiments.

The model for the capillary pressure in Equation 4.30 may not adequately describe the full decrease in velocity due to dual scale flow. There maybe some other significant flow hindrance at these low velocities.

### *Other shear effects*

There may be some other shear effect between the flowing resin and carbon fiber that is not accounted for in this model. This shear effect may be of a lesser magnitude for the paraffin oil – carbon interface. The epoxy is more of a polar hydrophilic substance than paraffin oil.

### *Permeability variation*

The aging of the material or the sizing may contribute to the slower flow. The in-plane permeability was shown in  $K_{zz}$  testing to be slightly lower for newer material of the same type when compared to material 14 months older. As mentioned in Section 4.3.3, a supplemental  $K_{xy}$  test showed in-plane permeability 34% lower for the newer material. But the age of the material used in the VARI experiments (Section 4.1) and  $K_{xy}$  testing (Section 4.2) was not noted. Thus the influence of this effect is impossible to predict. The high usual standard deviation in reported permeability values is a related source of error. But the  $K_{xy}$  results were in good agreement with a previous study and an analytical model (Section 4.2.4). And all the VARI infusions were significantly slower than their predictions, implying something besides random experimental error.

### *Inlet tube constriction*

[164] stated that  $P_i$  (pressure at the inlet in the mold) does not immediately go to  $P_A$  upon opening the inlet to start the infusion. There is some pressure resistance through the inlet pipe so that  $P_i$  rapidly increases from  $P_V$  to  $P_A$ . The pressure loss across the inlet tube was already deemed insignificant in Section 4.6.1. But perhaps a pressure loss results from local pipe constriction more than shear across the inner wall surface area at constant radius.

Examination by the author of the inlet pipe at the start of the infusion did indeed show slower movement than usual on occasion. This is thought to be due to the inlet tube being partially crimped by the stopper used to open and close the tube. This was evidenced by an increase in the resin flow rate in all cases as the stopper was opened more. During the VARI infusions in Section 4.1, neither the degree of pipe opening nor the initial resin flow rate in the inlet tube was noted. Thus the significance of this to simulation of the experimental flow cannot be determined.

### *Variation in ply count*

There were 6 layers in each NCF stack during  $K_{xy}$  testing in Section 4.2, to achieve appropriate  $v_F$  values at the minimum thickness of the test mold cavity. In the VARI testing, the NCF samples had four plies. An increase in ply count should imply higher nesting, thus a lower  $K$ . But the in-plane permeability tests achieved faster flow than the experimental VARI tests, so this cannot contribute to the slower flow. This phenomenon may cause slower in-plane flow in the  $K_{zz}$  tests where much higher ply counts were used. But this effect is assumed to be very small as in-plane flow measurements in  $K_{zz}$  testing involved only the top few layers to achieve the hemisphere shape (Section 4.3.1), and nesting is thought to be minimal in NCF materials.

#### *Loss of pressure at inlet*

Some measurements of the actual pressure on the resin by the inlet have recently been reported in which the pressure initially is much lower than predicted by modeling [313,314]. With time, the pressure field rises to meet predicted gradients. It has been suggested that this is due to a loss of the ambient pressure, either due to the inlet tubing geometry, or the evacuation of air from the tube as the resin fills it. This air must pass through the fabric and has a non-zero pressure loss associated with it.

## 5.5 Relative comparison of materials by fill time

The absolute comparison of values for  $t_{16}$  has shown significantly slower flow in the experimental results compared to the predicted. A relative comparison of the  $t_{16}$  values across materials for both experimental and predicted shows better agreement. Figure 5.11 shows the ratio of ( $t_{16}$  / ( $t_{16}$ ) of the first baseline infusion) for each VARI infusion in Section 4.1. This ratio was calculated for the predicted values of  $t_{16}$  as well (divided by predicted  $t_{16}$  of the first baseline infusion). Thus, the first baseline infusion shows a ratio of 1.0 for both.

90° flow in the baseline materials results in a ~1.8x higher  $t_{16}$  for both experiment and prediction. The differences in each for repetitions of the same material (example: the second baseline-0° infusion is lower) are influenced by minor changes in pressure and temperature. The experimental flow in the baseline NCF was faster than that for the NCF-6K and biax braids. But the predicted flow for the baseline NCF was slower than these materials. This may be due to differing ply counts between the  $K_{xy}$  measurements and the VARI experiments. This may also imply that race-tracking

increased the apparent flow, or problems with conforming to the mold shape occurred during  $K_{xy}$  testing.

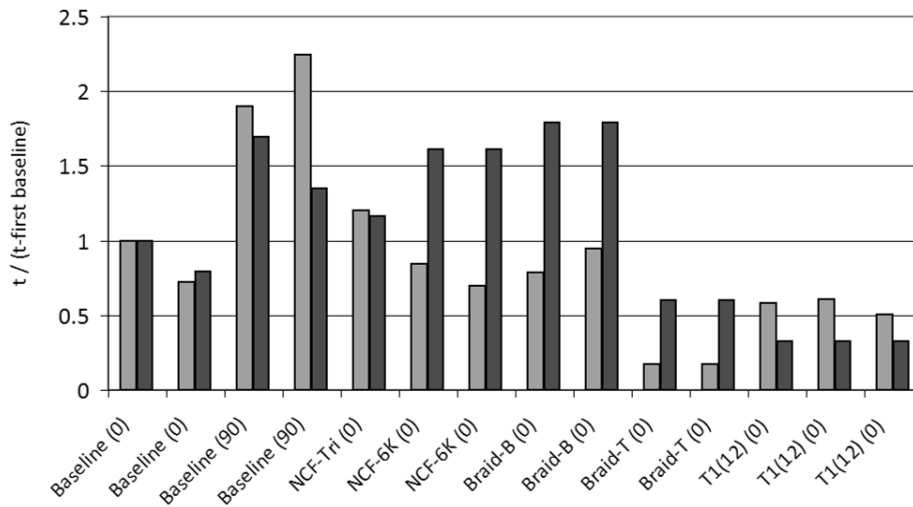


Figure 5.11 -  $t_{16}$  normalized by  $t_{16}$  for the first baseline infusion (light: experimental, dark: predicted).

## 5.6 Updating $K_{zz}$ test results for capillary pressure

As the coupled model evaluates the effects of  $P_{cap}$  at each point in the flow, the permeability used in the model must be independent of it. Unsaturated permeability tests only produce data for a particular development of  $P_{cap}$  dependent on the fluid-fiber sizing combination and flow orientation.

To demonstrate this, a calculation was made to determine the effects of capillary pressure on the relatively fast flow in the  $K_{xy}$  testing in Section 4.2. An average viscosity for the  $K_{xy}$  tests of 0.194 Pa·s was used. The surface tension for paraffin oil with a similar viscosity to that used in this study has been reported to be 0.0314 N/m [236]. For a 300 mm long sample, as used in  $K_{xy}$  testing,  $P_{cap}$  for the baseline 0° flow as per Equation 4.30 is 16.1 kPa. This is lower than the slower flow in the VARI experiments with an epoxy, as expected. But this is not an insignificant value and is why the saturated permeability testing results are used for flow modeling as they are determined independent of the capillary pressure.

In the case of  $K_{zz}$  testing, only unsaturated flow was able to be monitored. And these tests were done using the curing epoxy. Thus, the permeability results need to be adjusted for the capillary



pressure and the rising viscosity so that they may be applied to any other flow case with the same material.

All three components of the 3D permeability tensor were calculated from the  $K_{zz}$  test data in Section 4.3. Applying the 1D Darcy Equation to these resultant permeabilities with the same  $P_A$ ,  $P_V$ ,  $\mu$ , and porosity gives the 1D flow length-time relationship in each of the  $x$ ,  $y$ , and  $z$  directions. The flow will be faster in these calculations, as it assumes the entire pressure gradient is applied in the 1D flow direction, as opposed to distributed in all directions in a hemisphere. Applying the same time at the end of the  $K_{zz}$  experiment, the 1D flow length results for the “z2” test (constant thickness, viscosity,  $P_{cap} = 0$ ) are: ( $x_f$ ,  $y_f$ ,  $z_f$ ) 64.47 mm / 37.09 mm / 14.57 mm. Comparing these to the  $K_{zz}$  3D flow experimental results (36.5 mm / 21.0 mm / 8.25 mm), the 1D flow lengths are exactly 1.766 times the 3D flow length at this time, for all 3 directions. Thus, the 3D hemisphere point infusion results in 57% shorter flow lengths in any given direction when compared to pure 1D flow with the same properties.

For all infusions in fact, regardless of material, the ratio is about 1.8. The 1D/3D ratio for  $z_f$  (flow length in the z-direction) for each of the  $K_{zz}$  infusions is listed in Figure 5.12. The average of the ratios for all but the last two infusions is  $1.779 \pm 0.034$ . The two lowest thicknesses, for z12 and z14, are also the lowest ratios, so there may be a correlation to thickness. Cutting the pressure or time in half doubles the calculated permeability (calculations per Figure 4.31), but results in no change in the ratio. Cutting the viscosity in half results in the inverse; the permeabilities are also decreased by 50%, but the ratios still remain unchanged. Only when one of the component radii values is changed from the measured values does this ratio deviate from this constant value.

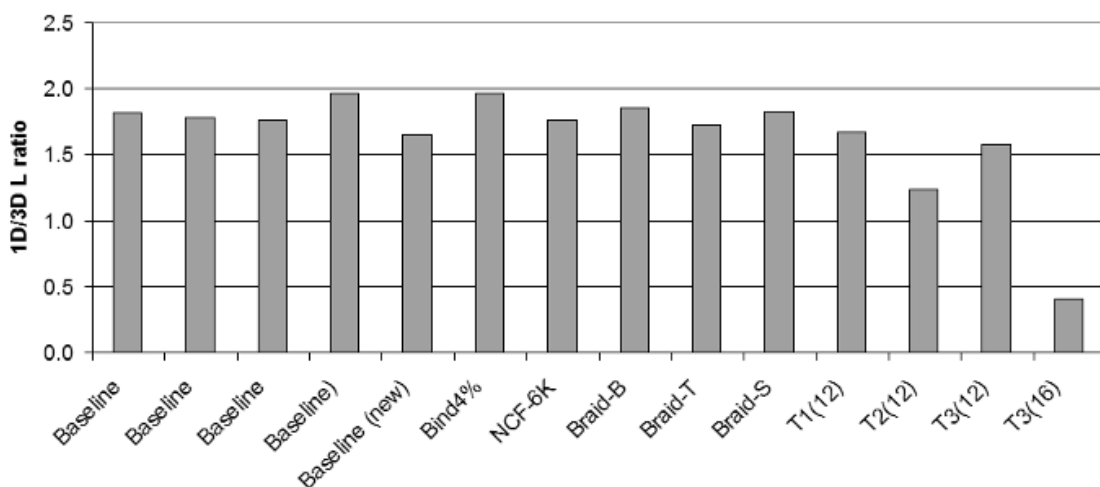


Figure 5.12: 1D/3D  $x_z$  ratio for  $K_{zz}$  infusions.

This supports the approach of evaluating Darcy's Law separately for each of the  $K$  tensor's directional components. The ratio simplification method was expanded to incorporate portions of the 1D coupled model. The isotropic transformation solution (Equation 4.6) was formulated for constant viscosity, thickness, and no capillary pressure. Part of this solution is the non-dimensionalization of all the variables. The infusion time is non-dimensionalized by dividing all times by the constant  $t_c$  [148]:

$$t_c = \frac{16\mu L_t \phi h^3}{P_l b_t^4} \quad (5.29)$$

This non-dimensionalization results in no further appearances of the viscosity or pressure in the model (implemented in Mathcad in Figure 4.31), they are all lumped into this expression. The pressure at the inlet,  $P_l$  is the gradient between  $P_A$  and  $P_V$ , reduced by any pressure loss in the inlet tube. As this pressure loss was determined insignificant for the infusions in this study (Section 4.6.1), and with the incorporation of capillary pressure,  $P_l$  becomes  $\Delta P$  as evaluated in Equation 2.42. In this exercise, the capillary pressure is subtracted from the pressure gradient. To apply the loss of a dynamic  $P_{cap}$  in Equation 5.29 would require a new solution of greater complexity. But the contributions of the capillary pressure can be estimated by incorporating the capillary pressure (as in Equation 4.30) with a constant contact angle given constant thickness.

Due to dynamic flow, the static contact angle  $\theta_{CS}$  is increased to the dynamic angle  $\theta_{CD}$  for this calculation. The stack height ( $h$ ) in the  $K_{zz}$  tests was anywhere from 0.945 mm to 0.4 mm. Z-direction flow of this length produces a minimum  $\theta_{CD}$  of  $30^\circ$  for the typical flowrates in those tests. This is only slightly higher than  $\theta_{CS}$ . At half of this thickness,  $\theta_{CD}$  is only  $\sim 31^\circ$ .  $\theta_{CD}$  decreases quickly from very high angles by the inlet to close to the static contact angle by the vent. This is because the flow slows down very rapidly with increasing length, especially in the case of 3D flow in a point infusion. Thus  $\theta_{CD} = 31^\circ$  is assumed for a middle value over the flow length for all capillary pressure calculations for the  $K_{zz}$  test data. This makes integration of  $t_c$  over time unnecessary as the pressure gradient is a constant.

A form factor of  $F = 2.5$  is assumed for the evaluation of  $P_{cap}$  in the point-infusion experiments. This is a middle value between the assumed in-plane value of 3 (Section 4.6.3) and the reported value of  $\sim 2$  for z-direction flow in a plain weave [232].

Use of Equation 5.29 implies constant viscosity, but it could accommodate a constant total contribution of viscosity over the experiment time, as is done for the fully coupled model above. In the 1D Darcy equation, the  $\mu(t)$  model from Section 4.5 was integrated with respect to time and then multiplied by  $C$  representing the other side of the equation (the side evaluated with respect to  $x$ ). This same integrated  $\mu(t)$  expression can be applied to Equation 5.29 to yield  $t_c$  modified for the total contribution of a dynamic viscosity over the flow time:

$$\frac{dt_c}{\mu(t)} = \frac{16L_t\phi h^3}{\Delta P b_t^4} dx \quad (5.30)$$

where  $\Delta P$  is the new pressure gradient incorporating a constant reduction by  $P_{cap}$ . If  $C$  is the other side of  $dt/\mu(t)$ , then from Equation 5.4:

$$t_c = \frac{1}{B_v} \ln \left( \frac{1}{1 - \left( \left( \frac{16\mu L_t \phi h^3}{P_t b_t^4} \right) dx \right) A_v B_v} \right) \quad (5.31)$$

The change in length and width of the sample due to compression from  $z$ -direction flow is assumed to be negligible. Regardless, compressibility modeling is excluded from these calculations as compressibility was shown to be the least significant of each of the models.

Mathcad was again used to evaluate the permeability components (Figure 4.31). Substitution of Equation 5.31 in the isotropic transformation solution with ratio simplification (Section 4.3.2.3) does in fact yield higher permeability components, now that they are evaluated independently from the viscosity development and  $P_{cap}$ . Table 5.6 lists the permeability components, as well as the percent increase for each compared to the earlier results listed in Table 4.6.

The values for  $K_{zz}$  for the NCF materials of  $\sim 1e-13 \text{ m}^2$  are consistent with measurements made elsewhere for other carbon NCF's [191,242]. The in-plane permeabilities are still much lower than those predicted for these  $v_F$ 's from the  $K_{xy}$  testing in Section 4.2. The lower in-plane permeability for these measurements using an epoxy supports the idea that some shear effect between epoxy and carbon is reducing the flow rate from that predicted with permeabilities measured with paraffin oil. A one degree order of magnitude difference between in-plane and out of plane

permeabilities is evident in most of the data, as has been reported in many sources elsewhere for composite reinforcements.

Table 5.6 – Updated point-infusion  $K$  components, and % increase from earlier results.

ID	material	$v_F$	Updated $K$ components			% increase over previous		
			$K_{xx} (m^2)$	$K_{yy} (m^2)$	$K_{zz} (m^2)$	$K_{xx} (m^2)$	$K_{yy} (m^2)$	$K_{zz} (m^2)$
z1	Baseline	0.585	2.67E-12	1.24E-12	1.46E-13	21.8%	21.8%	21.8%
z2	Baseline	0.571	1.82E-12	6.01E-13	9.85E-14	16.6%	16.6%	16.6%
z3	Baseline	0.588	3.17E-12	1.34E-12	1.84E-13	23.3%	23.3%	23.3%
z4	Baseline)	0.568	3.67E-12	1.35E-12	1.33E-13	16.1%	16.1%	16.1%
z5	Baseline (new)	0.607	1.60E-12	6.19E-13	1.10E-13	24.8%	24.8%	24.8%
z6	Bind4%	0.578	1.88E-12	1.09E-12	1.16E-13	14.7%	14.6%	14.7%
z7	NCF-6K	0.611	2.51E-12	1.09E-12	1.33E-13	26.0%	26.1%	26.0%
z8	Braid-B	0.641	8.75E-13	8.09E-13	4.71E-14	31.9%	31.9%	31.9%
z9	Braid-T	0.530	4.82E-12	3.45E-12	1.81E-13	18.1%	18.0%	18.0%
z10	Braid-S	0.573	2.63E-12	2.17E-12	1.48E-13	20.4%	20.4%	20.4%
z11	T1(12)	0.490	4.71E-12	4.24E-12	5.36E-13	15.7%	15.8%	15.7%
z12	T2(12)	0.470	2.28E-12	2.08E-12	3.00E-13	14.7%	14.8%	14.7%
z13	T3(12)	0.478	7.36E-12	6.39E-12	1.11E-12	15.6%	15.6%	15.6%
z14	T3(16)	0.491	7.82E-13	7.82E-13	4.88E-13	14.9%	14.9%	14.9%

## 5.7 Bonded samples permeability determination

No trustworthy in-plane permeability data for the bonded samples due to problems with conforming to the mold shape (Section 4.2.3.4). But an approximate permeability can be calculated by comparing the times to the length milestones between the bonded samples and the baseline un-bonded material, for which the permeability was well characterized. Assuming all other parameters in Darcy's Law are equal for baseline and bonded samples, the permeabilities and times to a particular length are inversely proportional:

$$\frac{K_{baseline}}{K_{binder}} = \frac{t_{binder}}{t_{baseline}} \quad (5.32)$$

This assumption of constant parameters nullifies the compressibility differences for fabric architecture, as well as the capillary pressure and viscosity differences for the slower flow. Adjustments for these could be modeled into this calculation. But for now, the approximation of constant effects from viscosity, compressibility, and  $P_{cap}$  is used. In-plane permeability data for the baseline material comes from the measurements in Section 4.2. A  $v_F$  of 60% was assumed, for which  $K_0 = 6.26e-11 \text{ m}^2$  and  $K_{90} = 3.80e-11 \text{ m}^2$  for the baseline material. The time to reach 100 mm, as well as 160 mm for the bindered NCF infusions were compared to the times for their unbindered equivalent and bindered permeabilities were calculated per Equation 5.32. The results are shown in Table 5.7. The calculated permeabilities from  $t_{10}$  and  $t_{16}$  times were averaged for the  $0^\circ$  flow. The  $90^\circ$  flow infusions of bindered materials never made it to 160 mm flow length due to resin gelation.

Table 5.7 – Calculation of bindered NCF permeabilities from a flow progression comparison.

<u>Material / Direction:</u>	$0^\circ$	$0^\circ$	$0^\circ$	$90^\circ$
Baseline (60% $v_F$ )	6.26 E-11	6.26 E-11	6.26 E-11	3.80 E-11
	<i>t<sub>10</sub> results</i>	<i>t<sub>16</sub> results</i>	<i>average</i>	<i>t<sub>10</sub> results</i>
Bind1%	7.09 E-11	7.18 E-11	7.13 E-11	1.18 E-11
Bind2%	2.39 E-11	1.93 E-11	2.16 E-11	5.56 E-12

The 1% bindered NCF infusion along the stitching achieved slightly faster flow than the unbindered NCF. This is thought to be caused by some type of edge effects, as the application of binder decreased all other calculated permeabilities.



## 6 Final part quality characterization

This section details the characterization of final composite parts. Various methods to measure the fiber volume content and the void content were employed. These methods were compared to determine the best method based on difficulty and applicability to the composite materials in this study.

Later in this section, a comparison of resultant  $v_F$  and  $v_D$  will be made for various VAP membranes. The  $v_F$  and  $v_D$  will then be compared to shear strength results for the same samples. This is all done as a demonstration of the applicability of the measurement methods and their correlation to final mechanical properties.

### 6.1 Fiber content measurement methods

#### 6.1.1 Density

Density measurements were performed with a Mettler Toledo mass balance and its “density accessory kit”. A sample of the material is weighed when dry ( $M_D$ ) and then immersed in water ( $M_W$ ). The density of the sample,  $\rho_T$  is then:

$$\rho_T = \frac{M_D}{M_D - M_W}(\rho_W - \rho_A) + \rho_A \quad (6.1)$$

The density of air is assumed to be  $\rho_A = 1.2 \text{ kg/m}^3$ . The density of water,  $\rho_W$  is dependent on the temperature, which was measured during each weighing. Tables for the temperature-dependent density of water are readily available in the literature or on the internet.

The fiber volume content,  $v_F$  can be determined from the sample density. In the case of NCF materials it must incorporate any difference in the density of the stitching,  $\rho_S$ . The stitching in all the NCF materials in this study is PES (polyethersulfone), for which  $\rho_S = 1370 \text{ kg/m}^3$  [316]. The  $v_F$  is then calculated from the rule of mixtures, and results in:

$$v_F = \frac{\rho_T - \rho_R}{\left[ \rho_F \left( 1 + \beta_S - \frac{\beta_S \rho_R}{\rho_S} \right) - \rho_R \right]} \quad (6.2)$$

The fiber density,  $\rho_F$  is assumed to be that of pure carbon ( $1760 \text{ kg/m}^3$  for these fibers from Toho Tenax).  $\beta_S$  is the ratio between the mass of stitching and mass of fiber in the sample. Saertex specifies an areal weight of  $534 \text{ g/m}^2$  of carbon, and  $6 \text{ g/m}^2$  of stitching in the baseline NCF fabric;  $\beta_S = 6/534$ .

A minor weakness to this method is its reliance on component densities, but measurements for these standard materials are widely reported in the literature. The major weakness of this method is its reliance on mass measurements while immersed in a liquid. Carbon/epoxy composite materials have a small degree of water absorption which makes the samples heavier than they should be. The surface is often pitted due to a peel-ply, which causes the samples to hold onto small air bubbles. This can be reduced by keeping finger oils off of the samples, applying a wetting fluid to the samples, slowly dipping them in the liquid, and brushing the bubbles off the surface once immersed. Despite all these efforts, the wet mass  $M_W$  was observed to continuously slowly increase/decrease in many cases. Thus measurements were taken early before more water absorption/bubble catching could throw off the results.

### 6.1.2 Acid digestion

The acid digestion tests were performed according to DIN 2564 with sulfuric acid and hydrogen peroxide. The  $v_F$  is calculated from the mass of the sample before and after solvent digestion. To accurately determine the fiber content of the sample from this test, the solvent resistance of each of the sample components must be known to both sulfuric acid and hydrogen peroxide.

Cured epoxy dissolves readily in these solvents. This is why the sulfuric acid/hydrogen peroxide solution is typically used for this test. The PES stitching has good resistance to the peroxide, but dissolves to some extent in concentrated sulfuric acid [317]. In all acid digestion tests, the appearance of white streaks in the remaining carbon fiber suggests that at least some of the stitching remains over the course of the acid digestion test. The nylon (polyamide) binder has no resistance to this solvent combination and should readily be dissolved with the resin [318].



If some PES remains the mass of the fibers is not the same as the mass of the residue. Assuming that a small portion (1/6) of the PES stitching remains ( $M_S$ ) with the fibers during solvent digestion, the mass of the carbon fibers ( $M_F$ ) can be determined from the total residue mass ( $M_{residue}$ ):

$$M_{residue} = M_F + M_S = M_F + (1/534)M_F = (535/534)M_F \quad (6.3)$$

Density data is also required in fiber content calculation from acid digestion test. The density of the non-carbon materials is calculated by the rule of mixtures. The resin  $\rho_R$  (1110 kg/m<sup>3</sup>) is about the same as polyamide (1100 kg/m<sup>3</sup>). As mentioned above the PES density is slightly higher (1370 kg/m<sup>3</sup>). The volume concentration of PES is only ~2% ; ROM results show that the higher density of PES results in little change to the bulk density of non-carbon materials. Thus, the bulk density of “everything else” is assumed to be that of the resin,  $\rho_R = 1110$  kg/m<sup>3</sup>. The  $v_F$  is related to the mass fraction of the fibers and the component densities, which after incorporation of Equation 6.3 becomes:

$$v_F = \frac{1}{1 + \frac{\rho_F}{\rho_R} \left( \frac{M}{M_{residue}} \frac{535}{534} - 1 \right)} \quad (6.4)$$

where  $M$  is the mass of the sample before solvent digestion.

### 6.1.3 Optical microscopy

A more direct method of measurement of  $v_F$  is employed using image analysis methods based on optical microscopy. Three methods of  $v_F$  measurement are detailed here: fiber areal percent, fiber count, and part thickness.

These methods require more sample preparation than the density or solvent digestion methods. Small composite samples (~20 mm long) are cut from the cured part with a diamond-tipped saw blade and oriented so that at least one fabric ply has fibers aligned perpendicular to the cut. The samples are mounted in epoxy plugs and the cross-section surface is polished. Samples were polished with traditional metallography methods: progressive polishing steps of decreasing grit size down to a fine diamond-slurry. The samples were then washed in an Ultrasonic bath.

For the fiber areal and fiber count measurements optical light microscopy was performed with a Leitz Metallux 3. The thickness measurements were either performed with the same Leitz

microscope, or an Olympus SZX10 for higher quality pictures at lower magnifications. An epoxy plug with a sample is placed in holding putty and placed under the microscope. The images were transposed to a computer through a camera mounted on the microscope and converted to digital images through DHS image analysis software. For all digital images, image analysis was performed using Image-J, a freeware public-domain Java-based program available on the internet. Image-J was developed at the National Institutes of Health as an open architecture program to enable customization for individual analysis tasks via Java plug-in's and recordable macros.

#### 6.1.3.1 Fiber areal percent

Once a digital image of the fibers is obtained, it must be cropped down to only include fibers pointing straight at the viewer (perpendicular to cut). Any color images must be split into three monochrome images (red, blue, and green). A Gaussian blur filter followed by contrast enhancement cleans the image of any artifacts between the fibers. The monochrome image must then be converted to a binary image of black (resin) and white (fibers) (Figure 6.1). The threshold gray level that delineates between the fiber and the matrix is difficult to determine manually with precision [160]. To remove any operator subjectivity Image-J has various algorithms for automated thresholding. A survey of these different algorithms is found in [319]. The “Shanbhag dark” algorithm was experimentally determined to establish the most appropriate threshold in the composite samples in this study.

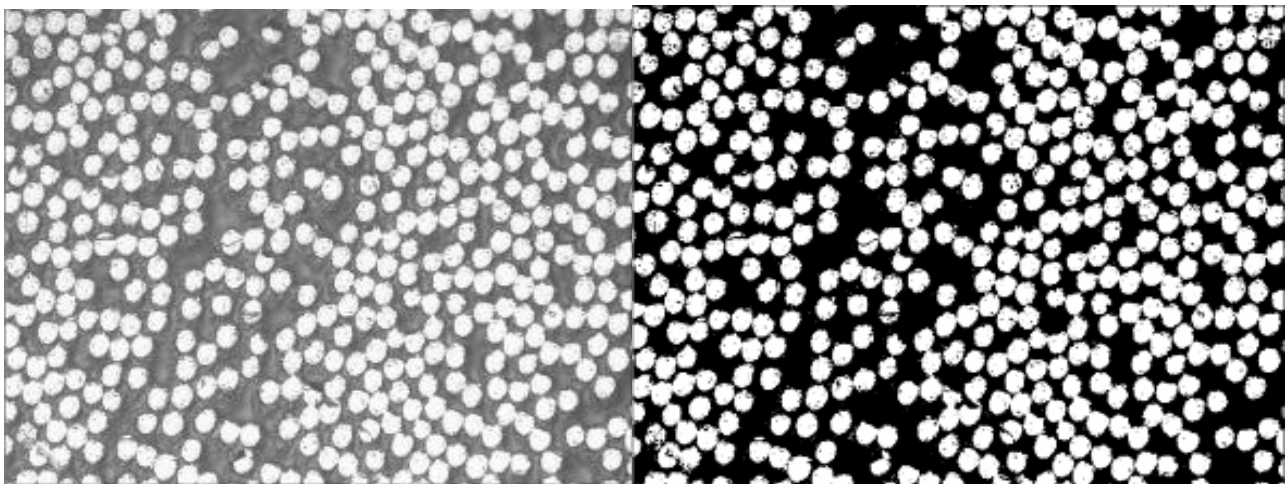


Figure 6.1 – Example color image (left) and resultant binary image (right).

Once all the pixels are defined as either fiber or resin, Image-J simply calculates the percentage of the white pixels in the sample, which is the resultant  $v_F$  value. Little variation exists between the

calculated areal  $v_F$  for each of the three monochrome images. Thus measurements are averaged between the result for the red, green, and blue images. This image analysis was automated by creating a macro script in Image-J to run all of these steps on each image in a designated file directory and output the list of results for export. Two versions of the script are included in Appendix 5: one is optimized for images at 500x magnification, and the other for images at 200x.

#### 6.1.3.2 Fiber count

The fiber count method of  $v_F$  determination requires all the same sample preparation steps as in the fiber areal percentage method. After thresholding, the binary image must have a watershed applied to it to separate each of the fibers. This step looks for separate shapes by their curvature and applies a 1-pixel wide empty line in between each. The “analyze particles” command in Image-J then counts the number of shapes with a surface area within designated min and max limits. This is the number of fibers in the image. As the diameter of each fiber is controlled in the manufacturing process, the surface area of each fiber times the fiber count determines the total fiber surface area in the image. This divided by the total area of the image is the resultant  $v_F$  value.

The limits on particle size must be optimized to include all the fibers, but not any artifacts that do not represent fibers. With adequate polishing and constant lighting across the sample, the fibers should be about the same size when converted to binary white circles. It was found that setting the minimum surface area to 400 pixels<sup>2</sup> resulted in optimum inclusion of fibers and exclusion of non-fiber white shapes for images at 500x magnification. This is about half of the surface area of a fiber. An example of this particle analysis is shown in Figure 6.2, where the binary image from Figure 6.1 (with white and black switched) results in the defined particles set show in the right-hand image.

The conversion between pixels and SI units is done by taking images of a micro-scale ruler at each magnification. The distance in pixels between some arbitrary length on the micro-scale (2 to 0.1 mm for 50x to 500x) is measured. The ratio of pixels to mm allows the calculation of the height in mm for any distance in pixels.

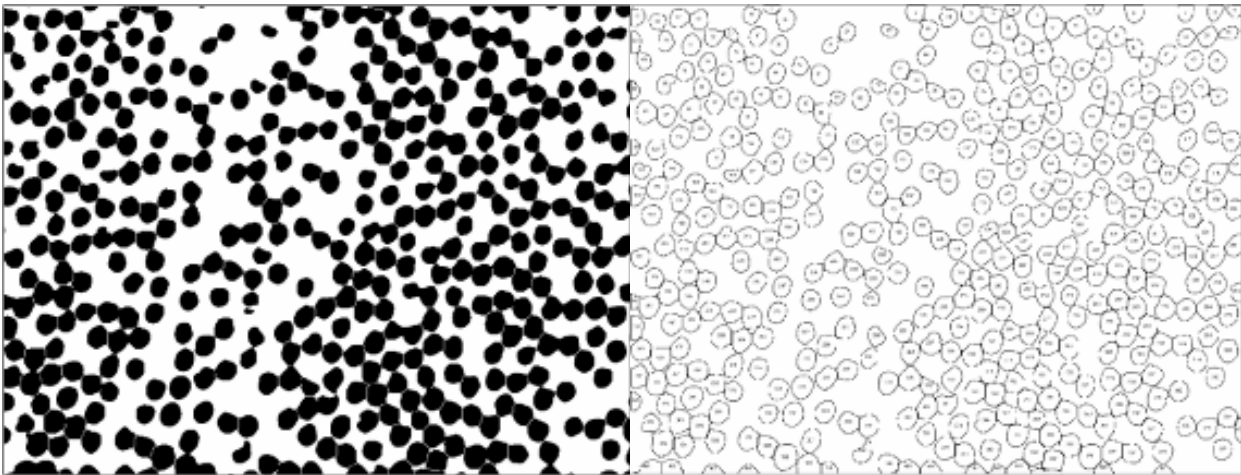


Figure 6.2 – Example binary watershed image (left) and resultant particle analysis (right).

A half-fiber size limit counts anything on the edges that is more than half in the image. The limit leaves out any one that is less than half in the image. It is assumed that the distribution of fibers “more-than-half-in-image” and those “less-than-half-in-image” is approximately equal. If one counted both of these types of partial fibers in the total fiber count, then the  $v_F$  would be over-estimated by treating the fibers on the edge as full fibers. If one assumes that each more-than-half-in-image fiber on the image edge has a corresponding less-than-half-in-image fiber somewhere along the edge, where the sum-area of the pair of partial fibers is equivalent to the area of a complete fiber, then counting only the more-than-half-in-image fibers towards the total fiber count produces a valid representation of the image. An example of this is shown in Figure 6.3, which corresponds to the bottom-left hand corner of the binary image in Figure 6.2. If a more-than-half-in-the-image fiber is combined with a less-than-half-in-image fiber, a full fiber is counted towards the fiber count.

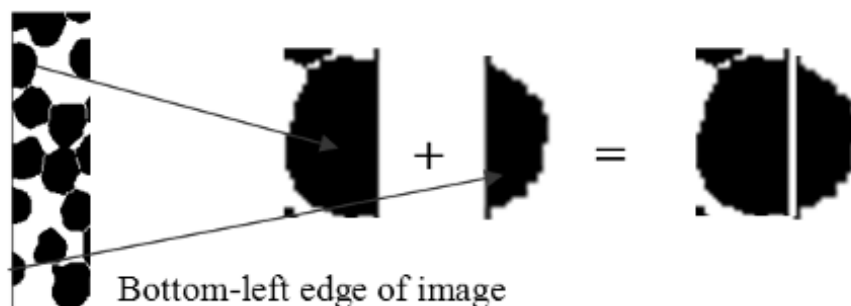


Figure 6.3 – Combining “more-than-half-in-image” fibers with “less-than-half-in-image” fibers.

This size of the fiber was verified by image analysis. An image of a single fiber was analyzed at 500x. A diameter of 43 pixels translates to 7.14  $\mu\text{m}$ , which is close to the reported value of 7  $\mu\text{m}$  from Toho Tenax. A higher magnification would be required for better resolution to make the pixel count more accurate, but would reduce the representation of the bulk material. The areal percentage of the square image when cropped to the diameter of the fiber also produced logical results. The default threshold algorithm resulted in an areal percentage of  $\sim 78\%$  which agrees with the ratio of the area of a circle inscribed in a square.

Some images showed unbalanced lighting; a corner or two were often visibly darker than the rest of the image. This was more evident with images at 500x than images at 200x. An example is shown in Figure 6.4 where the top left, and to a lesser extent, the top right corners, are darker than the rest of the image. When converted to a binary image, these fibers generate less areal content over the threshold. This prevents some fibers from appearing in the fiber count.

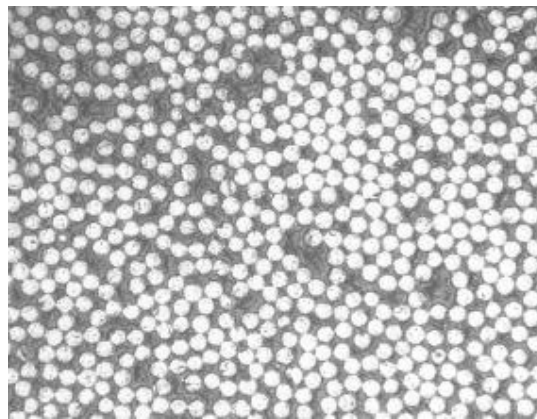


Figure 6.4 - Example image with non-constant shading.

There are two methods recommended by Image-J for background shading correction: either by manual correction from control images (before taking images), or “a posteriori” correction of sample images (after they have been taken).

The first step to manual shading correction is to check for any “hot-pixel” areas in the camera. By placing the camera over a dark surface, no particular location showed any “hot-pixels”. The second step is to convert an all-epoxy image in the microscope to a binary image to check for differences in the microscope lighting field. Figure 6.5 shows the results, clearly showing the darker top corners. The non-binary image was filtered with a Gaussian blur of 30 pixel radius to smooth out the micro-features in the epoxy surface. The resultant grey image can be “background-subtracted” from any later image to correct the dark corners.



Figure 6.5 – Binary image of plain epoxy showing dark lighting.

The “a posteriori” approach to shading correction is embedded in a macro for Image-J, created at the University of Reims [320]. A number of markers are spread regularly over the image. The background is modeled as a polynomial over those markers and the image is divided by the estimated background. Figure 6.6 shows a comparison between the two methods of shading correction and their resultant particle analysis fiber counts.

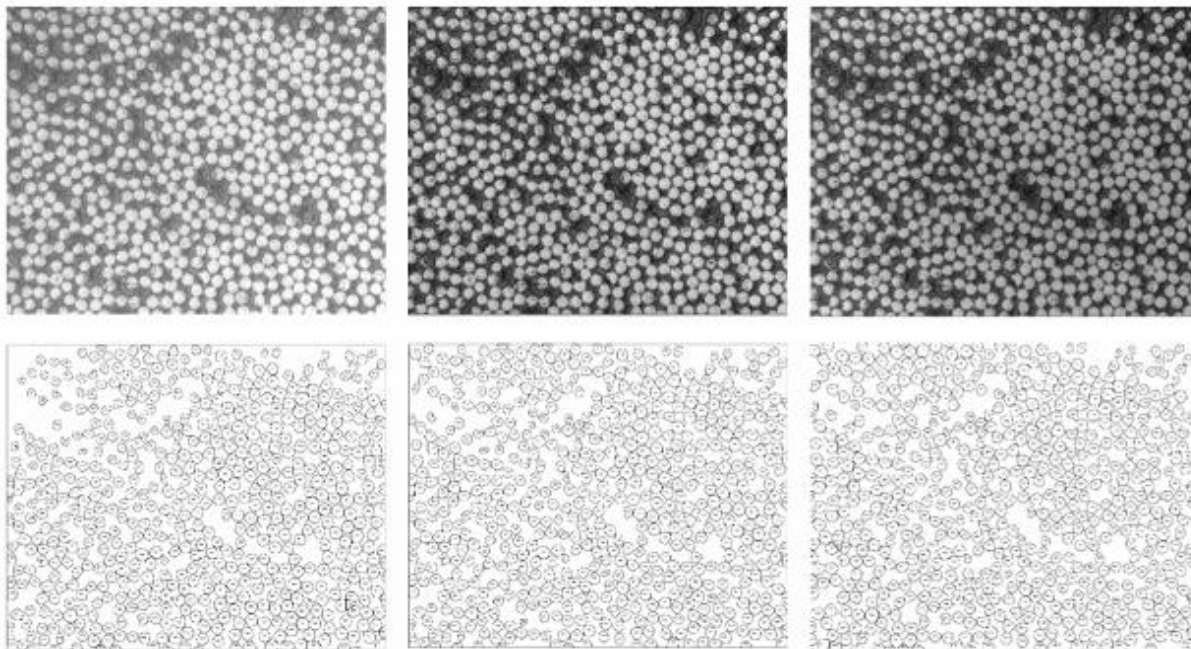


Figure 6.6 – Comparison of shading correction methods: (left) unmodified image, (middle) background subtraction, (right) “a posteriori” correction. Images in top row, resultant fiber counts in bottom row.

As seen in Figure 6.6, both lighting correction methods seem to restore the lost fibers in the dark corners; however the manual shading correction was considered inferior because the lighting field (seen in Figure 6.5) was not the same for all images, despite controlling camera rotation. To

eliminate the need to apply a new background-subtraction image every time, the “a posteriori” macro method was deemed as the better choice for lighting correction.

Macro scripts were written to automate all of the tasks in this fiber count analysis method and apply them to all the images in an entire designated file directory. The scripts incorporating “a posteriori” shading correction, for both 500x and 200x magnification images are included in Appendix 6. Note that 200x images encompass more of the bulk and are hence a representation of more of the sample; however 500x images provide more accurate fiber counts than 200x images as the fiber shapes are larger and easier to define.

A control group of composite samples was chosen for comparison of the four  $v_F$  measurement methods thus far discussed. The control group is the eight variations of bindered NCF’s in the parallel study on binder application effects reported in [15]. They are the 8 permutations from varying the binder content (0.5% and 1%), flow direction ( $0^\circ$  and  $90^\circ$ ), and binder application temperature ( $110^\circ$  and  $130^\circ$ ). Many replicate measurements (10 to 20) were performed with all measurement methods except for solvent digestion. Due to the difficulty, time, and hazardous chemicals required for this test, only one replicate measurement was made for each sample. Standard error bars are shown along with the results in Figure 6.7.

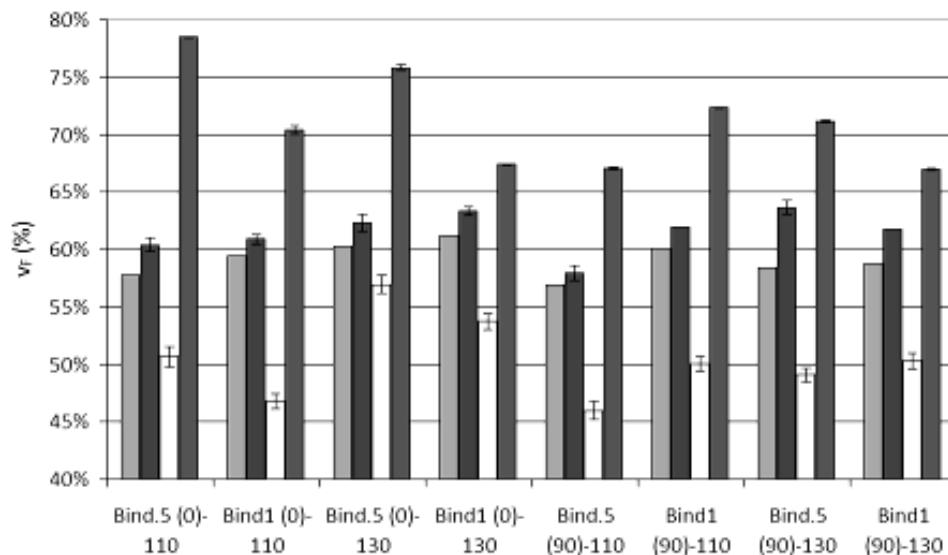


Figure 6.7 – Comparison of  $v_F$  measurement methods for bindered NCF control group (light gray: solvent digestion, black: density, white: areal, dark gray: fiber count).

The solvent digestion method is considered the benchmark method (the most accurate). One can immediately see that the fiber areal percentage method results in lower  $v_F$  measurements, while the fiber count method results in higher measurements. Density testing, despite the problems with porosity and air bubble adherence, gave results much closer to the solvent digestion results.

The low measurements in the areal percent method are attributed to the fragmenting of the fiber cross-sections as seen in Figure 6.1. The fibers are damaged when cutting the samples. The damage of the fiber ends from cutting is supposed to be mitigated by polishing. But the degree of polishing in these images appears to be insufficient to get an accurate areal shape of the fiber. Contrast Figure 6.1 to the shape of the fibers in Figure 6.8 – an image from a professionally polished sample included in a previous publication [160].

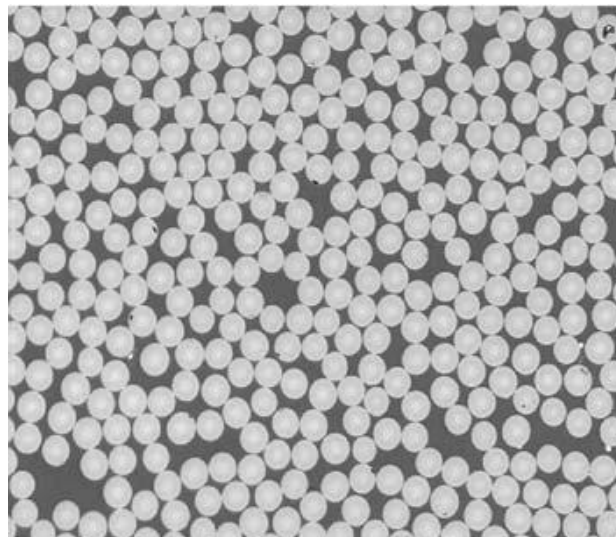


Figure 6.8 - Sample cross section with professional polishing [160].

The high measurements from the fiber count method are attributed to the choice of images. Each sample was panning over in the microscope to find areas of good fiber polishing. This implies that only the local areas of highest  $v_F$  were measured. Constraining the measurement to areas with perpendicular fibers means that the resin rich areas between the plies are not included. Both of these effects contribute to a higher measured  $v_F$  than should be reported.

Thus, the areal method requires very high polishing for accurate results, while the fiber count method suffers from the inability to examine the material bulk. The fiber count method was proposed as the best  $v_F$  measurement method in [160] for fairly homogenous prepreg materials. But the non-homogenous nature of these advanced preform materials require a better option.



### 6.1.3.3 Thickness

As per Equation 2.19, the  $v_F$  is a function of the preform thickness. Thus, with accurate areal weight, fiber density, and thickness measurements, a suitable determination of  $v_F$  can be obtained.

Measuring the thickness of a sample does not require lots of polishing or any image optimization. Polishing helps remove the “burring” of the edges from cutting, but very little coarse grain polishing all but eliminates any edge fragmentation.

Another advantage of the method is that results show a composite average of the entire thickness, so averaging the micro- and meso-level variation is achieved. The thickness should be measured from a magnification adjusted to fit the entire thickness in the image. Any thickness measurements of a partial thickness, even if multiplied to represent the full thickness, reduce the representation of the bulk variation in  $v_F$  in the through-thickness direction. Any non-fiber layers such as glass or resin pooling (Figure 6.9) must be included in the thickness measurements to encompass all contributions to the sample weight. Note that the  $v_F$  calculation does not include the non-carbon solids in the fiber mass. Increasing the thickness of resin or glass or binder material increases only the thickness and not the assumed fiber areal weight.

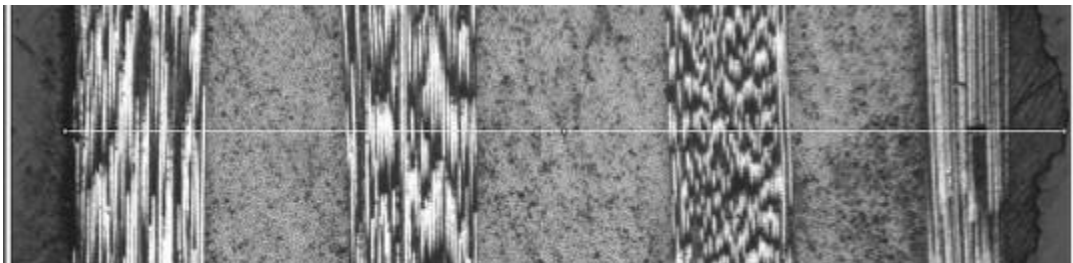


Figure 6.9 – Example thickness measurement for sample with pooled resin on one side.

Image-J has an easy tool to measure any distance in an image. This distance is in pixels, which must be converted to an SI length unit (meters) by the calibration mentioned above.

Thickness measurements made manually with calipers are easier than those made with microscopy analysis. Calipers, no matter how thin the contact area, measure the thickness of any ridge caused by micro-level variation. Thus they always show a larger thickness than the true average. This is illustrated in Figure 6.10 through a comparison between caliper and microscopy measurements. Caliper measurements were made along the length of each of the bindered

samples and then averaged into one thickness for each. This set of caliper measurements was repeated to measure the repeatability of the measurements. Both sets of measurements resulted in good consistency for each binder material. But they resulted in thicknesses 0.05 to 0.2 mm higher than microscopy based thickness measurements. These higher thicknesses resulted in lower calculated  $v_F$ 's than those measured by the acid digestion technique. The differences between samples are less apparent than with the microscopy-based measurements. Thus microscopy measurements would seem to be the only adequate method of thickness measurement for  $v_F$  calculation.

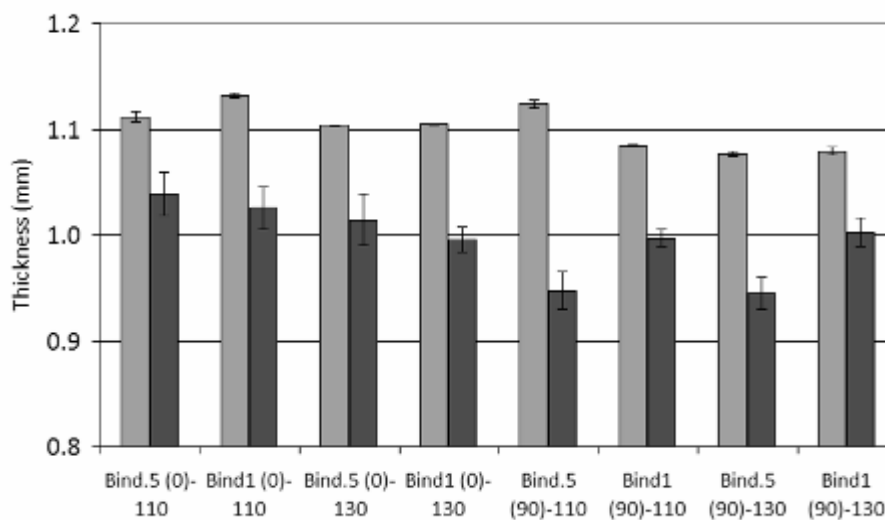


Figure 6.10 - Thickness measurement comparison of bindered samples: by calipers (light) and by microscopy (dark).

As polishing is not strictly required in this method, a long sample (such as 100 mm) can be fixed in putty and placed directly under the microscope, thus enabling thickness measurements along the entire length without the need to even change samples. This greatly assists in the characterization of the thickness gradients, as seen back in Section 4.4.7.

Measurements should be made at regular intervals to exclude any operator subjectivity of where to measure. This can be done by placing the magnified image of the micro-ruler used in calibration above the sample image. The thickness measurements can be aligned with a regular interval, such as at every millimeter along the length. This is demonstrated in Figure 6.11 for a TFP sample. This image is of an unpolished sample. As seen, the glass base layer in the TFP sample is frayed from cutting and hides the top edge of the sample. The top edge can be seen with close inspection of the part.

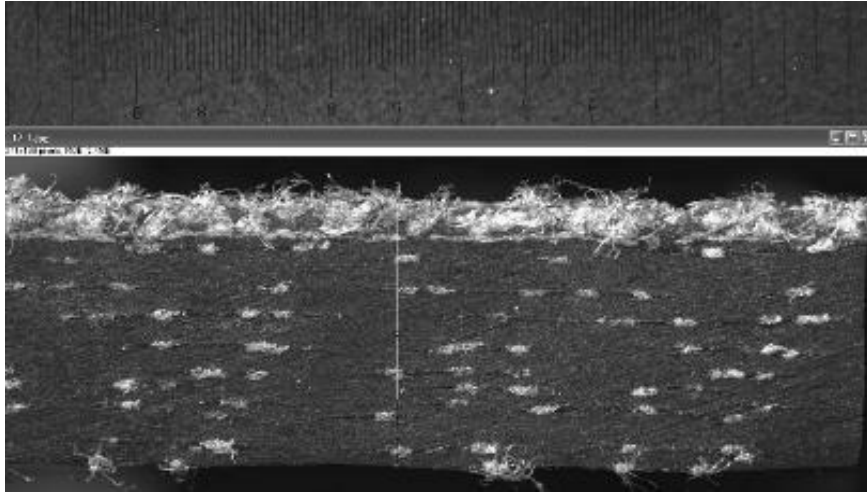


Figure 6.11 – Using micro-ruler (top) to regularly space thickness measurements.

The resultant  $v_F$  values for the control group of bindered samples were compared between the thickness measurement method, solvent digestion and density methods. The results (Figure 6.12) show that the thickness method measurements are very close to the solvent digestion measurements for the  $0^\circ$  flow. Assuming the solvent digestion method as the benchmark, this suggests the thickness method provides higher accuracy than the density method. As proven by these results, higher temperature and binder amount yields greater consolidation of the preform and thus a higher  $v_F$ .

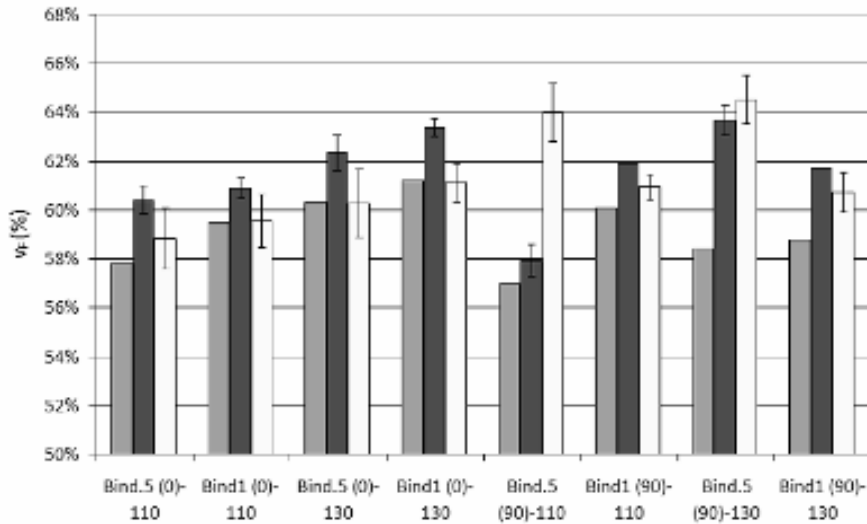


Figure 6.12 – Comparison of  $v_F$  measurement methods for bindered NCF control group (gray: solvent digestion, black: density, white: thickness).

The results are more difficult to interpret for the  $90^\circ$  flow. The  $0^\circ$  flow samples had pressure applied to resin pot after filling, as done for the VARI infusions in Section 4.1. This should apply a

constant thickness over the entire part. The 90° flow samples had slow enough of flow that the pressure gradient froze into place during cure. Thus the location of the sample along the flow length becomes more significant in determining the local  $v_F$ . The one sample tested by solvent digestion may be from the inlet while the other samples were averaged along the length.

Due to the relative ease of measurement method, its examination of the bulk properties, and ability to do full length profiling of the  $v_F$ , the thickness measurement method is proposed as the best method for  $v_F$  determination of such samples.

## 6.2 Void content measurement methods

The determination of  $v_0$  by comparing experimental and theoretical solid densities is difficult with composite samples because this relies on accurate sample density measurements. The samples are prone to water absorption and air bubble buoyancy discrepancies. The dimensions of the samples are also difficult to measure with accuracy, especially when pitted from a peel-ply.

The problem of sample measurement can be avoided by determining the mass fractions of the individual components. This can be determined via the solvent digestion tests and the sample density measurements. Voids will naturally contribute no mass to the sample. The sample mass is then only fiber, resin, stitching, and any binder. The fiber mass content is determined in solvent digestion testing. The stitching mass content is easily determined from the ratio  $\beta_S$ . The binder mass content is controlled by how much is applied during preforming. The resin mass is the remainder of the total mass reduced by the other components. The volume fraction of each component can be calculated by multiplying each mass fraction by the ratio of the sample density to the component density. The volume fraction of the voids,  $v_0$ , is the remainder after subtracting the component volume fractions from unity:

$$v_0 = 1 - \left[ \frac{M_F \rho_T}{M \rho_F} + \frac{M_F \beta_S \rho_T}{M \rho_S} + \frac{M_B \rho_T}{M \rho_B} + \frac{(M - M_F - M_F \beta_S - M_B) \rho_T}{M \rho_R} \right] \quad (6.5)$$

This relies on accurate measurements of the fiber mass from solvent digestion in addition to the accuracy of the density testing.

Image analysis from optical microscopy has been shown to achieve higher accuracy than density based methods as it is a direct measurement of the actual void [276]. Voids should appear as the darkest areas in a sample image from light microscopy, thus an areal percentage calculation can determine the void content.

Both micro and macro voids are difficult to delineate with an automated threshold algorithm as they represent a small percentage of the grey scale. This might be easier with better polishing and more constant lighting across the sample. With the facilities available in this study, however, microvoids ended up being very difficult to distinguish from the resin. The area of macrovoids could be measured, but required an image cropped around each void to minimize inclusion of resin pockets in the void area percent.

An automated script for the areal calculation of the void for each image in a file directory is included in Appendix 6. The automated threshold in this script produced a binary image that had to be manually adjusted in more than half of the void images. Thus a manual threshold adjustment is recommended to reduce the areal percentage of selected pixels to the shape of the voids. The “measure” command in Image-J gives a quick pixel areal comparison and percentage, which is then converted to area in  $m^2$  by the above calibration.

The same control group of bindered NCF materials was used for a comparison of void content measurement methods. The  $v_0$  was measured through the solvent digestion/density measurement method represented in Equation 6.5. Three 20 mm samples were cut along the length of each part (by the inlet, middle and vent). These samples were mounted and polished as per the fiber areal percent image analysis methods of  $v_F$  measurement. Each sample was then scanned under the microscope and pictures of every visible macrovoid were taken. These macrovoids were measured for areal content as in Figure 6.13.

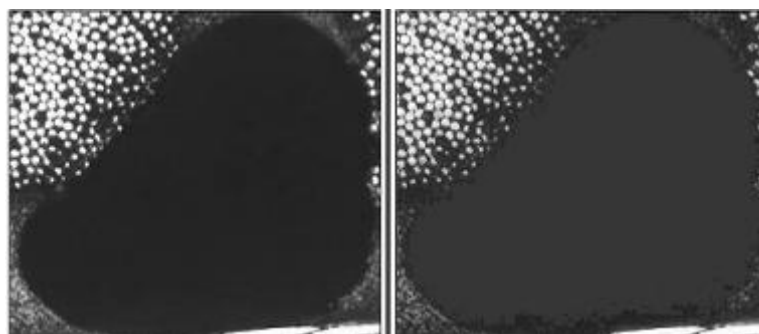


Figure 6.13 – Example areal measurement of macrovoid.

The areal sum of all voids in a sample, divided by the total examined surface area of the sample gives the  $v_0$  for each sample. The average  $v_0$  of all three samples is assumed to represent the bulk  $v_0$  of the entire sample. A comparison of the resulting  $v_0$  with the calculated  $v_0$  from the solvent digestion/density measurement method is shown in Figure 6.14.

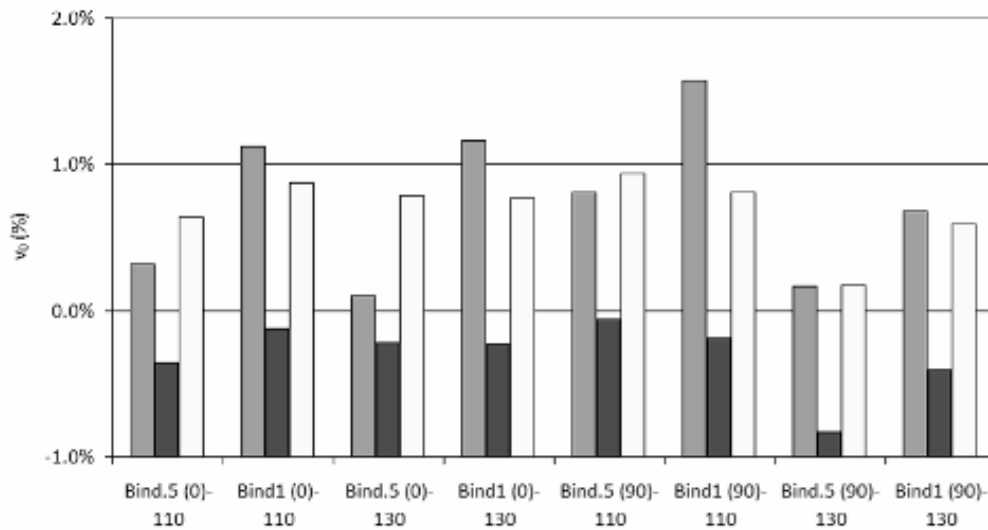


Figure 6.14 – Comparison of  $v_0$  measurement methods for bindered NCF control group (gray: areal image analysis, black: digestion/density, white: adjusted digestion/density).

The digestion/density method resulted in negative void contents for all samples. This implies that the component density or mass fractions were slightly inaccurate. As the  $v_0$  usually represents only ~1% of the volume, high precision and accuracy are required when employing the digestion/density method. The relative degree of  $v_0$  between samples shows fairly good agreement between the two methods. This is demonstrated by adding a third column in Figure 6.14, representing an adjusted  $v_0$  from the digestion/density method. This was generated by adding 1% to all  $v_0$  values from the digestion/density method and produces results that agree well with  $v_0$  from the optical analysis for each material.

The digestion/density method has many more possible sources of measurement error than the optical method. Unfortunately the optical method can only look at one localized cross-section and not the entire sample like the digestion/density method. Therefore, many measurements may be required to accurately characterize  $v_0$ .

## 6.3 VAP membrane qualification

VAP manufacturing has proven its ability to reduce the void content of parts produced in resin infusion (Section 2.2.3.4). It represents a promising step towards achieving the properties of prepreg materials. As it is a relatively new technology, there is much room for characterization and optimization of the unique feature to this process variant – the semi-permeable membrane. This section discusses the characterization of various VAP membranes. Hence, this section is not only included as a demonstration of final part characterization techniques, but is also a contribution towards optimization of the resin infusion process.

Since the introduction of VAP to industry, the need for robust yet inexpensive membranes has grown coincidentally with VAP's success. W.L. Gore & Assoc., in co-operation with EADS, developed a PTFE-based membrane soon after the VAP patent, which has since been the standard membrane choice. Saertex licensed the patented process from EADS to take on the business of equipping manufacturers with all the resources needed to do VAP. They sell both a PTFE membrane as well as a PUR-based membrane.

The 3x price difference (Section 2.2.3.4) between PTFE and PUR membranes necessitates cost justification for a manufacturer to choose one membrane material or the other. The differences in morphology and wettability between PTFE and PUR membranes have been reported [23]. But no data is known to exist in the literature comparing the two beyond this. The aim of this study is to produce more complete performance data comparing the two, in order to fulfill this need. The comparison will be based on membrane wetting during infusion, resin flow speed during infusion, final fiber volume content, thickness gradient, and void content.

### 6.3.1 Materials

Various companies who distribute PTFE and PUR membranes were included in this study. Only Saertex is licensed to provide these materials to interested manufacturers. Membranes were procured from Saertex, as well as W.L. Gore, PIL Membranes, and Airtech Advanced Materials Group. These three other companies are producers of membranes for various industrial applications, and had a product that could be theoretically used with VAP. The membranes were provided voluntarily and free of charge by each company. The membranes included in this study are listed in Table 6.1.

Table 6.1 – Evaluated VAP membranes.

<i>Evaluated Membranes</i>	<i>Material</i>	<i>Support</i>
Saertex 98386	PTFE-white	Light Blue
Saertex 96847	PUR-white	Light Blue
Saertex 94167 (SAERME)	PUR-white	(SAERME) White
Gore Albatross	PTFE-white	White
PIL (provided)-PTFE1	PTFE-white	Light Gray
PIL (provided)-PTFE2	PTFE-white	Light Gray
PIL-P355 fabric	PUR-white	Light Blue
PIL-P355/1	PUR-white	(none)
PIL-P3125	PUR-dark blue	(none)
PIL-P3250	PUR-black	(none)
Airtech SP	PUR (assumed) –white	Light Blue

It should be noted that some of these membranes are the same as others in the list, with only a different backing. To preserve supplier confidentiality, this was not researched and will not be further discussed. It is only assumed that a pore size difference exists across these products due to different membrane manufacturing conditions, and the difference in results across the PUR membranes should be attributed to this pore size difference. Similarly, all PTFE membranes should perform similarly to each other, and differences in results will be assumed to come from pore size differences.

VAP Infusions were performed with each of these membranes. In all cases, the baseline NCF (Section 3) was used as the reinforcement. Four plies were used in each case. RIM 235R, was again used, along with the mix of 1/3 RIM235H and 2/3 RIM236H, or in some cases the RIM237H hardener. RIM 237 takes about 36 hours to fully cure at room temperature (compare to 24 hours for the mix).

### 6.3.2 Infusion processing and membrane wetting

As described in Section 4.1, resin is usually degassed after mixing and before infusion to reduce  $v_0$ . And as described in Section 2.2.3.4 an inherent advantage of VAP is to increase the in-situ degassing abilities during infusion. To better compare each membrane’s ability to accomplish this,



no degassing was performed on the resin before infusion so as to purposefully magnify the issue of  $v_0$ .

The pressure on the outlet side of the membrane was decreased by vacuum down to  $\sim 1.5$  kPa. The pressure on the inlet resin pot was always atmospheric pressure (average  $\sim 98.5$  kPa). Another standard practice in resin infusion is to apply vacuum pressure to the resin pot after infusion to reduce the thickness gradient in the part. Another inherent quality of VAP is thickness gradient reduction, so no reverse pressure was applied afterwards to better quantify this as well.

Twelve total infusions were performed in three groups of four. The first four (A,B,C, and D) were done with DM (distribution media) both on the top and bottom. The second four (E,F,G, and H) were performed without any DM. The last four (I,J,K, and L) were performed with DM only on the top. Whenever DM was used, a peel-ply fabric and perforated foil were also laid between the DM and the fabric. Inlet pipes were made with omega tubing along one short side of each part. Each membrane was sealed over this setup with tacky tape. Breather cloth was laid over each membrane and sealed with the vacuum outlet tube over the membrane. Vacuum checks were performed on each bagging prior to infusion.

A pot of 400 grams resin was used for each set of four infusions. The total resin amount allowed into the cavities was controlled by leaving the pot on a mass scale and closing the inlet pipe once a particular amount was allowed into the parts. This amount was based on the measured weight of the fabric preform and a target  $v_F$  of 60%, as well as uptake calculations for all the disposables as described in Section 2.2.3.4.1.

One initial observation was that fabric backing made sealing the membrane easier. Sealing the PIL-P355/1 membrane (with no backing) was more difficult and ended up with many wrinkles but was safely sealed with some work.

A summary of all 12 infusions is listed in Table 6.2. The orientation angle of the NCF stitching to the flow, as well as a degree of resin bag wetting and wetting description are all included. The degree of wetting is based on visual comparison between 0 for completely dry membranes (after infusion), and 10 for near-immediate saturation as was the case in infusion J.

Table 6.2 – Infusion summary and membrane wetting.

<i>ID</i>	<i>Membrane</i>	<i>angle</i>	<i>resin</i>	<i>wet degree</i>	<i>notes</i>
A	PTFE1 (PIL)	0/90	237	9	Leaked significantly
B	PTFE2 (PIL)	0/90	237	0	Dry
C	P355 fabric	0/90	237	1	A couple darkened spots
D	P3125	0/90	237	2	Some breather cloth fibers stuck to membrane
E	Gore PTFE	0	235/236	1	Slightly darkened by inlet, but otherwise dry
F	Saertex PTFE	90	235/236	0	Dry
G	Saertex PUR	0	235/236	1	Slightly wetted by inlet
H	Airtech SP	90	235/236	1	Slightly wetted by inlet
I	P355	90	235/236	5	Breather cloth not removable
J	P3250	0	235/236	10	Membrane leaked within first couple minutes
K	Airtech SP	0	235/236	1	Slight darkening around tape edges and inlet
L	Saertex PUR (SAERME)	0	235/236	3	Some breather cloth fibers stuck to membrane

### 6.3.3 Resin flow velocity comparison

Only the second set of 4 infusions was done with no DM. This greatly reduces the resin travel through the cavity and allows a better look at any flow velocity differences from the membranes. The time versus length of flow along the 300 mm long part was measured through the bottom of a glass mould. Results showed an understandably significantly higher velocity when the stitching is oriented at 0° to the flow (E and G) compared to 90° flow (F and H). But there was no significant difference in resin flow speed due to the membranes. This was the case for the infusions with DM as well. This indicates that no significant difference in vacuum compaction exists.

### 6.3.4 Fiber volume content and thickness gradient measurement

The fiber volume content was measured by optical image analysis. The  $v_F$  of each sample was measured by the thickness measurement method. 45 thickness measurements were made at regular intervals along the length of each part. Resulting averages and standard error for all measurements are reported by infusion in Figure 6.15.

The target  $v_F$  in resin take-up calculations was 60%. Yet all  $v_F$  values were about 2 to 3 % lower than this, agreeing with the assumption for in-situ nesting in Section 2.2.3.4.1. It should be noted that if the membranes performed equally, the  $v_F$  should be equal in each of the three sets of four

infusions, as the resin quantity was controlled and shared between all four cavities with an equal pressure distribution. Regardless, a difference of 2 to 3 % for each set of four infusions is not much, especially when considered the thickness variation across these samples.

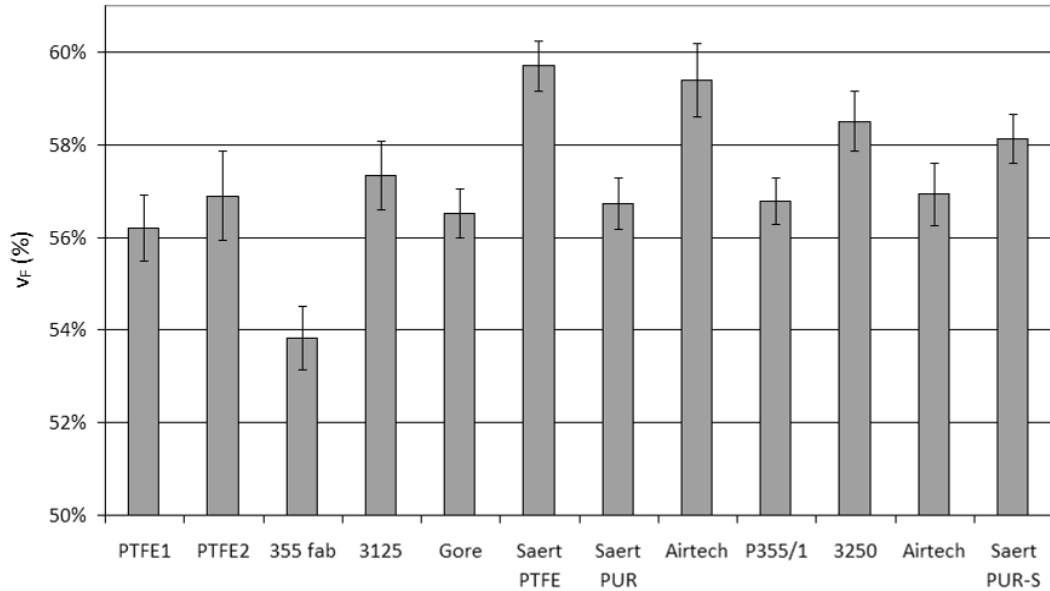


Figure 6.15 – Average  $v_F$  by thickness measurement.

To see if there is any significant trend in  $v_F$  along the part length, the average  $v_F$  and standard error was calculated for the thickness measurements when separated into three categories: by the inlet, in the middle, and by the vent. Figure 6.16 shows the results, grouped by location and infusion.

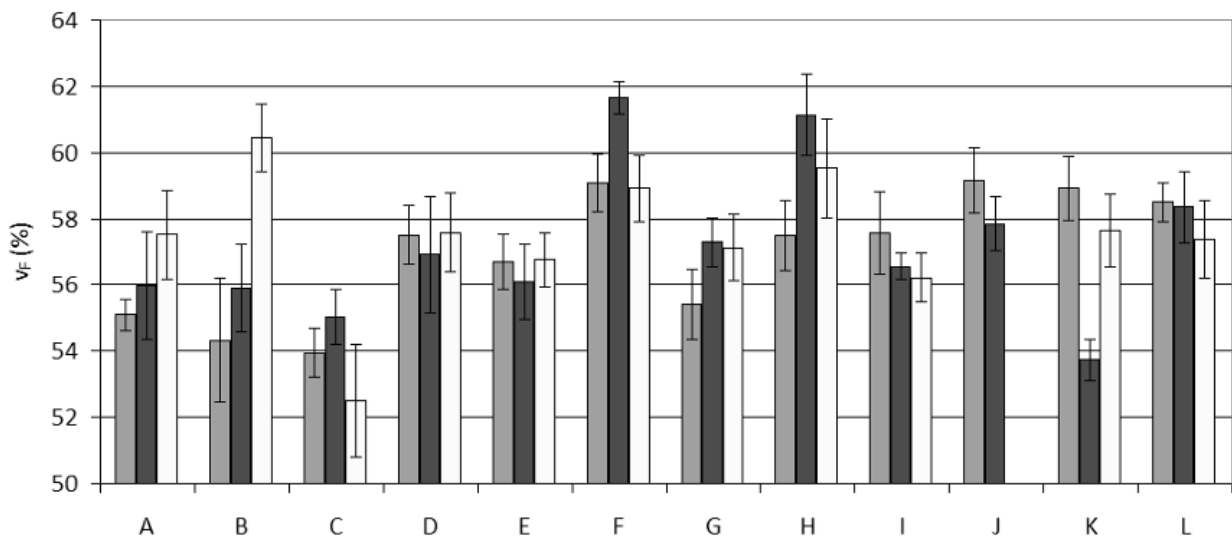


Figure 6.16 – Average  $v_F$  for each sample (gray=by inlet, black=mid, white=last point).

One would assume that without reverse pressure, and with the epoxy gelling right about when the part is filled, that the lowest  $v_f$  should be by the inlet – where the highest resin pressure is “frozen” in place by rising viscosity. For the 237H infusions (A,B,C, and D), there would be time for the membrane to allow equalization of this pressure gradient. But no significant trends are seen in Figure 6.16, suggesting that all membranes resulted in no significant thickness gradient. The high last  $v_f$  for “B” (PIL-PTFE2) and to a lesser degree “A” (PIL-PTFE1) may be from curing a gradient in place. But E and F (the other PTFE infusions) don’t show a similar trend. No real improvement in gradient reduction can be seen between PTFE and PIL membranes.

### 6.3.5 Void content measurement

In traditional resin infusion processes, voids are reduced by degassing the resin, and bleeding resin through the part for some amount of time after the part has been filled. VAP can theoretically eliminate the need for both of these time-intensive steps by continually degassing the entire part through the thickness direction. A larger pore size would naturally allow more degassing, but would also allow for quicker resin saturation of the membrane. Thus pore size is a critical design parameter in producing VAP membranes.

The volume percent content of voids ( $v_0$ ) was measured in each of the microscope samples by the areal percent image analysis method in Section 6.2. As done in the control group there, three 20 mm long samples were cut from each cured part: by the resin inlet, the middle, and by the vent. The samples were prepared for image analysis as described in Section 6.1.4. Figure 6.17 lists the averaged results by each sample, again arranged by distance along the flow length for each infusion.

As is clearly seen, there exists a high degree of variation across the samples. Keep in mind that the resin was not degassed prior to infusion, so it would be unfair to directly compare the void contents here to resin infusion with degassed resin. Also note that the 3250 membrane leaked enough that the resin did not flow very far, so only 2 samples were taken. In all other cases, when no bar is seen, it indicates a void-free sample. This is the noteworthy case for all three samples taken from infusion “B” (PIL-PTFE2).

The sample by the inlet may sometimes have a higher void content due to having less time to degas through the VAP membrane than the resin by the vent. Where part filling was not a problem due to ample DM coverage (both the first 4 and last 4 infusions), the sample “by inlet” indeed has

the highest  $v_0$  in 7 of 8 of the infusions. Thus, when infusing via VAP, void minimization may be aided by leaving a gap of space between the resin inlet and the fabric (connected by DM).

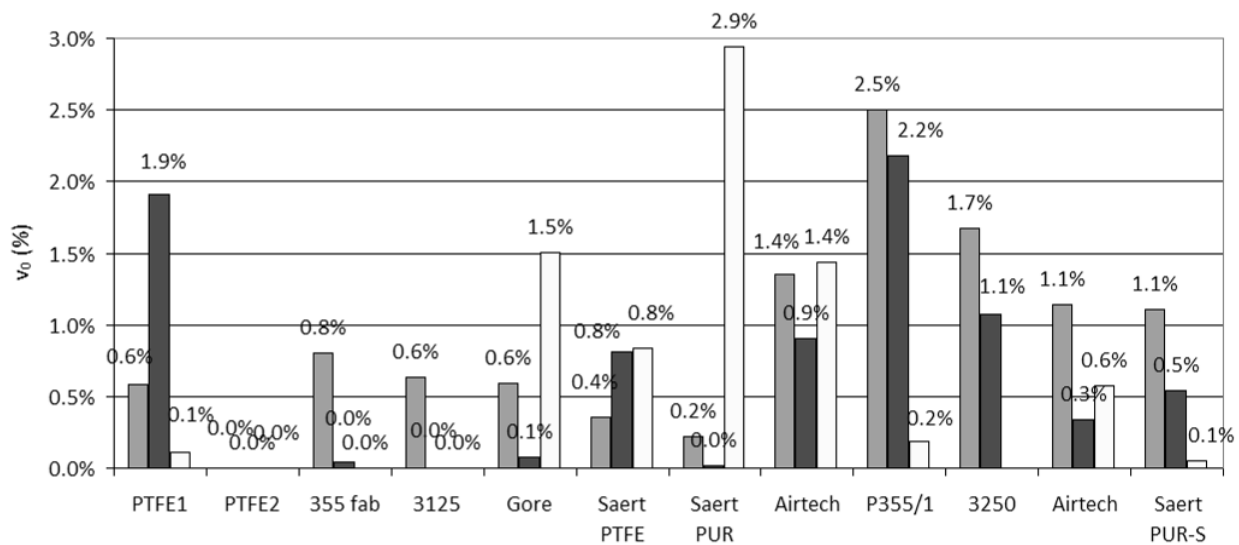


Figure 6.17 – Average  $v_0$  for each sample (gray=inlet, black=mid, white=last point).

In contrast, the middle 4 infusions (no DM) all had the highest  $v_0$  at the “last point” sample. Incomplete tow saturation may be a problem for the infusions using no DM. For these samples with very slow resin flow velocity, the resin is at a high viscosity by the time it is filling the last points in the mould. This emphasizes the need to infuse the entire part at low enough of a viscosity, to properly take advantage of the VAP membrane capabilities.

The average  $v_0$  was calculated for each infusion and is presented in Figure 6.18. The void content is highest in the four middle infusions without DM, next highest with DM on top (3<sup>rd</sup> set of 4 infusions), and lowest with double DM (1<sup>st</sup> set of 4 infusions). Infusions A, I, and J showed unusually high void amounts. For infusions that leaked (A and J), the curing resin blocking the pores could hamper degassing and explain the high  $v_0$ . The P355/1 membrane was the only thin membrane without a fabric backing. The breather cloth was sticking to the membrane afterwards across the part, signifying some resin leakage as well. This would suggest that resin leakage caused reduced degassing for all the high  $v_0$  samples.

Directly comparing the repeated membranes allows for general comparisons between infusion setups. For example, the first Airtech infusion, done with no DM, has about twice the  $v_0$  (1.2%) as the second Airtech, using DM on top (0.7%). The Sartex PUR membrane with no DM (1.1%) is also about twice the  $v_0$  for the Saertex PUR-S membrane done with DM on top (0.6%), which is in turn

about twice the  $v_0$  of the PIL-P355 fabric membrane done with double DM (0.3%). These PUR membranes with different fabric backings are assumed to perform nearly identical to each other. The Gore Albatross PTFE and Saertex PTFE membranes have nearly the same  $v_0$  (both 0.7%) as they should perform similarly and are both done with no DM.

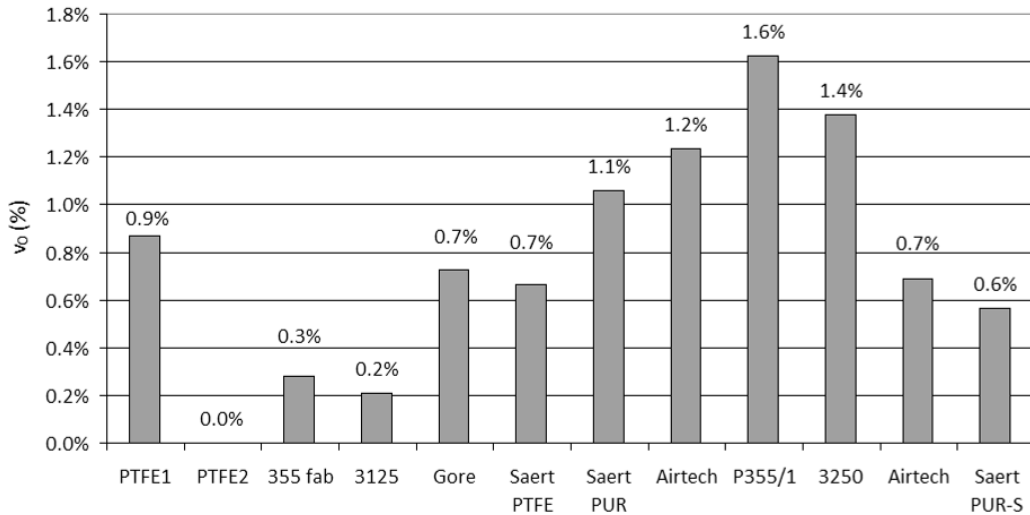


Figure 6.18 – Average  $v_0$  for each infusion.

To further illustrate these comparisons, an average  $v_0$  was calculated for each DM setup and each membrane material (either PUR or PTFE) (Figure 6.19). Infusions A, I, and J were excluded due to membrane leakage. Note that there are only 3 PTFE samples represented in this figure, and none for the single DM category. But the linear relationship between DM setup and void content for PUR is apparent.

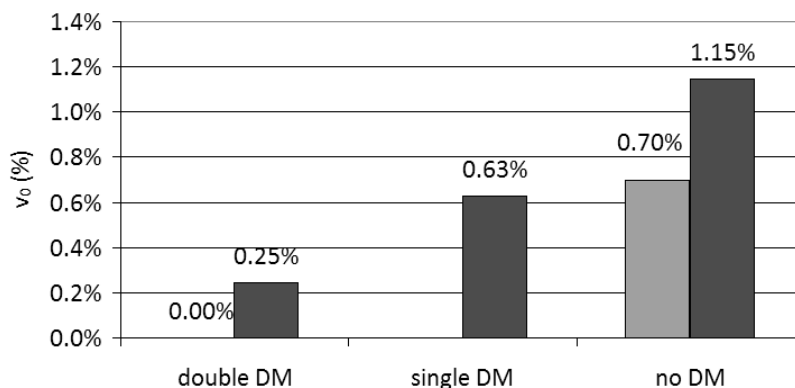


Figure 6.19 – Average  $v_0$  for each material and DM setup (light=PTFE, dark=PUR).

Figure 6.19 also allows the best direct comparison possible from this study between the PTFE and PUR membranes. PTFE membranes illustrate superior void content reduction. The difference is

significant when  $v_0$  must be less than 1%. In other cases, such as with the double DM infusions, or when the tolerance is higher, the increase in voids using a PUR membrane seems to be insignificant.

The PIL-P3150 membrane is particularly noteworthy as it has no fabric backing, yet scored the lowest  $v_0$  of any of the PUR membranes (about 0.2% with double DM). It also showed a higher  $v_f$  and less thickness variation than the PTFE membranes.

### 6.3.6 Shear property determination and correlation

Of all the mechanical properties for high-performance composite applications, shear properties have become the most requested test, as this has shown to be the most common mode of failure. Shear is a resin-dominated property, rather than a fiber-dominated property, thus can be sensitive to both  $v_f$  and  $v_0$  (Section 2.1).

ILSS (inter-laminar shear strength) measurements for ~10 samples from each of the infusions were performed as per DIN 2563. The average and standard error for each infusion is presented in Figure 6.20. To correlate the ILSS measurements with void content, the infusions were arranged according to lowest ILSS to highest ILSS, and the plotted along the x-axis with void content as the y-axis, and in another graph with fiber content as the y-axis (Figure 6.21). Some correlation between ILSS and void content is seen in Figure 6.21. ILSS is inversely proportional to  $v_0$ . This agrees with previous reported findings in a comparison between VAP and VARI [21].

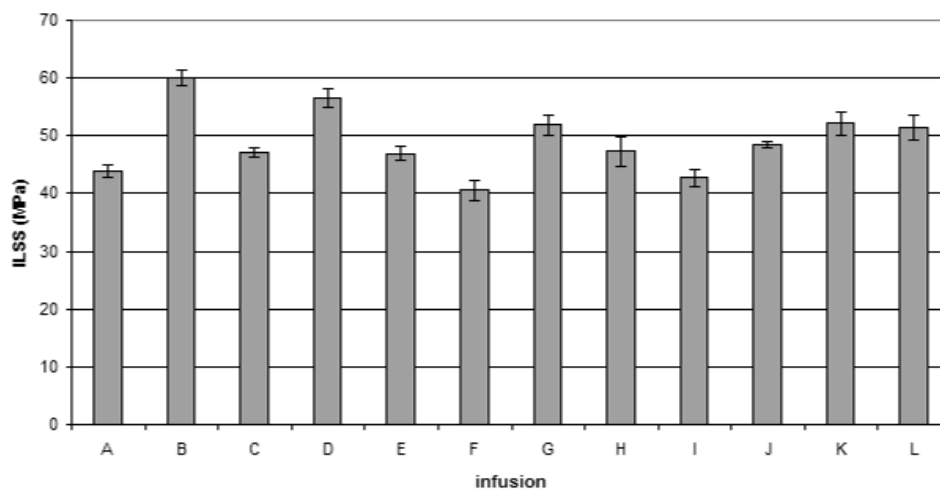


Figure 6.20 – Average ILSS result for each infusion.

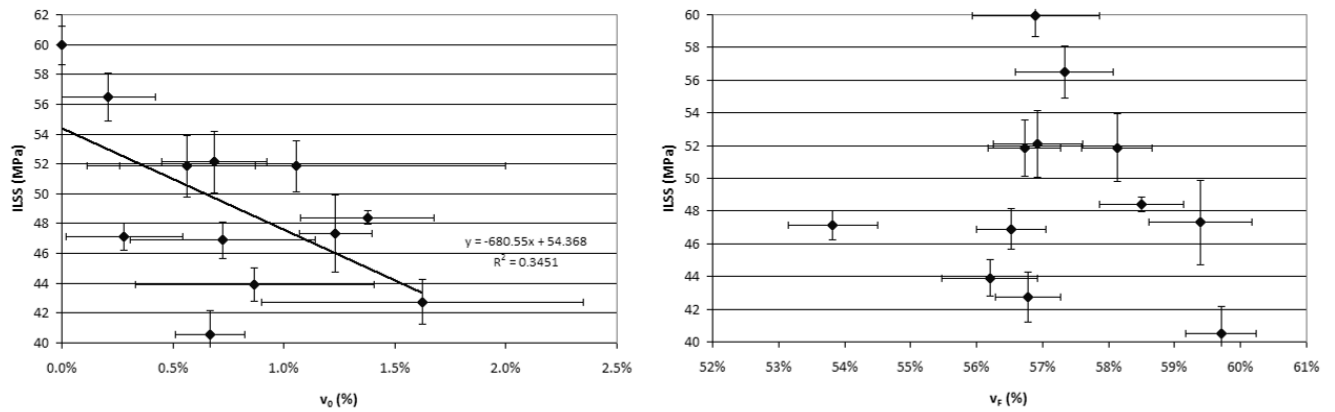


Figure 6.21 – Comparison of ascending ILSS values with corresponding void content (left) and fiber content (right).

In contrast, there is no clear correlation between ILSS and  $v_f$ . A weaker relationship was expected with a resin-dominated property as already mentioned. But these tests consist of a range of only about 5% fiber content. With a greater range, and/or more testing, it is assumed that a positive relationship between ILSS and fiber content would be demonstrated.

### 6.3.7 VAP membrane qualification summary

Some of the PTFE and some of the PUR membranes were wetted by the epoxy too much for applicability to this room-temperature infusion setup. But most of them showed adequate resin impermeability. No significant difference between flow velocity, fiber content, or thickness variation could be seen between the different membranes. The greatest determinant of void content in this study was whether DM was used in the infusion or not, and how much. In the same DM setup, PTFE membranes showed lower void contents than PUR. But the difference is small enough for PUR to be considered due to its lower cost given a particular manufacturing setup. ILSS measurements confirmed a direct relationship between a low void content and high shear properties.



## 7 Final Conclusions

The three-fold approach of this study, repeated here, is meant to address the challenges to industrial application of composite materials:

1. To model the most significant phenomena in flow processing to improve simulation capabilities
2. To develop tools to characterize composite parts and predict their final properties in service
3. To use those characterization tools to optimize resin infusion processing

To improve simulation capabilities, a numerical model was presented for one-dimensional flow, in which models for the permeability, compressibility, dynamic viscosity, and capillary pressure are all coupled. These models were each developed based on relationships previously proposed in the literature, which were fit empirically to modern carbon fabrics in this study and adapted to the coupled model. This is the first model known to couple all of these flow phenomena into one solution.

The coupled model works well at describing the independent effects and interactions of each of the separate flow phenomenon models. The effects of dual scale flow, as modeled by incorporation of a modeled capillary pressure, proved to be the more significant to flow velocity than the viscosity or compressibility for the range in lengths, thickness, and curing discussed here.

This coupled model was compared to benchmark experimental VARI infusions of a variety of modern carbon preforming materials. Comparing the relative change in flow velocity due to fabric selection achieved fairly good consistency in results between experiment and prediction. An absolute comparison between experiment and prediction for each of the materials however resulted in poor consistency. The experimental infusions all flowed slower than predicted by the numerical model. Part of this problem is naturally due to the through-thickness flow involved in infusing from the top of a fabric stack, which cannot be accounted for in a strictly 1D flow model. This was expounded upon by FEM simulation of the 3D geometry, as well as experimental infusions where the flow was attempted to be forced into only 1D flow. But this could only account for a portion of the decrease in flow velocity shown in experimentation.

The coupled model was successfully applied to the analysis of flow front data in point-infusion permeability measurements. Although each component of the 3D permeability tensor cannot be assumed to have 1D flow, 1D relationships can be incorporated into the isotropic transformation solution used in this study. Thus, the permeability in each of the three component directions for 3D flow can be determined from a single point-infusion experiment, independent of any dual scale flow or viscosity effects as they are modeled in the coupled solution. Despite the independent analysis of the permeability from the other flow phenomena, the flow was again slower than predicted by the model based on in-plane permeability testing.

The slower flow in the VARI benchmark testing and point-infusion experiments could be due to some shear effect between the flowing epoxy resin and the carbon fiber sizing. In the in-plane permeability characterization tests, paraffin oil was used. The paraffin oil may result in less shear than the epoxy, thus resulting in the faster flowrates seen in the in-plane permeability characterization. The accurate simulation of resin infusion will require characterization of the permeability for each liquid-fiber combination until these differences, whether from shear or something else, can be explained and modeled.

Empirical fitting of the various models to modern carbon fabrics allowed many comparisons between fabric types to be made:

- NCF materials: flow is enhanced along the stitching, both along in-plane flow, and through-thickness flow. 6K NCF's exhibit lower permeability than 12K (binder-like consolidation). Compliance in NCF's is low due to the stitching consolidation. The compliance shows a slight decrease as the number of plies is increased from 2 to 10. High viscoelasticity is seen in compression cycling.
- Bonded: a 1 to 4% by weight application of binder to NCF significantly decreases the permeability and compliance. At least in the case of permeability, more binder produces a lower permeability. Through-thickness flow in NCF's is not impeded by binder application as much as in-plane flow due to the flow enhancement of the stitching. As with NCF's, high viscoelasticity was demonstrated, by low compression hysteresis (decay).
- Braids: high in-plane permeability due to tow undulation from crimps, but low through-thickness permeability due to the absence of through-thickness stitching. Triax braids naturally show greater permeability along the standing fibers, whereas biax braids are

isotropic in-plane. The braids are highly compliant, and have low compression hysteresis (decay) due to looser tow packing than in NCF's.

- TFP materials: 12 layer TFP's have permeability slightly higher than the NCF's. But 16 layer TFP's have a lower permeability due to heavy stitching density. The through thickness permeability is high due to high z-direction stitching flow enhancement. Like braids, the looseness of the tow packing results in high compliance, and low compression hysteresis (decay).

The contribution of this study towards part characterization is a review of the measurement methods for fiber content and void content. Due to the relative ease of measurement method, its examination of the bulk properties, and ability to do full length profiling of the  $v_F$ , the thickness measurement method is proposed as the best method for  $v_F$  determination for such samples. For measurement of  $v_0$ , the digestion/density method has many more possible sources of measurement error than the optical method. Thus, accuracy in absolute values is difficult to obtain. But a relative comparison between materials is enabled with this method. This should be compared to the areal percentage image analysis method, which is a direct measurement of the void size. Thus absolute measurements are more accurate. But this method can only look at one localized cross-section, and not the entire sample like the digestion/density method. Therefore, many measurements may be required to accurately characterize an absolute value for  $v_0$ .

This study also contributed to the optimization of resin infusion by characterizing the final part qualities in VAP. A comparison between PTFE and PUR membranes was made, where it was shown that both materials can provide adequate resin impermeability. No significant difference between flow velocity, fiber content, or thickness variation could be seen between the different membranes. The greatest determinant of void content in this study was whether DM was used in the infusion or not, and how much, as opposed to membrane selection. In the same DM setup, PTFE membranes showed lower void contents than PUR. But the difference is small enough for PUR to be considered due to its lower cost given a particular manufacturing setup. By applying the optimized methods of  $v_0$  measurement, ILSS measurements for the VAP infusions confirmed a direct relationship between a low void content and high shear properties.

## References

1. Beaumont, Matthew (EADS Innovation Works). "Coping with Ramp-up in Composite Aero Structures". In *GE Global Research Composite Symposium, Garching, Germany Oct 7-8, (2009)*.
2. Stauber, Rudolf (BMW AG). "Materials for Automotive Applications – Technologies and Trends." In *GE Global Research Composite Symposium, Garching, Germany Oct 7-8, (2009)*.
3. Strong, A.B. *Plastics Materials and Processing*. Upper Saddle River, New Jersey: Prentice Hall (2006).
4. Judd, N.C.W. and Wright, W.W., "Voids and their Effects on the Mechanical Properties of Composites – An Appraisal," *SAMPE Journal* Jan/Feb (1978): 10-14.
5. Nijonhou, A, F. Berthet, and B. Castanie. "Parameters Affecting Mechanical Properties of Composite Manufactured by Liquid Resin Infusion (LRI)" In *17th International Conference on Composite Materials: Edinburgh, UK, July 27-31 (2009)*.
6. Drechsler, K. *Werkstoffe und Fertigungsverfahren der Luft- und Raumfahrt Vorlesungsscript*. Technical report, IFB, Universität Stuttgart (2004).
7. Gdoutos, E.E., K. Pilakoutas, and C.A. Rodopoulos. *Failure Analysis of Industrial Composite Materials*. McGraw-Hill Professional (2000).
8. Potter, K. *Resin Transfer Molding*. New York: Chapman & Hall, 1997.
9. Jensen, D.K. "Experimental Investigation of Fibre Preform Resin Infiltration in the Vacuum Assisted Process." Practical Placement Report for EADS Deutschland GmbH, Ottobrunn, Germany. Aalborg University, Denmark (January 2003).
10. Parnas, R.S. *Liquid composite molding*. Cincinnati, USA: Hanser Gardner Publications (2000).
11. Benjamin, W.P., and S.W. Beckwith, ed. *Resin Transfer Molding; SAMPE Monograph No. 3*. Covina, CA: SAMPE (1999).
12. Amouroux, S.C., D. Heider, S. Lopatnikov, and J.W. Gillespie. "Membrane-based VARTM: Membrane and resin interactions". In *SAMPE Fall Technical Conference, Seattle (2005)*.
13. Stadtfeld, H.C., M. Erninger, S. Bickerton, and S.G. Advani. "An experimental method to continuously measure permeability of fiber preforms as a function of fiber volume fraction." *Journal of Reinforced Plastics & Composites* 21(10) (2002): 879–900.
14. Seemann, W.H. "Plastic Transfer Molding Apparatus for the Production of Fiber Reinforced Plastic Structures." U.S. Patent 5,052,906, 1991.
15. Ahlborn, H. *Characterization of Binder Application on Carbon Fibre Non-Crimped Fabric: Permeability and Flow Modeling*. Studienarbeit, Institute for Aircraft Design, University of Stuttgart, Germany (2009).
16. Filsinger, J., T. Lorenz, F. Stadler, and S. Utecht. "Method and device for producing fiber-reinforced components using an injection method." U.S. Pat. 6,843,953, March 5, 2002.
17. <http://www.saertex.com>. Accessed September 2008.
18. Filsinger, J. Interview by author, 9 Aug 2007, EADS, Ottobrunn, Germany.
19. Shröder. W. "VAP Technology: Cost-effective reduction of aircraft weight." *JEC Composites* 10 (2004): 42-43.
20. Black, S. "Inside Manufacturing: A400M Cargo Door — Out of the Autoclave." <http://www.compositesworld.com/hpc/issues/2007/May/111536>. Accessed October 2007.
21. Li, W., J. Krehl, J. W. Gillespie, Jr., D. Heider, M. Endrulat, K. Hochrein, M. G. Dunham and C. J. Dubois. "Process and Performance Evaluation of the Vacuum-Assisted Process," *Journal of Composite Materials* 38 (2004): 1803-1814.
22. Zimmermann, K., M. Siemetzki, and D. Zenkert. "Analysis and Manufacturing of Ultra Thick Laminates for Future Aircraft Applications." In *ECCM-13, Stockholm, June (2008)*.

23. Amouroux, S. C., D. Heider, S. Lopatnikov, and J. W. Gillespie, Jr. "On the Role of Membrane to Improve Quality of VARTM-Processed Composites," In *American Society for Composites (ASC) 20th Annual Technical Conference, Drexel University, Philadelphia, USA, Sept. 7-9 (2005)*.
24. Heider, D., C. Newton, and J.W. Gillespie. *VARTM Variability and Substantiation*. Technical Report, Joint Advanced Materials and Structures Center of Excellence, 18 June (2008).
25. Amouroux, S.C., J.F. Henau, D. Heider, and J.W. Gillespie. "Membrane Based VARTM Processing: Modelling and Characterization." In *38th International SAMPE Technical Conference, Dallas, USA, November 6-9 (2006)*.
26. Iagulli, G., S.I. Imparato. "A statistical model to correlate the variability of used materials and part resin content for closed infusion process." In *37th International SAMPE Technical Conference, Seattle, USA, October 31 – November 3 (2005)*.
27. Advani, S.G., M.V. Brusckhe, and R. Parnas. "Resin transfer molding." In *Flow and rheology in polymeric composites manufacturing*, ed. S.G. Advani, 465–526. Amsterdam: Elsevier (1994).
28. Darcy, H.P.G. *Les fontaines publiques de la ville deDijon*. Paris: Dalmont (1856).
29. Bréard, J., Y. Henzel, F. Trochu, and R. Gauvin. "Analysis of Dynamic Flows Through Porous Media. Part I: Comparison Between Saturated and Unsaturated Flows in Fibrous Reinforcements." *Polymer Composites* 24(3) (June 2003): 391-408.
30. Stauffer, P.H. "Flux Flummoxed: A Proposal for Consistent Usage." *Ground Water* 44 (2) (2006): 125–8.
31. Scheidegger, A.E. *The Physics of Flow Through Porous Media* Toronto: University of Toronto Press (1974).
32. Kaviany S. *Principles of heat transfer in porous media*. NewYork: Springer-Verlag (1991).
33. Young, W.B., K. Han, L.H. Fong, L.J. Lee, and M.J. Liou. "Flow Simulation in Molds with Preplaced Fiber Mats." *Polymer Composites* 12(6) (1991): 391–403.
34. Trochu, F., R. Gauvin, and D.M. Gao. "Numerical analysis of the resin transfer molding process by the finite element method." *Advances in Polymer Technology* 12(4) (1993): 329–42.
35. Bickerton, S., and S.G. Advani. "Experimental Analysis and Numerical Modeling of Flow Channel Effects in Resin Transfer Molding." *Polymer Composites* 21(1) (Feb 2000): 134-153.
36. Tucker III, C.L., and R.B. Dessenberger. "Governing equations for flow and heat transfer in stationary fiber beds." In *Flow and Rheology in polymer composites*, S.G. Advani, ed. Elsevier Science B.V. (1994).
37. Happel J. and H. Brenner. *Low Reynolds Number Hydrodynamics*. Dordrecht, Netherlands: Martinus Nijhoff Publishers (1983).
38. Adams, K.L., and L. Rebenfeld. "In-Plane Flow of Fluids in Fabrics: Structure/Flow Characterization." *Textile Research Journal* 57 (1987): 647-654.
39. Adams, K.L., B. Miller, and L. Rebenfeld. "Forced in-plane flow of an epoxy resin in fibrous networks." *Polymer Engineering and Science* 26(20) (1986): 1434–41.
40. Williams, J.G., C.E.M. Morris, and B.C. Ennis. "Liquid flow through aligned fiber beds." *Polymer Engineering and Science* 14 (1974): 413-419.
41. Fracchia, C.A., and C.L. Tucker III. "Simulation of Resin Transfer Mold Filling." In *6th Annual Meeting of the Polymer Processing Society. Nice, France (1990)*.
42. Gebart, B.R., P. Lidström. "Measurement of in-plane permeability of anisotropic fiber reinforcements." *Polymer Composites* 17(1) (1996): 43–51.
43. Robitaille, F., and R. Gauvin. "Compaction of textile reinforcements for composites manufacturing. I. Review of experimental results." *Polymer Composites* 19(2) (1998): 198–216.
44. Robitaille, F., and R. Gauvin. "Compaction of textile reinforcements for composites manufacturing. II. Compaction and relaxation of dry and H<sub>2</sub>O-saturated woven reinforcements." *Polymer Composites* 19(5) (1998): 543–57.
45. Mogavero, J., and S.G. Advani. "Experimental Investigation of Flow Through Multi-Layered Preforms." *Polymer Composites* 18(5) (1997): 649-655.

46. Lundström, T.S., B.R. Gebart, and E. Sandlund. „In-plane permeability measurements on fibre reinforcements by the multi-cavity parallel flow technique.” *Polymer Composites* 20(1) (1999): 146–54.
47. Young, W.B., and S.F. Wu. “Permeability Measurement of Bidirectional Woven Glass Fibers,” *Journal of Reinforced Plastics and Composites*, 14 (1995): 1108–20.
48. Kim, S.K., and I.M. Daniel. “Observation of Permeability Dependence on Flow Rate and Implications for Liquid Composite Molding.” *Journal of Composite Materials* 41 (2007): 837-849.
49. Steenkamer, D.A., S.H. McKnight, D.J. Wilkins, and V.M. Karbhari. “Experimental characterization of permeability and fibre wetting for liquid moulding.” *Journal of Materials Science* 30(12) (1995): 3207-3215.
50. Foley, F.M., and T. Gutowski. "The Effect of Process Variables on Permeability in the Flexible Resin Transfer Molding (FRTM) Process." In *23rd International SAMPE Technical Conference, Kiamesha Lake, USA November 22-24 (1991)*.
51. Gauvin, R., and M. Chibani. “A study of permeability of non-woven reinforcements in composite molding.” *SAMPE Quarterly* (April 1990): 52–58.
52. Skartsis, L., J.L. Kardos, and B. Khomami. “Resin flow through fiber beds during composite manufacturing processes. Part I: Review of newtonian flow through fiber beds.” *Polymer Engineering & Science* 32(4) (1992): 221-230.
53. Hammond, V.H., and A.C. Loos. “The effects of fluid type and viscosity on the steady-state and advancing front permeability behavior of textile preforms.” *Journal of Reinforced Plastics and Composites* 16 (1997): 50-72.
54. Luo, Y., I. Verpoest, K. Hoes, M. Vanheule, H. Sol, A. Cardon. “Permeability measurement of textile reinforcements with several test fluids.” *Composites Part A* 32(10) (2001): 1497-1504.
55. Slade J., K.M. Pillai, and S.G. Advani. “Investigation of unsaturated flow in woven, braided and stitched fiber mats during mold-filling in resin transfer molding.” *Polymer Composites* 22(4) (2001): 491–505.
56. Parseval, Y.D., K.M. Pillai, and S.G. Advani. “A simple model for the variation of permeability due to partial saturation in dual scale porous media.” *Transport Porous Media* 27 (1997): 243–64.
57. Ferland, P., D. Guittard, and F. Trochu. “Concurrent Methods for Permeability Measurement in Resin Transfer Molding” *Polymer Composites* 17(1) (1996): 149-158.
58. Mathur, R., D. Heider, C. Hoffman, J.W. Gillespie Jr, S.G. Advani, and B.K. Fink. “Flow Front Measurements and Model Validation in the Vacuum Assisted Resin Transfer Molding Process.” *Polymer Composites* 22(4) (2001): 477-490.
59. Martin, G.Q., and J.S. Son. “Fluid mechanics of mold filling for fiber reinforced plastics.” In *Advanced Composites: The Latest Developments, Proceedings of the ASM/ESD 2nd Conference on Advanced Composites, Dearborn, USA, Nov 18-20 (1986)*.
60. Gauvin, R., F. Trochu, Y. Lemenn, and L. Diallo. “Permeability measurement and flow simulation through fiber reinforcement.” *Polymer Composites* 17(1) (1996): 34–42.
61. Koorevaar, A. “Liquid injection moulding flow analysis: beyond state of the art.” In *International SAMPE Conference, Long Beach, USA, April 30 - May 4 (2006)*.
62. Šimáček, P. and S.G. Advani. “Modeling resin flow and fiber tow saturation induced by distribution media collapse in VARTM.” *Composites Science and Technology*, 67(13) (2007): 2757-2769.
63. ESI-Group. *PAM-RTM User's Guide & Tutorials* (2008).
64. Hsiao, K.T., R. Mathur, S.G. Advani, J.W. Gillespie Jr., and B.K. Fink. “A close form solution for flow during the vacuum assisted resin transfer molding process.” *Journal of Manufacturing Science and Engineering* 122 (2000): 463-475.
65. Šimáček, P., and S.G. Advani. “Modeling and simulation of resin flow in resin infusion processes such as VARTM, VAP and compression RTM.” In *International SAMPE Fall Technical Meeting 52 (2007)*.
66. Chandrabalan, S., Ö. Eksik, H. Deffor, P. Šimáček, J.W. Gillespie, Jr., S. Advani, and D. Heider. “Pressure Behavior during Vacuum Assisted Processing (VAP).” In *SAMPE Fall Technical Conference, Kansas, USA, October (2009)*.

67. Modi, D. "Numerical issues in mold filling simulations for composites processing." thesis, University of Delaware (2003).
68. Šimáček, P., and S.G. Advani. "Desirable features in mold filling simulations for liquid composite molding processes." In *SAMPE, Baltimore, USA* (2002).
69. Song, X., A. C. Loos, B. W. Grimsley, R. J. Cano, and P. Hubert. "Modeling the VARTM composite manufacturing process." In *SAMPE 2004, Long Beach, USA, May 16-20* (2004).
70. Correia, N.C., F. Robitaille, A.C. Long, C.D. Rudd, P. Šimáček, and S.G. Advani. "Use of resin transfer molding simulation to predict flow, saturation and compaction in the VARTM process." In *2002 ASME-IMECE, New Orleans, November 17 - 22* (2002).
71. Ouahbi, T., A. Saouab, J. Bre'ard, P. Ouagne, and S. Chatel. "Modelling of hydro-mechanical coupling in infusion processes." *Composites Part A* 38 (2007): 1646–1654.
72. Ngo, N. D., R. V. Mohan, P. W. Chung, K. K. Tamma, and D. R. Shires. "Recent developments encompassing non-isothermal/isothermal liquid composite molding process modeling/analysis: physically accurate, computationally effective, and affordable simulations and validations." *Journal of Thermoplastic Composite Materials* 11 (1998): 493-532.
73. Andersson, H.M., T.S. Lundström, and N. Langhans. "Computational fluid dynamics applied to the vacuum infusion process." *Polymer Composites* 26(22): 231-239.
74. Koorevaar, A. "Simulation of liquid injection molding." In *23<sup>rd</sup> International SAMPE Europe Conference, Paris, France, April 9-11* (2002).
75. Šimáček, P., and S. G. Advani. "Desirable features in mold filling simulations for liquid composite molding processes." *Polymer Composites* 25(44): 355-367.
76. Trochu, F., E. Ruiz, V. Achim, and S. Soukane. "Advanced numerical simulation of liquid composite molding for process analysis and optimization." *Composites Part A* 37 (2006): 890–902.
77. Loendersloot, R. "The structure-permeability relation of textile reinforcements." PhD thesis, University of Twent, Enschede, The Netherlands, April (2006).
78. Ranganathan, S., F.R. Phelan, and S.G. Advani. "Generalized model for the transverse fluid permeability in unidirectional fibrous media." *Polymer Composites* 17(2) (1996): 222–30.
79. Brouwer, W.D., E.C.F.C. van Herpt, and M. Labordus, "Vacuum injection moulding for large structural applications." *Composites Part A* 34 (2003): 551-558.
80. Young, W.B., K. Rupel, K. Han, L.J. Lee, and M.J. Liou. "Analysis of resin injection molding in molds with preplaced fiber mats. II: Numerical Simulation and Experiments of Mold Filling." *Polymer Composites* 12(1) (1991): 30–38.
81. Pan, R., Z. Liang, C. Zhang, and B. Wang. "Statistical characterization of fiber permeability for composite manufacturing." *Polymer Composites* 21(6) (2000): 996–1006.
82. Joubaud, L., V. Achim, and F. Trochu. "Numerical simulation of resin infusion and reinforcement consolidation under flexible cover." *Polymer Composites* 26 (2005): 417–427.
83. Li, J., C. Zhang, R. Liang, and B. Wang. "Optimum Design of Resin Injection Process for Resin Transfer Molding with In-situ Permeability Measurement and Process Simulation." In *SAMPE, Long Beach, USA, May 1-5* (2005).
84. Hoes, K, D. Dinescu, H. Sol, M. Vanheule, R.S. Parnas, Y. Luo, and I. Verpoest. "New set-up for measurement of permeability properties of fibrous reinforcements for RTM." *Composites Part A* 33(7) (2002): 959–69.
85. Adler, P.M. *Porous media: geometry and transports*. Stoneham, USA: Butterworth-Heinemann (1992).
86. Woerdeman, D.L., F.R. Phelan Jr., and R.S. Parnas. "Interpretation of 3D permeability measurements for RTM modelling." *Polymer Composites* 16(6) (1995): 470–80.
87. Brusckhe, M.V., and S.G. Advani. "RTM filling simulation of complex three dimensional shelllike structures." *SAMPE Quarterly* 23(1) (1991): 2–11.
88. Dullien, F.A.L. *Porous Media-Fluid Transport and Pore Structure*. New York: Academic Press (1992).

89. Bruschke, M.V. "A predictive model for permeability and non-isothermal flow of viscous and shear-thinning fluids in anisotropic fibrous media." Ph.D. dissertation, University of Delaware (1992).
90. Gebart, B.R. "Permeability of unidirectional reinforcements for RTM." *Journal of Composite Materials* 26 (1992): 1100–33.
91. Trevino, L., K. Rupel, W.B. Young, M.J. Liou, and L.J. Lee. "Analysis of resin injection molding in molds with preplaced fiber mats. I: Permeability and compressibility measurements." *Polymer Composites* 12(1) (1991): 20–9.
92. Kozeny, J. "Ueber kapillare Leitung des Wassers im Boden." *Sitzungsber. Akad. Wiss. Wien* 136(2a) (1927): 271-306.
93. Carman, P.C. *Journal of the Society of Chemical Industry* 58 (1939): 1.
94. Lomov, S.V., I. Verpoest, T. Peeters, D. Roose, and M. Zako. "Nesting in textile laminates: geometrical modelling of the laminate." *Composites Science Technology* 63(7) (2003): 993–1007.
95. Hoes, K., D. Dinescua, H. Sol, R.S. Parnas, and S. Lomov. "Study of nesting induced scatter of permeability values in layered reinforcement fabrics." *Composites: Part A* 35 (2004): 1407–1418.
96. Liu, Q., R.S. Parnas, and H.S. Giffard. "New set-up for in-plane permeability measurement." *Composites: Part A* 38 (2007): 954–962.
97. Dullien. "Single phase flow through porous media and pore structure." *Chemical Engineering* 10 (1975): 1–34.
98. Bickerton, S., E.M. Sozer, P. Šimáček, and S.G. Advani. "Fabric structure and mold curvature effects on preform permeability and mold filling in the RTM process. Part II. Predictions and comparisons with experiments." *Composites: Part A* 31 (2000): 439–458.
99. Wang, T.J., C.H. Wu, and L.J. Lee. "In-plane permeability measurement and analysis in liquid composite molding." *Polymer Composites* 15 (1994): 278-288.
100. Modi, D., N. Correia, M. Johnson, A. Long, C. Rudd, and F. Robitaille. "Active control of the vacuum infusion process." *Composites Part A* 38(5) (2007): 1271-1287.
101. Lomov, S. V., E.B. Belov, T. Bischoff, S.B. Ghosh, C. T. Truong, I. Verpoest. "Carbon composites based on multiaxial multiply stitched preforms. Part 1: Geometry of the preform." *Composites Part A* 33(9) (2002): 1171-1183.
102. Verpoest, I., and S. V. Lomov. "Virtual textile composites software wisetex: integration with micro-mechanical, permeability and structural analysis." *Composite Science and Technology* 65(15-16) (2005): 2563-2574.
103. Wu, J.H. M.Sc. thesis, National Taiwan University (2003).
104. Loos, A.C. "VARTM processing tailored composite structures for aerospace applications." In *SAMPE 2005, Long Beach, USA, May 1 – 5* (2005).
105. Parnas, R.S., J.G. Howard, T.L. Luce, and S.G. Advani. "Permeability characterization. Part I: a proposed standard reference material for permeability." *Polymer Composites* 16(6) (1995): 429–45.
106. Salem, A.J., and R.S. Parnas. "The unidirectional and radial in-plane flow of fluids through woven composite reinforcements." In *6th Technical Conference, American Society for Composites, Albany, USA* (1991).
107. Parnas, R.S., and A.J. Salem. "A comparison of the unidirectional and radial in-plane flow of fluids through woven composite reinforcements." *Polymer Composites* 14(5) (1993): 383–94.
108. Stedile. "Felt permeability testing apparatus." US Patent No. 3577767, May 4, 1971.
109. Ding, L., C. Shih, Z. Liang, C. Zhang, and B. Wang. "In situ measurement and monitoring of whole-field permeability profile of fiber preform for liquid composite molding processes." *Composites: Part A* 34 (2003): 779–789.
110. Eksik, Ö., P. Schulze, J. W. Gillespie, Jr., and D. Heider "An experimental method for continuous measurement of in-plane fabric permeability as a function of fiber volume fraction using air flow." In *1st Joint Canadian & American Technical Conference, University of Delaware, September* (2009).



111. Bickerton, S., and S.G. Advani. "Characterization and modeling of race-tracking in liquid composite molding processes." *Composites Science and Technology* 59(15) (1999): 2215–2229.
112. Devillard, M., K.T. Hsiao, A. Gokce, and S.G. Advani. "On-line characterization of bulk permeability and race-tracking during the filling stage in resin transfer molding process." *Journal of Composite Materials* 37 (2003): 1525–41.
113. Buntain, M.J., and S. Bickerton. "Compression flow permeability measurement: a continuous technique." *Composites Part A* 34 (2003): 445-457.
114. Lundström, T.S., S. Toll, and J.M. Håkanson. "Measurements of the permeability tensor of compressed fibre beds." *Transport in Porous Media* 47 (2002): 363-380.
115. Parnas, R.S., K.M. Flynn, and M.E. Dal-Favero. "A permeability database for composite manufacturing." *Polymer Composites* 18(5) (1997): 623–33.
116. Neale, G., and W. Nader. "Practical significance of Brinkman's extension of Darcy's law: coupled parallel flows within a channel and a bounding porous medium." *Canadian Journal of Chemical Engineering* 52 (1974): 475–8.
117. Parnas, R.S., and Y. Cohen. "Coupled parallel flows of power-law fluids in a channel and a bounding porous medium." *Chemical Engineering Communications* 53 (1987): 3–22.
118. Diallo, M.L., R. Gauvin, and F. Trochu. "Key factors affecting the permeability measurement in continuous fiber reinforcements." In *ICCM-11, Gold Coast, Australia* (1997).
119. Binetruy C., B. Hilaire, and J. Pabiot. "The interactions between flows occurring inside and outside fabric tows during rtm." *Composites Science and Technology* 57(5) (1997): 587-596.
120. Lekakou, C., M.A.K. Johari, D. Norman, and M.G. Bader. "Measurement techniques and effects on in-plane permeability of woven cloths in resin transfer molding." *Composites Part A* 27(5) (1996): 401–8.
121. Lundström, T.S., R. Stenberg, R. Bergstrom, H. Partanen, and P.A. Birkeland. "In-plane permeability measurements: a nordic round-robin study." *Composites Part A* 31(1) (2000): 29–43.
122. Gonzalez, V.M. "Studies of reactive polymer processing with Fiberglass Reinforcement." PhD dissertation, University of Minnesota (1983).
123. Weiztenböck, J.R., R.A. Shenoi, and P.A. Wilson. "Radial flow permeability measurement. Part A: theory." *Composites Part A* 30(6) (1999): 781–96.
124. Adams K.L., and L. Rebenfeld. "Permeability characteristics of multilayer fiber reinforcements. part I: experimental observations." *Polymer Composites* 12(3) (1991): 179-185.
125. Wu, C.H., Wang, T.J. and Lee, L.J. "Trans-plane fluid permeability measurement and its application in liquid composite molding." *Polymer Composites* 15(4): 289–298.
126. Weiztenböck, J.R., R.A. Shenoi, and P.A. Wilson. "Measurement of three-dimensional permeability." *Composites Part A* 29(1) (1998): 159–169.
127. Gebart, B.R., P. Gudmundson, L.A. Strombeck, and C.Y. Lundemo. In *ICCM-8, Honolulu, USA* (1991).
128. Lai, Y.H., B. Khomami, and J.L. Kardos. "Accurate permeability characterization of preforms used in polymer matrix composite fabrication processes." *Polymer Composites* 18(3) (1997): 368–77.
129. Lee, Y.J., J.H. Wu, Y. Hsu, and C.H. Chung. "A prediction method on in-plane permeability of mat/roving fibers laminates in vacuum assisted resin transfer molding." *Polymer Composites* 27 (2006): 665–670.
130. Wu, X., and J. Li. "A new method to determine fiber transverse permeability." *Journal of Composite Materials* 41(6) (2007): 747-56.
131. Calado, V.M.A., and S.G. Advani. "Effective average permeability of multi-layer preforms in resin transfer molding." *Composite Science and Technology* 56 (1996): 519-531.
132. Liu, X. L., P.J. Falzon, R. Sweeting, and R. Paton. "Effective compressibility and permeability of multi-layer non-crimp fiberglass reinforcements." *Journal of Reinforced Plastics and Composites* 23(8): 861-879.
133. Luce, T., S.G. Advani, G. Howard, and R. Parnas. "Permeability characterization: part 2: flow behavior in multiple-layer preforms." *Polymer Composites* 16(6) (1995): 446–458.

134. Endruweit, A., T. Luthy and P. Ermanni. "Investigation of the influence of textile compression on the out-of-plane permeability of a bidirectional glass fiber fabric." *Polymer Composites* 23 (2002): 538-554.
135. Comas-Cardona, S., C. Binetruy, and P. Krawczak. "Unidirectional compression of fibre reinforcements. Part 2: A continuous permeability tensor measurement." *Composites Science and Technology* 67 (2007): 638–645.
136. Scholz, S., J.W. Gillespie, and D. Heider. "Measurement of transverse permeability using gaseous and liquid flow." *Composites: Part A* 38 (2007): 2034–2040.
137. Drapier, S., A. Pagot, A. Vautrin, and P. Henrat. "Influence of the Stitching Density on the Transverse Permeability of Non-crimped New Concept (NC2) Multiaxial Reinforcements: Measurements and Predictions." *Composites Science and Technology* 62(15) (2002): 1979–1991.
138. Andersson, H.M., T.S. Lundström, B.R. Gebart, and R. Långström. "Flow enhancing layers in the vacuum infusion process." *Polymer Composites* 23(5) (2002): 895-901.
139. Stöven, T., F. Weyrauch, P. Mitschang, and M. Neitzel. "Continuous monitoring of three-dimensional resin flow through a fibre perform." *Composites Part A* 34(7) (2003): 475–480.
140. Neacsu, V., J. Leisen, H.W. Beckham, and S.G. Advani. "Use of magnetic resonance imaging to visualize impregnation across aligned cylinders due to capillary forces." *Experiments in Fluids* 42 (2007): 425–440.
141. Breard, J., A. Saouab, and G. Bouquet. "Dependence of the reinforcement anisotropy on a three dimensional resin flow observed by x-ray radiography." *Journal of Reinforced Plastics and Composites* 18 (1999): 814–26.
142. Ahn, S.H., W.L. Lee, and G.S. Springer. "Measurement of the Three-dimensional Permeability of Fiber Performs using Embedded Fiber Optic Sensors." *Journal of Composite Materials* 29(6) (1995): 714–733.
143. Walsh, S.W. "In situ sensor method and device." U.S. Patent No. 5210499, 11 May 1993.
144. Tuncol, G., M. Danisman, A. Kaynar, and E.M. Sozer. "Constraints on monitoring resin flow in the resin transfer molding (RTM) process by using thermocouple sensors." *Composites Part A* 38 (2007): 1363–1386.
145. Nedanov, P.B., S.G. Advani, S.W. Walsh, and W.O. Ballata. *Advances in Aerospace in Materials and Structures*. Vol. 58. New York: ASME (1999).
146. Weiztenböck, J.R., R.A. Sheno, and P.A. Wilson. "Radial flow permeability measurement. Part B: application." *Composites Part A* 30(6) (1999): 797–813.
147. Neacsu, V., A. Abu-Obaid, S.G. Advani. "Spontaneous radial capillary impregnation across a bank of aligned micro-cylinders—Part II: Experimental investigations." *International Journal of Multiphase Flow* 32 (2006): 677–691.
148. Nedanov, P.B. and S.G. Advani. "A Method to Determine 3D Permeability of Fibrous Reinforcements." *Journal of Composite Materials* 36(2) (2002): 241–254.
149. Brusckke, M.V., and S.G. Advani. RTM filling simulation of complex three dimensional shelllike structures." *SAMPE Quarterly* 23(1) (1991): 2–11.
150. Kim, S.K., and I.M. Daniel. "Determination of three-dimensional permeability of fiber preforms by the inverse parameter estimation technique." *Composites: Part A* 34 (2003): 421–429.
151. Gokce, A., M. Chohra, S.G. Advani, and S.M. Walsh. "Permeability estimation algorithm to simultaneously characterize the distribution media and the fabric preform in vacuum assisted resin transfer molding process." *Composites Science and Technology* 65 (2005): 2129–2139.
152. Friedman, H.L., R.A. Johnson, V. Gusev, A.V. Neidmark, D. Buvel, and D.R. Salem. "Visualization and Quantification of Forced In-Plane Flow Through Deformed Porous Media." *Polymer Composites* 20(5) (1999): 613-627.
153. Rudd, C.D., A.C. Long, P. McGeehin, and P. Smith. "In-Plane Permeability Determination for Simulation of Liquid Composite Molding of Complex Shapes." *Polymer Composites* 17 (1996): 52-59.
154. Slade, J., M. Sozer, and S.G. Advani. "Effect of shear deformation on permeability of fiber preforms." *Journal of Reinforced Plastics & Composites* 19 (2000): 552–68.

155. Pan, R., Z. Liang, C. Zhang, and B. Wang. „Statistical characterization of fiber permeability for composite manufacturing.” *Polymer Composites* 21(6) (2000): 996–1006.
156. Bickerton, S., E.M. Sozer, P.J. Graham, and S.G. Advani. “Fabric structure and mold curvature effects on preform permeability and mold filling in the RTM process. Part I. Experiments.” *Composites: Part A* 31 (2000): 423–438.
157. Li, J., C. Zhang, Z. Liang, and B. Wang. “Stochastic Simulation Based Approach for Statistical Analysis and Characterization of Composites Manufacturing Processes.” *Journal of Manufacturing Systems* [on-line], Society of Manufacturing Engineers (2006).
158. Phelan, F.R., Y. Leung, and R.S. Parnas. “Modeling of microscale flow in unidirectional fibrous porous media.” *Journal of Thermoplastic Composite Materials* 7 (1994): 208-218.
159. Lundström, T.S. “The permeability of non-crimp-stitched fabrics”, *Composites: Part A* 31 (2000): 1345-1353.
160. Cann, M.T., D.O. Adams, and C.L. Schneider. “Characterization of fiber volume fraction gradients in composite laminates.” *Journal of Composite Materials* 42 (2008): 447-466.
161. Sun, X., S. Li, and L.J. Lee. “Mold Filling Analysis in Vacuum-Assisted Resin Transfer Molding. Part I: SCRIMP Based on a High-Permeable Medium.” *Polymer Composites* 19(6) (1998): 807-817.
162. Montgomery, D.C., G.C. Runger, and N.F. Hubele. *Engineering statistics*. New York: Wiley (2001).
163. Hoes, K. “Development of a new sensor-based set-up for experimental permeability Identification of Fibrous Media.” PhD dissertation, Vrije Universiteit Brussels (2003).
164. Gonçalves, P.C.T., and N.C. Correia. “A study on the determination of stochastic reinforcement permeability in constant injection pressure conditions.” In *ICCM 17, Edinburgh, UK, July 27-31* (2009).
165. Sozer, E.M., B. Chen, P.J. Graham, T.W. Chou, and S.G. Advani. “Characterization and prediction of compaction force and preform permeability of woven fabrics during the resin transfer molding process.” In *Fifth International Conference on Flow Processes in Composite Materials, Plymouth, U.K., July 12–14* (1999).
166. Šimáček P., and S.G. Advani. “Modeling and simulation of resin flow in resin infusion processes such as VARTM, VAP and compression RTM.” In *SAMPE Fall Technical Meeting 52* (2007).
167. Grimsley B.W., R.J. Cano, P. Hubert, A.C. Loos, C.B. Kellen, and B.J. Jensen. “Preform Characterization in VARTM process model development.” In *SAMPE 2004, Long Beach, USA, May 16-20* (2004).
168. Han, K., S. Jiang, C. Zhang, and B. Wang. “Flow modeling and simulation of SCRIMP for composites manufacturing.” *Composites: Part A* 31(79) (2000).
169. Pearce, N., and J. Summerscales. “Compressibility of a reinforcement fabric.” *Composites Manufacturing* 6(1) (1995): 15–21.
170. Chen, B., and T.W. Chou. “Compaction of woven-fabric preforms in liquid composite molding processes: Single-layer deformation.” *Composites Science and Technology* 59 (1999):1519–26.
171. Li, J., C. Zhang, R. Liang, B. Wang, and S. Walsh. “Modeling and analysis of thickness gradient and variations in vacuum-assisted resin transfer molding process.” *Polymer Composites* (2008): 473-482.
172. Heider, D., and J.W. Gillespie Jr. “Compaction development during vacuum assisted resin transfer molding (VARTM).” In *SAMPE Europe conference 22, Paris, France* (2001).
173. Acheson, J.A., P. Šimáček, and S.G. Advani. “The implication of fiber compaction and saturation on fully coupled VARTM simulation.” *Composites: Part A* 35 (2004): 159–69.
174. Lam, R.C., and J.L. Kardos. “The permeability and compressibility of aligned and cross-ply carbon fiber beds during processing of composites.” *Polymer Engineering Science* 31(14) (1991): 1064-1070.
175. Chen, B., E.J. Lang, and T.W. Chou. “Experimental and theoretical studies of fabric compaction behavior in resin transfer molding.” *Materials Science and Engineering A317* (2001): 188–96.
176. Saunders, R.A., C. Lekakou, and M.G. Bader. “Compression in the processing of polymer composites: A mechanical and microstructural study for different glass fabrics and resins.” *Composites and Science Technology* 59(10) (1999): 983-993.

177. Robitaille, F., and R. Gauvin. "Compaction of textile reinforcements for composites manufacturing: Reorganization of the fiber network. III. Reorganization of the fiber network." *Polymer Composites* 20(1) (1999): 48–61.
178. Sewell, T.A., S. Wanthal, and B. Rapp. "Improved laminate physical and mechanical properties using "HY-TEST" vacuum assisted resin transfer molding." In *SAMPE 200, Long Beach, USA, May 1-5* (2005).
179. Tackitt, K.D., and S.M. Walsh. "Experimental study of thickness gradient formation in the VARTM process." *Materials and Manufacturing Processes*, 20 (2005): 607–627.
180. Govignon, Q., S. Bickerton, J. Morris, and P.A. Kelly. "Full field monitoring of the resin flow and laminate properties during the resin infusion process." *Composites: Part A* 39 (2008): 1412–1426.
181. Kelly, P.A., R. Umer, and S. Bickerton. "Viscoelastic response of dry and wet fibrous materials during infusion processes." *Composites: Part A* 37 (2006): 868–873.
182. Saunders, R.A., C. Lekakou, and M.G. Bader. "Compression in the processing of polymer composites: Modelling of the viscoelastic compression of resin-impregnated fiber networks." *Composites and Science Technology* 59(10) (1999): 1483–94.
183. Gutowski, T.G., T. Morigaki, and Z. Cai. "The consolidation of laminate composites." *Journal of Composite Materials* 21(7) (1987): 172–88.
184. Gutowski, T.G., and G. Dillon. "The elastic deformation of lubricated carbon fiber bundles: Comparison of theory and experiments." *Journal of Composite Materials* 26 (1992): 2331-47.
185. Chen, B., A.H.D. Cheng, and T.W. Chou. "A nonlinear compaction model for fibrous preforms." *Composites: Part A* 32 (2001): 701–7.
186. Gauvin, R. and M. Chibani. "Modelization of the clamping force and mold filling in RTM." In *43rd Annual SPI Composites Institute, February 1-5* (1988).
187. Lopatnikov, S., P. Šimáček, J. Gillespie Jr., and S.G. Advani. "A closed form solution to describe infusion of resin under vacuum in deformable fibrous porous media." *Modelling and Simulation in Materials Science and Engineering* 12 (2004): S191–S204.
188. Gutowski, T.G. "A resin flow fiber deformation model for composites." *SAMPE Quarterly* 16(4) (1985): 58–64.
189. Lomov, S.V., and I. Verpoest. "Compression of woven reinforcements: A mathematical model." *Journal of Reinforced Plastics and Composites* 19(16) (2000):1329–50.
190. Hammami, A., and B.R. Gebart. "Analysis of the vacuum infusion molding process." *Polymer Composites* 27(7) (2000).
191. Grimsley, B.W. "Characterization of the Vacuum Assisted Resin Transfer Molding Process for Fabrication of Aerospace Composites." M.Sc. thesis, Virginia Polytechnic Institute and State University, Blacksburg, USA (2005).
192. Song, X., A. C. Loos, B. W. Grimsley, R. J. Cano, and P. Hubert. "Modeling the VARTM composite manufacturing process." In *SAMPE 2004, Long Beach, USA, May 16-20* (2004).
193. Grimsley, B.W., R.J. Canol, P. Hubert, A.C. Loos, C.B. Kellen, and B.J. Jensen. "Preform characterization in VARTM process model development." In *SAMPE 2004, Long Beach, USA, May 16-20* (2004).
194. Andersson, H.M., T.S. Lundström, B.R. Gebart, and P. Synnergren. "Application of digital speckle photography to measure thickness variations in the vacuum infusion process." *Polymer Composites* 24(3) (2003): 448-455.
195. Kruckenberg, T., L. Ye, and R. Paton. "Static and vibration compaction and microstructure analysis on plain-woven textile fabrics." *Composites: Part A* 39 (2008): 488–502.
196. Bickerton, S., M.J. Buntain, and A.A. Somashekar. "The viscoelastic compression behavior of liquid composite molding preforms." *Composites: Part A* 34 (2003): 431–444.
197. Somashekar, A.A., S. Bickerton and D. Bhattacharyya. "An experimental investigation of non-elastic deformation of fibrous reinforcements in composites manufacturing." *Composites: Part A* 37(6) (2006): 858-867.

198. Echaabi, J., M.B. Nziengui, and M. Hattabi. "Compressibility and relaxation models for fibrous reinforcements in liquid composites moulding." *International Journal of Material Forming* 1(S1) (2008): 851-854.
199. Kim, Y.R., S.P. McCarthy, J.P. Fanucci, S.C. Nolet, and C. Koppernaes. *SAMPE Quarterly* (April 1991): 16.
200. Gama, B.A., H. Li, W. Li, A. Paesano, D. Heider, and J.W. Gillespie Jr. "Improvement of dimensional tolerances during VARTM processing." In *SAMPE Europe conference 22, Paris, France* (2001).
201. Niggemann, C., Y.S. Song, J.W. Gillespie, and D. Heider. "Experimental investigation of the controlled atmospheric pressure resin infusion (CAPRI) process." *Journal of Composite Materials* 42 (2008): 1049-1061.
202. Sathir R.K., R.M. Luck. *Expanding monomers: synthesis, characterization, and applications*. CRC Press (1992).
203. Ramos, J.A., N. Pagani, C.C. Riccardi, J. Borrajo, S.N. Goyanes, and I. Mondragon. "Cure kinetics and shrinkage model for epoxy-amine systems." *Polymer* 46 (2005): 3323-3328.
204. Elbouazzaoui, O., S. Drapier, and P. Henrat. "An Experimental Assessment of the Saturated Transverse Permeability of Non-crimped New Concept (NC2) Multiaxial Fabrics." *Journal of Composite Materials* 39 (2005): 1169-1193.
205. Kiuna, N., C.J. Lawrence, Q.P.V. Fontana, P.D. Lee, T. Selerland, and P.D.M. Spelt. "A model for resin viscosity during cure in the resin transfer moulding process." *Composites: Part A* 33 (2002) 1497-1503.
206. Kamal, M.R. and S. Sorour. "Kinetics and thermal characterization of thermosetting resin." *Polymer Engineering Science* 13 (1973): 356-69.
207. Kendall, K.N., and C.D. Rudd. "Flow and Cure Phenomena in Liquid Composite Molding." *Polymer Composites* 15(5) (1994): 334-348.
208. Theriault, R.P., T. A. Osswald, and J.M. Castro. "A Numerical Model of the Viscosity of an Epoxy Prepreg Resin System." *Polymer Composites* 20(5) (1999): 628-63.
209. Pichaud, S., X. Duteurtre, A. Fit, F. Stephan, A. Maazouz, and J.P. Pascault. "Chemorheological and dielectric study of epoxy-amine for processing control." *Polymer International* 48 (1999): 1205-1218.
210. Lienhard, J.H. and J.H. Lienhard. *A heat transfer textbook*. Cambridge: Phlogiston Press (2008).
211. Fujii, T. and H. Imura. "Natural-convection heat transfer from a plate with arbitrary inclination." *International Journal of Heat and Mass Transfer*. Elsevier (1972).
212. Rohsenow, W.M., J.P. Hartnett, and Y.I. Cho. *Handbook of heat transfer: McGraw-Hill handbooks*. McGraw-Hill Professional (1998).
213. Warrington, R.O., S. Smith, R.E. Powe, and R. Mussulman. "Boundary Effects on Natural Convection for Cylinders and Cubes." In *Transactions of the ASME* 39 (1984): 63-69.
214. Goldenberg, H. "A problem in radial heat flow." *British Journal of Applied Physics* 2 (1951): 233-237.
215. Goldenberg, H. "Heat flow in an infinite medium heated by a sphere" *British Journal of Applied Physics* 3 (1952): 296-298.
216. Shojaei, A., F. Trochu, S.R. Ghaffarian, S.M.H. Karinian, and L. Lessard. "An Experimental Study of Saturated and Unsaturated Permeabilities in Resin Transfer Molding Based on Unidirectional Flow Measurements." *Journal of Reinforced Plastics & Composites* 23(14) (2004): 1515-1536.
217. Molnar, J.A., L. Trevino, and L.J. Lee. "Session 20-A." In *44th Annual Conference, Composites Institute, The Society of Plastics Industry, Feb 6-9* (1989).
218. Chan, A.W., D.E. Larive, and R.J. Morgan. "Anisotropic permeability of fiber preforms: constant flow rate measurement." *Journal of Composite Materials* 27(10) (1993): 996-1008.
219. Karniadakis, G., A. Beskok, and N. Aluru. *Micro Flows*. Dordrecht, Netherlands: Springer (2001).
220. Dungan, F.D., and A.M. Sastry. "Saturated and Unsaturated Polymer Flows: Microphenomena and Modeling." *Journal of Composite Materials* 36(13) (2002): 1581-1603.
221. Lekakou C, Bader MG. "Mathematical modelling of macro- and micro-infiltration in resin transfer moulding (RTM)." *Composites: Part A* 29 (1998): 29.

222. Babu B.Z., and K.M. Pillai. "Experimental investigation of the effect of fiber architecture on the unsaturated flow in liquid composite molding." *Journal of Composite Materials* 38(1) (2004): 57–79.
223. Babu , B.Z., and K.M. Pillai. "New experimental findings on resin impregnation process for woven, stitched or braided fiber mats in liquid composite molding," In *SAMPE 2002, Long Beach, USA* (2002).
224. Kuentzer, N., P. Šimáček, S.G. Advani, S. Walsh. "Permeability characterization of dual scale fibrous porous media." *Composites: Part A* 37 (2006) 2057–2068.
225. Stadtfeld, H.C., M. Erninger, S. Bickerton, and S.G. Advani. "An experimental method to continuously measure permeability of fiber preforms as a function of fiber volume fraction." *Journal of Reinforced Plastics & Composites* 21(10) (2002): 879–900.
226. Binetruy, H.B. "Tow impregnation model and void formation mechanisms during RTM." *Journal of Composite Materials* 32(3) (1998): 223–45.
227. Pillai, K.M., and S.G. Advani. "Numerical and Analytical Study to Estimate the Effect of Two Length Scales upon the Permeability of a Fibrous Porous Medium." *Transport in Porous Media* 21 (1995): 1-17.
228. Pillai, K.M., and S.G. Advani. "A model for unsaturated flow in woven fiber preforms during mold filling in resin transfer molding." *Journal of Composite Materials* 32(19) (1998): 1753–83.
229. Zhou, F., N. Kuentzer, P. Šimáček, S.G. Advani, S. Walsh. "Analytic characterization of the permeability of dual-scale fibrous porous media." *Composites Science and Technology* 66 (2006): 2795–2803.
230. Roy, T. and K.M. Pillai. "Characterization of dual-scale fiber mats for unsaturated flow in liquid composite molding." *Polymer Composites* 26(6) (2005): 756-769.
231. Roy, T., B.Z. Babu, and K.M. Pillai. "First steps towards quantitative validation of the unsaturated flow theories in liquid composite molding." In *ASME International: Summer Heat Transfer Conference, Las Vegas, USA, July 21-23* (2003).
232. Ahn, K. J., Seferis, J. C. and Berg, J. C. "Simultaneous Measurement of Permeability and Capillary Pressure of Thermosetting Matrices in Woven Fabric Reinforcements." *Polymer Composites* 12(3) (1991): 146–152.
233. Williams, J.G., C.E.M. Morris, and B.C. Ennis. "*Polymer Engineering Science* 14 (1973): 413.
234. Amico, S. and C. Lekakou. "An experimental study of the permeability and capillary pressure in resin transfer moulding." *Composites Science and Technology* 2001;61:1945–59.
235. Scher, K.E. "Comparison of Wicking and Single Filament Techniques for Determining Contact Angles." M.Sc. thesis, University of Washington, USA (1983).
236. Lee, W.J., J.C. Seferis, and J.C. Berg. "Characterizing High Performance Composite Processability With Dynamic Fiber Wettability Measurements." *Polymer Composites* 9(1) (1988): 36-41.
237. Lee, Y., and S. Chiao. "Visualization of Dynamic Contact Angles on Cylinder and Fiber." *Journal of Colloid and Interface Science* 181 (1996): 378–384.
238. Jiang, T.S., S.G. Oh, and J.C. Slattery. "Correlation for dynamic contact angle." *Journal of Colloid and Interface Science* 69 (1979): 74-77.
239. Rohatgi, V., N. Patel, and L.J. Lee. "Experimental Investigation of Flow-Induced Microvoids During Impregnation of Unidirectional Stitched Fiberglass Mat." *Polymer Composites* 17(2) (1996): 161-170.
240. Hsiao, K., M. Devillard, and S.G. Advani. "Simulation based flow distribution network optimization for vacuum assisted resin transfer moulding process." *Modelling and Simulation in Materials Science and Engineering* 12 (2004): S175–S190.
241. Huang, C., S. Thomas, S. Nutt, C. Bongiovanni, and J. Boyd. "Permeability Prediction in Resin Infusion Flow by Finite Element Method." In *SAMPE 2008, Long Beach, USA, May 18-22* (2008).
242. Šimáček, P., and S.G. Advani. "Risk Mitigation with Liquid Molding Process Simulation." In *SAMPE 2009, Baltimore, USA, May 18-21* (2009).
243. Klunker, F., , G. Ziegmann, S. Aranda, Y.M. Liu. "Permeability Measurement of Flow Enhancement Layers by an Indirect Measurement Technique Using Flow Simulation." In *SAMPE Europe, Paris, March 31- April 2* (2008).

244. Aranda, S., F. Klunker, H. Gabber, G. Ziegmann „Void content and void formation mechanisms in resin infusion processes” In *SAMPE Europe, Paris, France, March 23-25* (2009).
245. Liu, L., Z. Guo, B. Zhang “Experimental investigation of porosity and its effects on interlaminar shear strength in composite laminates.” In *SAMPE 2006, Long Beach, USA, April 30 - May 4* (2006).
246. Tang, J., W.I. Lee and G.S. Springer. “Effects of Cure Pressure on Resin Flow, Voids, and Mechanical Properties.” *Journal of Composite Materials* 21 (1987): 421-440.
247. Guo, Z., L. Liu, B. Zhang, and S. Du. “Critical Void Content for Thermoset Composite Laminates.” *Journal of Composite Materials* (published online May 19, 2006): 1-16.
248. Njionhou, A., F. Berthet, B. Castanie. ”Optimization of The Mechanical Properties of Composites made by Liquid Resin Infusion (LRI) According to The Manufacturing Parameters.” In *3rd Conference on Rotomoulding Thermoforming Stretch-Blow Moulding, Ecole des Mines d’Albi, France, March 11-13* (2009).
249. Labordus, M. *Voids and bubbles during vacuum infusion*. Technical Report, Society of Manufacturing Engineers, EM01-352 (2001).
250. Lundström, T.S. “Bubble Transport Through Constricted Capillary Tube with Application to Resin Transfer Moulding.” *Polymer Composites* 17 (1996): 770-779.
251. Chang, C., and M. Shih. “Numerical Simulation on the Void Distribution in the Fiber Mats During the Filling Stage of RTM.” *Journal of Reinforced Plastics and Composites* 22(16) (2003): 1437-1454.
252. Lundström, T.S., B.R. Gebart, C.Y. Lundemo. “Void Formation in RTM.” *Journal of Reinforced Plastics and Composites* 12 (1993): 1340-1349.
253. Khattab, A. “Exploratory development of VARIM process for manufacturing high temperature polymer matrix composites.” PhD. Dissertation, University of Missouri-Columbia (2005).
254. Chang, C., L. Hourng. “Numerical Simulation for the Transverse Impregnation in Resin Transfer Moulding.” *Journal of Reinforced Plastics and Composites* 17 (1998): 165-182.
255. Lundström, T.S., Gebart, B.R., “Influence from Process Parameters on Void Formation in RTM.” *Polymer Composites* 15 (1994): 25-33.
256. Olsson J, S. Lundström, K. Olofsson. “Compression moulding of SMC: coupling between the flow and the local void contents.” In *ICCM 17: Edinburgh, UK, July 27-31* (2009).
257. Lundström, T.S., V. Frishfelds, A. Jacovics. “A statistical approach to permeability of clustered fibre reinforcements.” *Journal of Composite Materials* 38(3) (2004): 1137-1149.
258. Ruiz, E., V. Achim, S. Soukane, F. Trochu, and J. Bread. “Optimization of injection flow rate to minimize micro/macro-voids formation in resin transfer molded composites.” *Composites Science and Technology* 66 (2006): 475–486.
259. Kuentzer, N., P. Šimáček, and S.G. Advani. “Modeling and simulation of dual scale flow in woven or stitched preforms in liquid molding processes.” In *SAMPE 2006, Long Beach, USA, April 30 - May 4* (2006).
260. Lundström, T.S. “Measurement of Void Collapse during Resin Transfer Moulding.” *Composites: Part A* 28A (1997): 201-214.
261. Patel, N., and L.J. Lee. “Effects of Fiber Mat Architecture on Void Formation and Removal in Liquid Composite Molding.” *Polymer Composites* 16(5) (1995): 386–399.
262. Breard, J., A. Saouab, and G. Bouquet. “Numerical simulation of void formation in LCM.” *Composites: Part A* 34(6) (2003): 517.
263. Hattabi, M., J. Echaabi, M.O. Benalah, J. Breard, and A. Saouab. “Flow Analysis during On-line and Radial Injection Applications in Permeability Measurements.” *Journal of Reinforced Plastics and Composites* 24(18) (2005): 1909-1920.
264. Mahale, A.D., R.K. Prud’Homme, and L. Rebenfeld. “Quantitative Measurement of Voids Formed During Liquid Impregnation of Nonwoven Multifilament Glass Networks Using an Optical Visualization Technique.” *Polymer Engineering and Science* 32(5) (1992): 319-326.
265. Gourichon, B., C. Binetruy, P. Krawczak. “A new numerical procedure to predict dynamic void content in liquid composite molding.” *Composites: Part A* 37 (2006): 1961–1969.

266. Patel, N., and L.J. Lee. "Modeling of Void Formation and Removal in Liquid Composite Molding. Part II: Model Development and implementation." *Polymer Composites* 17(1) (1996): 104-114.
267. Fabritius, N. *Experimentelle Untersuchungen zur Dry-Spot Entstehung an Vakuuminfusionsverfahren*. Studienarbeit, University of Stuttgart (2008).
268. Jinlian, H., L. Yi, S. Xueming. "Study on void formation in multi-layer woven fabrics." *Composites: Part A* 35 (2004): 595–603.
269. Lundström, T.S., Frishfelds, V., Jakovics, A., "Bubble formation and motion in non-crimp fabrics with perturbed bundle geometry" *Composites: Part A* (in press) (2009).
270. Jock, C.P. "Quantitative Optical Microscopy Fiber Volume Methods for Composites." *Journal of Reinforced Plastics and Composites* 5 (1986): 110-119.
271. Wilding, S.E., K.A. Stevens, and D.T. Fullwood. "Statistical methods in quality control of composites." In *SAMPE 2008, Long Beach, USA, May 18-22* (2008).
272. Dorsey, D. J., R. Hebner, and W.S. Charlton. "Nondestructive Evaluation of Carbon Fiber Composite Reinforcement Content." *Journal of Composite Materials* 38(17) 2004.
273. Berube, K.A., and R.A. Lopez-Anido. "Variability of Marine Composite Properties in a Manufacturing Round Robin Study." In *SAMPE 2008, Long Beach, USA, May 18-22* (2008).
274. Liu, L., B. Zhang, D. Wang, and Z. Wu. "Effects of cure cycles on void content and mechanical properties of composite laminates." *Composite Structures* 73 (2006): 303–309.
275. Yang, S.W., and C.K. Huang. "Curvature Predictions of Flat Advanced Composite Tools Based on Measured Volume Fraction Gradient." *Journal of Advanced Materials*, 28(2) (1997): 47–55.
276. Ghiorse, S.R. *A Comparison of Void Measurement Methods for Carbon/Epoxy Composites*. Report to Army Lab Command, Material Technology Lab, Watertown, USA (1991).
277. Kuentzer, N., P. Šimáček, S.G. Advani, S. Walsh. "Correlation of void distribution to VARTM manufacturing techniques." *Composites: Part A* 38 (2007): 802–813.
278. Purslow, D. "On the Optical Assessment of the Void Content in Composite Materials." *Composites* 15(3) (1984): 207-210.
279. Cohen, D., S.C. Mantell, and L. Zhao. "The Effect of Fiber Volume Fraction on Filament Wound Composite Pressure Vessel Strength" *Composites Part B* 32(5) (2001): 413–429.
280. Endruweit, A., P. McGregor, A.C. Long, and M.S. Johnson. "Influence of the fabric architecture on the variations in experimentally determined in-plane permeability values." *Composites Science and Technology* 66 (2006): 1778–1792.
281. Rieber, G., P. Mitschang. "Affected 2D-Permeability of Reinforcements by Sewing." In *SAMPE Europe, Paris, France, March 31- April 2* (2008).
282. Yuexin, D., T. Zhaoyuan, Z. Yan, and S. Jing. "Compression Responses of Preform in Vacuum Infusion Process." *Chinese Journal of Aeronautics* 21(2008): 370-377.
283. Pollard, M.. "Permeabilities of Fiber Mats Used in Resin Transfer Molding." In *24th SAMPE Technical Conference, Toronto* (1992).
284. Estrada, G., C. Vieux-Pernon, and S.G. Advani. "Experimental Characterization of the Influence of Tackifier Material on Preform Permeability." *Journal of Composite Materials* 36(19) (2002): 2297-2310.
285. Rohatgi, V. and L.J. Lee. "Moldability of Tackified Fiber Preforms in Liquid Composite Molding." *Journal of Composite Materials* 31 (1997): 720-744.
286. Shih, C.H., and L.J. Lee. "Tackification of Textile Fiber Preforms in Resin Transfer Molding." *Journal of Composite Materials* 35(21) (2001): 1954-1981.
287. Long, A.C. "Process modelling for liquid moulding of braided preforms." *Composites: Part A* 32 (2001): 941-953.



288. Charlebois, K.M., R. Boukhili, O. Zebdi, F. Trochu, and A. Gasmi. "Evaluation of the Physical and Mechanical Properties of Braided Fabrics and their Composites." *Journal of Reinforced Plastics and Composites* 24 (2005): 1539-1554.
289. Wu, X., J. Li, and R.A. Shenoi. "Measurement of braided preform permeability." *Composites Science and Technology* 66 (2006): 3064–3069.
290. Myslinski, P.J. "Analysis of cyanate ester resins and graphite fabric for use in resin infusion processing." M.Sc. thesis, Virginia Polytechnic Institute and State University, USA (1997).
291. Loendersloot, R., S.V. Lomov, R. Akkerman, and I. Verpoest. "Architecture and Permeability of Sheared Carbon Fibre Non-Crimp Fabrics." In *SAMPE Europe Conference 24, Paris, France* (2003).
292. Buchs, W., S. Kunze, T. Springer and C. Weimer. "Development of CFRP Hinge Arms for Aircraft Passenger Doors." In *SAMPE Europe Conference 28, Paris, France* (2007).
293. Schürmann, M. *Konstruieren mit Faser-Kunststoff-Verbunden*. Berlin: Springer-Verlag (2007).
294. (Anonymous) "Fiber Laying Process Automated." *Reinforced Plastics* 52 (6) (2008): 18.
295. Kittelson, J. and S.C. Hackett. "Tackifier/Resin Compatibility is Essential for Aerospace Grade Resin Transfer Molding." In *39th International SAMPE Symposium* (1994).
296. ElGhareeb, M. "Standardization, modeling and simulation of liquid resin molding processes for optimized highly efficient production of complex composite structures." M.Sc. thesis, German University in Cairo, Egypt (2009).
297. Chen, J., D. Backes, and K. Jayaraman. "Dynamics of binder displacement in liquid molding." *Polymer Composites* 17 (1996): 23-33.
298. George, A., K. Drechler, and A. Holmberg. "The Permeability of Tackified, Stitched, and Braided Carbon Fiber Textiles: Experimental Characterization and Design Modeling." In *SAMPE 2009, Baltimore, USA, May 18-21* (2009).
299. George, A., K. Drechler, and A. Holmberg. "The Permeability of Carbon Fiber Preforming Materials: Sensitivity to Fabric Geometry." In *20<sup>th</sup> Annual International SICOMP Conference, Piteå, Sweden, May 8-9* (2009).
300. Chiu, C.H., and C.C. Cheng. "In-Plane Permeability of Stitched MMWK Laminates in Resin Transfer Molding." *Journal of Reinforced Plastics and Composites* 20 (2002): 391-408.
301. Shih, C.H. and L.J. Lee. "Effect of fiber architecture on permeability in liquid composite molding." *Polymer Composites* 19 (1998): 626-639.
302. Song, Y. S., Chung, K., Kang, T. J., & Youn, J. R. "Prediction of permeability tensor for three dimensional circular braided preform by applying a finite volume method to a unit cell." *Composites Science and Technology* 64 (2004): 1629–1636.
303. Endruweit, A., A. Long. "The permeability of 3D woven reinforcements: influence of the weaving pattern." In *SAMPE Europe, Paris, France, March 23-25* (2009).
304. K. Han, L. Trevino, L.J. Lee, and M. Liou. "Fiber mat deformation in liquid composite molding I: experimental analysis." *Polymer Composites* 14(2) (1993): 144-150.
305. Saunders, R.A., C. Lekakou, M.G. Bader. "Compression and microstructure of fibre plain woven cloths in the processing of polymer composites." *Composites: Part A* 29(4) (1998): 443–54.
306. <http://www.specialchem4adhesives.com/home/editorial.aspx?id=1785>. Accessed November 2009.
307. Maples, R.E. *Petroleum Refinery Process Economics*. Pennwell Books (2000).
308. Kim, J.G., K.H. Shin, H.S. Ryu, and J.W. Lee. "Monitoring the Change of Viscosity During Cure Reaction of Epoxy Resins with Resin Position Sensor." *Journal of Reinforced Plastics and Composites* 21(2) (2002): 139-152.
309. Tanaeva, S.A., and L.E. Evseeva. "Thermophysical properties of epoxy compounds at low temperatures." *Journal of Engineering Physics and Thermophysics* 70(1) (1997): 13-17.

310. Garrett, K.W., and H.M. Rosenberg. "The thermal conductivity of epoxy-resin powder composite materials." *Journal of Physics D: Applied Physics* 7 (1974): 1247-1258.
311. <http://Internet-specialchem4adhesives.com>, [internet-omnexus4adhesives.com](http://internet-omnexus4adhesives.com). Accessed October 2009.
312. Fernberg, P. *A simple analytical model for 1D-mould filling with reactive fluids*. Technical report, SICOMP CR06-039 (2006).
313. Modi, D. "Modeling and Active Control of the Vacuum Infusion Process for Composites Manufacture." PhD thesis, University of Nottingham (2008).
314. Correia, N. "Analysis of the vacuum infusion moulding process." PhD thesis, University of Nottingham (2004).
315. Ohara, T., I. Ueno, S. Ogihara, K. Watanabe. "Wetting behavior between fibre & resin in vacuum assisted resin transfer molding (VARTM)." In *ICCM 17: Edinburgh, UK, July 27-31* (2009).
316. <http://www.steinwall.com/PDF/S-PES.pdf>. Accessed October 2009.
317. [http://www.tangram.co.uk/TI-Polymer-PES\\_Chemical.html](http://www.tangram.co.uk/TI-Polymer-PES_Chemical.html). Accessed October 2009.
318. [http://techcenter.lanxess.com/scp/americas/en/docguard/PIB\\_Durethan\\_Chemical\\_Resistance.pdf?docId=76983](http://techcenter.lanxess.com/scp/americas/en/docguard/PIB_Durethan_Chemical_Resistance.pdf?docId=76983). Accessed October 2009.
319. Sezgin and Sankur. "Survey over image thresholding techniques and quantitative performance evaluation." *Journal of Electronic Imaging* 13 (2004): 146-165.
320. <http://helios.univ-reims.fr/Labos/INSERM514/ImageJ/#List>. Accessed October 2009.

## Appendices

### 7.1 Appendix 1 - In-plane permeability model constants.

The in-plane permeability components for each of the materials tested in Section 4.2 were fitted to the power law in Equation 2.13. All the fitted constants  $A_k$  and  $B_k$  are presented for the general (Table A1.1) and principle coordinate systems (Table A1.2). Also presented is the average value for  $\theta$  for each material, as no trend in  $\theta$  with respect to  $v_f$  was observed. The  $K_{45}$  constants for 16-layer TFP materials (not tested in the 45° direction) were fit to estimated  $K_{45}$  values from the approximation in [77]:

$$K_{45} = \frac{\sqrt{2}K_0K_{90}}{\sqrt{(K_0)^2 + (K_{90})^2}} \quad (\text{A1.1})$$

Table A1.1: Fitted constants  $A_k$  and  $B_k$  for general coordinate system permeability components.

<i>Material</i>	$K_0 (m^2)$		$K_{90} (m^2)$		$K_{45} (m^2)$	
	$A_k$	$B_k$	$A_k$	$B_k$	$A_k$	$B_k$
Baseline	2.403E-11	-1.875	8.781E-12	-2.867	1.340E-11	-2.786
NCF-6K	1.846E-11	-1.635	5.968E-12	-2.777	1.298E-11	-2.079
NCF-Tri	8.706E-12	-3.650	9.786E-12	-2.316	1.080E-11	-3.630
Braid-B	6.725E-12	-3.701	1.514E-11	-2.678	9.150E-12	-3.671
Braid-T	3.520E-13	-9.083	1.866E-12	-4.078	1.286E-13	-9.236
T1(12)	2.499E-10	-0.170	5.937E-11	-1.706	2.876E-10	0.226
T2(12)	2.877E-10	-0.077	1.725E-10	-0.763	3.615E-11	-2.176
T3(12)	6.887E-12	-4.358	4.337E-10	0.581	5.348E-12	-4.539
T1(16)	4.627E-13	-5.634	8.847E-13	-4.312	7.260E-13	-4.762
T2(16)	1.439E-12	-4.262	6.288E-12	-2.470	2.656E-12	-3.518
T3(16)	3.441E-12	-3.354	3.791E-12	-3.018	3.645E-12	-3.165
Bind1%	3.518E-12	-3.921	8.971E-13	-5.698	1.246E-12	-5.698
Bind2%	4.714E-12	-3.747	6.057E-13	-5.910	1.722E-12	-5.582
Bind3%	2.149E-13	-8.465	1.392E-12	-5.320	1.933E-12	-5.320
Bind4%	2.012E-12	-4.905	4.120E-12	-3.048	1.493E-12	-5.536

Table A1.2: Fitted constants  $A_k$  and  $B_k$  for principle coordinate system permeability components.

<i>Material</i>	$K_{xx} (m^2)$		$K_{yy} (m^2)$		$\theta (^\circ)$
	$A_k$	$B_k$	$A_k$	$B_k$	
Baseline	2.202E-11	-2.165	9.519E-12	-2.644	19.4
NCF-6K	2.129E-11	-1.505	5.554E-12	-2.828	16.5
NCF-Tri	9.079E-12	-4.285	8.411E-12	-2.302	27.6
Braid-B	1.222E-11	-3.260	8.261E-12	-3.192	28.9
Braid-T	1.183E-10	2.031	1.325E-12	-4.646	5.0
T1(12)	1.246E-10	-0.839	1.274E-10	-0.618	20.9
T2(12)	2.514E-12	-6.024	3.792E-11	-2.117	41.9
T3(12)	9.040E-10	-1.239	1.270E-11	-3.449	18.0
T1(16)	4.608E-13	-5.641	8.863E-13	-4.309	1.7
T2(16)	6.316E-12	-2.465	1.434E-12	-4.265	2.0
T3(16)	3.441E-12	-3.354	3.792E-12	-3.017	1.0
Bind1%	2.450E-12	-4.713	1.152E-12	-5.146	23.3
Bind2%	5.118E-12	-4.208	6.930E-13	-5.464	25.3
Bind3%	1.217E-12	-6.076	3.617E-13	-7.191	34.8
Bind4%	1.571E-12	-5.657	6.781E-12	-2.096	22.4

## 7.2 Appendix 2 - Viscosity modeling for 235H system in $K_{zz}$ measurements.

Some of the  $K_{zz}$  measurement infusions (Section 4.3) were performed using RIM235R and 235H. The viscosity is already well modeled for the 33% 235H / 67% 236H system used in the majority of the VARI experiments. This degree of modeling cannot be done for the 235H (only) system due to a lack of characterization data. Only one isothermal curve was available, for  $T_A = 40^\circ\text{C}$  (from Hexion), but at least two curves, at different  $T_A$  are needed to model the curve at any temperature. If it is assumed that the rate of isothermal viscosity development is proportional between the 235H and the mix, then an approximate viscosity development curve can be predicted for any  $T_A$ .

The maximum  $T_A$  recorded during any  $K_{zz}$  measurements was  $23.6^\circ\text{C}$ . The modeled isothermal viscosity curve for the mix system at this temperature, as well as the  $40^\circ\text{C}$  curves for 235H and the mix is shown in Figure A2.1. All have good exponential function fits over the first 20 minutes:

$$\mu = \mu_0 e^{tb} \quad (\text{A2.1})$$

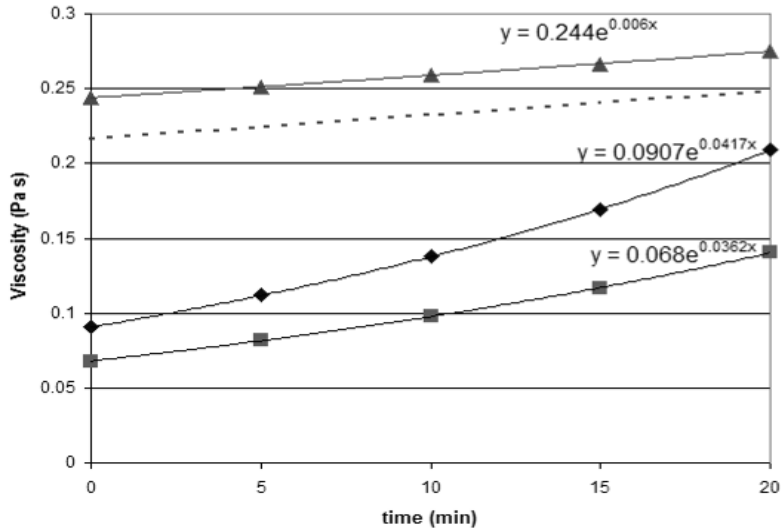


Figure A2.1 – Isothermal  $\mu(t)$  model for 23.6°C (▲: mix) and 40°C (◆: 235H, ■: mix), and estimate for 235H at 23.6°C (dashes).

$\mu_0$  is the initial viscosity at the point of mixing ( $t = 0$ ). For the 235H system,  $\mu_0(T_A)$  was already fit to a power law (Figure 4.61):

$$\mu_0 = 70.163T_A^{-1.8287} \tag{A2.2}$$

The rate of viscosity development due to curing,  $b$ , is the relative steepness of the curve. Given the higher amine value of 235H and thus higher reactivity compared to 236H, or a mix of both,  $b$  should be higher for 235H than the mix at any temperature.

The ratio between rates ( $b$ ) at 40°C is:  $0.0417 / 0.0362 = 1.152$  (235H : mix). If one assumes that the rate for 235H is proportionally greater than the mix' rate at any temperature, then a rate can be calculated from the rate of the mix times this ratio. For example, at 23.6°C, the rate for the mix is 0.006 (much slower due to the lower temperature). This multiplied by the 40°C ratio is:

$$b_{235}(23.6) = b_{mix}(23.6) \cdot ratio(235 : mix) = 0.006 \cdot 1.152 = 0.0069 \tag{A2.3}$$

This rate ( $b$ ) and the initial viscosity ( $\mu_0$ ) yield the theoretical viscosity profile shown in the dashed line in Figure A2.1.

The isothermal curves for the mix at various temperatures between 19.9 and 40°C were modeled, and the resultant rate  $b(T)$  is also well fitted to an exponential function of the temperature (Figure A2.2). By multiplying the ratio from the 40°C curves (1.152) by each  $b(T)$ , the rates at any

temperature for the 235H system can be generated, producing a curve of slightly higher rates at each  $T$ .

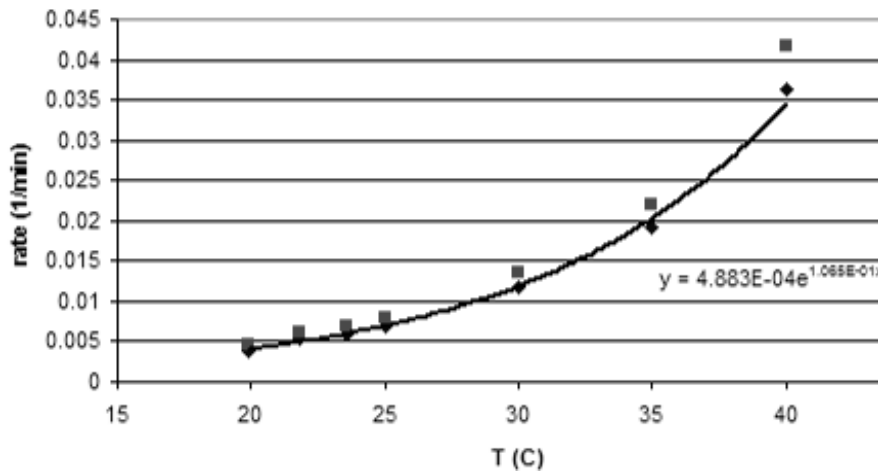


Figure A2.2 - Rate  $b(T)$  for mix (◆) and estimated for 235H (■).

Thus, the estimated viscosity (Pa·s) at any  $t$  (minutes) and  $T$  (°C) for the 235H resin system is:

$$\mu = (70.163T^{-1.8287})e^{tb(T)} \quad (\text{A2.4})$$

where :

$$b(T) = (1.152) \cdot 4.883 \cdot 10^{-4} \cdot e^{0.1065T} \quad (\text{A2.5})$$

### 7.3 Appendix 3 - PAM-OPT code for solving all three permeabilities.

```

ALGKEY/ GENETIC
  POPULATION_SIZE 30
  ITER_NB 30
END
DESPAR/ &p1despar          0
        5e-11          5e-12          5e-10          0.01
  STICKER/ p1
DESPAR/ &p2despar          0
        5e-11          5e-12          5e-10          0.01
  STICKER/ p2
DESPAR/ &p3despar          0
        5e-13          5e-14          5e-12          0.01
  STICKER/ p3
CPFILE/ 05x4CDS.unv
$---5---10---5---20---5---30---5---40---5---50---5---60---5---70---5---80
INPFIL/ 1 dtf
$
$
EXECAL/ 0 1 0

```

```

pamrtm
3    5x4CDS.dtf
END
GETCRV/  &&filling1                0    0
          5x4CDS_Filling_Treshold.dat  1
          3                          0
          0    2    13
          41    52
GETCRV/  &&filling2                0    0
          5x4CDS_Filling_Treshold.dat  1
          3                          0
          0    15   26
          41    52
GETCRV/  &&filling3                0    0
          5x4CDS_Filling_Treshold.dat  1
          3                          0
          0    28   39
          41    52
CALVAL/  &timez                    1
          &&filling1
          Y (XMAX)                    0
CALVAL/  &timey                    1
          &&filling2
          Y (XMAX)                    0
CALVAL/  &timez                    1
          &&filling3
          Y (XMAX)                    0
OBJFCT/  &matchtime                0    0
          ( 1125. - &timez ) ^INT 2 + ( 1125. - &timey ) ^INT 2 +
          ( 1125. - &timez ) ^INT 2
END
EXEINP/
generator : "PAM-RTM 2008.0";

```

**Note: this is first line of the entire .dtf file for the PAM-RTM model to be run. For brevity, it is cut out except for the fabric definition area, where “stickers” must be inserted to designate what parameters to iterate.**

```

reinforcement_type : fabric;
permeability_curve_k1 {
    family : function;
    name : noname;
    nb_ind_vars : 1;
    type : Constant;
#STICKER/p1,7,19
    C : 4.550000E-005;
}
permeability_curve_k2 {
    family : function;
    name : noname;
    nb_ind_vars : 1;
    type : Constant;
#STICKER/p2,7,19
    C : 2.000000E-005;
}
permeability_curve_k3 {
    family : function;

```

```

name : noname;
nb_ind_vars : 1;
type : Constant;
#STICKER/p3, 7, 19
C : 1.500000E-006;

```

#### 7.4 Appendix 4 - Compressibility model constants.

The constants for the Grimsley model of wet expansion (Equation 4.14) are listed here. Table A4.1 lists the constants for the rapeseed oil wetted samples. Table A4.2 lists the constants for the silicon oil wetted samples, both for the first expansion, and the 2<sup>nd</sup> expansion.

Table A4.1 - Rapeseed-wetted expansion constants

<i>Material</i>	$v_{F0}$	$a_w$	$b_w$	$c_w$ (Pa)
Baseline-2	0.3813	0.1950	0.1957	5872
Baseline-4	0.4038	0.1803	0.1645	7136
Baseline-4L	0.3826	0.2765	0.1286	9408
Baseline-6	0.4029	0.2265	0.1257	8711
Baseline-8	0.4052	0.1778	0.1518	6813
Baseline-8L	0.4070	0.1462	0.1986	4800
Baseline-10	0.3941	0.1296	0.2208	4324
NCF-6K	0.4077	0.0679	0.1527	6263
NCF-Tri	0.4756	0.0469	0.1983	9490
Braid-B	0.4419	0.1440	0.1901	7104
Braid-T	0.3407	0.1642	0.2150	6182
Bind1%-4	0.4968	0.1012	0.1185	6340
Bind.5%-4	0.4782	0.0859	0.1604	5925
T1(12)	0.3660	0.0680	0.1815	11201
T2(12)	0.3584	0.0840	0.1665	13356
T3(12)	0.3890	0.0309	0.1467	19260
DM-1	0.1175	0.2064	0.2279	22051
DM-5	0.0336	0.8161	0.2345	26133

Table A4.2 - Silicon-wetted expansion constants.

	$v_{F0}$	<i>First expansion</i>			<i>Second expansion</i>		
		$a_w$	$b_w$	$c_w$ (Pa)	$a_w$	$b_w$	$c_w$ (Pa)
Baseline-4	0.4038	0.3304	0.1032	19638	0.3618	0.0788	21543
Baseline-4A	0.4038	0.3086	0.1089	20116	0.3378	0.0852	18984
NCF-6K	0.4077	0.2870	0.1026	19274	0.3308	0.0662	20596
NCF-Tri	0.4756	0.2391	0.1113	17016	0.2693	0.0929	17187
Braid-B	0.4419	0.3111	0.0942	15379	0.3419	0.0597	25363
Braid-T	0.3407	0.3252	0.1513	11871	0.3337	0.1509	8181
bind(1)-4	0.4968	0.2439	0.1474	23027	0.2435	0.1454	20474



bind(0.5)-4	0.4954	0.2037	0.1796	16461	0.2198	0.1917	13866
T1(12)	0.3660	0.1924	0.1333	18469	0.2475	0.1077	16835
T1(16)	0.2968	0.3580	0.0679	26305	0.3702	0.0567	24652
T2(12)	0.3584	0.1712	0.1242	19861	0.2125	0.1088	17505
T3(12)	0.3890	0.1196	0.1457	23890	0.1146	0.1335	21292

## 7.5 Appendix 5 – MATLAB code for 1D flow simulation.

This code starts with material inputs, and then calculates the fill time for every model combination possibility discussed in Section 5.

```

clear; clc; %set mesh properties:
Lt=.16; dt=1; nnodes=100; da=1/nnodes; imax=100; tol=1e-6; %set properties:
Pamb=100000; Pi=Pamb; Pv=0; T=27; Sd=.534; n=4; rho=1760; Ak=2.403e-11; Bk=-1.875; vf0=0.4038; Aw=.1803;
Bw=.1645; Cw=7136; Av=1.2169*exp(T*-0.068287); Bv=0.000007643*exp(0.11164*T);
F=3; Df=7e-6; gamma=0.047; phetaCS=28.5; radCS=phetaCS*pi/180;
%constant property guesses, evaluated at the flow front:
visci=Av*exp(0*Bv); vfi=vf0/(1-Aw-(Bw*(Pamb-Pv)/(Cw+(Pamb-Pv)))); phii=1-vfi; Ki=Ak*vfi^Bk;

%fill-time for each model printed as "t_x" where x is the model combination
t_K=Lt^2*phii*visci/(2*Ki*(Pi-Pv))
t_KV=(1/Bv)*log(1/(1+Av*Bv*(Lt^2*phii/(2*Ki*(Pv-Pi))))))

%add compressibility
L=0; t=0; %use secant method to optimize dPda to get last Pr=0. Need 2 initial guesses for 1st node dP/da:
xA=-Pi/4; xB=-3*Pi/4; for j=1:imax, for i=1:nnodes, if i==1, Pr=Pi; dPda=xA; else, Pr=Pr+dPda*da;
dPda=dPda-(da*((dkdp/K)+((phi+(alph^2))/(h*phi))*dhdP))*dPda^2); %based on previous nodes properties
end %evaluate properties at this node:
alph=(i-1)/nnodes; Pc=Pamb-Pr; vf=vf0/(1-Aw-(Bw*(Pc)/(Cw+(Pc)))); phi=1-vf; K=Ak*vf^Bk; h=Sd*n/(rho*vf);
dhdP=(Sd*n/(rho*vf0))*(Bw*Cw/((Cw+Pc)^2));
dkdp=-Ak*Bk*vf0*((vf0/(1-Aw-(Bw*(Pc)/(Cw+Pc))))^(Bk-1))*((Bw/(Pc+Cw))-(Bw*Pc/((Pc+Cw)^2)))/((1-Aw-
(Bw*Pc/(Pc+Cw))^2));, end, PrA=Pr+dPda*da;
for i=1:nnodes, if i==1, Pr=Pi; dPda=xB; else, Pr=Pr+dPda*da; dPda=dPda-
(da*((dkdp/K)+((phi+(alph^2))/(h*phi))*dhdP))*dPda^2);, end
alph=(i-1)/nnodes; Pc=Pamb-Pr; vf=vf0/(1-Aw-(Bw*(Pc)/(Cw+(Pc)))); phi=1-vf; K=Ak*vf^Bk; h=Sd*n/(rho*vf);
dhdP=(Sd*n/(rho*vf0))*(Bw*Cw/((Cw+Pc)^2));
dkdp=-Ak*Bk*vf0*((vf0/(1-Aw-(Bw*(Pc)/(Cw+Pc))))^(Bk-1))*((Bw/(Pc+Cw))-(Bw*Pc/((Pc+Cw)^2)))/((1-Aw-
(Bw*Pc/(Pc+Cw))^2));, end, PrB=Pr+dPda*da; xl=xB-PrB*(xB-xA)/(PrB-PrA);
if abs((xl-xB)/xB)<tol, xS=xl; break, end, xA=xB; xB=xl; end, if j==imax, 'did not converge!!!!', end
%dPda is carried over from last node on the B-iteration - the P-gradient over last node for the P-field solution:
t_KC=Lt^2*phii*visci/(2*Ki*(-dPda))
%using dPda for last node, carried over from CK model:
t_KVC=(1/Bv)*log(1/(1+Av*Bv*(Lt^2*phii/(2*Ki*(dPda))))))

%no compressibility, but add capillary pressure, for both increasing and decreasing the pressure gradient
L=0; t=0; %first step done with Pcap=0:
vi=((2*Ki*(Pi-Pv)*dt/(phii*visci))^0.5)/dt; L=L+vi*dt; t=t+dt;
%subsequent time steps:
while L<Lt, phi=phii; K=Ki; visc=visci; v=pcapS(L,K,phi,visc,Pi,Pv); L=L+v*dt; t=t+dt; end, L_KP_decrease=L;
t_KP_decrease=t
L=0; t=0; vi=((2*Ki*(Pi-Pv)*dt/(phii*visci))^0.5)/dt; L=L+vi*dt; t=t+dt;

```

```

while L<Lt, phi=phii; K=Ki; visc=visci; v=pcapS2 (L,K,phi,visc,Pi,Pv); L=L+v*dt; t=t+dt;, end, L_KP_increase=L;
t_KP_increase=t
L=0; t=0; vi=((2*Ki*(Pi-Pv)*dt/(phii*visci))^0.5)/dt; L=L+vi*dt; t=t+dt;
while L<Lt, phi=phii; K=Ki; visc=Av*exp(t*Bv); v=pcapS (L,K,phi,visc,Pi,Pv); L=L+v*dt; t=t+dt;, end, L_KVP_decrease=L;
t_KVP_decrease=t
L=0; t=0; vi=((2*Ki*(Pi-Pv)*dt/(phii*visci))^0.5)/dt; L=L+vi*dt; t=t+dt;
while L<Lt, phi=phii; K=Ki; visc=Av*exp(t*Bv); v=pcapS2 (L,K,phi,visc,Pi,Pv); L=L+v*dt; t=t+dt;, end, L_KVP_increase=L;
t_KVP_increase=t

```

%do both compressibility and capillary pressure

```

L=0; t=0; while L<Lt %solve pressure field for this time step, use secant method again:
xA=-Pi/4; xB=-3*Pi/4; for j=1:imax, for i=1:nnodes, if i==1, Pr=Pi; dPda=xA;, else, Pr=Pr+dPda*da; dPda=dPda-
(da*((dkdp/K)+((phi+(alph^2))/(h*phi))*dhdp))*dPda^2;, end
alph=(i-1)/nnodes; Pc=Pamb-Pr; vf=vf0/(1-Aw-(Bw*(Pc)/(Cw+(Pc)))); phi=1-vf; K=Ak*vf^Bk; h=Sd*n/(rho*vf);
dhdp=(Sd*n/(rho*vf0))*(Bw*Cw/((Cw+Pc)^2));
dkdp=-Ak*Bk*vf0*((vf0/(1-Aw-(Bw*Pc/(Cw+Pc))))^(Bk-1))*((Bw/(Pc+Cw))-(Bw*Pc/((Pc+Cw)^2)))/((1-Aw-
(Bw*Pc/(Pc+Cw)))^2);, end, PrA=Pr+dPda*da;
if L==0, Pcapillary=0;, else, Pcapillary=(F/Df)*gamma*(vf/phi)*cos(acos(cos(radCS)-
(cos(radCS)+1)*tanh(4.96*((visci/gamma)*(-K*dPda/(phi*visci*L))^0.702)));, end, fA=PrA-Pv-Pcapillary;
for i=1:nnodes, if i==1, Pr=Pi; dPda=xB;, else, Pr=Pr+dPda*da; dPda=dPda-
(da*((dkdp/K)+((phi+(alph^2))/(h*phi))*dhdp))*dPda^2;, end
alph=(i-1)/nnodes; Pc=Pamb-Pr; vf=vf0/(1-Aw-(Bw*(Pc)/(Cw+(Pc)))); phi=1-vf; K=Ak*vf^Bk; h=Sd*n/(rho*vf);
dhdp=(Sd*n/(rho*vf0))*(Bw*Cw/((Cw+Pc)^2));
dkdp=-Ak*Bk*vf0*((vf0/(1-Aw-(Bw*Pc/(Cw+Pc))))^(Bk-1))*((Bw/(Pc+Cw))-(Bw*Pc/((Pc+Cw)^2)))/((1-Aw-
(Bw*Pc/(Pc+Cw)))^2);, end, PrB=Pr+dPda*da;
if L==0, Pcapillary=0;, else, Pcapillary=(F/Df)*gamma*(vf/phi)*cos(acos(cos(radCS)-
(cos(radCS)+1)*tanh(4.96*((visci/gamma)*(-K*dPda/(phi*visci*L))^0.702)));, end
fB=PrB-Pv-Pcapillary; xl=xB-fB*(xB-xA)/(fB-fA);
if abs((xl-xB)/xB)<tol, xS=xl;, break, end, xA=xB; xB=xl;, end, if j==imax, 'did not converge!!!!', end
%dPda, K, phi, visc carried over from last node on the B-iteration, quadratic of L=L0+dL, to accomodate dP/dalpha
instead of dP/dx
L=(L+(L^2-4*dt*K*dPda/(phi*visci))^0.5)/2; t=t+dt;, end, L_KCP_decrease=L; t_KCP_decrease=t

```

```

L=0; t=0; while L<Lt
xA=-Pi/4; xB=-3*Pi/4; for j=1:imax, for i=1:nnodes, if i==1, Pr=Pi; dPda=xA;, else, Pr=Pr+dPda*da; dPda=dPda-
(da*((dkdp/K)+((phi+(alph^2))/(h*phi))*dhdp))*dPda^2;, end
alph=(i-1)/nnodes; Pc=Pamb-Pr; vf=vf0/(1-Aw-(Bw*(Pc)/(Cw+(Pc)))); phi=1-vf; K=Ak*vf^Bk; h=Sd*n/(rho*vf);
dhdp=(Sd*n/(rho*vf0))*(Bw*Cw/((Cw+Pc)^2));
dkdp=-Ak*Bk*vf0*((vf0/(1-Aw-(Bw*Pc/(Cw+Pc))))^(Bk-1))*((Bw/(Pc+Cw))-(Bw*Pc/((Pc+Cw)^2)))/((1-Aw-
(Bw*Pc/(Pc+Cw)))^2);, end, PrA=Pr+dPda*da;
if L==0, Pcapillary=0;, else, Pcapillary=(F/Df)*gamma*(vf/phi)*cos(acos(cos(radCS)-
(cos(radCS)+1)*tanh(4.96*((visci/gamma)*(-K*dPda/(phi*visci*L))^0.702)));, end, fA=PrA-Pv+Pcapillary;
for i=1:nnodes, if i==1, Pr=Pi; dPda=xB;, else, Pr=Pr+dPda*da; dPda=dPda-
(da*((dkdp/K)+((phi+(alph^2))/(h*phi))*dhdp))*dPda^2;, end
alph=(i-1)/nnodes; Pc=Pamb-Pr; vf=vf0/(1-Aw-(Bw*(Pc)/(Cw+(Pc)))); phi=1-vf; K=Ak*vf^Bk; h=Sd*n/(rho*vf);
dhdp=(Sd*n/(rho*vf0))*(Bw*Cw/((Cw+Pc)^2));
dkdp=-Ak*Bk*vf0*((vf0/(1-Aw-(Bw*Pc/(Cw+Pc))))^(Bk-1))*((Bw/(Pc+Cw))-(Bw*Pc/((Pc+Cw)^2)))/((1-Aw-
(Bw*Pc/(Pc+Cw)))^2);, end, PrB=Pr+dPda*da;
if L==0, Pcapillary=0;, else, Pcapillary=(F/Df)*gamma*(vf/phi)*cos(acos(cos(radCS)-
(cos(radCS)+1)*tanh(4.96*((visci/gamma)*(-K*dPda/(phi*visci*L))^0.702)));, end
fB=PrB-Pv+Pcapillary; xl=xB-fB*(xB-xA)/(fB-fA);
if abs((xl-xB)/xB)<tol, xS=xl;, break, end, xA=xB; xB=xl;, end, if j==imax, 'did not converge!!!!', end
L=(L+(L^2-4*dt*K*dPda/(phi*visci))^0.5)/2; t=t+dt;, end, L_KCP_increase=L; t_KCP_increase=t

```

```

L=0; t=0; while L<Lt, xA=-Pi/4; xB=-3*Pi/4;, for j=1:imax, for i=1:nnodes, if i==1, Pr=Pi; dPda=xA;, else, Pr=Pr+dPda*da;
dPda=dPda-(da*((dkdp/K)+((phi+(alph^2))/(h*phi))*dhdp))*dPda^2;, end
alph=(i-1)/nnodes; Pc=Pamb-Pr; vf=vf0/(1-Aw-(Bw*(Pc)/(Cw+(Pc)))); phi=1-vf; K=Ak*vf^Bk; h=Sd*n/(rho*vf);
dhdp=(Sd*n/(rho*vf0))*(Bw*Cw/((Cw+Pc)^2));

```

```

dkdp=-Ak*Bk*vf0*((vf0/(1-Aw-(Bw*Pc/(Cw+Pc))))^(Bk-1))*((Bw/(Pc+Cw))-(Bw*Pc/((Pc+Cw)^2)))/((1-Aw-
(Bw*Pc/(Pc+Cw)))^2);, end, PrA=Pr+dPda*da;
if L==0, Pcapillary=0; else, visc=Av*exp(t*Bv); Pcapillary=(F/Df)*gamma*(vf/phi)*cos(acos(cos(radCS)-
(cos(radCS)+1)*tanh(4.96*((visc/gamma)*(-K*dPda/(phi*visc*L)))^0.702));, end, fA=PrA-Pv-Pcapillary;
for i=1:nnodes, if i==1, Pr=Pi; dPda=xB; else, Pr=Pr+dPda*da; dPda=dPda-
(da*((dkdp/K)+((phi+(alph^2))/(h*phi))*dhdp))*dPda^2; end
alph=(i-1)/nnodes; Pc=Pamb-Pr; vf=vf0/(1-Aw-(Bw*(Pc)/(Cw+(Pc))))); phi=1-vf; K=Ak*vf^Bk; h=Sd*n/(rho*vf);
dhdp=(Sd*n/(rho*vf0))*(Bw*Cw/((Cw+Pc)^2));
dkdp=-Ak*Bk*vf0*((vf0/(1-Aw-(Bw*Pc/(Cw+Pc))))^(Bk-1))*((Bw/(Pc+Cw))-(Bw*Pc/((Pc+Cw)^2)))/((1-Aw-
(Bw*Pc/(Pc+Cw)))^2);, end, PrB=Pr+dPda*da;
if L==0, Pcapillary=0; else, visc=Av*exp(t*Bv); Pcapillary=(F/Df)*gamma*(vf/phi)*cos(acos(cos(radCS)-
(cos(radCS)+1)*tanh(4.96*((visc/gamma)*(-K*dPda/(phi*visc*L)))^0.702));, end
fB=PrB-Pv-Pcapillary; xl=xB-fB*(xB-xA)/(fB-fA);
if abs((xl-xB)/xB)<tol, xS=xl; break, end, xA=xB; xB=xl; end, if j==imax, 'did not converge!!!!', end
%Dpa, K, phi, visc carried over from last node on the B-iteration, quadratic of L=L0+dL again
L=(L+(L^2-4*dt*K*dPda/(phi*visc))^0.5)/2; t=t+dt; end, L_KVCP_decrease=L; t_KVCP_decrease=t

```

```

L=0; t=0; while L<Lt, xA=-Pi/4; xB=-3*Pi/4; for j=1:imax, for i=1:nnodes, if i==1, Pr=Pi; dPda=xA; else, Pr=Pr+dPda*da;
dPda=dPda-(da*((dkdp/K)+((phi+(alph^2))/(h*phi))*dhdp))*dPda^2; end
alph=(i-1)/nnodes; Pc=Pamb-Pr; vf=vf0/(1-Aw-(Bw*(Pc)/(Cw+(Pc))))); phi=1-vf; K=Ak*vf^Bk; h=Sd*n/(rho*vf);
dhdp=(Sd*n/(rho*vf0))*(Bw*Cw/((Cw+Pc)^2));
dkdp=-Ak*Bk*vf0*((vf0/(1-Aw-(Bw*Pc/(Cw+Pc))))^(Bk-1))*((Bw/(Pc+Cw))-(Bw*Pc/((Pc+Cw)^2)))/((1-Aw-
(Bw*Pc/(Pc+Cw)))^2);, end, PrA=Pr+dPda*da;
if L==0, Pcapillary=0; else, visc=Av*exp(t*Bv); Pcapillary=(F/Df)*gamma*(vf/phi)*cos(acos(cos(radCS)-
(cos(radCS)+1)*tanh(4.96*((visc/gamma)*(-K*dPda/(phi*visc*L)))^0.702));, end, fA=PrA-Pv+Pcapillary;
for i=1:nnodes, if i==1, Pr=Pi; dPda=xB; else, Pr=Pr+dPda*da; dPda=dPda-
(da*((dkdp/K)+((phi+(alph^2))/(h*phi))*dhdp))*dPda^2; end
alph=(i-1)/nnodes; Pc=Pamb-Pr; vf=vf0/(1-Aw-(Bw*(Pc)/(Cw+(Pc))))); phi=1-vf; K=Ak*vf^Bk; h=Sd*n/(rho*vf);
dhdp=(Sd*n/(rho*vf0))*(Bw*Cw/((Cw+Pc)^2));
dkdp=-Ak*Bk*vf0*((vf0/(1-Aw-(Bw*Pc/(Cw+Pc))))^(Bk-1))*((Bw/(Pc+Cw))-(Bw*Pc/((Pc+Cw)^2)))/((1-Aw-
(Bw*Pc/(Pc+Cw)))^2);, end, PrB=Pr+dPda*da;
if L==0, Pcapillary=0; else, visc=Av*exp(t*Bv); Pcapillary=(F/Df)*gamma*(vf/phi)*cos(acos(cos(radCS)-
(cos(radCS)+1)*tanh(4.96*((visc/gamma)*(-K*dPda/(phi*visc*L)))^0.702));, end
fB=PrB-Pv+Pcapillary; xl=xB-fB*(xB-xA)/(fB-fA);
if abs((xl-xB)/xB)<tol, xS=xl; break, end, xA=xB; xB=xl; end, if j==imax, 'did not converge!!!!', end
L=(L+(L^2-4*dt*K*dPda/(phi*visc))^0.5)/2; t=t+dt; end, L_KVCP_increase=L; t_KVCP_increase=t

```

## 7.6 Appendix 6 – Image-J macro scripts for automation of image analysis.

***This macro calculates the areal percent of fibers in each image contained within a chosen directory, optimized for images at a magnification of 500x. Shading correction is included.***

***Thresholding is by the “Shanbhag dark” algorithm.***

```

macro "areal folder 500x" {
print("Starting 'areal folder light-corrected'");
//the shading correction macro does not support batch mode;
dir = getDirectory("Choose a Directory ");
list = getFileList(dir);
count = 0;
for (i=0; i<list.length; i++) {
path = dir+list[i];
open(path);
run("Split Channels");

```

```

run("A posteriori shading correction 514 v3", "image=["+list[i]+" (red)] automatic initial_x=0 initial_y=0
number_of_points_on_x=30 number_of_points_on_y=30 x_degree=2 y_degree=2");
selectWindow("Shading-corrected image");
run("Gaussian Blur...", "sigma=3.5");
run("Enhance Contrast", "saturated=0.5");
setAutoThreshold("Shanbhag dark");
run("Measure");
close();
close();
selectWindow("'" + list[i] + " (red)");
close();
run("A posteriori shading correction 514 v3", "image=["+list[i]+" (green)] automatic initial_x=0 initial_y=0
number_of_points_on_x=30 number_of_points_on_y=30 x_degree=2 y_degree=2");
selectWindow("Shading-corrected image");
run("Gaussian Blur...", "sigma=3.5");
run("Enhance Contrast", "saturated=0.5");
setAutoThreshold("Shanbhag dark");
run("Measure");
close();
close();
selectWindow("'" + list[i] + " (green)");
close();
run("A posteriori shading correction 514 v3", "image=["+list[i]+" (blue)] automatic initial_x=0 initial_y=0
number_of_points_on_x=30 number_of_points_on_y=30 x_degree=2 y_degree=2");
selectWindow("Shading-corrected image");
run("Gaussian Blur...", "sigma=3.5");
run("Enhance Contrast", "saturated=0.5");
setAutoThreshold("Shanbhag dark");
run("Measure");
close();
close();
selectWindow("'" + list[i] + " (blue)");
close();
count++;
}
{
if (isOpen("Log")) {
selectWindow("Log");
run("Close" );
}
}
}

```

***This macro also calculates the areal percent of fibers in each image contained within a chosen directory, but is optimized for images at a magnification of 200x. Thresholding is also by the “Shanbhag dark” algorithm. No shading correction is deemed necessary.***

```

macro "areal folder 200x" {
print("Starting 'areal folder'");
dir = getDirectory("Choose a Directory ");
list = getFileList(dir);
setBatchMode(true);
count = 0;
for (i=0; i<list.length; i++) {
path = dir+list[i];
open(path);

```

```

run("Split Channels");
    run("Gaussian Blur...", "sigma=2");
    run("Enhance Contrast", "saturated=0.5");
setAutoThreshold("Shanbhag dark");
    run("Measure");
    close();
    run("Gaussian Blur...", "sigma=2");
    run("Enhance Contrast", "saturated=0.5");
setAutoThreshold("Shanbhag dark");
    run("Measure");
    close();
    run("Gaussian Blur...", "sigma=2");
    run("Enhance Contrast", "saturated=0.5");
setAutoThreshold("Shanbhag dark");
    run("Measure");
    close();

count++;
}
{
if (isOpen("Log")) {
    selectWindow("Log");
    run("Close" );
}
}

```

***This macro counts the number of fibers in each image contained within a chosen directory, optimized for images at a magnification of 500x. Shading correction is included. The “default” threshold algorithm is employed.***

```

macro "count folder 500x" {
print("Starting 'count folder light-corrected'");
//the shading correction macro does not support batch mode;
dir = getDirectory("Choose a Directory ");
list = getFileList(dir);
count = 0;
for (i=0; i<list.length; i++) {
    print(count+" files processed of "+list.length);
    path = dir+list[i];
    open(path);
    run("Split Channels");
        run("A posteriori shading correction 514 v3", "image=["+list[i]+" (red)] automatic initial_x=0 initial_y=0
number_of_points_on_x=30 number_of_points_on_y=30 x_degree=2 y_degree=2");
        selectWindow("Shading-corrected image");
        rename(list[i] + " (red)-c");
        run("Gaussian Blur...", "sigma=3.5");
        run("Enhance Contrast", "saturated=0.5");
        setAutoThreshold();
        getThreshold(L, U);
        if (L==0) {
            L = U; U=255;
        }
        setThreshold(L, U);
        // This ensures black objects and white background, as particle analysis is done on black
        run("Convert to Mask");
        run("Watershed");

```

```

        run("Analyze Particles...", "size=400-6000 circularity=0.00-1.00 show=Nothing clear summarize");
        close();
        close();
selectWindow(""+list[i]+" (red)");
close();
        run("A posteriori shading correction 514 v3", "image=["+list[i]+" (green)] automatic initial_x=0 initial_y=0
number_of_points_on_x=30 number_of_points_on_y=30 x_degree=2 y_degree=2");
        selectWindow("Shading-corrected image");
        rename(list[i] + " (green)-c");
        run("Gaussian Blur...", "sigma=3.5");
        run("Enhance Contrast", "saturated=0.5");
        setAutoThreshold();
        getThreshold(L, U);
        if (L==0) {
            L = U; U=255;
        }
        setThreshold(L, U);
        run("Convert to Mask");
        run("Watershed");
        run("Analyze Particles...", "size=400-6000 circularity=0.00-1.00 show=Nothing clear summarize");
        close();
        close();
selectWindow(""+list[i]+" (green)");
close();
        run("A posteriori shading correction 514 v3", "image=["+list[i]+" (blue)] automatic initial_x=0 initial_y=0
number_of_points_on_x=30 number_of_points_on_y=30 x_degree=2 y_degree=2");
        selectWindow("Shading-corrected image");
        rename(list[i] + " (blue)-c");
        run("Gaussian Blur...", "sigma=3.5");
        run("Enhance Contrast", "saturated=0.5");
        setAutoThreshold();
        getThreshold(L, U);
        if (L==0) {
            L = U; U=255;
        }
        setThreshold(L, U);
        run("Convert to Mask");
        run("Watershed");
        run("Analyze Particles...", "size=400-6000 circularity=0.00-1.00 show=Nothing clear summarize");
        close();
        close();
selectWindow(""+list[i]+" (blue)");
close();
count++;
}
{
if (isOpen("Log")) {
selectWindow("Log");
run("Close" );
}
}
}

```

***This macro also counts the number of fibers in each image contained within a chosen directory, but is optimized for images at a magnification of 200x. Smaller particle size limits and a smaller***

***Gaussian blur filter radius accommodate the smaller fibers. Shading correction is included. The “default” threshold algorithm is employed.***

```

macro "count folder 200x" {
print("Starting 'count folder 200x'");
//the shading correction macro does not support batch mode;
dir = getDirectory("Choose a Directory ");
list = getFileList(dir);
count = 0;
for (i=0; i<list.length; i++) {
print(count+" files processed of "+list.length);
path = dir+list[i];
open(path);
run("Split Channels");
run("A posteriori shading correction 514 v3", "image=["+list[i]+" (red)] automatic initial_x=0 initial_y=0
number_of_points_on_x=30 number_of_points_on_y=30 x_degree=2 y_degree=2");
selectWindow("Shading-corrected image");
rename(list[i] + " (red)-c");
run("Gaussian Blur...", "sigma=2");
run("Enhance Contrast", "saturated=0.5");
setAutoThreshold();
getThreshold(L, U);
if (L==0) {
L = U; U=255;
}
setThreshold(L, U);
// This ensures black objects and white background, as particle analysis is done on black
run("Convert to Mask");
run("Watershed");
run("Analyze Particles...", "size=25-6000 circularity=0.00-1.00 show=Nothing clear summarize");
close();
close();
selectWindow("'" + list[i] + " (red)");
close();
run("A posteriori shading correction 514 v3", "image=["+list[i]+" (green)] automatic initial_x=0 initial_y=0
number_of_points_on_x=30 number_of_points_on_y=30 x_degree=2 y_degree=2");
selectWindow("Shading-corrected image");
rename(list[i] + " (green)-c");
run("Gaussian Blur...", "sigma=2");
run("Enhance Contrast", "saturated=0.5");
setAutoThreshold();
getThreshold(L, U);
if (L==0) {
L = U; U=255;
}
setThreshold(L, U);
run("Convert to Mask");
run("Watershed");
run("Analyze Particles...", "size=25-6000 circularity=0.00-1.00 show=Nothing clear summarize");
close();
close();
selectWindow("'" + list[i] + " (green)");
close();
run("A posteriori shading correction 514 v3", "image=["+list[i]+" (blue)] automatic initial_x=0 initial_y=0
number_of_points_on_x=30 number_of_points_on_y=30 x_degree=2 y_degree=2");
selectWindow("Shading-corrected image");
rename(list[i] + " (blue)-c");

```

```

run("Gaussian Blur...", "sigma=2");
run("Enhance Contrast", "saturated=0.5");
setAutoThreshold();
getThreshold(L, U);
if (L==0) {
    L = U; U=255;
}
setThreshold(L, U);
run("Convert to Mask");
run("Watershed");
run("Analyze Particles...", "size=25-6000 circularity=0.00-1.00 show=Nothing clear summarize");
close();
close();
selectWindow(""+list[i]+" (blue)");
close();
count++;
}
{
if (isOpen("Log")) {
selectWindow("Log");
run("Close" );
}}

```

***This macro calculates the area of voids in each image contained within a chosen directory. It employs the “MinError” threshold algorithm to distinguish voids from the rest of the image.***

```

macro "void folder min-error" {
print("Starting 'void measurement'");
dir = getDirectory("Choose a Directory ");
list = getFileList(dir);
setBatchMode(true);
count = 0;
for (i=0; i<list.length; i++) {
    path = dir+list[i];
    open(path);
    print(path);
    run("Split Channels");
setAutoThreshold("MinError(I)");
run("Measure");
close();
setAutoThreshold("MinError(I)");
run("Measure");
close();
setAutoThreshold("MinError(I)");
run("Measure");
close();
count++;
}
{
if (isOpen("Log")) {
selectWindow("Log");
run("Close" );
}}

```



## Curriculum Vitae (CV)

### ANDREW R. GEORGE

Ostronstigen 24, 94135 Piteå, SE  
2050193

byuandy@gmail.com

+46(0)72-

#### EDUCATION

**M.S. Degree**, Engineering Technology, Brigham Young University, December 2006

-Emphasis: Plastics/Composites Materials

-Thesis: "A New Spectroscopic Method for the Non-Destructive Characterization of Weathering Damage in Plastics"

**B.S. Degree**, Chemical Engineering, Brigham Young University, December 2000

-Emphasis: Biomedical Engineering

#### PROFESSIONAL EXPERIENCE AND EMPLOYMENT

**Research Engineer: Mechanics**

Feb. 2010-present

*Swerea SICOMP AB*

Piteå, Sweden

-Composites materials/processing engineer: developing new/current processes, as well as process modeling and simulation strategies

**Marie Curie Research Fellow**

March 2007-Feb. 2010

*Stuttgart University – Institute Of Aircraft Design*

Stuttgart, Germany

-Prestigious European fellowship; granted complete funding for duration of Ph.D. studies

-Researched novel technologies in resin infusion composites manufacturing and modeling

-Directly consulted for European and American industrial and academic entities

-Organized 3-day seminar for 17 peers/professors on composites processes/modeling

-Assisted in preparation of successful European Commission funding proposals

**Instructor (part time faculty)**

Sept. 2006-April 2007

*Brigham Young University – School Of Technology*

Provo, Utah, USA

-Head Instructor, class of 250 students: History of Creativity in arts, science, and technology

-Head Instructor, class of 20 students: Introduction to Manufacturing Processes

**Research Assistant**

Sept. 2001-April 2007

*Brigham Young U. – School Of Technology/Chemical Engineering*

Provo, Utah, USA

-Planned, executed, and reported on various plastics/composites experiments contracted from

industry companies: material property testing, structural failure investigation, chemically-induced

degradation research, reverse engineering of gel pad manufacture

**Chief Information Officer/Secretary**

Feb. 2006-Jan. 2007

*National Association Of Graduate/Professional Students*

Washington DC, USA

-Executive board member charged with information transparency and communications for a non-profit umbrella group for the 2 million graduate/professional students in the USA

-Supervised website content for a virtual organization: [www.nagps.org](http://www.nagps.org)

**Manager – Plastics and Composites Lab**

Sept. 2005-Aug. 2006

*Brigham Young University*

Provo, Utah, USA

-Supervised usage of plastics and composites processing facilities and materials inventory

- Consulted faculty and students with all phases of manufacturing projects: idea generation for product solutions, mold and process setup, manufacturing, post-processing
- Directed lab tours for engineering classes from BYU and the University of Utah

**Teaching Assistant – Plastics Materials and Processing** Sept. 2003-Aug. 2006  
*Brigham Young University* Provo, Utah, USA

- Prepared/Graded exams and substitute-lectured for a class of 60 students
- Maintained plastics/composites processing and testing equipment and prepared/gave laboratory demonstrations

**Teaching Assistant – History of Creativity** Sept. 2001-Aug. 2006  
*Brigham Young University* Provo, Utah, USA

- Prepared/Graded exams and substitute-lectured for a class of 250 students

**Vice President** April 2005-April 2006  
*Brigham Young University Graduate Student Association* Provo, Utah, USA

- Part of 4-person presidency representing 3000 BYU graduate students to the administration
- Directed a committee of 20 student representatives charged with organizing monthly academic presentations/symposia and social activities with up to 1200 attendees

**Intern – Research and Development** May 2001-Aug. 2001  
*Advanced Technology Materials, Inc.* Danbury, CT

- Researched development of new product: Gallium Nitride semiconductor wafers
- Managed inventory (\$40K/month), negotiated contracts, and created parts database

**Grader – Advanced Engineering Math** Sept. 1998-Dec. 1998  
*Brigham Young University* Provo, UT

**Office/Lab Assistant – Operations Department** May 1998-Aug. 1998  
*Northrop Grumman, Norden Systems* Norwalk, CT

- Executed various lab operations: reagent titration, dielectric, oil-particulate analysis
- Researched plant operations shortcomings and completed capital investment proposals
- Revised procedure manuals and time standard databases for ISO 9001 readiness

**Volunteer Representative - Guatemala, Belize** Sept. 1995-Aug.1997

- Responsible for training, motivating, and supervising over twenty-eight full-time volunteers.
- Provided humanitarian aid

## SKILLS/INTERESTS

Engineering: Composite/Polymer Design and Process Design, Processing Simulation, Bioengineering, Fluids, Chemical Reactions, Statistics, Quality, Semiconductors, Creating New Ventures  
 Sciences: Mathematics, Physics, Inorganic/Organic/Biochemistry, Human Physiology  
 Machines: Processing equipment (Resin Infusion, Textile Preforming, Injection/Rotational Molding, Thermoforming, Casting, Pre-preg Layup, Filament Winding), Electron and Light Microscopy, Mechanical Property Testing Equipment (Tensile, Flexural, Compression, Impact, Shear)  
 Software: Finite element analysis, image analysis, mathematics, simulation, 3D modeling, various programming languages, databases, word processing, publishing  
 Languages: Spanish, fluent oral and written; German, conversational; K'ekchi', conversational

## PROFESSIONAL SOCIETIES

- Society for the Advancement of Material and Process Engineering (SAMPE)

#### **SCHOLARLY WRITING – PEER REVIEWED**

- George, A., K. Drechlsler, and A. Holmberg, "The Permeability of Carbon Fiber Preforming Materials: Sensitivity to Fabric Geometry," *Proceedings 20<sup>th</sup> Annual International SICOMP Conference, Piteå (Sweden)*, May 8-9, 2009.
- George, A., K. Drechlsler, and A. Holmberg, "The Permeability of Tackified, Stitched, and Braided Carbon Fiber Textiles: Experimental Characterization and Design Modeling," *Proceedings SAMPE 2009, Baltimore*, May 18-21.
- George, A. and B. Strong, "Weathering of Composites," *Composites Manufacturing*, Vol. 24, No. 10, November 2008, pp. 22-28, 55-56.
- George, A. and B. Strong, "A New Spectroscopic Method for the Non-Destructive Characterization of Weathering Damage in Plastics," *Journal of Advanced Materials*, Vol. 40, No. 2, April 2008, pp. 41-56.
- George, A. / Pitt, W.G., "Comparison of corneal epithelial cellular growth on synthetic cornea materials," *Biomaterials*, Vol. 23, No. 5, March 2002, pp. 1369-1373.

#### **SCHOLARLY WRITING – NON-PEER REVIEWED**

- George, A., 4 Technical Reports for GE Energy to characterize and evaluate experimental membranes for the VAP process in oven-curing resin infusion. Munich, Germany, June-November 2008.
- George, A. and H. Ringwald, 2 Technical Reports for Cornerstone Research Group (CRG) to study the applicability of merging two new technologies: microwaving polymer heating and heat activation of shape memory polymers. Dayton, Ohio, USA, September 2007.
- George, A., Technical Report for PolyProcessing to compare the chemical resistance to hydrofluoric acid of cross-linked high-density polyethylene (XLPE) containers with that of linear high-density polyethylene (HDPE). French Camp, California, USA, March 2005.
- George, A., Technical Report for PolyProcessing to compare the chemical resistance to nitric acid of cross-linked high-density polyethylene (XLPE) containers with that of linear high-density polyethylene (HDPE). French Camp, California, USA, December 2004.
- George, A. and B. Pitt, Manufacturing Plan for a Return Electrode Gel Pad for MegaDyne Medical. Sandy, Utah, September 2003.
- Strong, B. and A. George, Technical Report for Superyacht Solutions on the nature of UV and oxidative degradation in FRP gelcoats, Gold Coast Australia, March 2003.
- George, A., Technical Report for Dr. Brent Strong on the changes in flexural strength of acetal when exposed to hydrochloric acid, used in his expert witness in *Brody Chemical Co. v. Hydro Engineering*, 2001 (a case involving possible chemical attack on plastic parts in a pump assembly). Provo, Utah, USA, December 2001.